Deformation capacity of reinforced concrete beams:

New insights for the assessment of sound and corroded members

Alberto Stella

DEFORMATION CAPACITY OF REINFORCED CONCRETE BEAMS: NEW INSIGHTS FOR THE ASSESSMENT OF SOUND AND CORRODED MEMBERS

DEFORMATION CAPACITY OF REINFORCED CONCRETE BEAMS: NEW INSIGHTS FOR THE ASSESSMENT OF SOUND AND CORRODED MEMBERS

Doctoral thesis

for the fulfillment of the degree of Doctor of Philosophy

from the Iuav Doctoral school in Architecture, City and Design – Cycle XXXIV

Track: *Innovation for building and cultural heritage*

defended on 11 October 2022 by

Alberto Stella

Born on 21 September 1991 in Marostica, Italy

Dipartimento di Culture del Progetto
Università Iuav di Venezia
Venezia, Italy

Supervision board

Prof. eng. Anna Saetta	Università Iuav di Venezia	Supervisor
Dr. eng. Luisa Berto	Università Iuav di Venezia	Co-supervisor
Dr. eng. Diego Alejandro Talledo	Università Iuav di Venezia	Co-supervisor

External reviewers

Prof. eng. Alberto Meda	Università di Roma "Tor Vergata"
Dr. ir. Yuguang Yang	Technische Universiteit Delft

Examination committee

Prof. arch. Antonella Cecchi	Università Iuav di Venezia
Prof. eng. Rosario Ceravolo	Politecnico di Torino
Prof. eng. Alberto Meda	Università di Roma "Tor Vergata"

Università Iuav
di Venezia

Keywords:
Reinforced concrete beams, deformation capacity, ductility, reinforcement corrosion, deformation demand, ground settlements, MT-DInSAR

Front & Back:
Artwork from the author and picture courtesy of Prof. Alberto Meda.

To my family

SUMMARY

Inelastic deformation capacity is a fundamental characteristic for reinforced concrete (RC) members, since it allows redistribution of internal actions in structures and it provides them with the ability to withstand imposed inelastic deformation demands, such as those due to settlement of supports. In addition, deformation capacity really is a design-governing parameter for RC structures in seismic prone areas, which should be able to survive strong seismic events without reaching collapse. In performance-based design and assessment practices, the evaluation of deformation demands and deformation capacity in structural RC elements represents one of the backbones of the structural assessment procedure.

Approaches for the estimation of the deformation capacity are needed both for the design of new buildings and for the assessment of existing ones. Effective methods, based on the actual mechanical behaviour of structures, should be adopted for such estimation, rather than using opaque rules or prescriptions which often are based on simplified and not always valid assumptions.

When dealing with existing RC structures, additional aspects need to be considered, since it is widely recognized that deterioration of structural properties due to various phenomena, such as rebars corrosion, freeze-thaw cycles, alkali-aggregate reaction, can have significant negative impacts on the structural behaviour. Among the various deterioration mechanisms, corrosion of steel rebars is one of the most relevant and widespread. It affects not only rebars geometry and mechanical characteristics, but also the behaviour of surrounding concrete and steel-concrete interface. Consequences on the behaviour of RC members involve the change of resisting mechanism and failure mode and, in many cases, reduction of strength and deformation capacity.

An equally important aspect of the structural assessment is related to the estimation of deformation demands at structural members, which can involve several difficulties due to uncertainties and lack of information on the actions affecting the structures. In the case of deformation demands induced by differential ground settlements, one of the major issues lays in determine the magnitude and distribution of ground settlements. Traditional methods largely adopted in practice to do so are often based on strongly simplified assumptions, and cannot consider effects due to the soil-structure interaction, which can be relevant in many cases.

This research work provides tools and useful insights and recommendations aimed at improving practice-oriented structural assessment procedures based on deformation capacity vs. demand checks.

First, a comprehensive analytical framework for the analysis of sectional behaviour of doubly reinforced concrete beams is proposed, specifically tailored for an effective estimation of curvature capacity and ductility. The proposed framework can be adopted to analyze sections in both undamaged and corroded conditions. The formulation considers all the possible different failure modes achievable by a doubly reinforced concrete beam section, taking into account of actual strain values in bottom and top

reinforcement layers and considering the possible spalling of the concrete cover, so allowing to overcome some of the limits of many traditional formulations.
A subsequent part of the research presents the analysis of results from a two-steps experimental campaign on sound and corroded concrete beams, in which the sensors layout and the adopted measuring techniques allowed to detect the evolution of the crack pattern and to get useful information to study the deformation capacity of the tested members. Results from the tests have are used as reference to perform analytical and numerical analyses aimed at testing the performances of some practice-oriented modelling tools, focusing on checking their ability to correctly predict the failure mode and deformation capacity of corroded RC members.
The last part of this research work aims at investigating potentials and limitations of a class of satellite remote sensing techniques which can be used to monitor ground settlements in urban areas, and so improving the analysis of settlement-induced deformation demand in structural members of RC buildings. In particular, the study investigates the employability of remote sensing techniques based on multi-temporal differential satellite radar interferometry (MT-DInSAR) for the monitoring of low-rate deformations of soil and buildings, to be used to provide helpful information for structural monitoring and assessment of constructions.
Overall, the tools and recommendations proposed in the present work aim to be useful in fostering the improvement of engineering practices employed for the design and assessment of RC structures.

SINTESI

La capacità deformativa in campo anelastico è una proprietà fondamentale per gli elementi in calcestruzzo armato (c.a.), in quanto consente la ridistribuzione delle sollecitazioni in strutture iperstatiche e permette agli edifici di far fronte a campi di deformazione imposte, come quelli generati dai cedimenti dei vincoli. Inoltre, la capacità deformativa spesso risulta una caratteristica fondamentale per le strutture in c.a. in zona sismica, che devono essere in grado di sopravvivere a forti terremoti senza raggiungere il collasso.
Negli approcci di progettazione e verifica strutturale basati sul controllo delle prestazioni, la valutazione delle domande e della capacità di deformazione degli elementi strutturali rappresenta una delle colonne portanti. Approcci per la stima della capacità deformativa sono necessari sia per la progettazione di nuovi edifici che per la verifica di quelli esistenti. Per tale stima, si dovrebbero adottare metodi efficaci e basati sull'effettivo comportamento meccanico delle strutture, piuttosto che regole o prescrizioni opache, spesso derivate da ipotesi semplificate e non sempre valide. Nell'analisi di strutture in calcestruzzo armato esistenti, è necessario poi considerare ulteriori aspetti, poiché è ampiamente noto come il deterioramento delle proprietà strutturali causato da vari fenomeni, come la corrosione delle armature, i cicli di gelo e disgelo, le reazioni alcali-aggregati, può avere un significativo impatto negativo sul comportamento strutturale. Tra i vari meccanismi di deterioramento, la corrosione delle armature è sicuramente uno dei più rilevanti e diffusi. Essa influenza non solo la geometria e le caratteristiche meccaniche delle barre, ma anche il comportamento del calcestruzzo circostante e dell'interfaccia acciaio-calcestruzzo. Tali aspetti spesso comportano conseguenze importanti sul comportamento degli elementi in c.a., come possibili modificazione dei meccanismi resistenti e della modalità di rottura e, in molti casi, la riduzione della capacità portante e della capacità deformativa.
Un aspetto altrettanto importante della valutazione strutturale è legato alla stima delle richieste di deformazione, che può essere spesso difficile a causa delle incertezze e della mancanza di informazioni sulle azioni che interessano le strutture. Nel caso di richieste di deformazione indotte da cedimenti differenziali del terreno, uno dei problemi principali consiste nel determinare l'entità e la distribuzione dei cedimenti. I metodi tradizionali, largamente adottati nella pratica, si basano spesso su ipotesi fortemente semplificate e spesso non considerano gli effetti dovuti all'interazione terreno-struttura, che possono essere rilevanti in molti casi.
Questo lavoro di ricerca fornisce strumenti, nonché utili spunti e raccomandazioni, volti a migliorare alcune procedure di analisi e verifica strutturale pensate per l'utilizzo nella pratica professionale, e basate sulle verifiche della capacità deformativa confrontata con la rispettiva domanda.
Per prima cosa, viene proposto un approccio analitico completo per l'analisi del comportamento sezionale di travi in calcestruzzo con doppia armatura, formulato specificamente per fornire una stima della capacità in curvatura e della corrispondente duttilità. L'approccio proposto può essere adottato per analizzare sezioni sia in

condizioni non danneggiate che in condizioni corrose. La formulazione presentata considera tutti le possibili modalità di rottura raggiungibili da una sezione in calcestruzzo con doppia armatura, tenendo conto dei valori effettivi delle deformazioni sviluppate nelle armature inferiori e superiori, e considerando la possibile espulsione del copriferro, consentendo così di superare alcuni dei limiti di molte formulazioni tradizionali.

Una parte successiva della ricerca presenta l'analisi dei risultati di una campagna sperimentale su travi in calcestruzzo corrose che si è svolta in due fasi, e in cui la disposizione dei sensori e le tecniche di misurazione adottate hanno permesso di seguire l'evoluzione delle fessure e di ottenere informazioni utili per studiare la capacità deformativa degli elementi. I risultati delle prove sono stati utilizzati come riferimento per eseguire una serie di analisi volte a testare le prestazioni di alcuni strumenti di modellazione analitici e numerici utilizzabili nella pratica professionale, focalizzando l'attenzione sulla valutazione della loro capacità di simulare correttamente la modalità di rottura e la capacità deformativa di travi in calcestruzzo corrose.

L'ultima parte del presente lavoro di ricerca mira a indagare le potenzialità e i limiti di alcune tecniche di telerilevamento che possono essere utilizzate per monitorare i cedimenti del terreno nelle aree urbane, migliorando così l'analisi della domanda di deformazione negli elementi strutturali degli edifici in calcestruzzo armato soggetti a cedimenti del terreno. In particolare, lo studio analizza l'impiego di tecniche di telerilevamento basate sull'interferometria radar satellitare differenziale multi-temporale (MT-DInSAR) per il monitoraggio delle deformazioni lente del suolo e degli edifici, da utilizzare per fornire informazioni utili al monitoraggio strutturale e alla verifica degli edifici esistenti. Complessivamente, gli strumenti e le raccomandazioni proposte nel presente lavoro intendono essere utili per favorire il miglioramento delle pratiche ingegneristiche impiegate per la progettazione e la verifica delle strutture in c.a.

CONTENTS

1

Introduction

Earthquakes do not read the codes.
Thomas Paulay

Several countries all over the world are nowadays facing challenges related to the management and maintenance of their public and private built stock, of which a significant proportion are reinforced concrete structures [1]. *Aging constructions are susceptible to deterioration of material properties, often induced by environmental stressors, while loads on structures have in many cases grown significantly over the years, with respect to the values foreseen at the time of construction. Moreover, buildings and infrastructures built in areas prone to earthquakes, ground settlements, landslides or other natural hazards are often characterized by a high vulnerability* [2]. *The relevance of implementation of practices and the development of codes and recommendations to fostering disaster-resistant structures have been clearly remarked in the Sendai Framework for Disaster Risk Reduction 2015–2030* [3], *as well as the need to promote the resilience of new and existing critical infrastructures. With regards to this aim, performance-based engineering can be a valuable tool to be used in the design of new structures and assessment of existing ones, in order to provide a rational basis for solutions aimed at guaranteeing that engineering facilities could fulfill their intended purposes* [4]. *Structural performances in terms of resilience and robustness against various hazards require constructions to possess a ductile structural behaviour, which can only be achieved by ensuring a deformation capacity capable of withstanding the deformation demands. The research work presented in this thesis addresses aspects which are relevant for the deformation capacity and deformation demand estimations performed in the engineering practice for the structural assessment of reinforced concrete members. In this chapter, a general introduction is provided.*

1.1 Relevance of deformation capacity for reinforced concrete buildings subjected to various hazards

Inelastic deformation capacity is a fundamental property for reinforced concrete (RC) members. It allows redistribution of internal actions in structures and it provides them with the ability to withstand imposed inelastic deformation demands, such as those due to settlement of supports [5], [6]. Moreover, deformation capacity becomes a design-governing characteristic when it is to make an RC structure capable to survive strong seismic events without collapsing. In fact, it has been widely recognized nowadays that what really allows a structure to properly resist strong earthquakes is its ability to withstand the induced deformation demands at members – by means of exploiting their deformation capacity – rather than its strength [7]. In other words, the structure should behave in a ductile way, i.e., it must be able to undergo the induced large (cyclic) deformations almost without reducing its load-carrying capacity [8], [9].

The aforementioned concepts, although they may seem intuitive now, took quite a long time to be discovered, processed and understood in a clear way, starting from the first decades of the twentieth century and continuing till the present days [9], [10].

A starting point of this journey can be identified between the 1920s and 1930s, when it started to be noticed that buildings which have been designed against a certain amount of horizontal load associated to wind actions demonstrated better performances also during earthquakes. This understanding gradually led to the introduction of concepts related to horizontal inertia forces developed in buildings due to the imposed ground motion and to the adoption of minimum values of horizontal actions for the design of new buildings in earthquake prone areas.

Refinements of this approach matured between the 1940s and 1950s, when the availability of recorded ground motion data became more widespread, and significant advances in the analysis of dynamic response of structures have been made. This combined source of new knowledge started leading around 1960s to the adoption of design earthquake actions dependent on the vibration period of structures.

In the same years, however, it has started to be recognized that several buildings which survived strong earthquakes without collapsing or even developing heavy damages were actually designed for horizontal strength values much lower than the seismic loads calculated considering their elastic response to those seismic events. These observations, together with the advent of computer-based inelastic time-history analyses, paved the way to the understanding that the seismic-induced collapse of a building is not straightforward due to the reaching of its lateral strength capacity associated to the flexural yielding of its members. In fact, it has been clarified that if members reach flexural yielding but they are able to undergo inelastic flexural deformations without breaking (i.e., reducing their strength) for any cause, then the building can most likely survive the earthquake. This led also to a refinement in the understanding of the actual collapse mechanisms in RC buildings, and more awareness grew about some particular failure causes, such as: i) the development of significant flexural strength reductions in members when they experience too large inelastic flexural deformations; ii) the development of other failure mechanisms in members or joints, characterized by a brittle failure which leads to a sudden strength reduction.

Since the 1960s, the ductile behaviour of RC buildings has been gradually exploited, adopting design approaches based on inelastic response of structures [11], [12]. Emphasis has been placed on guaranteeing ductility capacity of members, defined as the ratio between the ultimate deformation capacity and the deformation at flexural yielding, and adopted as an indicator of the structure's ability to undergo inelastic deformations. The choice behind this adoption was mainly due to the design philosophy adopted at the time, and still widely present nowadays, which aims to express seismic demands in terms of equivalent inertia forces and to use them in design procedures based on linear elastic analyses. The definition of a ductility demand, which would require an adequate ductility capacity, was so intended to easily estimate reduced design strength values from elastically calculated strength demands, considering the benefits granted by the inelastic structural response [12].

In order to actually exploit the benefits of a ductile behaviour in RC structures, specific design expedients had been developed and associated design rules had been established. The backbone element for the design of buildings having a ductile behaviour against seismic actions has been defined by the set of rules commonly grouped under the term of "capacity design" philosophy [13]. These rules aim to guarantee that brittle failures would not occur in any structural part and/or component, so that the main deformation mechanism developing in the structure would be due to flexure at ends of ductile members (i.e., members which possess adequate deformation capacity). The first proposals of capacity design principles date back again to the 1960s [12], [14], while the process involving their formalization and widespread adoption took place starting from the 1970s and gradually continued in the subsequent decades [8], [9].

Along with capacity design principles, two other aspects of design have been recognized to be essential in order to achieve a ductile structural behaviour under seismic loading, namely, global conceptual design and local detailing [9], [4]. The first one involves considerations about mass, strength and stiffness distribution in the buildings, with the aim of avoiding as much as possible local concentrations of high ductility demands during earthquakes. The second aspect, on the other hand, aims at properly detailing the members (i.e., to design the member geometry, material characteristics and reinforcement layout) in order to provide them with sufficient ductility capacity to fulfil the seismic demand.

Despite code-adopted design approaches remained mainly focused on strength and ductility assessment, a renewed attention to design aspects directly addressing deformations – rather than strengths – arose during the early 1990s. This mainly occurred in an attempt to solve some critical aspects and shortcomings present in the design procedures based only on design actions derived from the trade-off between strength and ductility. In particular, one of the main gaps laid in the lack of checks for displacement capacity of members designed to carry only vertical loads. These elements, which were usually designed completely overlooking deformation demands, were prone to experience failure due to the exhaustion of their flexural deformation capacity or to P – Delta effects [15]. Emblematic examples have been provided in the mid-1990s, when the 1994 Northridge Earthquake stroke California, and several RC buildings experienced damages or collapse [16]. One of the most infamous examples is the parking facility of California State University in Northridge, Fig. 1.1, in which the perimeter columns were designed for ductile behaviour and lateral load-carrying capacity, while the inner ones have been designed only considering vertical loads. The

structure experienced the collapse of a significant portion, due to the failure of the inner columns for a combined effect of exceeded deformation demands and P – Delta effects [17]. While issues of deformation compatibility dramatically emerged and started to be considered also in the revisions of design codes, the idea of using deformation as main design and assessment parameter rose back again among the research community. In fact, the idea in itself – to directly use deformations instead of equivalent forces to express seismic demands – was not completely new, since some suggestions about a seismic design approach based on maximum displacement demands had already been proposed in the 1960s [18]. Evolving and refining this concept, several approaches have been proposed between the 1990s and the 2000s to implement what have been called "displacement-based design" (DBD) procedures [15], [19], [20], [21], [22].

Fig. 1.1. Parking facility of California State University at Northridge (CA) partially collapsed during the 1994 Northridge Earthquake [23]

The common core philosophy has been to propose design and/or assessment procedures in which the comparison between demands and capacities of structural members is performed in terms of deformations. The application of this type of approaches is more straightforward in the case of the assessment of an existing structure than in that of the design of a new building [4]. The simple reason lays in the fact that for new structures the geometry of the members is initially unknown and so several iterative checks are often needed within the procedure. In this context is significant to note that the first version of Eurocode 8 – Part 3 [24] has adopted a deformation-based approaches for the assessment of existing RC members.

During the 2010s and 2020s displacement-based seismic design approaches have been better formalized and consequently proposed in a more comprehensive and harmonized way [10], [4]. Several advances have been made in the formulation of member deformation capacity, also considering effects due to lap-splicing or member strengthening [25], [26]. Deformation

capacity have expanded its role in the assessment of concrete members and further codes have explicitly introduced formulations for its evaluation, such as the *fib* Model Code 2010 [27].

In recent years, renewed attention has been also devoted to the promising possibilities offered by energy-based design and assessment approaches, which can consider the combined contribution of strength and deformation capacity of members under cyclic loading [28]. In this kind of approaches, demands can be expressed in terms of input energy provided by the ground motion to the structure and the capacity in terms of energy absorbed and dissipated by cyclic deformations of members [29], [30]. While some advances have been made in the past regarding the approaches for estimating the seismic energy demands [31], [32], [33], several developments needs to be addressed on the side of seismic capacity of buildings in terms of energy [28].

The aforementioned advances in the understanding of dynamic structural behaviour, accompanied by the evolution experienced by approaches adopted for seismic design and assessment of RC structures, highlighted the key role of deformation capacity as a fundamental structural property which, combined with a good global conceptual design of the structure and the rigorous application of capacity design principles, allows to obtain a ductile structural response during seismic events.

However, the relevance of deformation capacity and capacity design rules has not only been acknowledged with regards to the structural response to seismic actions. As an example, it has been shown that the adoption of seismic design rules, intended to provide a ductile structural response by means of capacity design principles and detailing for deformation capacity, allows buildings to achieve better performances also in the case of imposed deformations due to ground settlements [34]. In fact, deformation capacity of RC members is particularly important in framed structures subjected to settlements of foundations, in order to guarantee vertical load-carrying capacity also after the occurrence of significant ground deformations, which can cause the members to undergo inelastic behaviour [35]. In this context, the definition of deformation values corresponding to different damage conditions of the elements is also relevant, in order to quantify damages associated to a certain value of angular distortions [36]. In addition, it is worth to mention that structures designed for a ductile seismic behaviour can also demonstrate good performances against other kind of extreme actions, such as for example blast loading [37]. In those cases, in fact, detailing for ductile behaviour can help hit members to survive impulsive loading, or can help the buildings to prevent the collapse of extensive parts, so improving their robustness [38], [39], [40].

It clearly appears then, that the importance of deformation capacity in RC elements cannot be overstated: it is a fundamental characteristic that members need to possess in order a building would behave in a ductile, robust and reliable manner against different type of extreme actions having uncertain intensities.

1.2 DEFORMATION CAPACITY OF REINFORCED CONCRETE MEMBERS: CAN WE TAKE IT FOR GRANTED?

In order to truly enable an actual performance-based design and assessment of RC structures, effective approaches and tools are needed for an adequate estimation of deformation demand and capacity values. With regard to capacity assessment, different calculation approaches having different levels of complexity may be adopted, depending on the desired level of accuracy. This kind of classification fits well with the concept of the "levels of approximation" (LoA), which was introduced within the Model Code 2010 [27] as a tool for identify different approaches for capacity assessment, associated to different accuracy of results and complexity of calculations [41]. Approaches associated to a low level of approximation are characterized by reduced complexity and computational burden and should provide quite conservative capacity values. Simple analytical formulations which make use of very few geometrical and/or material parameters belong to this level. On the other hand, calculation procedures which make use of more complex formulations or advanced numerical analysis which can provide a less conservative capacity estimation should belong to one of the highest levels of approximation.
In engineering practice, both low and high LoA are useful. The former ones can be employed for first attempt calculation of members capacity in preliminary design phases, or whenever a building would require a particular conservativism in the analysis of its structural response. The latter ones can instead be adopted for the assessment of existing structures, for design of members characterized by particularly complex geometries, or whenever a less conservative approach is desirable.
When addressing capacity assessment approaches for low LoA, important requirements are indeed those of simplicity and effectiveness. Analytical or numerical approaches for a simplified estimation of deformation capacity should be simple, though still avoid excessive underestimation or overestimation of capacity values.
For deformation capacity assessment of RC members various analytical formulations have been proposed [8], [42], [43], [44], [6]. These models usually depend on various parameters, among which the amount of longitudinal reinforcement, the effectiveness of concrete confinement and the acting axial load are particularly influential.
However, for some type of members, such as for example beams with symmetrical longitudinal reinforcement layout, the deformation capacity is sometimes taken for granted [45]. This of course doesn't mean that the actual deformation capacity is infinitely large, but that it is considerably high, compared to the usual values of the demand. Despite this kind of assumptions are sometimes very useful to speed-up the design process, in other cases an actual quantification of the effective deformation capacity is instead desirable, especially when unconventional steel-related failure could be expected, such as premature steel failure due to partial spalling of the concrete cover, buckling of longitudinal rebars or low-cycle fatigue effects on steel [4]. In fact, such kind of phenomena can change the flexural failure mode of the RC sections, sometimes leading to very low values of ultimate deformation, so making the deformation capacity quite far from being a property allowed to be taken for granted.

Other cases for which it is not feasible to avoid an actual quantification of the effective deformation capacity regard RC members affected by degradation phenomena. In fact, it has been extensively observed that degradation of structural properties due to various phenomena, such as reinforcement corrosion, freeze-thaw cycles, alkali-aggregate reaction, can have significant negative impacts on the structural performances [46], [47], [48]. Among the various degradation mechanisms, corrosion of the steel rebars is one of the most relevant and widespread [49]. Examples of corroded beams in RC frame buildings are illustrated in Fig. 1.2 [50]. Steel corrosion not only affects reinforcement geometry and mechanical characteristics, but also the behaviour of the surrounding concrete and the steel-concrete interface [51], [52], [53]. Consequences on the behaviour of RC members involve modifications in the resisting mechanism, changes in the failure mode and, in many cases, reductions of both strength and deformation capacity of the members [46], [54]. Focusing on deformation capacity, in the case of failure modes associated to concrete crushing, the most impactful consequences of rebar corrosion include the spread of cracking in the concrete which surrounds the corroded rebars and the loss of confinement effectiveness due to the corrosion of the stirrups [55]. Both these phenomena can in fact compromise the strain deformation capacity of concrete in compression and foster the buckling of the longitudinal reinforcement. On the other hand, for high corrosion levels, failure modes associated to longitudinal rebars rupture can also develop, due to significant reductions of the apparent ultimate strain in tension of steel bars, which can occur because of stress concentrations along the rebars caused by pitting corrosion [56], [57].

Fig. 1.2. Corroded beams in a RC building (From Ou et al. [50]*)*

For the assessment of corroded RC structures, approaches associated to low LoA are indeed useful in the engineering practice, allowing for a first check of the structural performances. From a theoretical point of view, it might seem to make sense that the general approaches and models used for the design of new members could be as well used for the assessment of existing or even deteriorated ones, since the underlying physical laws which govern the structural behaviour are the same [58]. Following this principle, in many cases the common practice has been to use assessment approaches which were originally developed for the analysis of undamaged elements, trying to straightforward extend them to analyze corroded members. These extensions were usually simply based on the use of proper values of

parameters which were already considered by the models, as a simple tentative to take into account corrosion effects.
This kind of approach, however, has raised some concerns and may not always represent an effective solution [59]. In fact, those models were in many cases originally calibrated and validated by using only data obtained from tests on undamaged RC specimens. In addition, parameters and hypotheses used in such models may not be suitable to account for all the consequences on the structural behaviour caused by rebars corrosion. Typical examples can be formulations for calculating plastic hinge lengths, sectional confinement effectiveness, or shear strength of RC elements.
In order to avoid an incorrect use of such modelling and assessment approaches, some care should be taken when extending models and formulations originally developed for undamaged members. Adopted procedures should be validated in advance, in order to prove their effectiveness for the analysis of deteriorated elements. Or, when extensions are proposed, they should suitably developed enhancing the original approaches in order to properly accounting for the considered effects of rebar corrosion [60]. In the end, summarizing the considerations highlighted throughout this section, an answer to the question reported in the section title can be proposed: the deformation capacity of RC members cannot be taken for granted and specific suitable approaches should be employed for its assessment, considering different possible conditions of the analyzed structures.

1.3 Deformation demand in structures subjected to differential settlements: modelling or monitoring?

In the former sections, the relevance of deformation capacity of RC members as well as the need for effective and suitable models for its estimation have been thoroughly highlighted. It is worth to recall, however, that an analogous need exists for effective approaches to estimate deformation demands, which are essential in order to assess the structural safety or determine the achieved level of deformation-induced damages.
For demand estimations, the most suitable approaches are indeed different and dependent on the causes responsible for the induced deformations. In fact, while numerical analyses considering nonlinear material behaviour and second order effects represent a useful and effective tool to estimate deformation demands at structural members, a challenging issue is the estimation of intensity, duration and spatial variability of the input action, specifically: the local seismic response, in the case of earthquakes; the spatial and temporal distribution of ground deformations around and below the buildings, in the case of ground settlements; or the location and extent of the hit zone, in the case of a possible progressive collapse scenario caused by an impact or explosion.
Appropriate models and modelling assumptions need to be adopted to determine the characteristics of every kind of input action, which are necessary for analyzing structural response and so calculate deformation demands at members.
However, a substantial difference exists among the causes mentioned above. In fact, while earthquakes or blasts are phenomena characterized by a short duration and which cannot be foreseen or detected in advance, ground deformations usually develop over a significantly longer period of time and in many cases are characterized by a relatively low rate. This is

indeed a significant aspect, since it makes theoretically possible to monitor over time the settlement-induced deformation demands. Although this may seem promising, an extensive adoption in practice of high spatial density long-term monitoring of ground settlements in urbanized areas is often limited by elevated costs and practical difficulties.
Recent developments achieved during the last two decades in the field of satellite remote sensing can offer an aid to monitor ground deformations. In particular, techniques based on multi-temporal differential synthetic aperture radar interferometry (MT-DInSAR) allow nowadays to monitor ground displacements at a very large scale, with high spatial density and limited costs [61]. These approaches, initially employed to measure land subsidence over large areas, have been only recently started to be considered an actual tool for the monitoring deformations of individual structures and infrastructures [62], [63].
Indeed, despite the wide variety of applications proposed in the recent years, the full potential of these techniques in the field of civil structural monitoring is far from being fully exploited. Further investigations are needed to test the applicability of these methods in different conditions, and advances in data processing are desired to overcome aspects which represent limitations to an extensive and fruitful use of this approach for the monitoring of the built stock. In fact, besides the several benefits, these approaches present also some limitations [64]. As an example, the information retrieved from these methods are in most cases not sufficient to completely identify the three-dimensional deformation of the objects in a monitored area. To overcome some of these issues, some works proposed the integration of MT-DInSAR data with various ancillary data (e.g., maps, digital elevation models, etc.) and other kind of data obtained from in-situ measurements [65].
On the other hand, MT-DInSAR data can be used their self as information to integrate and improve the predictions of ground deformations provided by commonly adopted models, for example in the case of tunnelling-induced ground settlements [66], [67]. So, data obtained from satellite remote sensing and other monitoring techniques can be valuable for the calibration or updating of theoretical models for the estimation of ground deformations in urbanized areas.
The aforementioned applications may suggest an answer to the provocative question contained in the title of the section: an integrated approach combining information provided by both modelling and monitoring tools may then significantly improve the accuracy of the ground settlement data used as an input for the estimation of deformation demands in structures. As a result of such approach, more refined and reliable structural assessment practices could be made available.

1.4 Research objectives

The research presented in this work addresses some of the gaps previously highlighted in sections 1.2 and 1.3 about the approaches for the estimation of deformation capacity and demand in reinforced concrete structures subjected to various hazards. The main topics encompassed in the dissertation are presented in Fig. 1.3.

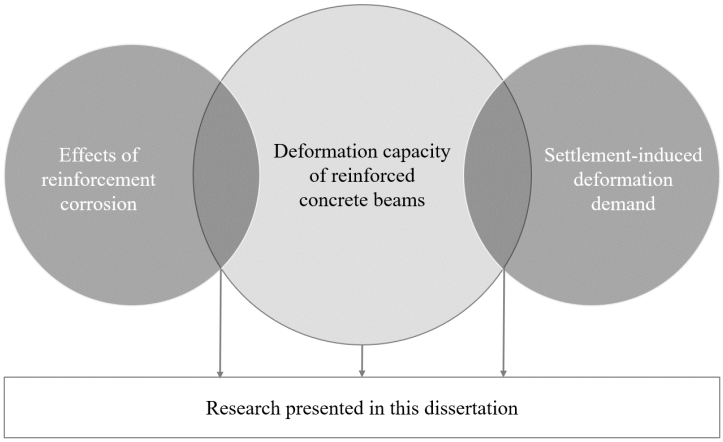

Fig. 1.3. Diagram illustrating the core topics addressed in the research work

In particular, a significant part of the presented research is devoted to the analysis of practice-oriented calculation approaches for providing effective estimations of deformation capacity, for both undamaged members and for deteriorated members affected by corrosion of the reinforcements. The study focuses specifically on reinforced concrete beams. The obtained results can also be useful as a base for the analysis of other member typologies such as columns and walls, which are although not directly addressed by the research presented in this work.

Another part of the research is related to the evaluation of deformation demands induced by ground settlements. In particular, it deals with the critical analysis of potentials and limitations of remote sensing approaches based on satellite radar interferometry used for measuring and monitoring ground deformations. The focus is put on aspects which are relevant for the use of these techniques in the context of structural assessment, with the aim of estimating ground deformations then used as an input to evaluate deformation demands in structures.

As a matter of fact, a common denominator adopted in addressing the various investigated aspects concerns the search for the limits of applicability of some of the commonly used approaches and the proposal of improvements and extensions, in order to make these methods more effective and applicable to a wider range of situations. More specifically, the research is motivated by the following research questions:

Q1: *To which extent traditional simplified analytical formulations for deformation capacity assessment of reinforced concrete beams sections can be used? And, how it is possible to generalize them?*

Q2: *Which are the major limits of practice-oriented analysis approaches used for the evaluation of deformation capacity in members affected by significant reinforcement corrosion? And, what enhancements are needed to overcome them?*

Q3: *Which are the most relevant potentials and current limitations of the use of satellite radar interferometry in the process of monitoring settlement-induced deformations demand in civil structures and infrastructures? And, what advances are necessary to fully exploit these tools?*

Each of the aforementioned research questions encompasses a wide range of aspects which would need to be investigated, so that it is not feasible to provide a comprehensive answer to each of them in the context of this work. However, some specific research objectives have been derived from the aforementioned research questions and have been addressed throughout the dissertation. They can be summarized as follows:

O1. *Developing a comprehensive understanding of the possible conditions by which a beam section can reach the yielding or failure stage and then define analytical formulations for deformation capacity and ductility assessment coherent with the most common types of yielding and failure mode actually occurring, considering both the cases of undamaged members and members affected by corrosion;*

O2. *Understanding and highlighting the limits of some of the commonly used practice-oriented approaches available for modelling the behaviour of corroded RC beams, especially in terms of deformation capacity, providing also new insights on relevant aspects about the definition of mechanical characteristic of corroded reinforcement;*

O3. *Surveying and clarifying the possibilities offered by satellite remote sensing technologies to improve the estimation of deformation demands induced by ground subsidence with particular reference to monitoring technologies based on satellite radar interferometry, highlighting their potential as well as the major limitations;*

Through the aforementioned objectives, various aspects are addressed regarding the design and assessment practices which are based on demand vs. capacity checks in terms of deformations. Ultimately, the hope is that the presented research could contribute to the knowledge on the structural behaviour of RC elements and to the improvement of procedures for their structural assessment.

1.5 Research roadmap and methodology

The work presented in this dissertation collects the results of research activities developed in the context of various research programs during the period 2019 – 2022, also involving collaborations between IUAV University of Venice and other research institutions. Each one of the three research objectives declared in section 1.4 has been addressed through a dedicated research project, as illustrated in Fig. 1.4.
A first part of the research has been devoted to the analysis of the response of RC beams in terms of sectional deformation capacity and ductility, by means of theoretical formulations. In order to pursue objective ***O1***, and so identify to which extent classical formulations are valid, an in-depth analysis of possible yielding (failure) modes for RC sections have been performed, deriving the limit conditions separating one type of yielding (failure) mode from

another. This way it has been possible to precisely define the validity domain of certain assumptions adopted by traditional analytical formulations for analyzing the yielding (failure) modes of RC sections. By exploiting the defined limit conditions and validity domains, it was possible to propose a simplified formulation for the estimation of curvature deformation capacity and ductility, which takes into account all the failure modes that occur more frequently for doubly reinforced concrete sections. Using the same developed tools, it was then possible to understand how the failure mode and deformation capacity change in the case of RC sections affected by reinforcement corrosion. The proposed formulations were implemented in Matlab [68] scripts for practical use.

The second part of the work, aimed at addressing objective ***O2***, has been specifically devoted to the study of flexural behaviour of reinforced concrete beams affected by reinforcement corrosion, with a particular focus on the assessment of structural response in terms of deformation capacity. The presented work has been developed as part of a joint research collaboration between IUAV University of Venice and Tor Vergata University of Rome, aimed at testing and modelling the structural behaviour of corroded RC beams. A first phase of the research involved the analysis of the results from a two-steps experimental campaign on corroded concrete beams performed at Tor Vergata University of Rome [69], [70]. In some of the performed tests special arrangements have been adopted in the sensors layout in order to detect the evolution of the crack pattern and to get additional measures to study deformation capacity of corroded beams. Results from the tests helped in the calibration of the adopted accelerated corrosion process and shown how the failure mode, bending strength and flexural deformation capacity change with an increasing amount of corrosion developed in the longitudinal tensile reinforcement of the beams. In a subsequent phase of the research, the previously obtained experimental results have been used as reference data for assessing the performances of different practice-oriented analytical and numerical approaches in the task of modelling the structural response of corroded RC beams. In particular, the analytical formulation developed in the first part of the research has been herein adopted to study the sectional behaviour of corroded beam members. In addition, approaches for the calculation of structural response at member level were adopted, considering in first instance a closed-form analytical formulation based on curvature integration, and then a more general numerical modelling approach involving nonlinear finite element analyses (NLFEA) with fiber-based elements. The proposed numerical modelling approach has been developed within the OpenSees [71] framework, making use of the pre- and post-processing software STKO [72]. This evaluation allowed to highlight some of the main limitations of traditionally adopted analysis approaches and in particular those regarding the procedures for estimating the mechanical characteristics of corroded reinforcement.

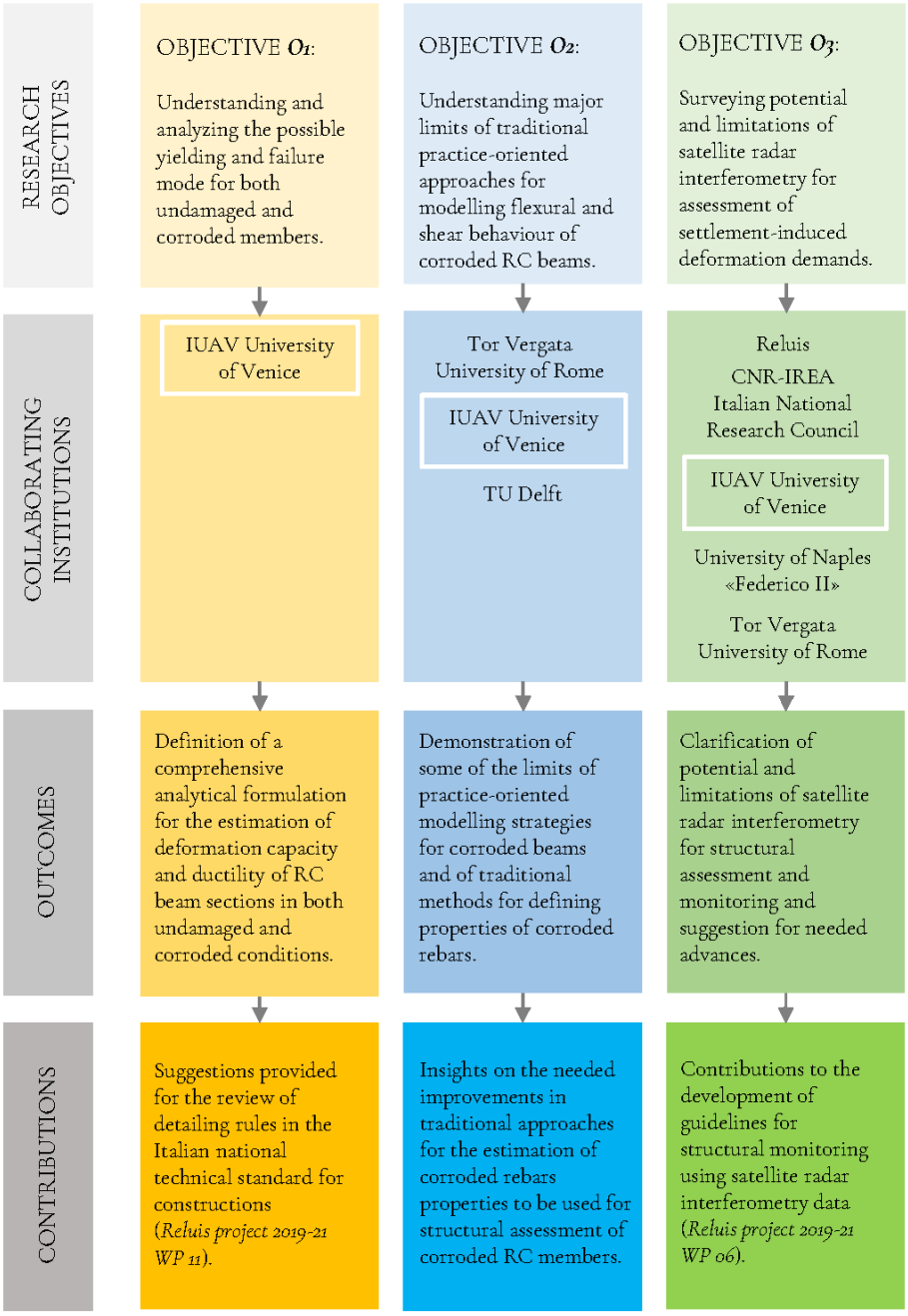

Fig. 1.4. Diagram illustrating the research work presented in the dissertation

An additional part of the research related to the behaviour of corroded elements involved an in-depth examination on some issues regarding shear behaviour of corroded reinforced concrete beams, which has been carried out during a visiting research period at Delft University of Technology (Delft, the Netherlands). However, by the time this dissertation is written, results related to this additional part of the research are still under development and are not herein presented. The initiated work addressed the analysis of some theoretical models for the evaluation of shear capacity of corroded reinforced concrete beams, focusing in particular on those based on extensions of models adopted by the norm EN1992-1-1 [73] and by the Model Code 2010 [27]. Following this, it has been started the development of a new experimental database for shear strength of corroded reinforced concrete beams using data from literature works, with the final aim of obtain insights to formulate proposals for the improvement of the analyzed code-oriented models for the shear capacity of corroded members.

A third part of the research work has been pursued in order to address objective ***O3***, aiming at investigating some recent advances in the estimation of deformation demands for structures subjected to ground settlements. In particular, the study explored the employability of satellite remote sensing techniques for the monitoring of low-rate deformations of soil and buildings, to be used to provide helpful information for structural monitoring and assessment of constructions. The study was funded by the Italian national research program "DPC-ReLUIS Project 2021-2021" and has been performed as part of the research working package 6 (WP6) "Satellite data and structural health monitoring" [74], which involved the collaboration of different Italian research institutions. The part of work presented in this dissertation which was developed within the aforementioned national research project has been done in the context of a collaboration between researchers from IUAV University of Venice, Tor Vergata University of Rome, University of Naples "Federico II" and the Institute for Electromagnetic Remote Sensing of the Environment of the Italian National Research Council (CNR-IREA). The study focused on the analysis of potential and limitations of the application in civil structural health monitoring of MT-DInSAR techniques, i.e., a class of remote sensing methods based on satellite radar interferometry [75]. Along with the analyses of relevant aspects and major issues of these methods, some examples are proposed, developed using MT-DInSAR data for a case study area in the city of Rome (Italy). Data were obtained using COSMO-SkyMed radar images [76], [77] made available by the Italian Space Agency (ASI) and processed by CNR-IREA using the Small-Baseline Subsets (SBAS) processing technique [78]. The MT-DInSAR data were then post-processed using Geographic Information Systems (GIS) ArcGIS Pro [79] and QGIS [80], using both built-in functions and new specifically developed routines implemented in the softwares for the generation of particular outputs. Ancillary data such as maps of the urban built stock and digital elevation models (DEM) have been used for a better visualization and interpretation of the MT-DInSAR data.

1.6 Research outcomes and impact

The novelties of this work are multiple. The first one lies in the proposal of an analytical approach for the deformation capacity and ductility estimation of RC beam sections which includes *new refinements* with respect to classical formulations. The second novelty consists in bringing *new evidence* about the major issues in current practice-oriented approaches for modelling the structural behaviour of corroded concrete beams, also highlighting how such issues can foster uncertainty in the obtained calculated values of member strength and deformation capacity. The third novel contribution of this work is an *updated synthesis* of major potentials and current limitations of the use of MT-DInSAR data in the field of structural monitoring and assessment, based on the results obtained considering the key features of this type of data and from the analysis of some applications on buildings of a case study area. The outcomes of the research obtained with reference to the three research objectives described in section 1.4 are reported in Fig. 1.4.

With the aim of addressing objective ***O1***, a comprehensive analytical formulation for the estimation of deformation capacity and ductility of RC beams in both undamaged and corroded conditions has been developed. The formulation considers all the possible different failure modes achievable by a doubly-reinforced concrete beam section, taking into account for actual strain values in bottom and top reinforcement layers. This approach allowed to overcome the limit of validity of traditional formulations [8], which have been usually developed considering only few possible failure conditions. Moreover, a further improvement regards the adoption of a constitutive law for concrete which allows to consider the spalling of the concrete cover and so to provide curvature deformation capacity values avoiding excessive conservativism. Some results [81], [82] obtained from this part of the research work contributed to the outcomes of the working package 11 (WP11) "Review of national codes for constructions – concrete structures" of the Italian national research program "DPC-ReLUIS Project 2021-2021" [74], [83]. In particular, limits and possible improvements of member detailing rules for ductility currently adopted in the Italian standard NTC18 [84] and in the European standard Eurocode 2- Part 1-1 [73] have been highlighted [81], [82].

The analysis of structural response of corroded RC beams developed in the second part of the research aimed to address objective ***O2*** described in section 1.4. Results of the experimental tests confirmed that, for high corrosion levels, flexural failures associated to steel rebars rupture can actually occur and can lead to abrupt drops of strength, reducing the deformation capacity of the elements. The analysis of the crack patterns obtained with digital image correlation (DIC) measurements shown how in the case of high corrosion levels, fewer and larger flexural cracks develop, due to localization of inelastic tensile strains in pits present on the corroded rebars. The simulation of the tested beams with the considered analytical and numerical approaches highlighted that the definition of mechanical characteristics of corroded rebars has a major influence on the structural response. In particular, the pitting factor value as well as of phenomenological models to estimate the ultimate tensile strain of the corroded rebars have a major relevance on the estimation of member deformation capacity, and uncertainties in the assumption of these

modelling parameters represent an important limit to an effective assessment of structural response.

With regards to the last objective ***O3***, the analysis of the information obtainable from MT-DInSAR monitoring techniques allowed to draw some considerations about the use of these data as a support for the monitoring and assessment of deformation demands in structural members of constructions subjected by ground settlements. In particular, insights about the conditions for which the technique is actually employable have been provided, as well as further improvements which are needed in the nearby future in order these techniques to become effective tools adoptable also in engineering practice. All the developed recommendations were collected and presented in a guideline document [85] made available as a final outcome of the WP6 of the research program "DPC-ReLUIS Project 2021-2021".

As a whole, the outcomes of the research work presented in this dissertation would aim to contribute to some improvements in practice-oriented procedures for structural assessment of RC structures, with a special emphasis on existing structures with elements affected by corrosion of the reinforcements. Improvements of structural assessment methods would allow to obtain refined estimations of current structural performances and of remaining service life. However, it is worth to point out that such knowledge improvements can have an impact which extend far beyond the horizon of the single building or infrastructure.

Many developed countries are nowadays facing the challenges of the planning of new constructions in earthquake prone areas and of the managing of an existing aging building stock. Many of the older existing concrete structures are susceptible of deterioration and in particular of corrosion of the reinforcement. In order to plan and schedule the renewal of a stock of existing structures deteriorated by reinforcement corrosion, it is essential to: i) collect as much information as possible on the actual current conditions of studied deteriorated structures; ii) develop and adopt suitable tools and approaches which would allow accurate analysis of their current structural performances [86]. Unfortunately, in some cases little information are available about drawings, design calculations, quality and grade of materials used to build the structure. Furthermore, an accurate quantification of corrosion damage without involving destructive tests is sometimes very difficult. Traditionally adopted structural analysis procedures may be not always suitable to deal with such unknowns and uncertainties, forcing the practitioners in charge of the assessment to make several safe-side assumptions. Such a combination of safe assumptions often leads to a very conservative assessment [87]. As a consequence, many structures which would in fact be safe, are classified as being in need of refurbishment. The uncertainties in the estimation of structural performances reflect in the difficulties in drawing up a priority list of interventions on existing facilities, which in turn contribute to hinder the arise of sufficient political priority about this issue. Because of this, the replacement and refurbishment of deteriorated structure are often not sufficiently present on the agenda of governments and stakeholders. The vicious circle is in the end closed by the fact that, without sufficient political priority, fundings and investments on the development of new technical and scientific knowledge for improving the assessment procedures for deteriorating structures are in lack [87]. It appears evident then, that the development of better assessment procedures which allow more accurate estimations of the structural response of deteriorated

structures can have a relevant impact on the challenge of managing the existing built stock of many developed countries.

1.7 Outline of the dissertation

The outline of the thesis is illustrated in Fig. 1.5 and can be summarized as follows:

- In chapter 2 the proposed analytical framework for the analysis of yielding and failure modes of RC beam sections is presented, along with the analytical formulation for estimation of curvature deformation capacity and ductility;
- In chapter 3 the two-steps experimental campaign on sound and corroded beams are reported, including information on the adopted setups and sensors layout, as well as a discussion of the results. In particular, the effect of increasing corrosion levels on the structural response is discussed;
- In chapter 4 the performance assessment of some considered analytical and numerical modelling approaches is presented, using the results presented in chapter 3 as a reference for comparison. Particular emphasis is put on highlighting the aspects which influence the response in terms of deformation capacity of the members;
- In chapter 5 analysis and considerations are proposed to assess the potential and limitations of MT-DInSAR monitoring approaches to improve the estimation of ground settlements used as input for the estimation of deformation demand on structural members of RC buildings and infrastructures;
- In chapter 6 a retrospective view of the research work is proposed, summarizing the obtained results as well as the aspects not yet fully addressed in the presented work, which although may be developed in future investigations.

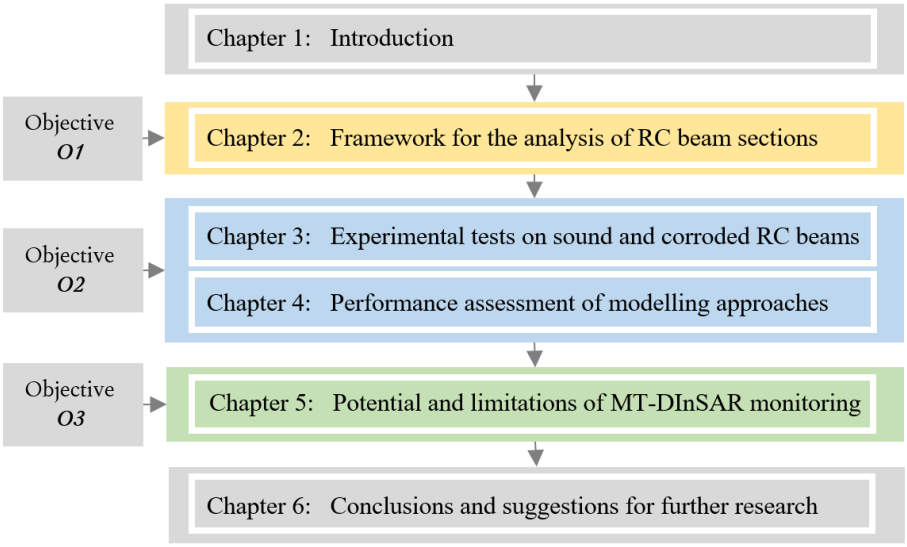

Fig. 1.5. Outline of the dissertation

2

An analytical framework for the analysis of deformation capacity and ductility of doubly reinforced concrete beam sections

An open 'beginner's mind' allows us to be receptive to new possibilities and prevents us from getting stuck in the rut of our own expertise, which often thinks it knows more than it does.
Jon Kabat-Zinn

This chapter presents a comprehensive analytical formulation for the analysis of doubly reinforced concrete beam sections, suitable for the estimation of deformation capacity and ductility. The adopted approach considers different possible yielding and failure modes that sections may develop, including those which involve the possible spalling of the concrete cover, and presents some significant refinements with respect to analytical methods available in literature. The proposed formulation allows for a straightforward calculation of yielding curvature, ultimate curvature and curvature ductility, whose evaluation are presented for selected section geometries and material parameters. Then, starting from the obtained general analytical framework, a simplified and practice-oriented approach is derived, which allows for the evaluation of ultimate curvature and curvature ductility for common sections used in design practice. This kind of tools can be an aid for estimating local ductility capacity, thus allowing a performance-based design of reinforced concrete members.

2.1 INTRODUCTION

Performance-based design and assessment of reinforced concrete (RC) structures require adequate formulations for the estimation of deformation capacity and ductility of RC members in order to actually be used in practice [6], [4], [26]. For reinforced concrete beam sections, *analytical formulations* for the estimation of curvature capacity and ductility have been proposed by various authors. One of the most classical formulations, proposed by Park and Paulay [8], considers two possible types of ultimate conditions for the beam section, both related to a "concrete failure". They differ for the strain level reached by compression reinforcement, i.e., elastic or yielded. Concrete was modeled adopting a linear constitutive law for the determination of yielding curvature, while a rectangular stress-block with ultimate strain $\varepsilon_{cu} = -3‰$ was adopted for ultimate curvature calculation. In the work of Park and Ruitong [88] the same failure conditions considered by Park and Paulay [8] have been adopted, although employing the concrete constitutive law proposed by Kent and Park [89] for the determination of both the yielding and failure conditions, using an ultimate compressive strain of unconfined concrete equal to $\varepsilon_{cu} = -4‰$.

Although useful for many practical cases, the applicability of the aforementioned approaches is limited to specific situations, since they do not consider other possible failure modes which can control the deformation capacity of the section, e.g., failure modes associated to steel rupture.

A step forward was made by the works of Fardis [4] and Biskinis and Fardis [25], in which a more comprehensive and general analytical framework for the calculation of strength, deformation capacity and ductility of RC sections with general layout (i.e. applicable to beam, column or wall sections) was proposed. This procedure considers both "steel failures" and "concrete failures" and also allows, when possible, to take into account those failure modes which can occur after the complete spalling of the concrete cover in compression.

Indeed, the assumption that a RC section would survive the concrete cover spalling actually relies on the hypothesis that it would maintain a sufficient amount of residual bending strength after the loss of the cover. This can be accomplished if the following conditions apply: i) the cover-to-height ratio of the section c/H is not too high, so that the strength contribution provided by the cover would not result in an excessive loss of strength; ii) the buckling of longitudinal rebars in compression is avoided, so that compressed rebars can still contribute to increase the section compression chord resistance while neutral axis is lowering after spalling; iii) the core concrete is provided with some confinement, which can increase its strength and deformation capacity in compression, so that it would not fail just after the complete spalling of the cover. All the three aforementioned requirements can be guaranteed by adopting a proper longitudinal and transverse reinforcement layout. In particular, with regards to the two latter points, transverse reinforcement can be used both to avoid the buckling of the longitudinal reinforcement [90], [10], and as a source of confinement for the core concrete [91], [92].

For concrete beams, the actual possibility to rely on the effects of confinement has been a debated subject over the years. As a matter of fact, Fardis [4] suggested that for practical design purposes it is not appropriate to rely on the confinement of core concrete to determine the ultimate deformation capacity and ductility of RC beams. However, by disregarding the existence of even partial contributions of confinement effects, and so avoiding the possible achievement of failure conditions occurring after the cover spalling, the obtained design or assessment approaches may be too severe and may deeply underestimate the actual ultimate deformation capacity of the beam sections, especially if appropriate transverse reinforcement detailing has been provided. This is particularly relevant for buildings subjected to severe earthquakes, for which the curvature demands in beam sections belonging to plastic hinge zones can be extremely high, especially if the structures are susceptible to torsional effects.
In order to avoid excessive underestimations of curvature capacity, some approaches have been proposed which allow to take into account cover spalling and confinement effects in beam sections. For generic RC members in flexure, Fardis [4] proposed to use the aforementioned framework [4] computing the cover spalling and calculating the confinement effect using an alternative expression for the coefficient of confinement effectiveness, that considers the effective depth of the compression zone which lay in the confined core of the section. Hao et al. [93] proposed a calculation of ultimate condition for beam section using a stress-block concrete law which includes effects of confinement specifically derived for RC beams.
This chapter illustrates a newly proposed analytical framework for the analysis of deformation capacity and ductility of doubly reinforced concrete beam sections, which considers several possible failure modes, including those occurring after the spalling of the compressed concrete cover. Closed-form analytical formulations for the calculation of yielding and ultimate conditions of double reinforced concrete beam sections are developed, providing the identification of the yielding and failure modes, as well as the associated curvature values. The derived analytical formulations are used to develop graphical domains for the determination of yielding and failure modes for doubly reinforced concrete beam sections, which are useful to analyze the section behavior as a function of its geometrical and mechanical properties, in the design phase. In addition, a simplified code-oriented approach for curvature ductility capacity evaluation is proposed. Its main innovation and advantage consist in allowing to quantify the effective available curvature ductility of a double reinforced concrete section explicitly considering possible contributions to deformation capacity due to cover concrete spalling, though assuring that associated loss of strength would not exceed specified limit values.
Failure modes which involve the spalling of the concrete cover are considered achievable by assuming that present transverse reinforcement is sufficient to avoid longitudinal bar buckling (e.g., according to detailing rules provided by NZS 3101 [90] or Priestley et al. [10]). In the procedure proposed by Fardis [4], the spalling of the concrete cover is considered as a unitary event, i.e., its intermediate stages are neglected. Accordingly, the section curvature is computed only before and after the complete spalling of the cover. Vice versa, in the proposed approach the concrete cover spalling is represented as a

continuous process, so all its intermediate stages are considered. This approach allows to identify possible ultimate conditions associated to steel failure which occur during the spalling process, characterized by values of ultimate curvature lower than those referred to the condition of complete spalling. Therefore, the determination of the possible failure modes and the calculation of the neutral axis at ultimate condition explicitly consider the possibility of reaching failure at the complete expulsion of the concrete cover, or at an intermediated stage of it. Loss of strength due to the total or partial expulsion of the concrete cover is analytically quantified, so that it can be determined whether or not the ultimate condition after spalling can be effectively considered. With regards to the adopted constitutive law for concrete, no increments of concrete strength or concrete ultimate compressive strain due to confinement are taken into account.
The chapter is organized as follows. First, the fundamental assumptions on material laws and adopted calculation approaches are presented and discussed. Then, the section yielding condition is analyzed, presenting formulations for the definition of domains which identify different yielding modes, together with a parametric study of the neutral axis position at yielding. Analysis of the ultimate condition follows, evaluating relations for the determination of failure modes and for the estimation of loss of strength due to the spalling of the concrete cover. Following this, ductility calculation according to the developed formulation is presented, together with a simplified code-oriented approach for ductility capacity estimation. In the last section relevant observations about results presented in the chapter are summarized.

2.2 FUNDAMENTAL HYPOTHESES

2.2.1 GEOMETRIC CHARACTERISTICS AND MATERIAL MODELLING

A doubly reinforced concrete beam section in flexure having rectangular compressed zone is depicted in Fig. 2.1, which is useful to introduce the symbology adopted in the following, and to provide an example of considered strain distributions. In particular, let b and H be the width and height of the section, respectively, while cross-sectional areas of bottom and top steel rebars are indicated as A_s and A'_s. Cover thickness c is assumed to be the same for bottom and top reinforcement, for simplicity. Throughout the presented work, tensile strains are taken as positive, while compressive strains are taken as negative. Given the strain ε_c of the most compressed section fiber and the neutral axis depth x, the strain values at bottom and top reinforcement, respectively ε_s and ε'_s, can be identified.

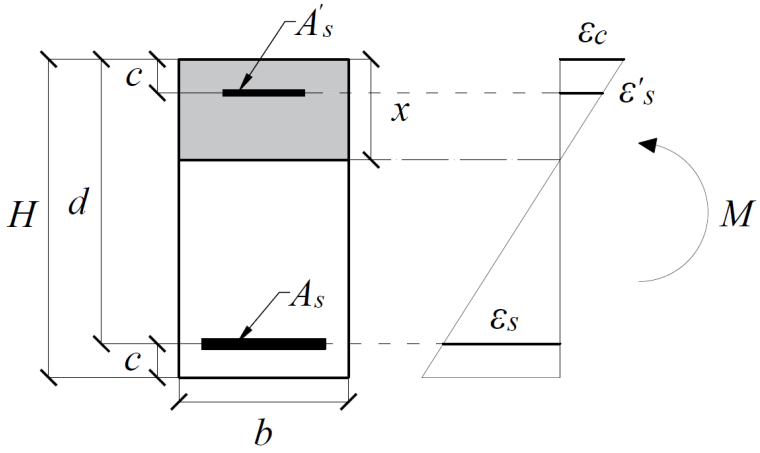

Fig. 2.1 Generic double reinforced concrete beam section in flexure with rectangular compressed zone: Section layout and example of strain distribution

In this work, simple constitutive laws have been adopted to model the materials behaviour. However, the structure of proposed framework is general, so that in principle it can be implemented using any type of constitutive laws. For reinforcing steel an elastic-perfectly plastic symmetrical law is adopted, with elastic modulus E_s, yielding strength f_y, yielding strain ε_{sy} and ultimate strain ε_{su}. In the adopted simplified constitutive law for steel, the strain values higher (in module) than the ultimate strain ε_{su} are associated with a null strength value. A representation of the adopted law for steel is provided in Fig. 2.2a.

Different choices are possible for the definition of the ultimate tensile strain ε_{su}, depending on whether, and to which extent, the adopted constitutive law is adjusted to represent a real stress-strain curve for steel rebars, eventually accounting for some effects due to loading process characteristics. Let define a nominal value of the rebar ultimate tensile strain for monotonic loading $\varepsilon_{su,mo}$. In case the beam section is subjected to a monotonic load process, the steel ultimate tensile strain ε_{su} may be assumed equal to the latter nominal value of the rebar ultimate tensile strain for monotonic loading, so that $\varepsilon_{su} = \varepsilon_{su,mo}$. The nominal monotonic ultimate tensile strain may be assumed equal to the strain at rebar failure measured in experimental tensile tests, $\varepsilon_{s,failure}$, so that it would be $\varepsilon_{su,mo} = \varepsilon_{s,failure}$. Otherwise, a common and safe option is to adopt as nominal value of monotonic ultimate steel strain the strain at peak strength A_{gt} measured in experimental tensile tests (defined according to norm EN ISO 15630-1 [94]), so having $\varepsilon_{su,mo} = A_{gt}$. Priestley et al. [10] pointed out that the rebar ultimate tensile strain used in the analysis of a RC section subjected to alternating cyclic loading should be assumed lower than the nominal value evaluated by monotonic tensile tests. The reason is that such nominal value can rarely be reached when the section reaches steel failure under cyclic loading conditions, because of the low-cycle fatigue phenomena affecting the reinforcing bars, which are cyclically tensioned and then compressed. For this and other reasons, Priestley et al. [10] suggested that for cyclic loading conditions in members for

which longitudinal bar buckling is prevented, the rebar ultimate tensile strain ε_{su} to be used in sectional analysis should be defined as $\varepsilon_{su} = 0.6 \cdot \varepsilon_{su,mo}$.
For a RC section subjected to cyclic loading for which the buckling of longitudinal rebars is not prevented, it is possible to analyze the sectional response setting an even lower limit for the rebar ultimate tensile strain. The reason lies in the fact that, often, bar buckling occurs due to a longer unsupported length, developed due to a previous plastic elongation of rebars in tension. A reduced value of rebar ultimate tensile strain to be possibly used in such a modelling scenario is provided by *fib* Model Code 2010 [27], which suggests to adopt $\varepsilon_{su} = 3/8 \cdot \varepsilon_{su,mo}$.
To model the behaviour of concrete in compression, a law composed by an initial parabolic branch followed by a linear decreasing softening branch was adopted. The model is defined using the concrete compressive strength f_c, the strain at peak strength ε_{c0}, the ultimate compressive strain ε_{cu} and the inclination angle β used to define the slope of the softening branch. In some concrete constitutive models, e.g. in the Kent and Park model [89], the slope of the softening branch is described using the parameter $Z = tg(\beta)/f_c$. In the model herein adopted, the strains ε_{c0} and ε_{cu} are taken as negative, while the compressive strenght f_c and the term Z have positive values. The adopted constitutive law for concrete is illustrated in Fig. 2.2b.

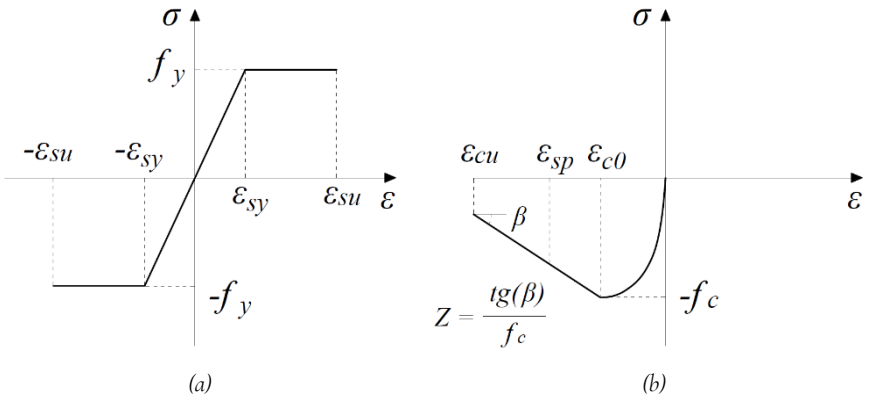

Fig. 2.2 Adopted constitutive models for reinforcing steel and compressed concrete

The definition of the slope of the softening branch, as well as the value of the ultimate compressive strain, is an important aspect of the modelling. In fact, it has been shown by Hillerborg [95], [96], [97], Bigaj [44] and Bigaj and Walraven [98], among others, that the stress-strain behaviour of concrete in compression can be dependent on the size and geometric characteristics of the considered concrete element and that such dependency can strongly influence the deformation capacity, from the material level up to the structural level. Concerning the definition of the slope of the softening branch, the adopted formulation can for example use some assumptions proposed by models available in literature.

As an example, two models are herein considered: i) the so-called Parabola-Rectangle (*PR*) law [27] (which should be better addressed as a "stress distribution" for ultimate limit state analysis, rather than as a "constitutive law"); ii) the constitutive law proposed by Kent and Park (*KP*) [89].
In particular, for the two aforementioned laws, the parameter Z associated to the slope of the post-peak branch of the stress-strain concrete law can be assumed as follows:

$$Z = 0 \qquad \textit{for Parabola-Rectangle law}$$
$$Z = \frac{0.5}{|\varepsilon_{50u} - \varepsilon_{c0}|} \qquad \textit{for Kent – Park law} \tag{2.1}$$

Where ε_{50u} is the strain at 50% strength loss, which for the *KP* model is defined according to the following equation:

$$\varepsilon_{50u} = -\frac{3+0.29 \cdot f_c[MPa]}{145 \cdot f_c[MPa] - 1000} \tag{2.2}$$

Indeed, the assumption of a post-peak branch with constant strength, as given by the *PR* model, is a bit unrealistic. On the other hand, the softening branch obtained using the *KP* model is quite steep and may be too conservative, especially neglecting contributions of confinement to the stress-strain curve, as is done in the current approach.
In Fig. 2.2 an additional strain term ε_{sp} belonging in the range $[\varepsilon_{cu}; \varepsilon_{c0}]$ is also indicated, which it is per se non necessary to define the stress-strain law. This term represents the maximum strain value considered in the stress distribution commonly used to calculate the maximum bending strength of a RC section. In the case of the *PR* model, such strain term assumes the value $\varepsilon_{sp} = -3.5‰$ for normal strength concrete, i.e., up to a concrete grade C50/60 [27]. For the *KP* model, the term is herein assumed equal to the strain associated to a 20% residual strength, though assuming upper and lower bound values equal to $-3.5‰$ and $-4‰$ respectively, since is fibers of the section would start to develop strain values higher than the latter (in module), the section may start to experience a noticeable loss of bending strength [89].

2.2.2 Modelling of the cover spalling process

In the proposed approach, it is assumed that when the outer fibers of the concrete cover start developing compressive strains ε_c larger (in module) than the strain ε_{sp}, the cracking of the concrete cover could spread and eventually the full spalling of the concrete cover could be triggered. Moreover, when in a concrete fiber the compressive strain reaches, or even overcome (in module), the value ε_{cu}, the concrete is considered completely crushed and its compressive strength is assumed to be null.
Considering a sectional deformation process involving increasing curvature values, once the outer fiber of the concrete cover reaches the strain ε_{cu}, the inner fibers will follow, as the strain profile on the section will become more and more inclined. The portion of the section characterized by concrete fibers which provide a null compressive strength contribution is considered a "spalled portion". Of course, in reality the spalling process

is complex, brittle and can be develop within an extremely short time. On the other hand, in the adopted simplified modelling approach, it is helpful to consider the spalling process as a continuous one.
Let s be the depth of concrete cover that is spalled (i.e., the "spalled portion"), the effective length of concrete compressed zone can be expressed as $x - s$. The complete concrete cover spalling is considered to be achieved when the spalling depth s reaches a maximum value s_{lim}, while in the intermediate stages of the process the following inequality applies:

$$0 \leq s \leq s\_lim \tag{2.3}$$

According to Fardis [4], the value s_{lim} can be assumed equal to the concrete cover thickness for the transverse reinforcement c_w, i.e., the distance from the section edge to the axis of the stirrups, despite other choices are possible. By adopting $s_{lim} = c_w$, the ratio s_{lim}/c becomes a function of concrete cover c, longitudinal rebars diameter d_{bl} and transverse rebars diameter d_{bw}:

$$s\_lim/c = 1 - \frac{d_{bl}+d_{bw}}{2 \cdot c} \tag{2.4}$$

In Fig. 2.3 concrete strain and stress distributions in the compressed portion of a rectangular RC section in uniaxial flexure are presented, for different stages of the spalling process defined according to the description given above. The *Stage I* represents the condition assumed as the formal beginning of the spalling process, characterized by a strain distribution having a strain value equal to ε_{sp} on the outer fibers of the concrete cover. Subsequent stages involve higher section curvatures and so an increase in strain values in the compressed zone (note that the neutral axis depth x can vary). The left column of Fig. 2.3 represents the possible different strain distributions which can develop during the spalling process according to the "general approach", i.e., using the general constitutive model for concrete defined above.
However, for the analyses presented in this chapter, a further simplification is made, in order to obtain more safe-sided estimations of deformation capacity and to simplify the developed mathematical expressions.
Namely, in the developments presented throughout this chapter the concrete ultimate compressive strain ε_{cu} is taken equal to the strain ε_{sp}, as stated in the following:

$$\varepsilon_{cu} = \varepsilon_{sp} \qquad \textit{Simplified assumption made throughout this Chapter} \tag{2.5}$$

Considering this simplification, the stages represented in the right column of Fig. 2.3 can be obtained. In particular, *Stage I* represents the beginning of the spalling process; *Stage II* denotes strain and stress distributions in an intermediate stage of the spalling process; *Stage III* is the last stage of the process, when the concrete cover is fully spalled or crushed.

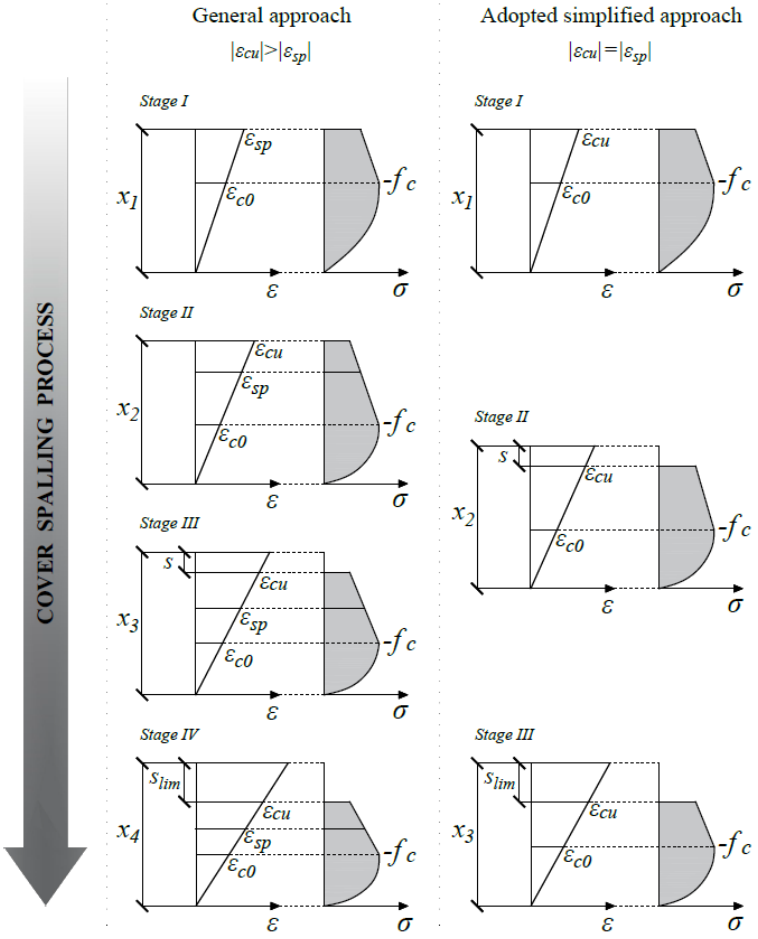

Fig. 2.3 Schematization of the concrete cover spalling process considered in the proposed framework

Regardless of the adoption or not of the simplified assumption expressed by eq. (2.5), a relevant question in the application of the proposed approach is whether or not it is feasible to consider the cover spalling in the sectional analysis. Specifically, considering the proposed description of the spalling process, the aforementioned question translates in whether or not it can be accepted for the outer fibers of the concrete cover to develop strains ε_c larger (in module) than the strain ε_{sp}, as stated in the flowchart represented in Fig. 2.4. The occurrence of concrete cover spalling during the deformation process of a RC beam section can be acceptable if it does not lead to a significant loss of bending strength and if it does not trigger potential phenomena which can compromise the section behaviour, e.g., buckling of the compressed longitudinal reinforcement. As mentioned in section 2.1, the prevention of longitudinal bar buckling can be implemented by means of adequate transverse reinforcement.

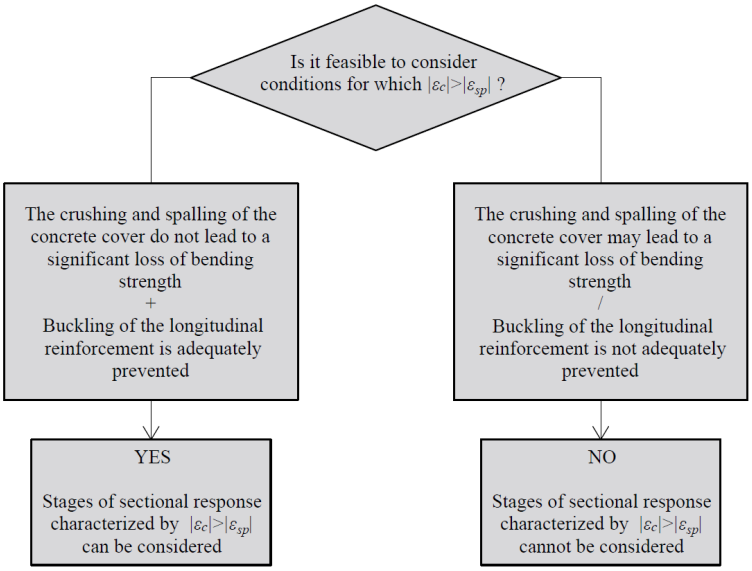

Fig. 2.4 Decision process to determine whether or not it is feasible to compute the sectional response considering the possible spalling of the concrete cover

For example, a simple formulation for the estimation of maximum stirrups spacing $s_{w,max}$ to be used in order to avoid longitudinal bar buckling has been proposed by Priestley et al. [10]:

$$s_{w,max} = \left[3 + 6 \cdot \left(\frac{f_t}{f_y} - 1\right)\right] \cdot d_{bl} \tag{2.6}$$

where f_t is the peak strength of longitudinal rebars.

Considering that the ratio f_t/f_y typically assumes value in the range $1 \leq f_t/f_y \leq 1.3$, a stirrup spacing $s_w = 5cm$ appears to be sufficient to prevent buckling of longitudinal rebars for the most commonly employed values of d_{bl}. Proper design indications to prevent longitudinal bar buckling can be also found in the standard NZS 3101 [90], in which an expression is provided for the calculation of the minimum area of transverse reinforcement. Rearranging such expression, an equation for the determination of maximum stirrups spacing to be guaranteed in order to prevent longitudinal bar buckling is obtained:

$$s_{w,max} = \frac{96 \cdot (A_{w1} \cdot f_{yw})}{\sum(A_{bl}) \cdot f_y} \cdot d_{bl} \tag{2.7}$$

In the previous expression f_y is the yielding strength of longitudinal rebars, f_{wy} is the yielding strength of the transverse rebars, $\sum(A_{bl})$ is the total cross-sectional area of longitudinal rebars restrained by a single stirrup leg and A_{w1} is the cross-sectional area of the single stirrup leg.

To avoid excessive loss of bending strength after the spalling of the concrete cover, the influence of several parameters should be considered. In the following of this chapter, results from parametric analyses are provided in order to explicitly quantify the dependence of spalling-induced strength loss on geometrical and mechanical properties of the RC beam sections. In particular, it will be shown that concrete compressive strength, steel yielding strength, ratio between cross-sectional area of top and bottom longitudinal reinforcement and cover-to-height ratio of the beam section are some of the most influencing parameters. With the regards to acceptable strength losses, traditional suggested values span in the range 15%÷20% [99], [10]. Indeed, the occurrence of a strength loss values higher than the aforementioned ones is commonly acknowledged as an ultimate condition for the section.
If the buckling of longitudinal rebars and excessive spalling induced strength losses are prevented, it is possible to compute the beam section response considering stages which develop after the beginning of the cover spalling. With regards to the proposed framework, this means that it is possible to compute sectional analysis accepting that the strain at the outer fiber of the cover ε_c may reach values higher (in module) than ε_{sp}, and that the maximum spalling depth s_{lim} can be non-null and for example be assumed equal to the stirrups cover c_w. On the other hand, if the aforementioned requirements are not satisfied, the sectional response can only be treated as acceptable up to the triggering of the cover spalling. In such a case, if the ultimate condition identified from the sectional analysis is on the concrete side, such condition simply represent the stage at which the spalling of the concrete cover is assumed to begin.

2.2.3 SECTION EQUILIBRIUM

According to the schemes reported in Fig. 2.1 and Fig. 2.3, the formulation of equilibrium of the section along the longitudinal beam axis can be expressed in a non-dimensional form as follows, considering a null value for the axial load:

$$k - \frac{\rho'}{\rho} \cdot k' - \alpha \cdot \frac{1}{\omega} \cdot \frac{x-s}{H} = 0 \tag{2.8}$$

where k and k' are coefficients which quantify the strain level of bottom and top steel reinforcements, respectively, while steel behavior is elastic. They are defined as follows:

$$k = \frac{\varepsilon_s}{\varepsilon_{sy}} \qquad -1 \le k \le 1 \tag{2.9}$$

$$k' = -\frac{\varepsilon_s'}{\varepsilon_{sy}} \qquad -1 \le k' \le 1 \tag{2.10}$$

The geometrical reinforcement ratios for bottom and top reinforcement, respectively indicated as ρ and ρ', are than defined as follows:

$$\rho = \frac{A_s}{b \cdot H} \tag{2.11}$$

$$\rho' = \frac{A_s'}{b \cdot H} \tag{2.12}$$

Despite the abovementioned choice may seem unconventional, it has some significant advantages since it allows the geometric reinforcement ratios to be defined independently of the cover thickness. The term $\omega = \frac{\rho \cdot f_y}{f_c}$ represents the mechanical ratio for bottom reinforcement. The mean stress factor α for section with rectangular compressed zone is a function of the concrete stress distribution $\sigma_c(y)$ along the section's vertical axis y starting at neutral axis level, and it can be expressed by the well-known relation [8]:

$$\alpha = -\frac{\int_0^{x-s} \sigma_c(y)\, dy}{f_c \cdot (x-s)} \tag{2.13}$$

Considering the concrete constitutive law adopted in this chapter, the value of α may be expressed as a function of strain in the extreme concrete fiber of the section ε_c.
In particular, to express the term α the general expressions reported hereafter can be used:

$$\begin{aligned}
&if \quad \varepsilon_c \geq \varepsilon_{c0} && \alpha = \alpha_I && where \;\; \alpha_I = -\tfrac{1}{3} \cdot \left(\tfrac{\varepsilon_c}{\varepsilon_{c0}}\right)^2 + \left(\tfrac{\varepsilon_c}{\varepsilon_{c0}}\right) \\
&if \quad \varepsilon_{cu} < \varepsilon_c < \varepsilon_{c0} && \alpha = \alpha_{II} && where \;\; \alpha_{II} = \left[1 - \tfrac{1}{3} \cdot \left(\tfrac{\varepsilon_{c0}}{\varepsilon_c}\right)\right] - Z \cdot \tfrac{\varepsilon_{c0} - \varepsilon_{cu}}{2} \cdot \left[1 - \left(\tfrac{\varepsilon_{c0}}{\varepsilon_c}\right)\right] \\
&if \quad \varepsilon_c \leq \varepsilon_{cu} && \alpha = \alpha_{III} && where \;\; \alpha_{III} = \left[1 - \tfrac{1}{3} \cdot \left(\tfrac{\varepsilon_{c0}}{\varepsilon_c}\right)\right] - Z \cdot \tfrac{\varepsilon_{c0} - \varepsilon_{cu}}{2} \cdot \left[1 - \left(\tfrac{\varepsilon_{c0}}{\varepsilon_c}\right)\right]
\end{aligned} \tag{2.14}$$

Equation (2.10) will be employed extensively throughout this work, since it allows to retrieve the neutral axis position, given the strain value at a certain depth. For concrete stress distributions with strain at the extreme fiber of the section $\varepsilon_c \leq \varepsilon_{cu}$, an equivalent uniform stress distribution is defined, which is useful in order to calculate the bending moment developed by the section. For the considered constitutive laws, the equivalent rectangular distribution is defined by a constant stress equal to $\delta \cdot f_c$ and a depth equal to $2 \cdot \gamma \cdot (x - s)$, measured downward from the fiber having strain equal to ε_{cu}. The expressions of coefficients δ and γ used to define the equivalent rectangular stress distribution are the followings:

$$\delta = \frac{\left\{\left[1 - \frac{1}{3}\frac{\varepsilon_0}{\varepsilon_{cu}}\right] - \left[Z \cdot \frac{\varepsilon_{c0} - \varepsilon_{cu}}{2} \cdot \left(1 - \frac{\varepsilon_0}{\varepsilon_{cu}}\right)\right]\right\}^2}{2 \cdot \left\{\left[\frac{1}{12} - \left(Z \cdot \frac{\varepsilon_{c0} - \varepsilon_{cu}}{6}\right)\right] \cdot \left(\frac{\varepsilon_{c0}}{\varepsilon_{cu}}\right)^2 - \left[\frac{1}{3} - \left(Z \cdot \frac{\varepsilon_{c0} - \varepsilon_{cu}}{3}\right)\right] \cdot \left(\frac{\varepsilon_{c0}}{\varepsilon_{cu}}\right) + \left[\frac{1}{2} - \left(Z \cdot \frac{\varepsilon_{c0} - \varepsilon_{cu}}{6}\right)\right]\right\}} \tag{2.15}$$

$$\gamma = \frac{\left[\frac{1}{12} - \left(Z \cdot \frac{\varepsilon_{c0} - \varepsilon_{cu}}{6}\right)\right] \cdot \left(\frac{\varepsilon_{c0}}{\varepsilon_{cu}}\right)^2 - \left[\frac{1}{3} - \left(Z \cdot \frac{\varepsilon_{c0} - \varepsilon_{cu}}{3}\right)\right] \cdot \left(\frac{\varepsilon_{c0}}{\varepsilon_{cu}}\right) + \left[\frac{1}{2} - \left(Z \cdot \frac{\varepsilon_{c0} - \varepsilon_{cu}}{6}\right)\right]}{\left[1 - \frac{1}{3}\frac{\varepsilon_{c0}}{\varepsilon_{cu}}\right] - \left[Z \cdot \frac{\varepsilon_{c0} - \varepsilon_{cu}}{2} \cdot \left(1 - \frac{\varepsilon_0}{\varepsilon_{cu}}\right)\right]} \tag{2.16}$$

It can be seen how, using expressions (2.15) and (2.16), the mean stress factor defined by eq. (2.13) can be expressed as $\alpha = 2 \cdot \delta \cdot \gamma$.
In Table 2.1and Table 2.2, values of coefficients α, δ and γ are reported, calculated considering two cases for the definition of the softening branch of the concrete constitutive law, i.e., the case of the *PR* law and the case of the *KP* law.

The coefficients are calculated for various values of concrete strength, with reference to cases in which strain at the extreme fiber of the section ε_c is equal or lower (i.e., greater in module) than $\varepsilon_{sp} = \varepsilon_{cu}$, namely, considering stages in which spalling is right at the beginning or has already initiated.

Table 2.1 Ultimate concrete compressive strain and parameters for equivalent rectangular stress distribution considering a concrete constitutive law with softening branch defined according to the PR law

f_c [MPa]	ε_{co}	ε_{cu}	Z	α	δ	γ
≤50	-0.0020	-0.0035	0	0.81	0.973	0.416

Table 2.2 Ultimate concrete compressive strain and parameters for equivalent rectangular stress distribution considering a concrete constitutive law with softening branch defined according to the KP law

f_c [MPa]	ε_{co}	ε_{cu}	Z	α	δ	γ
15	-0.0020	-0.0040	118	0.775	0.871	0.445
20	-0.0020	-0.0040	190	0.738	0.806	0.458
25	-0.0020	-0.0040	263	0.702	0.742	0.473
30	-0.0020	-0.0040	335	0.666	0.679	0.490
35	-0.0020	-0.0040	408	0.634	0.627	0.506
40	-0.0020	-0.0037	480	0.636	0.642	0.496
45	-0.0020	-0.0035	553	0.632	0.641	0.493
50	-0.0020	-0.0035	625	0.609	0.601	0.506

2.3 Analysis of yielding condition

2.3.1 Yielding modes, transition conditions and yielding mode domains

The yield condition of the section is conventionally considered to occur when at least one of the following conditions is reached: i) achievement of the yielding strain ε_{sy} in the tension reinforcement; ii) achievement of a certain strain value at the most compressed concrete fiber, which in the present work is assumed equal to ε_{c0} according to Priestley et al. [10], despite other choices are possible (e.g., Fardis [4] proposed to use a strain value equal to $-1.8 \cdot f_c/E_c$). The former condition is usually defined as "section yielding related to *steel* plasticization" (yielding mode *a* in the following), while the latter can be defined as "section yielding associated to *concrete* plasticization" (yielding mode *b* in the following), referring to an apparent section yielding due to the development of plastic strains in concrete. In both the two aforementioned possible yielding conditions, top steel is always elastic for sections of usual geometry (i.e., sections having cover-to-height ratio in the range $0.05 \leq c/H \leq 0.25$). Table 2.3 summarizes the considered possible yielding conditions, reporting values of bottom steel strain ε_s, top steel strain ε_s' and strain at section top fibers ε_c.

Table 2.3 Summary of considered yielding modes for a double reinforced concrete beam section

Yielding mode	Yielding occurring in:	Concrete peak strain	Bottom steel strain	Top Steel strain
a	*steel*	$\varepsilon_c < \varepsilon_{co}$	$\varepsilon_s = \varepsilon_{sy}$	$-\varepsilon_{sy} \le \varepsilon'_s \le \varepsilon_{sy}$
b	*concrete*	$\varepsilon_c = \varepsilon_{cu}$	$0 < \varepsilon_s \le \varepsilon_{sy}$	$-\varepsilon_{sy} \le \varepsilon'_s \le \varepsilon_{sy}$

The strain distribution for which both the aforementioned yielding conditions simultaneously occur defines a *transition condition*, which identify the transition between one yielding mode to the other and which can be determined imposing section equilibrium using equation (2.10). In particular, yielding mode *a* occurs if the following inequality applies:

$$1 - \frac{\rho'}{\rho} \cdot k' - \frac{2}{3} \cdot \frac{1}{\omega} \cdot \frac{x_{y,bal}}{H} \le 0 \tag{2.17}$$

The ratio $\frac{x_{y,bal}}{H}$ is the non-dimensional neutral axis depth ratio at simultaneously steel and concrete plasticization, computed using the depth H, and can be expressed as a function of the classical neutral axis depth ratio at yielding $\xi_{y,bal} = x_y/d$ as follows:

$$\frac{x_{y,bal}}{H} = \left(1 - \frac{c}{H}\right) \cdot \xi_{y,bal} \tag{2.18}$$

where $\xi_{y,bal}$ is the non-dimensional neutral axis depth ratio at simultaneously steel and concrete plasticization, computed using the depth d, which can be expressed as:

$$\xi_{y,bal} = \frac{\varepsilon_{c0}}{\varepsilon_{c0} - \varepsilon_{sy}} \tag{2.19}$$

Equation (2.17) can be conveniently split in order to separately consider the cases for which top steel is in tension or in compression. This can be performed defining the cover-to-height ratio limit value $\left(\frac{c}{H}\right)_0$, for which the simultaneously yielding condition occurs (i.e., steel plasticization and concrete plasticization) with top steel unloaded (i.e.,$\varepsilon'_s = 0$):

$$\left(\frac{c}{H}\right)_0 = \frac{1}{2 - \frac{\varepsilon_{sy}}{\varepsilon_{c0}}} \tag{2.20}$$

In the case c/H is lower than the value $(c/H)_0$ expressed by eq. (2.20), the simultaneously yielding condition occurs with top steel in compression; conversely, the simultaneously yielding condition occurs with top steel in tension.

Then, the condition for which yielding mode *a* occurs can be retrieved by splitting eq. (2.17) as follows:

$$\begin{aligned} &if \quad \frac{c}{H} \leq \left(\frac{c}{H}\right)_0 && \frac{\rho'}{\rho} > \frac{1}{k'} - \frac{2}{3}\cdot\frac{1}{k'}\cdot\frac{1}{\omega}\cdot\left(\frac{\varepsilon_{c0}}{\varepsilon_{c0}-\varepsilon_{sy}}\right)\cdot\left(1-\frac{c}{H}\right) \\ &if \quad \frac{c}{H} \geq \left(\frac{c}{H}\right)_0 && \frac{\rho'}{\rho} < \frac{1}{k'} - \frac{2}{3}\cdot\frac{1}{k'}\cdot\frac{1}{\omega}\cdot\left(\frac{\varepsilon_{c0}}{\varepsilon_{c0}-\varepsilon_{sy}}\right)\cdot\left(1-\frac{c}{H}\right) \end{aligned} \tag{2.21}$$

where k' is expressed as:

$$k' = -\frac{\varepsilon_{c0}}{\varepsilon_{sy}}\cdot\left(1+\frac{1}{1-\frac{1}{\frac{c}{H}}}\cdot\frac{\varepsilon_{c0}-\varepsilon_{sy}}{\varepsilon_{c0}}\right) \tag{2.22}$$

Equations (2.21) can be conveniently represented by plotting c/H as a function of ρ'/ρ, obtaining a limit curve which defines the transition condition between one yielding mode and the other, as for example the black curve in Fig. 2.5a. Moreover, setting a value for concrete cover c, the same condition can be expressed by plotting H against the ratio ρ'/ρ, as is the case of the black line represented in Fig. 2.6a. The transition curve expressed by eq. (2.21) allows to define the "yielding mode domains", namely, portions of the $\left(\frac{\rho'}{\rho}\right)-\left(\frac{c}{H}\right)$ graph area each one associated with a specific yielding mode, among those reported in Table 2.3. In Fig. 2.5a, it can be seen how for high ρ'/ρ and low c/H values yielding mode *a* is reached. Conversely, for low values of ρ'/ρ and high values of c/H section develop yielding mode *b*.

2.3.2 Calculation of yielding curvature

As widely known, for yielding mode *a* the section curvature at yielding ϕ_y can be expressed by the following relation (e.g., Fardis [4]):

$$\phi_y = \frac{1}{1-\xi_y}\cdot\frac{1}{1-\frac{c}{H}}\cdot\frac{\varepsilon_{sy}}{H} \tag{2.23}$$

Conversely, in the case of yielding mode *b* the section curvature at yielding ϕ_y can be calculated as:

$$\phi_y = \frac{1}{\xi_y}\cdot\frac{1}{1-\frac{c}{H}}\cdot\left(-\frac{\varepsilon_{c0}}{H}\right) \tag{2.24}$$

The non-dimensional neutral axis depth at section yielding $\xi_y = x_y/d$ vary as a function of reinforcing steel ratios ρ, ρ' and cover-to-height ratio c/H.

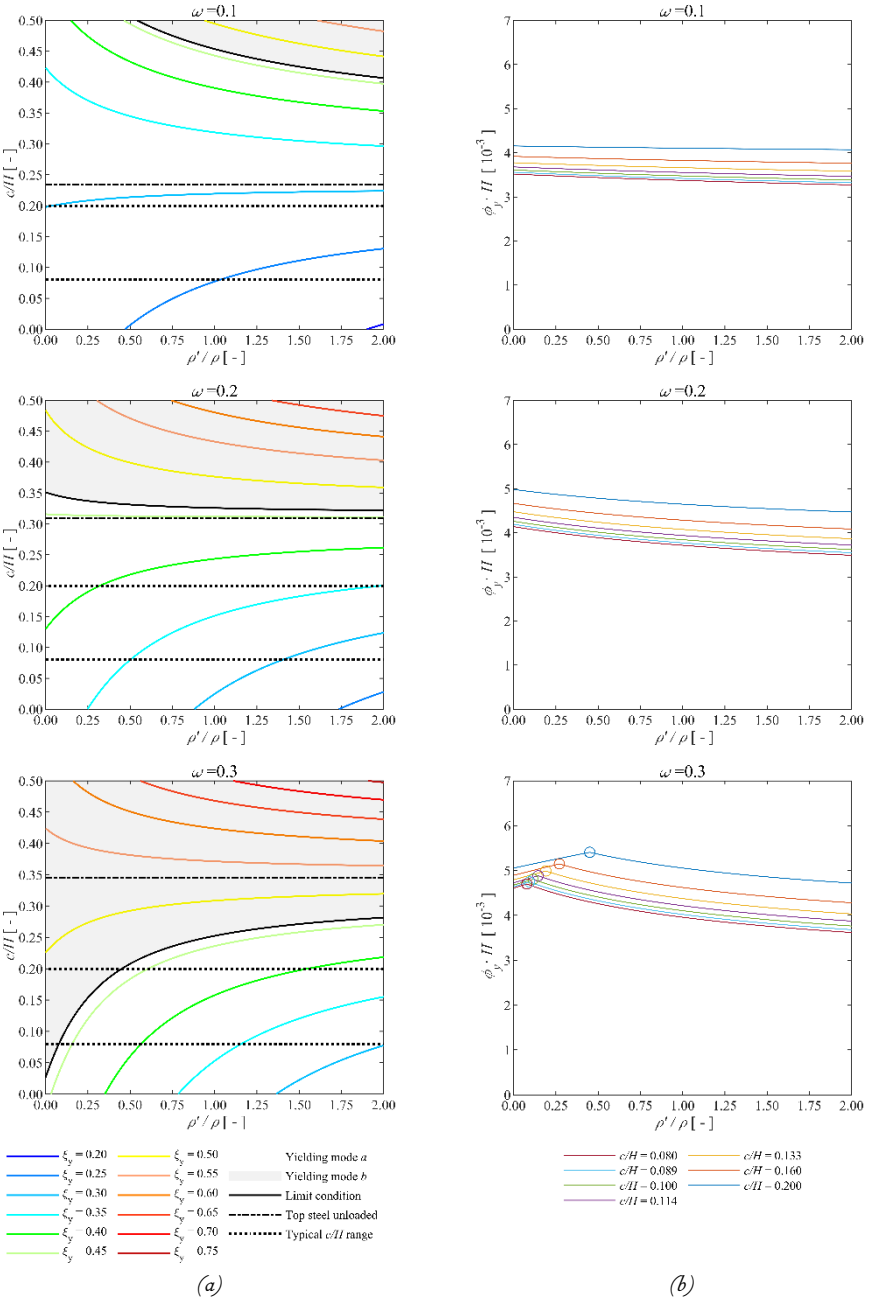

Fig. 2.5 a) Non-dimensional yielding mode domains and isocurves of non-dimensional neutral axis depth; b) Curves of yielding curvature multiplied by section height expressed as a function of reinforcement ratio ρ'/ρ. *Results were obtained using* $\varepsilon_{sy} = 2.5‰$ *and* $\varepsilon_{c0} = -2‰$.

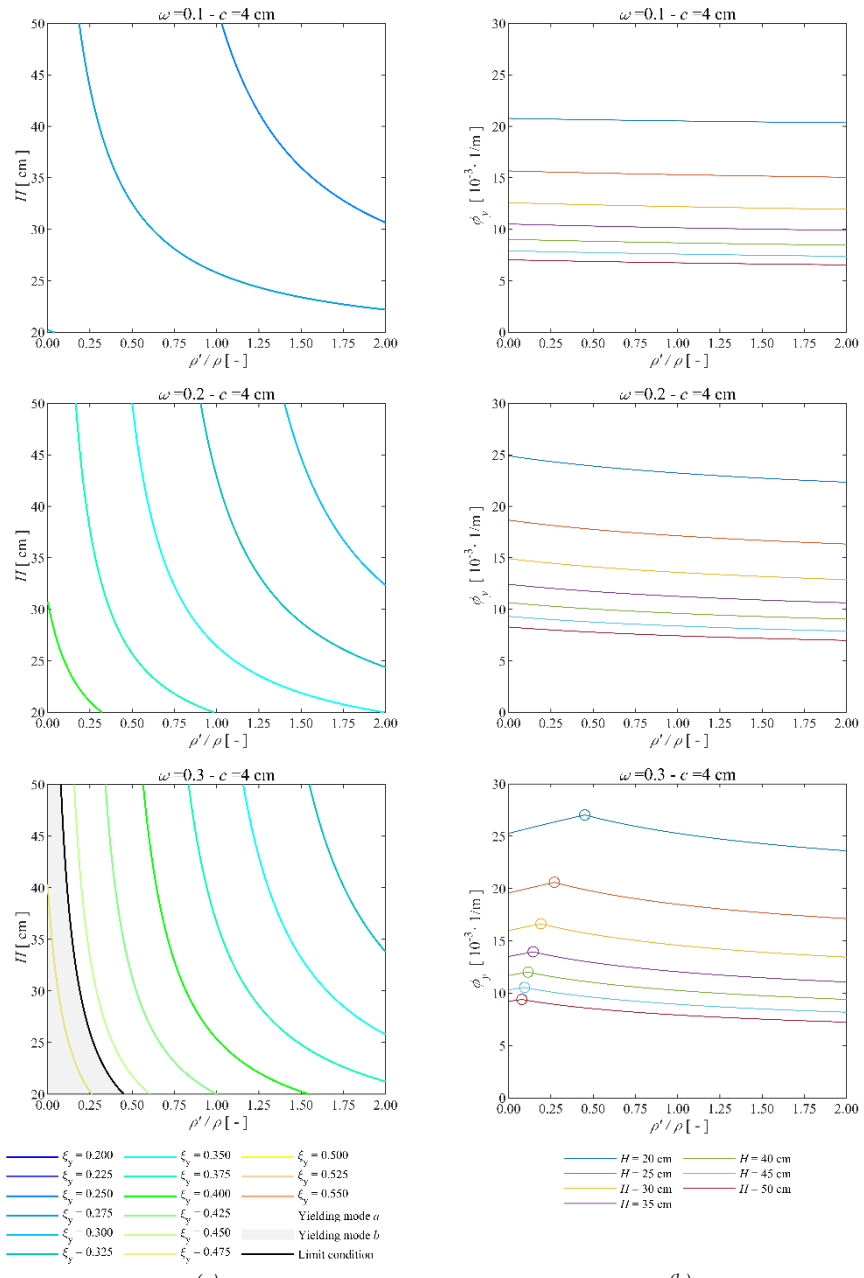

Fig. 2.6 a) Yielding mode domains and isocurves of non-dimensional neutral axis depth; b) Curves of yielding curvature as a function of reinforcement ratio ρ'/ρ. *Results were obtained using* $\varepsilon_{sy} = 2.5‰$ *and* $\varepsilon_{c0} = -2‰$.

Using axial equilibrium (2.17) it is possible to obtain an expression which identify all the yielding conditions characterized by a certain specific value of ratio ξ_y:

$$\frac{\rho'}{\rho} = \frac{1}{k'} - \alpha \cdot \frac{1}{k'} \cdot \frac{1}{\omega} \cdot \left(1 - \frac{c}{H}\right) \cdot \xi_y \tag{2.25}$$

Variables k' and α is calculated depending on the occurring yielding mode. In particular, in the case of yielding mode *a,* it holds:

$$\alpha = -\frac{1}{3} \cdot \left(-\frac{\varepsilon_{sy}}{\varepsilon_{c0}}\right)^2 \cdot \left(\frac{\xi_y}{1-\xi_y}\right)^2 + \xi_y \cdot \left(-\frac{\varepsilon_{sy}}{\varepsilon_{c0}}\right) \cdot \left(\frac{\xi_y}{1-\xi_y}\right) \tag{2.26}$$

$$k' = \left(\frac{\xi_y}{1-\xi_y}\right) \cdot \left[1 - \frac{\left(\frac{c}{H}\right)}{\left(1-\frac{c}{H}\right) \cdot \xi_y}\right] \tag{2.27}$$

Otherwise, in the case of yielding mode *b*:

$$\alpha = \frac{2}{3} \tag{2.28}$$

$$k' = -\frac{\varepsilon_{c0}}{\varepsilon_{sy}} \cdot \left[1 - \frac{\left(\frac{c}{H}\right)}{\left(1-\frac{c}{H}\right) \cdot \xi_y}\right] \tag{2.29}$$

Isocurves of non-dimensional neutral axis depth at yielding ξ_y are represented in Fig. 2.5a, together with the limit curve (2.21) which divides the graph area into the two yielding mode domains. Obviously, it can be clearly seen that type-*a* yielding modes are characterized by values of non-dimensional neutral axis depth ratio at yielding ξ_y lower than $\xi_{y,bal}$, while for type-*b* yielding modes the opposite situation holds. All ξ_y isocurves have a horizontal asymptote for ρ'/ρ that tends to infinity. Conversely, as ρ'/ρ decreases the isocurves approach a vertical asymptote. In particular, the isocurves tend to a positive infinite values of height H if the top steel is compressed at yielding; conversely, they tend to a negative infinite values of height H if the top steel is in tension at yielding.
The transition curve between yielding conditions with the top steel compressed and those with the top steel in tension consists of a horizontal line, whose c/H value is calculated differently depending on whether the yielding condition with top steel unloaded occurs with yielding mode *a* (steel side) or *b* (concrete side). In particular, the yielding condition with top steel unloaded occurs with the yield mode *a* (steel side) if the following inequality applies:

$$\rho \leq \frac{2}{3} \cdot \frac{f_c}{f_y} \cdot \frac{\varepsilon_{c0}}{2 \cdot \varepsilon_{c0} - \varepsilon_{sy}} \tag{2.30}$$

In that case, the value of the ratio c/H identifying the yielding conditions with unloaded top steel, denoted as $\left(\frac{c}{H}\right)_{0,y,s}$, is represented by the smallest positive root of the following equation:

$$\left[\frac{1}{3}\cdot\left(\frac{\varepsilon_{sy}}{\varepsilon_{c0}}\right)^2\cdot\frac{1}{\omega}-2\cdot\left(\frac{\varepsilon_{sy}}{\varepsilon_{c0}}\right)\cdot\frac{1}{\omega}\right]\cdot\left(\frac{c}{H}\right)_{0,y,s}^3+ \\ +\left[4+\left(\frac{\varepsilon_{sy}}{\varepsilon_{c0}}\right)\cdot\frac{1}{\omega}\right]\cdot\left(\frac{c}{H}\right)_{0,y,s}^2-4\cdot\left(\frac{c}{H}\right)_{0,y,s}+1=0 \tag{2.31}$$

Conversely, in the case condition (2.30) is not met, the yielding condition with unloaded top steel occurs with yielding mode *b* (concrete side) and the value of the ratio c/H identifying the yielding conditions with unloaded top steel, denoted as $\left(\frac{c}{H}\right)_{0,y,c}$, is expressed as follows:

$$\left(\frac{c}{H}\right)_{0,y,c}=\frac{\frac{\varepsilon_{c0}}{\varepsilon_{sy}}+\sqrt{\left(\frac{\varepsilon_{c0}}{\varepsilon_{sy}}\right)^2-\frac{2}{3}\frac{1}{\omega}\frac{\varepsilon_{c0}}{\varepsilon_{sy}}}}{\frac{2}{3}\frac{1}{\omega}} \tag{2.32}$$

For usual section geometry and material properties the yielding condition practically always occurs with top steel in compression, as in the cases represented in Fig. 2.5a.
The calculation of the actual value of the neutral axis depth at yielding, required for calculating the yielding curvature according to expression (2.23) or (2.24), needs to be performed distinguishing between the two possible yielding modes. Namely, for yielding mode *a,* the non-dimensional depth of neutral axis at yielding ξ_y is represented by the smallest positive root of the following equation:

$$\left\{\left[\frac{1}{3}\cdot\left(\frac{\varepsilon_{sy}}{\varepsilon_{c0}}\right)^2-\left(\frac{\varepsilon_{sy}}{\varepsilon_{c0}}\right)\right]\cdot\frac{1}{\omega}\cdot\left(1-\frac{c}{H}\right)\right\}\cdot\xi_y^3+\left\{1+\frac{\rho'}{\rho}+\left(\frac{\varepsilon_{sy}}{\varepsilon_{c0}}\right)\cdot\frac{1}{\omega}\cdot\left(1-\frac{c}{H}\right)\right\}\cdot\xi_y^2+ \\ -\left\{2+\frac{\rho'}{\rho}\cdot\left(\frac{1}{1-\frac{c}{H}}\right)\right\}\cdot\xi_y+\left\{1+\frac{\rho'}{\rho}\cdot\left(\frac{\frac{c}{H}}{1-\frac{c}{H}}\right)\right\}=0 \tag{2.33}$$

On the other hand, if yielding mode *b* occurs, the non-dimensional depth of neutral axis at yielding ξ_y can be obtained by means of the following expression:

$$\xi_y=\frac{\frac{\varepsilon_{c2}}{\varepsilon_{sy}}\cdot\left(1+\frac{\rho'}{\rho}\right)-\sqrt{\left[\frac{\varepsilon_{c2}}{\varepsilon_{sy}}\cdot\left(1+\frac{\rho'}{\rho}\right)\right]^2+4\cdot\frac{2}{3}\frac{1}{\omega}\frac{\varepsilon_{c2}}{\varepsilon_{sy}}\cdot\left[1-\frac{c}{H}\left(1-\frac{\rho'}{\rho}\right)\right]}}{-\frac{4}{3}\frac{1}{\omega}\left(1-\frac{c}{H}\right)} \tag{2.34}$$

Using the position of the neutral axis ξ_y obtained from the relations (2.33) and (2.34) in expression (2.23) or (2.24) it is then possible to calculate the yielding curvature for a generic rectangular doubly reinforced concrete section in uniaxial flexure. In order to study the dependence of the yielding curvature on the parameters ρ, ρ', c/H, a parametric analysis has been performed, whose results are plotted in Fig. 2.5b and Fig. 2.6b. It is obviously possible to observe how, when the parameter ρ'/ρ varies, the yielding curvature increases as long as the yielding mode is type *b*, while it starts to decrease if

the section yields according to mode *a*. For low-to-mid values of bottom reinforcement ratio ρ, yielding practically always occurs according to mode *a*.
Some considerations are worth regarding the yielding curvature values obtained from expressions (2.23) and (2.24). As it is well known, in the case of yielding mode *a* (steel side), the yielding curvature calculated according to (2.23) is actually associated with a significant reduction of stiffness in the moment-curvature curve of the section, which clearly identifies the plasticization. On the other hand, for yielding mode *b* (concrete side), in correspondence of the curvature value given by (2.24) the moment-curvature curve often does not present relevant changes of the slope.
Sometimes, it is useful to schematize the moment-curvature response as a bi-linear curve. In order to assure that such a simplified representation would best capture the trend of the actual moment-curvature relation, it is usually possible to refer to a conventional value of the yielding curvature, which is greater than that provided by the expressions (2.23) and (2.24) (e.g., Paulay and Priestley [9], Priestley et al. [10]). A possible expression for the conventional yielding curvature ϕ_y^* is the following:

$$\phi_y^* = \phi_y \cdot \frac{M_n}{M_y} \tag{2.35}$$

where the term M_y is the bending moment at section yielding and M_n is a nominal bending strength, which can be taken, for example, equal to the peak strength of the moment-curvature relation.
However, it is to be noted that for doubly reinforced concrete beam sections which reach yielding through yielding mode *a* (i.e., steel-side yielding), the value M_n/M_y is in many cases not so greater than 1, considering also the limitations on hardening of reinforcing steel used in high seismicity regions, required to satisfy capacity design principles. For this reason, in most cases the conventional yielding curvature ϕ_y^* is not so different from the yielding curvature ϕ_y retrieved by using Eq. (2.23) and so using the latter in place of the former is usually a fairly acceptable approximation.

2.4 ANALYSIS OF ULTIMATE CONDITION

2.4.1 FAILURE MODES, TRANSITION CONDITIONS AND FAILURE MODE DOMAINS

Failure of the section can be associated to several different strain distributions. In this work, different possible failure modes area considered, taking into account all the ones which a physically feasible. Failure modes are divided in two main categories, namely, concrete-related failures and steel-related failures. Among concrete failures, a further distinction is made based on the strain of bottom reinforcement (i.e., elastic or yielded in tension). On the other hand, steel failures are subdivided according to the strain value for the extreme section fiber (i.e., lower than concrete ultimate compression strain ε_{cu}, lower than strain at peak concrete strength ε_{c0} or greater than strain at peak concrete strength ε_{c0}). Moreover, for both concrete and steel failures, different failure modes are considered based on strain levels of the top reinforcement (i.e., yielded in tension, elastic or yielded in compression).

The ultimate conditions of the section associated to concrete failure, may be evaluated differently depending on whether the possibility of expelling the concrete cover is regarded to be acceptable or not. The possibility of taking into account the expulsion of the concrete cover can be considered acceptable if the section has sufficient transverse reinforcement and if the expulsion of the concrete cover generates a section strength loss not exceeding a fixed limit value. As mentioned before, this limit value can usually be assumed to be in the range 15%÷20%, as suggested by Park [99], Paulay and Priestley [9] and Priestley et al. [19].

If cover spalling is not acceptable, concrete failures needs to be computed with a spalling depth at failure s_u equal to zero, and the concrete side ultimate conditions are considered to be reached when the outer fiber of the concrete cover achieves the strain ε_{sp}. If, on the other hand, cover spalling is acceptable and the possibility of expelling the cover at failure is taken into account, the ultimate conditions associated to concrete failure are considered to be reached when the spalling depth at failure s_u equals s_{lim}. In this case, the concrete side failures are considered achieved when the outer fiber of the concrete core reaches the strain ε_{cu}. It is worth to point out that it is no meaningful to assume concrete-side failures with values of s_u comprised in the range $0 < s_u < s_{lim}$, since once the crushing-induced concrete spalling process begins, it is not possible to assure that it would stop before the total expulsion of the cover.

A list of considered in the present work is reported in Table 2.4, in which a capital letter is associated to each failure mode, specifying also the failure type and strains at relevant section fibers. In Table 2.4 the term $\varepsilon(s_u)$ indicates the concrete strain at the fibers having depth s_u. Also, the concrete strain values in Table 2.4 for concrete failure modes (modes A to E) are specified considering the simplified assumption for which $\varepsilon_{cu} = \varepsilon_{sp}$, which is adopted throughout all this chapter. To address the more general case for which $\varepsilon_{cu} \neq \varepsilon_{sp}$, different specifications for concrete failure modes can be defined to identify i) the set of failure mode achievable disregarding the cover spalling and ii) the set of failure modes achievable considering the possibility of cover spalling.

Table 2.4 Summary of considered failure modes for a double reinforced concrete beam section, considering the simplified assumption $\varepsilon_{cu} = \varepsilon_{sp}$ (Note: For concrete failures only, in case cover spalling is disregarded ε_c refers to the outer cover fiber, while in case cover spalling is considered ε_c refers to the outer core fiber)

Failure mode	Failure occurring in:	Concrete strain	Bottom steel strain	Top Steel strain
A	*concrete*	$\varepsilon(s_u) = \varepsilon_{cu}$	$\varepsilon_s \le \varepsilon_{sy}$	$-\varepsilon_{sy} \le \varepsilon'_s \le \varepsilon_{sy}$
B	*concrete*	$\varepsilon(s_u) = \varepsilon_{cu}$	$\varepsilon_s \le \varepsilon_{sy}$	$\varepsilon'_s \le -\varepsilon_{sy}$
C	*concrete*	$\varepsilon(s_u) = \varepsilon_{cu}$	$\varepsilon_{sy} \le \varepsilon_s \le \varepsilon_{su}$	$\varepsilon'_s \ge \varepsilon_{sy}$
D	*concrete*	$\varepsilon(s_u) = \varepsilon_{cu}$	$\varepsilon_{sy} \le \varepsilon_s \le \varepsilon_{su}$	$-\varepsilon_{sy} \le \varepsilon'_s \le \varepsilon_{sy}$
E	*concrete*	$\varepsilon(s_u) = \varepsilon_{cu}$	$\varepsilon_{sy} \le \varepsilon_s \le \varepsilon_{su}$	$\varepsilon'_s \le -\varepsilon_{sy}$
F	*steel*	$\varepsilon_c > \varepsilon_{co}$	$\varepsilon_s = \varepsilon_{su}$	$\varepsilon'_s \ge \varepsilon_{sy}$
G	*steel*	$\varepsilon_c > \varepsilon_{co}$	$\varepsilon_s = \varepsilon_{su}$	$-\varepsilon_{sy} \le \varepsilon'_s \le \varepsilon_{sy}$
H	*steel*	$\varepsilon_{cu} \le \varepsilon_c \le \varepsilon_{co}$	$\varepsilon_s = \varepsilon_{su}$	$\varepsilon'_s \ge \varepsilon_{sy}$
I	*steel*	$\varepsilon_{cu} \le \varepsilon_c \le \varepsilon_{co}$	$\varepsilon_s = \varepsilon_{su}$	$-\varepsilon_{sy} \le \varepsilon'_s \le \varepsilon_{sy}$
J	*steel*	$\varepsilon_{cu} \le \varepsilon_c \le \varepsilon_{co}$	$\varepsilon_s = \varepsilon_{su}$	$\varepsilon'_s \le -\varepsilon_{sy}$
K	*steel*	$\varepsilon_c \le \varepsilon_{cu}$	$\varepsilon_s = \varepsilon_{su}$	$-\varepsilon_{sy} \le \varepsilon'_s \le \varepsilon_{sy}$
L	*steel*	$\varepsilon_c \le \varepsilon_{cu}$	$\varepsilon_s = \varepsilon_{su}$	$\varepsilon'_s \le -\varepsilon_{sy}$

Considering steel failures, for failure modes F to J the most compressed concrete fiber in the section does not reach the ultimate concrete compressive strain ε_{cu}, and so spalling of the concrete cover is not triggered, i.e. $s_u = 0$. On the other hand, failure modes K and L represent peculiar cases, and some considerations are worth. These failure modes assume that steel failure is reached during the spalling process of the compressed cover concrete. As a consequence, the depth of the spalled portion of the cover at the ultimate condition s_u is comprised in the range $0 < s_u < s_{lim}$. It should be noted that this assumption does not contradict what was previously said about the unitary nature of the cover ejection process (once the cover ejection process has been triggered, it cannot be guaranteed that it will stop before complete spalling). The failure modes K and L, in fact, refer to a distribution of deformations associated with a partial expulsion of the concrete cover because their strain distribution represent ultimate conditions for the section, in which the bottom steel reaches ultimate steel strain ε_{su}. Actually, the disregard of these ultimate conditions when they could occur would result in considering a concrete side failure with complete cover expulsion. This assumption could indeed lead to possible overestimations of the ultimate curvature. Therefore, in order to provide a conservative approach, it is useful to also consider the failure modes K and L.

It is worth to underline that for standard geometry and sound material mechanical properties, not all the failure modes mentioned in Table 2.4 can actually occur. Failure modes F and G, that are associated to ultimate conditions for which the concrete does not reach its compressive strength, can only take place for sections having reinforcing

steel with a low ultimate tensile strain and low bottom reinforcement ratio and a high c/H ratio. On the other hand, failure mode J can only be reached for extremely low values of c/H ratio, hardly found in sections designed according to nowadays durability requirements. A special mention deserves the failure mode L, which can actually take place only if the reinforcing steel has a very steep hardening branch. Indeed, since in the framework presented in this chapter the steel has been modeled using a plastic-perfectly plastic law, the failure mode L cannot be achieved at all in the studied cases.
Similarly to what has been done for the study of the yielding modes, it is also possible to define conditions representing transitions between failure modes. The transition conditions can be defined according to the failure modes given in Table 2.4 and are presented in the flow-chart reported in Fig. 2.7. A total of eleven transition conditions have been identified. Analytical expression for each condition can be determined by following an approach similar to that used for the yielding modes transition condition. Specifically, the equilibrium equation (2.8) is employed, for which the terms k, k', and α are determined by imposing that the section develops an ultimate condition which represent a transition condition between two different failure modes.
Transition conditions U1 - U4 can be expressed by considering four different strain levels for the top steel at the section ultimate condition, namely, yielded in compression, elastic in compression, elastic in tension and yielded in tension. For this purpose, it is useful to introduce the terms $\left(\frac{c}{H}\right)_{u,y,c}$, $\left(\frac{c}{H}\right)_{u,0}$, $\left(\frac{c}{H}\right)_{u,y,t}$, which represent the values of the ratio c/H for which the analyzed transition condition occurs respectively with top steel having strain $\varepsilon'_s = -\varepsilon_{sy}$ (onset of compression yielding), $\varepsilon'_s = 0$ (unloaded), and $\varepsilon'_s = \varepsilon_{sy}$ (onset of tensile yielding). On the other hand, the transition conditions U5 - U11 are already associated with specific strain values of the top steel at failure condition, so they can be defined each by a single expression. The closed-form analytical expressions of all the transition conditions shown in Fig. 2.7, are given in Appendix A.
Similarly to the approach presented for the analysis of the yielding mode, the limit conditions which identify the transitions between one failure mode and another can be conveniently represented as curves in a Cartesian coordinate system with the non-dimensional variables ρ'/ρ and c/H on the axes. In this way, graphs are obtained in which the limit condition curves divide the area into domains, each one identifying one of the failure modes presented in Table 2.4. Considering the variability of the mechanical parameters of the section, three possible configurations of failure mode domains are identified [100], indicated as *Type 1*, *Type 2* and *Type 3*, as depicted in Fig. 2.8. The three possible identified configurations for failure mode domains are distinguished each other by the differernt configurations assumed by transition conditions U3 and U4. The domains configuration changes from *Type 1* to *Type 2* and up to T*ype 3*, when either ultimate steel strain ε_{su} and/or mechanical reinforcement ratio ω decrease. Fig. 2.8a,b represent *Type 1* configuration, which occurs when the branches of curves U3 and U4 visible in the graphs are both concave. For this configuration, steel failures almost never occur, considering reasonable values of c/H. For *Type 2* configuration, which occur when curve U4 become convex while curve U3 remains concave, steel failures may be achieved for beams with low values of parameters ρ'/ρ and c/H (Fig. 2.8c,d). In *Type 3*

configuration, Fig. 2.8e,f, both curves U3 and U4 are convex and domains related to steel failures overwhelm the other ones. Since *Type 2* and *Type 3* configurations are characterized by low values of ultimate steel strain, the deformation capacity of the section associated with steel failures for those cases will be very low.
Considering the analytical expressions of transition conditions U3 and U4, it is possible to determine the analytical conditions which define what configuration type will takes place. In particular, the *Type 1* configuration occurs when the following inequality applies:

$$\varepsilon_{su} - \varepsilon_{cu} \cdot \left(\frac{\alpha}{\omega} - 2\right) > 0 \tag{2.36}$$

The *Type 3* configuration occurs instead when:

$$\varepsilon_{su} - \varepsilon_{c2} \cdot \left(\frac{\alpha}{\omega} - 2\right) < 0 \tag{2.37}$$

In case when nor eq. (2.36) neither eq. (2.37) are satisfied, the *Type 2* configuration is achieved. Additional examples of graphs of failure mode domains belonging only to T*ype 1* configuration are provided in Fig. 2.9a, in which three different values of mechanical reinforcement ratio ω have been considered. An alternative representation of the domains can be obtained by selecting a fix value for the cover c and by plotting the section height on the vertical axis of the graphs, see Fig. 2.10a. It can be seen in the presented examples that, considering the adopted values for mechanical reinforcement ratio and the usual height range of interest for double reinforced concrete beams, ultimate condition is reached in the majority of cases by means of failure modes D and E, while modes B and K are also achieved in some cases. Comparing the three cases depicted in Fig. 2.9a and Fig. 2.10a, it is possible to observe how the mechanical reinforcement ratio ω affects the shape and location of failure mode domains.

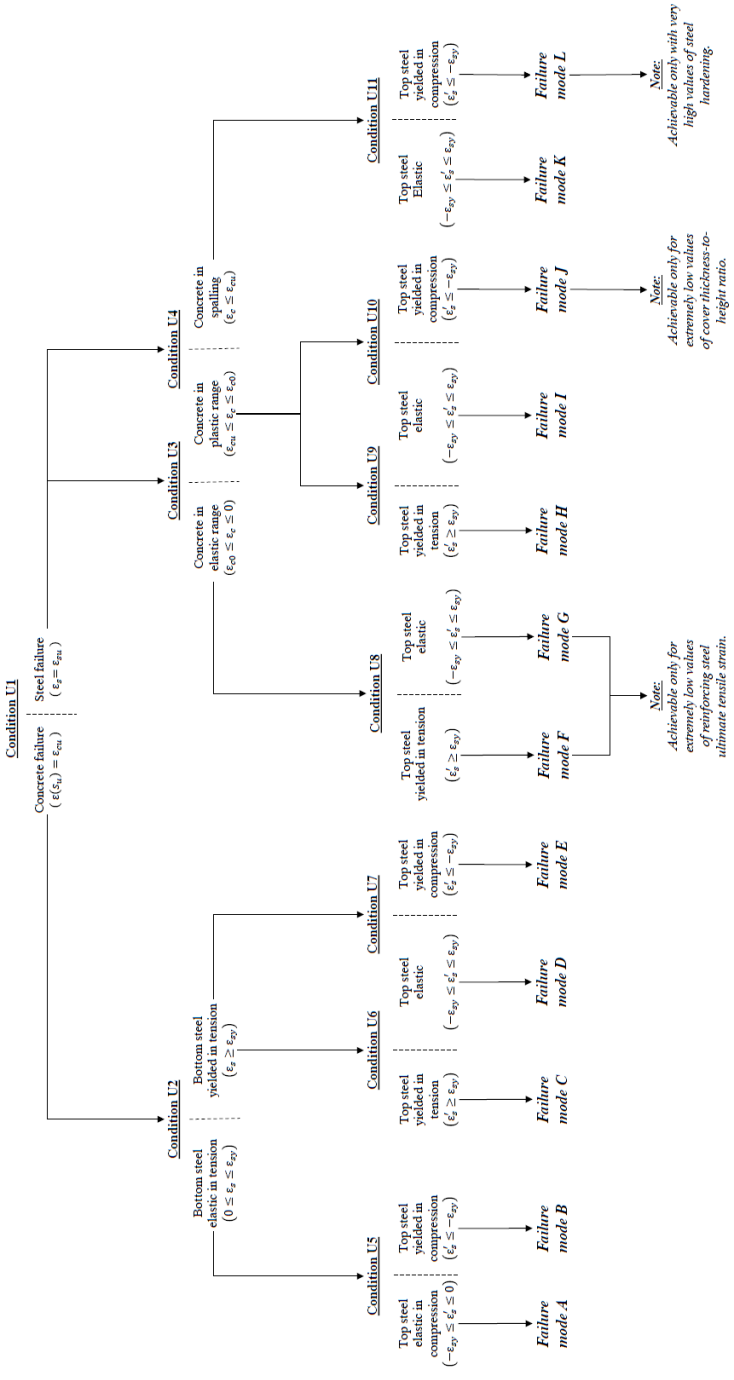

Fig. 2.7 Transition conditions between different failure modes, considering the possibility of cover spalling

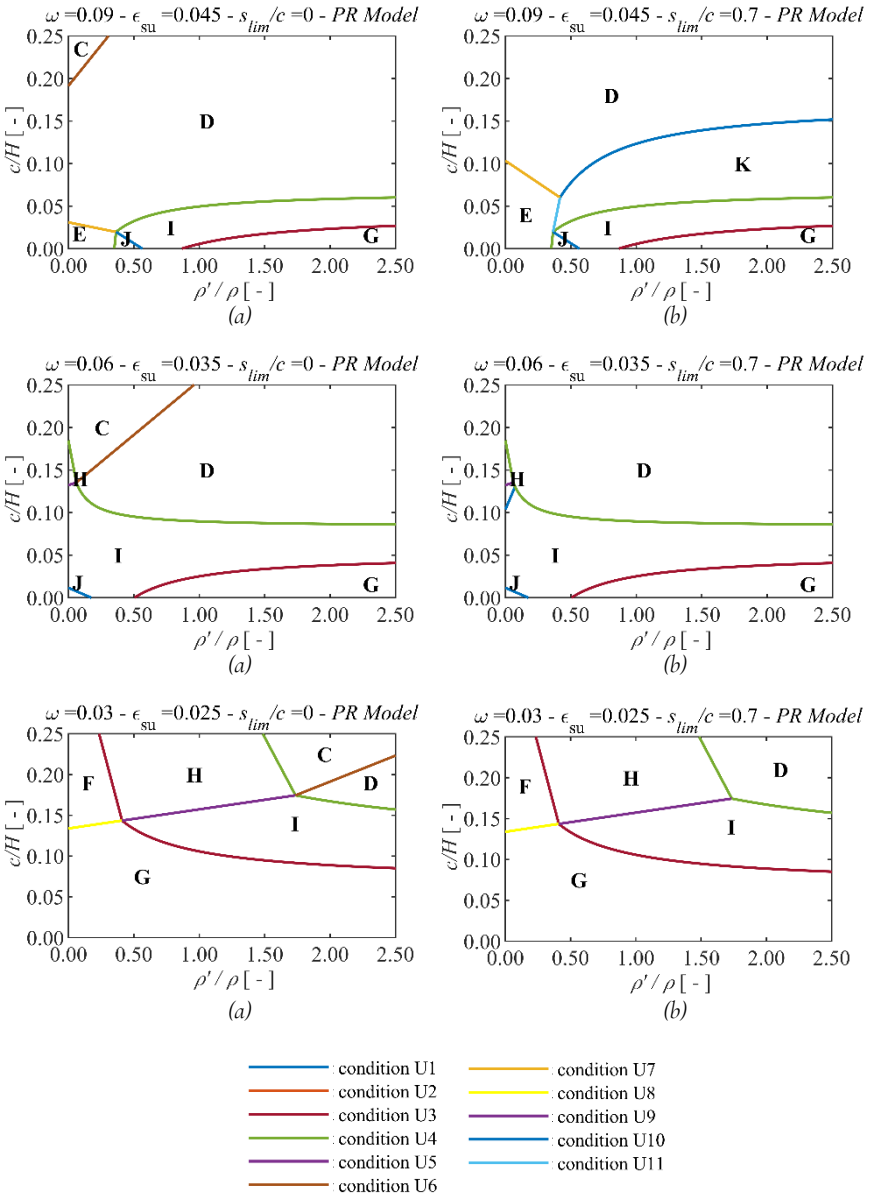

Fig. 2.8 Example of domains for identification of the ultimate condition for doubly reinforced concrete beams (a), (b) Type 1 configuration; (c), (d) Type 2 configuration; (e), (f) Type 3 configuration.

2.4.2 Calculation of ultimate curvature and spalling-induced strength loss

Ultimate curvature ϕ_u of a RC section can be expressed, as widely known, as a function of neutral axis depth at failure x_u. In case of a failure mode associated to concrete failure (failure modes A to E), the ultimate curvature can be conveniently expressed as follows:

$$\phi_u = -\frac{\varepsilon_{cu}}{H} \cdot \frac{1}{\left(\frac{x_u - s_u}{H}\right)} \tag{2.38}$$

In the previous equation, the term s_u indicates the value of spalling depth s reached at the section ultimate condition. If a failure mode associated to steel failure is instead considered (failure modes F to K), the ultimate curvature can be calculated as:

$$\phi_u = \frac{\varepsilon_{su}}{H} \cdot \frac{1}{\left(1 - \frac{c}{H} - \frac{x_u}{H}\right)} \tag{2.39}$$

Expressions for the terms $\left(\frac{x_u - s_u}{H}\right)$ and $\left(1 - \frac{c}{H} - \frac{x_u}{H}\right)$ have been analytically derived for failure modes considered in the proposed framework and are reported in Appendix B. In Fig. 2.9b the ultimate curvature multiplied by section height, $\phi_u \cdot H$, is plotted against the ρ'/ρ ratio, for different values of c/H. By comparing these graphs with those of non-dimensional failure mode domains reported in Fig. 2.9a, it is possible to analyze the dependence of $\phi_u \cdot H$ on the parameter c/H. In particular, it can be seen that for failure mode D the term $\phi_u \cdot H$ is independent on c/H, while for failure mode E higher values of c/H lead to lower values of $\phi_u \cdot H$. The latter tendency inverts for failure mode K, in which an increase in c/H produces a very slightly increase in $\phi_u \cdot H$. Fig. 2.10b shows how the ultimate curvature varies as a function of the ρ'/ρ ratio and the height H of the beam section, having chosen a typical value for the cover equal to $c = 4cm$. It can be seen that, by considering the spalling of the concrete cover, values of the ultimate curvature in the range $150 \div 200 \cdot 10^{-3}\, 1/m$ can be reached for a unitary ρ'/ρ ratio. Such curvature values are considerably greater than those relative to ultimate conditions computed not considering the spalling of the concrete cover.

Comparing the curves in Fig. 2.9b and Fig. 2.10b with the domains of the failure modes presented in Fig. 2.9a and Fig. 2.10a, it is possible to note how the trend of the ultimate curvature changes when the failure mode changes. In the graphs in Fig. 2.10b, the points at which the failure mode changes are indicated by circular markers. It can be seen, in particular, how the value of the ultimate curvature that occurs in correspondence with the transition condition U7 (transition between failure modes D and E) is independent on the height of the section.

Observing the graphs presented in Fig. 2.9b and Fig. 2.10b, it can then be seen that the ultimate curvature cannot increase indefinitely by increasing the ρ'/ρ ratio. In fact, it reaches its maximum value when the ultimate condition occurs at the transition condition between a concrete-side failure and a steel-side failure. At the occurrence of such ultimate condition, the spalling depth at failure s_u is equal to s_{lim}, and the strain at bottom rebars is equal to the rebar ultimate tensile strain ε_{su}.

According to the derived strain distribution, the maximum value attainable by the ultimate curvature $\phi_{u,max}$ can be evaluated using eq. (2.40). It can be noted that by increasing parameters c/H or s_{lim}, the maximum value of ultimate curvature increases.

$$\phi_{u,max} = \frac{1}{H} \cdot \frac{\varepsilon_{su} - \varepsilon_{cu}}{1 - \frac{c}{H}\left(1 + \frac{s_{lim}}{c}\right)} \tag{2.40}$$

Fig. 2.11a shows an example of the failure mode domains obtained by neglecting (left-hand graphs) or considering (right-hand graphs) the spalling of the concrete cover in the ultimate condition, for a value $\rho = 0.01$ and considering concrete laws representative of both *PR* and *KP* laws. It can be seen that domains of all the failure modes on the steel side, except for the failure mode K, remain unchanged. Vice versa, the domains related to the concrete side failure modes and the domain associated to the mode K (steel side failure occurring during the spalling of the concrete cover) vary appreciably. In particular, by accepting to consider the occurrence of cover spalling, the deformation at the compressed side of the section is much higher and the top steel will reach yielding more easily at the ultimate condition of the section.
For this reason, it is reasonable to observe the expansion of failure mode domain related to failure mode E (failure at the concrete side with both reinforcements yielded, respectively in tension and compression).
In Fig. 2.11b the variation of the term $\phi_u \cdot H$ is presented for the cases obtained neglecting and considering concrete cover spalling, and analyzing again the different results which are obtained adopting the *PR* or the *KP* constitutive law for concrete. The curves can be compared with the domains in Fig. 2.11a. In Fig. 2.11b it can be seen that for cases in which the section reaches the ultimate condition on the concrete side, the calculation performed using the *KP* concrete law provides greater values of ultimate curvature than that performed using the *PR* concrete law. In addition, the observed increment in ultimate curvature is greater if the section failure occurs with the top steel elastic (e.g. failure mode D). Such increase in deformation capacity can be attributed mainly to the fact that a value of concrete ultimate deformation $\varepsilon_{cu} = \varepsilon_{sp} = 0.004$ was assumed for the *KP* constitutive law, which is greater than that adopted for the *PR* law.

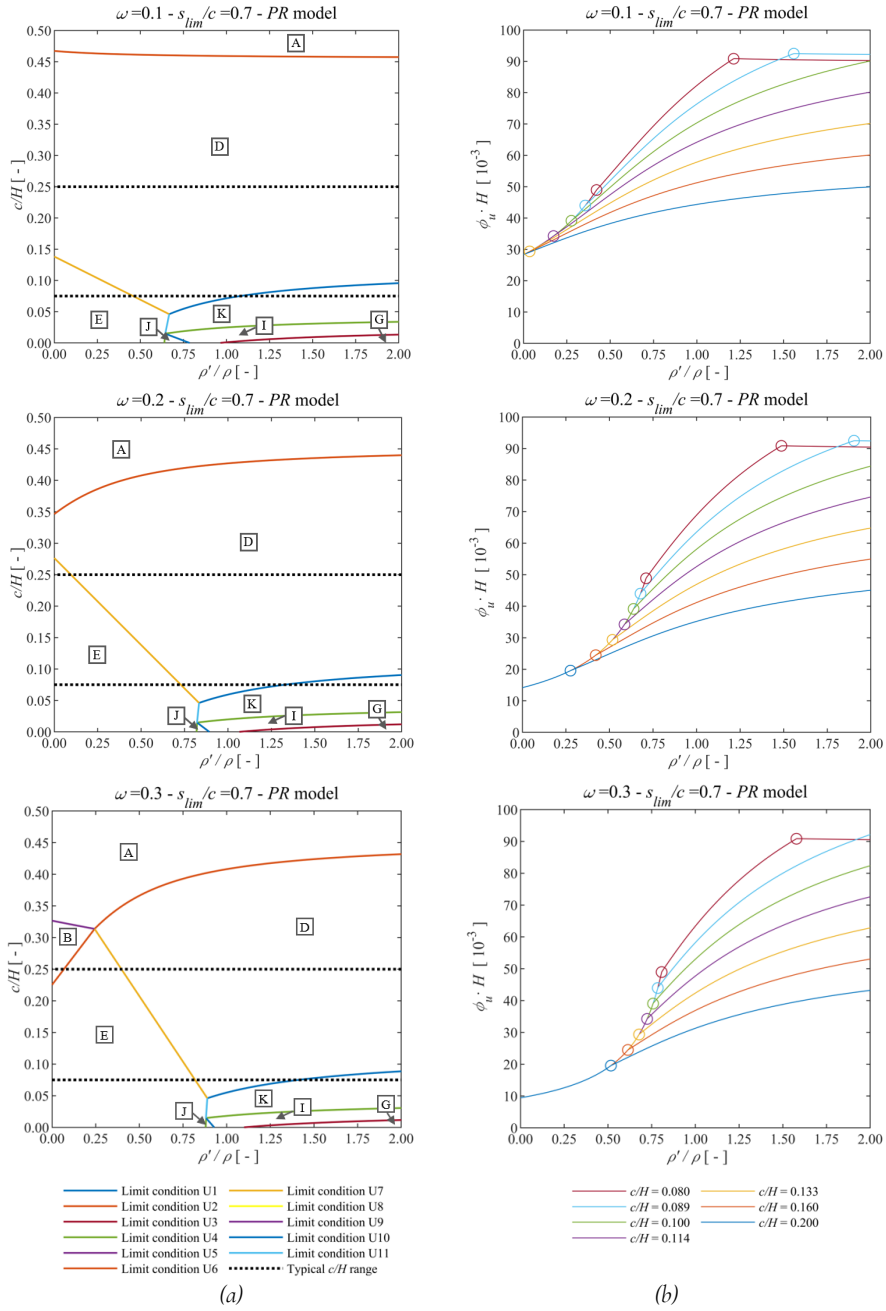

Fig. 2.9 (a) Non-dimensional failure mode domains for different values of ω *assuming PR law for concrete; (b) Ultimate curvature multiplied by section height, evaluated for different* c/H *and* ω*. Calculations have been performed considering steel strains* $\varepsilon_{sy} = 2.5‰$ *and* $\varepsilon_{su} = 75‰$*.*

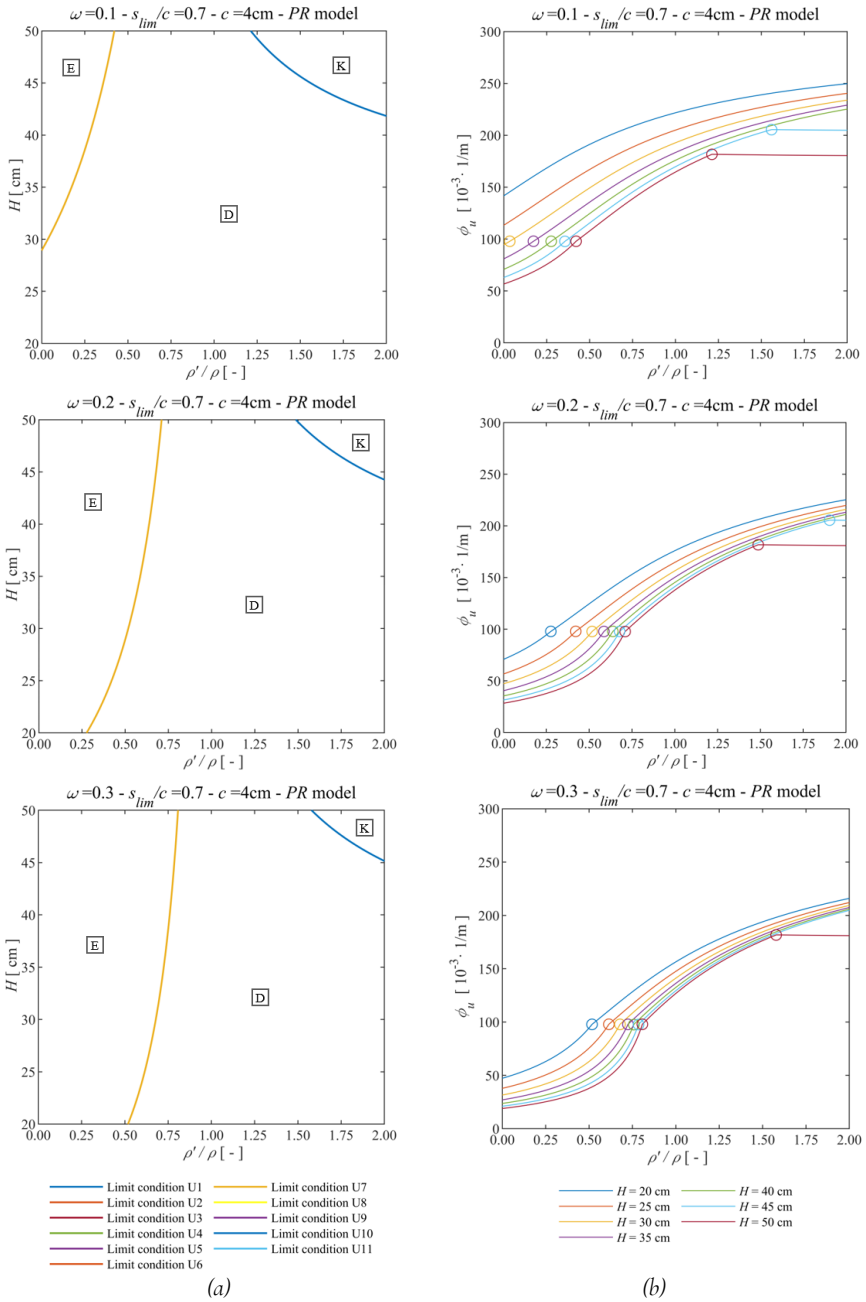

Fig. 2.10 (a) Failure mode domains for different values of ω *assuming PR law for concrete; (b) Ultimate curvature multiplied by section height, evaluated for different* H *and* ω*. Calculations have been performed considering steel strains* $\varepsilon_{sy} = 2.5‰$ *and* $\varepsilon_{su} = 75‰$.

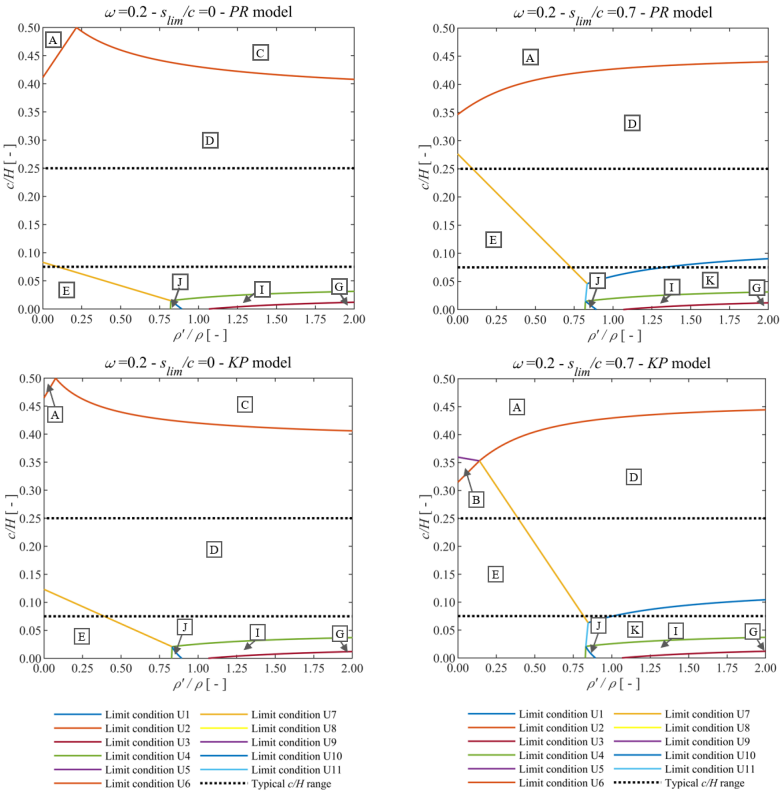

(a)

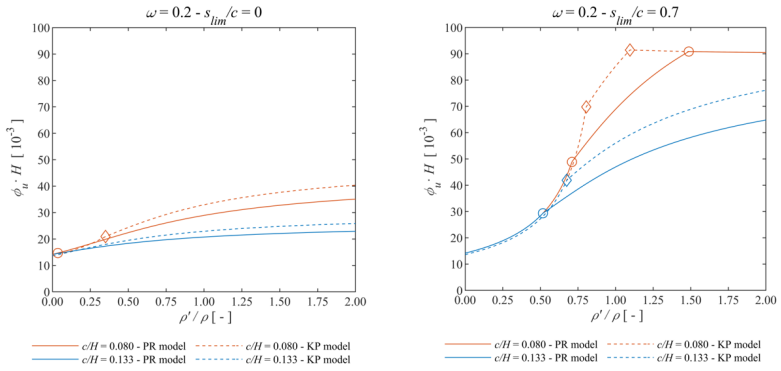

(b)

Fig. 2.11 (a) Non-dimensional failure mode domains evaluated considering parabola-rectangle (PR) or Kent-Park (KP) models for concrete, exploiting cases without cover spalling ($s_{lim}/c = 0$) and with cover spalling ($s_{lim}/c \neq 0$); (b) Ultimate curvature multiplied by section height, for two c/H values and considering cases with and without cover spalling at failure, comparing the two adopted concrete models (i.e., PR and KP). Calculations have been performed considering steel strains $\varepsilon_{sy} = 2.5‰$ and $\varepsilon_{su} = 75‰$.

It can be useful to analyze in more detail which is the increment of ultimate curvature that can be attained by considering the cover spalling in the computation of the ultimate condition. With this aim, the increment ratio of ultimate curvature Δ_c is defined as follows:

$$\Delta_c = \frac{\phi_u(s_u \geq 0) - \phi_u(s_u = 0)}{\phi_u(s_u = 0)} \tag{2.41}$$

In order to evaluate the ratio Δ_c, it is necessary to calculate the ultimate curvature both neglecting cover spalling $\phi_u(\varepsilon_{sp}\ at\ s_u = 0)$ and considering cover spalling at failure $\phi_u(\varepsilon_{cu}\ at\ s_u \geq 0)$. As mentioned before, a typical value for s_{lim} can be the concrete cover measured from the stirrup axis c_w, which leads to values of ratio s_{lim}/c typically belonging to the range $0.6 \div 0.8$. In Fig. 2.12 the variability of non-dimensional increment of ultimate curvature Δ_c is plotted considering a value $s_{lim}/c = 0.7$, and it can be seen that, by considering concrete cover spalling at failure, ultimate curvature increments up to $150 \div 200\%$ can be obtained for high values of ρ'/ρ. Following the approach adopted for the increment of ultimate curvature, a non-dimensional measure of bending strength loss due to the occurrence of cover spalling can be defined as:

$$\Delta_s = \left|\frac{M_u(s_u \geq 0) - M_u(s_u = 0)}{M_u(s_u = 0)}\right| \tag{2.42}$$

It is important to note that, having adopted an elastic-perfectly plastic steel constitutive law, for failure modes A to F, i.e., concrete side failures with complete spalling of the cover, the calculation of the strength loss is independent of the ultimate tensile strain of the steel ε_{su}. For failure mode K, i.e. the failure mode on the steel side that occurs during the process of cover spalling, according to the adopted modelling strategy there is a loss of strength related to this partial expulsion. The value of the strength loss in this case depends also on the value of the ultimate tensile strain of the steel ε_{su}. Finally, for failure modes F to J, i.e., steel side ultimate conditions which are reached without triggering the spalling of the cover, there is no point in assessing a loss of strength, since it is zero by definition.

In Fig. 2.13 are presented graphs which illustrate the variation of non-dimensional strength loss Δ_s as a function of the cover-to-height ratio and the ratio between reinforcement amounts. The values of strength loss span in the range $0 \div 30\ \%$. The most favorable cases are obtained for low values of the cover-to-height ratio and high values of ratio between reinforcement amounts, for which bending strength loss is low and increment of ultimate curvature is high.

As opposite, the worst cases appear to be those with high values of the cover-to-height ratio and low values of ratio between reinforcement amounts. In fact, in those cases the bending strength loss is the highest and increments of ultimate curvature are quite low. By comparing the strength loss isocurves reported in Fig. 2.13 with the graphs of failure mode domains presented in Fig. 2.9, it can be seen that for failure mode D the strength loss is nearly independent of the ρ'/ρ ratio. On the other hand, failure mode E is characterized by a strength loss which decreases if the ratio between reinforcement amounts increases.

As previously mentioned, one of the requirements for which the computation of cover spalling at ultimate condition would be admissible is that the bending strength loss caused by cover spalling does not exceed a certain limit. Graphs of Fig. 2.13 are useful to check if a limit value of strength loss has been exceeded, for a section with specified characteristics. However, a more compact and useful representation can be provided.
In particular, a limit value for the bending strength loss has been selected, equal to $\Delta_{s,lim} = 0.15$, being it a typical acceptable value of loss of strength indicating that ultimate condition of a RC section has been reached. Then, in the Cartesian graph with coordinates c/H and ρ'/ρ, isocurves of points having a strength loss $\Delta_s = \Delta_{s,lim}$ has been evaluated, varying the mechanical ratio ω of bottom reinforcement and the ratio s_{lim}/c. A sufficiently wide range of values have been adopted for the mechanical ratio ω, in order to consider the majority of usual practical cases. On the other hand, three typical values of the ratio s_{lim}/c have been chosen. Examples of the obtained graphs are proposed in Fig. 2.14. The isocurves represented in graphs of Fig. 2.14 can be seen as "limit curves", for which a strength loss equal to $\Delta_s = \Delta_{s,lim}$ is reached. In this way, the curves represent the upper limit value of the c/H ratio for which the bending strength loss does not exceed the target limit value $\Delta_{s,lim}$. In other words, for c/H values higher than those provided by the isocurves, the obtained spalling-induced strength loss would be higher than the chosen target limit $\Delta_{s,lim}$. In Fig. 2.14 it can be observed that by varying the ratio s_{lim}/c, only a very slightly variation of the isocurves is obtained. On the other hand, the mechanical ratio of bottom reinforcement has a relevant role in their distribution. In particular, in cases for which failure mode D occurs, the isocurves are nearly independent on ratio ρ'/ρ and present higher values of c/H for increasing values of mechanical reinforcement ratio ω.
For sections which develop failure mode E instead, by varying the ratio ω the curves are distributed in a more complex manner, showing a slope which increases for higher values of ratio ω. The curves obtained using the *KP* constitutive law for concrete with an ultimate compressive strain $\varepsilon_{cu} = \varepsilon_{sp} = -0.004$ provide curves which stay above those obtained considering the parabola – rectangle law with $\varepsilon_{cu} = \varepsilon_{sp} = -0.0035$, since the contribution provided by core concrete to the compression chord at failure condition is directly related to its ultimate compressive strain.
Graphs reported in Fig. 2.14 can be profitably employed to check if the spalling of the concrete cover induces a strength loss which exceed the adopted limit, i.e., $\Delta_{s,lim} = 0.15$. As an example, it can be seen that considering a typical value $\omega = 0.2$ for the mechanical reinforcement ratio and ρ'/ρ values greater than 0.75, the spalling-induced strength loss is lower than the target limit for all the beam sections with c/H values up to 0.2. Thus, the concrete spalling can be considered in the analyses, once assured that arrangements have been adopted to avoid longitudinal bar buckling.

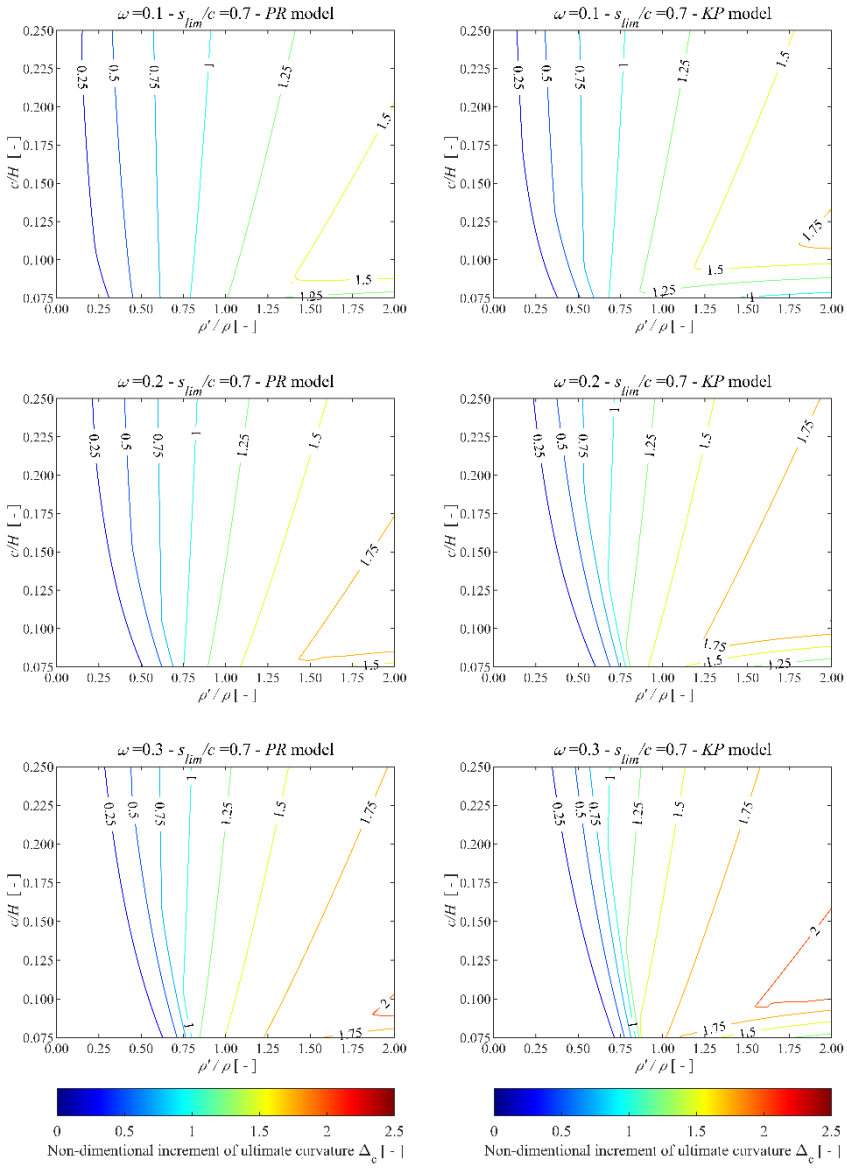

Fig. 2.12 Example of values for ultimate curvature increment ratio Δ_c, which measure ultimate curvature increment obtained considering concrete cover spalling at failure. (a) Results obtained using PR model for concrete, (b) Results obtained using KP model for concrete. Calculations have been performed considering steel strains $\varepsilon_{sy} = 2.5‰$ and $\varepsilon_{su} = 75‰$.

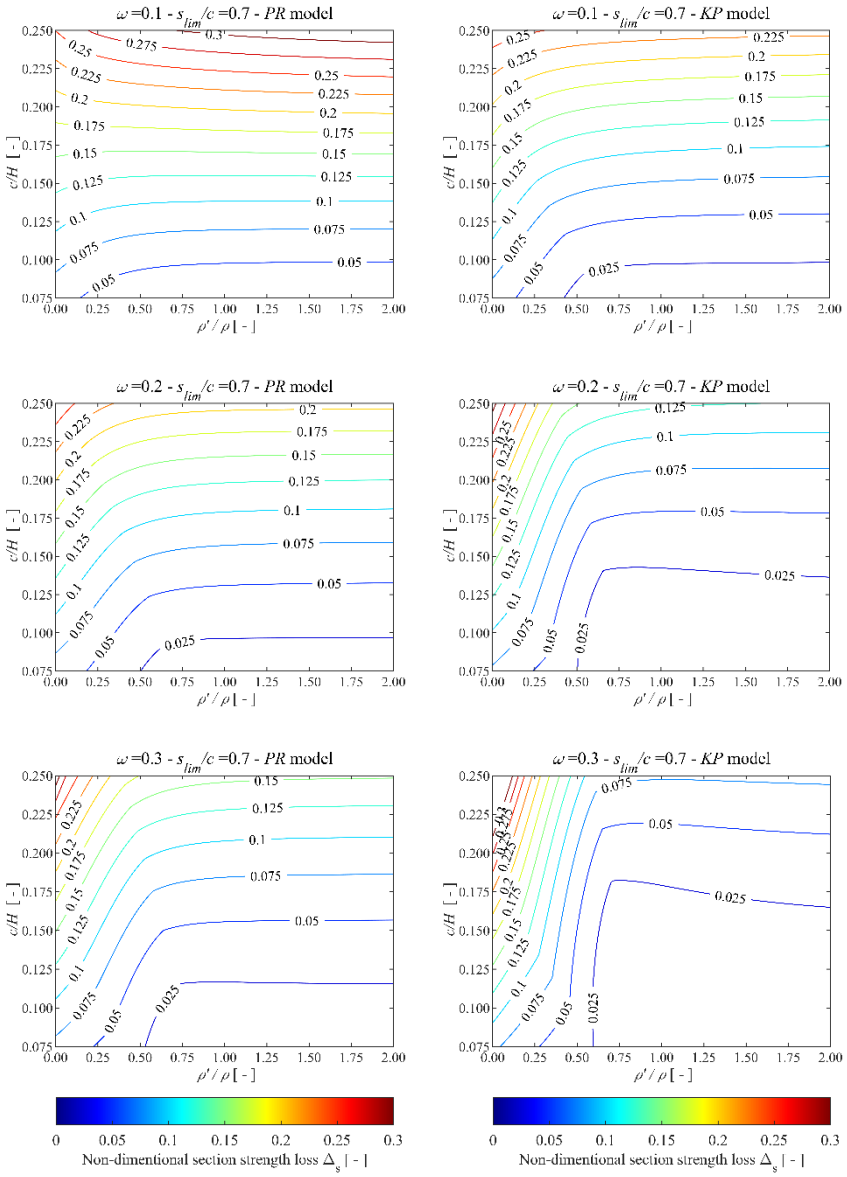

Fig. 2.13 Example of values for bending strength loss ratio Δ_s, which measure ultimate bending strength reduction due to concrete cover spalling at failure. (a) Results obtained using PR model for concrete, (b) Results obtained using KP model for concrete. Calculations have been performed considering steel strains $\varepsilon_{sy} = 2.5‰$ and $\varepsilon_{su} = 75‰$.

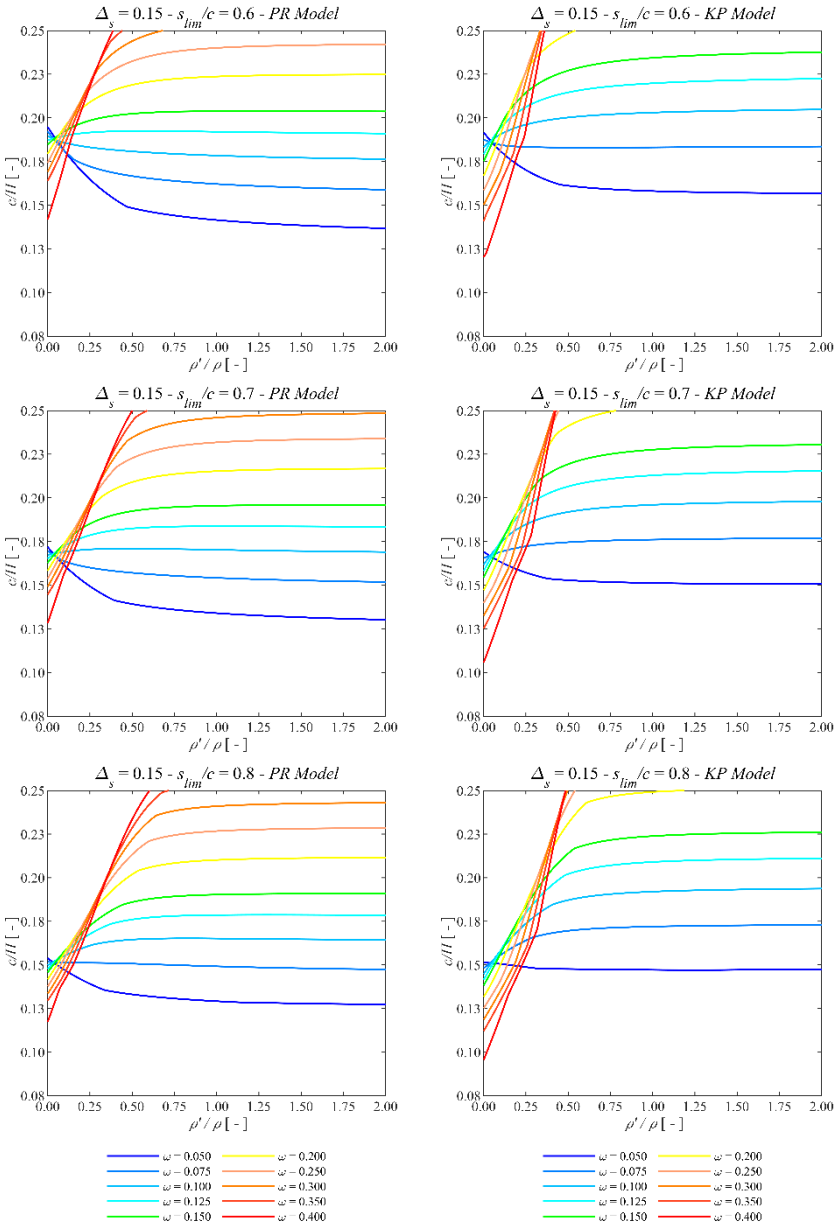

(a) *(b)*

Fig. 2.14 Isocurves of bending strength loss $\Delta_s = 0.15$ for various values of bottom reinforcement mechanical ratio ω and different values of ratio s_{lim}/c. Calculations have been performed considering steel strains $\varepsilon_{sy} =$ 2.5‰ and $\varepsilon_{su} =$ 75‰.

2.5 ANALYSIS OF CURVATURE DUCTILITY CAPACITY

Curvature ductility capacity of the section is expressed by the ratio of ultimate and yielding curvature. The ultimate curvature can be computed according to expressions (2.38) and (2.39), while the yielding curvature is calculated using relations (2.23) and (2.24). Using such expressions, in combination with those reported in Appendix B for the determination of neutral axis depth at failure, curvature ductility has been calculated for a series of cases, and its variation is illustrated in Fig. 2.15. Curvature ductility is plotted varying the ratio ρ'/ρ, for two typical values of c/H ratio and three values of mechanical ratio for bottom reinforcement ω. Results obtained using concrete constitutive laws resembling *PR* and *KP* laws are both considered.

The curvature ductility is predominantly affected by the ultimate curvature, especially for small values of bottom reinforcement ratio ρ, for which the yielding curvature varies negligibly with the ratio ρ'/ρ. For usual values of the ratio c/H and for which condition (2.36) applies, the ultimate condition generally occurs according to modes B, C, D, E or K. For the first four modes, the failure occurs on the concrete side, the ultimate curvature increases as the ratio ρ'/ρ increases, and the curvature ductility generally follows the same trend. In fact, the yielding curvature varies slightly and, for concrete-side yielding, it decreases, generating an increase in curvature ductility.

In cases the section reaches failure mode E, the ultimate curvature increases hyperbolically as ρ'/ρ increases and the ductility follows the same trend. For sections with failure mode D, on the other hand, the ultimate curvature increases with decreasing slope. Furthermore, as is well known, for concrete-side failure modes ductility increases with decreasing c/H ratio. For sections reaching the ultimate condition according to the mode K, i.e. with a steel-side failure, the ultimate curvature decreases slightly as ρ'/ρ increases, but the curvature ductility increases due to the decrease of the yielding curvature. The peak ductility value, which is associated to the peak of the ultimate curvature, is obtained for sections that develop a failure mode at the transition between a concrete-side failure and a steel-side failure (e.g. D-K, or E-K). The maximum value of curvature ductility can be evaluated from the maximum value of ultimate curvature, expressed by equation (2.40).

Taking into account the spalling of the cover at the ultimate condition, maximum ductility values ranging from 15 to 25 are observed, which are significantly higher than those obtained without allowing the concrete cover spalling. Regarding the effect of different concrete laws adopted, the use of the *KP* constitutive law provides higher ultimate curvatures, and therefore higher curvature ductility, with respect to the use of the *PR* law only in cases for which the failure occurs according to the mode D.

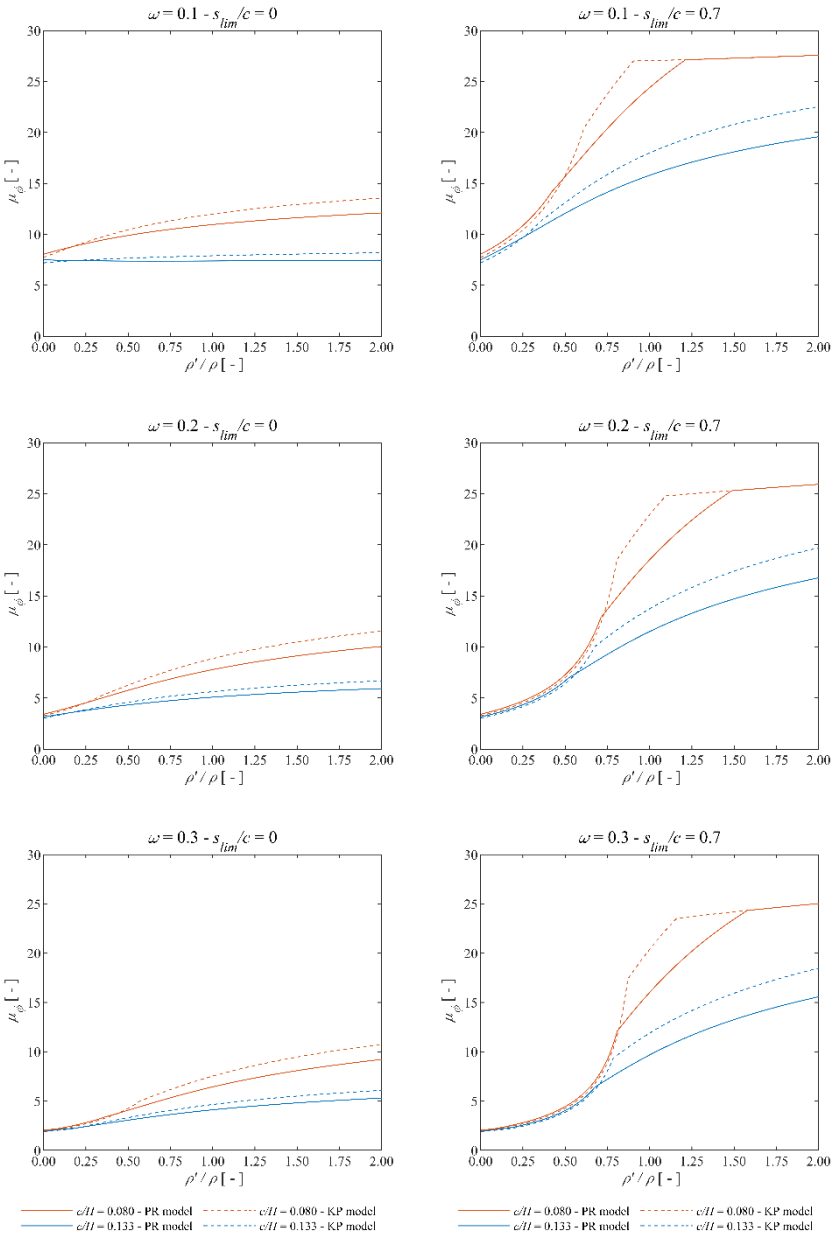

Fig. 2.15 Examples of curvature ductility capacity for different values of mechanical ratio for bottom reinforcement, obtained considering $\varepsilon_{sy} = 2.5‰$ *and* $\varepsilon_{su} = 75‰$.

2.6 SIMPLIFIED FORMULATION FOR THE EVALUATION OF ULTIMATE CURVATURE AND CURVATURE DUCTILITY CAPACITY

In the previous sections, it was shown how beam sections with usual characteristics would reach ultimate condition only through failure modes B, C, D, E, or K, in the cases for which condition (2.36) applies. Moreover, it has been noted that failure modes D, E and K are the most frequent. Keeping this in mind, it is worth recall that in the classical formulation by Park and Paulay [8] failure modes D and E were the only ones which were taken into account (cover spalling at failure was not considered).

The aforementioned considerations are helpful to derive a simplified formulation for the calculation of ultimate curvature and curvature ductility, starting from the presented comprehensive framework. Such a simplified formulation should provide conservative estimation of deformation capacity and ductility, so to be suitable for design practice, but at the same time it should allow for the possibility of considering cover spalling at failure, when its occurrence would be acceptable. With this aim, some simplifying hypothesis can be made regarding the yielding and ultimate conditions, as explained in the following.

With regard to the analysis of the yielding condition, a simplification can be introduced by assuming a priori that steel side yielding occurs, in view of the fact that concrete side yielding occurs only in a limited number of cases for beams, i.e. when there are simultaneously high values ρ and low values of ratio ρ'/ρ. Under this assumption, the yielding curvature ϕ_y is evaluated by the expression (2.23), which can be rewritten as:

$$\phi_y = C_y \cdot \frac{1}{1-\frac{c}{H}} \cdot \frac{\varepsilon_{sy}}{H} \tag{2.43}$$

where:

$$C_y = \frac{1}{1-\xi_y} \tag{2.44}$$

From expressions (2.19) e (2.44) it can be retrieved that coefficient C_y assumes values in the range:

$$1 < C_y \leq \frac{\varepsilon_{sy}-\varepsilon_{c0}}{\varepsilon_{sy}} \qquad with \qquad \varepsilon_{c0} < 0 \tag{2.45}$$

For the purposes of design practice it is usual to introduce an approximation, namely, to assume a constant value for the term C_y. With this regard some works in the literature have proposed possible values, e.g., Paulay and Priestley [9] proposes $C_y = 1.7$, while Biskinis [101] and Fardis [4] proposed $C_y = 1.54$ (specifically derived for beams). A further possibility, more cautious from the point of view of ductility capacity evaluation, is to assume for C_y its maximum theoretical value, given by the right-hand member of inequality (2.46).

It is important to remember, as already mentioned above, that the actual curvature values at which the moment-curvature curve appreciably changes its slope is often better described by a conventional value of the yielding curvature ϕ_y^*, defined by equation (2.35). However, as described above, for sections with steel-side yielding the difference

between the values of the yielding curvature obtained from relations (2.44) and (2.35) is usually small. So, with regard to curvature ductility evaluation, the effect of such difference is in many cases negligible.
With reference to the ultimate condition of the section, in order to define a simplified approach, only failure modes D, E and K are considered. To ensure that the considered failure modes are indeed always representative of the ultimate condition developed by the analyzed sections, three conditions must be guaranteed.
The first is the compliance with condition (2.36), which may be expressed in terms of a lower bound limit of the mechanical ratio of longitudinal bottom reinforcement:

$$\omega > \frac{\alpha}{2-\frac{\varepsilon_{su}}{\varepsilon_{cu}}} \qquad with \qquad \varepsilon_{cu} < 0 \tag{2.46}$$

The second one is to ensure that the c/H values of the analyzed sections would belong to the following range:

$$0.075 \leq \frac{c}{H} \leq 0.25 \tag{2.47}$$

Finally, the third condition consists in assuring a lower bound limit of the ratio ρ'/ρ applies, which is also a typical requirement for the critical zones of RC elements designed in seismic prone areas in order to foster a ductile sectional response. The adopted lower bound limit is the following:

$$\frac{\rho'}{\rho} \geq 0.5 \tag{2.48}$$

Considering conditions (2.47), (2.48) and (2.49) to be satisfied, the calculation of the ultimate curvature takes place according to failure mode E (equations (2.38) and eq. (B.6) from Appendix B) or according to failure mode D (equations (2.38) and eq. (B.5) from Appendix B), depending on whether or not transition condition U7, expressed by equation (A.34) from Appendix A, is satisfied. The possibility of developing failure mode K is taken into account by limiting the maximum attainable value of ultimate curvature, which is assumed lower or equal to the maximum ultimate curvature calculated according to relation (2.40). The curvature ductility capacity is then calculated using the corresponding expressions for the ultimate curvature, together with relation (2.44) for the yielding curvature.
For the sake of clarity, a summary of the proposed approach is given below:

- From equation (A.34) of Appendix A, the value of ratio ρ'/ρ which identifies the transition between failure modes E and D, denoted by $\left(\frac{\rho'}{\rho}\right)_{DE}$, can be retrieved:

$$\left(\frac{\rho'}{\rho}\right)_{DE} = 1 - \alpha_{III} \cdot \frac{1}{\omega} \cdot \frac{\varepsilon_{cu}}{\varepsilon_{cu}+\varepsilon_{sy}} \cdot \frac{c}{H} \cdot \left(1 - \frac{s_u}{c}\right) \tag{2.49}$$

- If, $\frac{\rho'}{\rho} \leq \left(\frac{\rho'}{\rho}\right)_{DE}$, failure mode E is considered:

$$\phi_u = -\frac{\varepsilon_{cu}}{H} \cdot \frac{\alpha_{III}}{\omega} \cdot \frac{1}{1-\frac{\rho'}{\rho}} \tag{2.50}$$

$$\mu_\phi = -\frac{\varepsilon_{cu}}{\varepsilon_{sy}} \cdot \frac{\alpha_{III}}{C_y \cdot \omega} \cdot \left(1 - \frac{c}{H}\right) \cdot \frac{1}{1-\frac{\rho'}{\rho}} \tag{2.51}$$

- If, otherwise, $\frac{\rho'}{\rho} \geq \left(\frac{\rho'}{\rho}\right)_{DE}$, failure mode D is considered:

$$\phi_u = -\frac{\varepsilon_{cu}}{H} \cdot \frac{\alpha_{III}}{\omega} \cdot \frac{2}{1+\frac{\varepsilon_{cu}}{\varepsilon_{sy}}\frac{\rho'}{\rho}+\sqrt{\left(1+\frac{\varepsilon_{cu}}{\varepsilon_{sy}}\frac{\rho'}{\rho}\right)^2-4\cdot\frac{\alpha_{III}}{\omega}\frac{\varepsilon_{cu}}{\varepsilon_{sy}}\frac{\rho'}{\rho}\frac{c}{H}\left(1-\frac{s_u}{c}\right)}} \tag{2.52}$$

$$\mu_\phi = -\frac{\varepsilon_{cu}}{\varepsilon_{sy}} \cdot \frac{\alpha_{III}}{C_y \cdot \omega} \cdot \left(1 - \frac{c}{H}\right) \cdot \frac{2}{1+\frac{\varepsilon_{cu}}{\varepsilon_{sy}}\frac{\rho'}{\rho}+\sqrt{\left(1+\frac{\varepsilon_{cu}}{\varepsilon_{sy}}\frac{\rho'}{\rho}\right)^2-4\cdot\frac{\alpha_{III}}{\omega}\frac{\varepsilon_{cu}}{\varepsilon_{sy}}\frac{\rho'}{\rho}\frac{c}{H}\left(1-\frac{s_u}{c}\right)}} \tag{2.53}$$

- In order to take into account for the possible occurrence of failure mode K, the following inequalities must be satisfied:

$$\phi_u \leq \phi_{u,max} = \frac{1}{H} \cdot \frac{\varepsilon_{su}-\varepsilon_{cu}}{1-\frac{c}{H}\left(1+\frac{s_u}{c}\right)} \tag{2.54}$$

$$\mu_\phi \leq \mu_{\phi,max} = \frac{1}{C_y} \cdot \frac{\varepsilon_{su}-\varepsilon_{cu}}{\varepsilon_{sy}} \cdot \frac{1-\frac{c}{H}}{1-\frac{c}{H}\left(1+\frac{s_u}{c}\right)} \tag{2.55}$$

The approach described above for the calculation of ultimate curvature and curvature ductility is schematically illustrated in Fig. 2.16. As discussed above, the value of spalling depth at failure s_u to be used in the previous expressions may be taken as s_{lim} if the section strength loss Δ_s associated with the cover spalling is less than a chosen limit value and if buckling of the longitudinal reinforcement is prevented, for example by ensuring compliance with equation (2.6). Unless the compliance with both of these two conditions is assured, it is necessary to assume $s_u = 0$.

The approach for calculating ultimate curvature described in this section by means of expressions (2.53), (2.51) and (2.55) is simplified in the sense that it considers only some of the possible failure modes that double reinforced concrete beam sections may develop. Although, as far as only the considered failure modes are concerned, it is worth to underline that the approach takes up the exact analytical formulation proposed in the general framework. An actual approximation is only introduced in the calculation of curvature ductility, through the assumption that yielding always occurs on the steel side and that the coefficient C_y could be assumed as constant, as an alternative to its analytical calculation performed by means of equations (2.33) o (2.34).

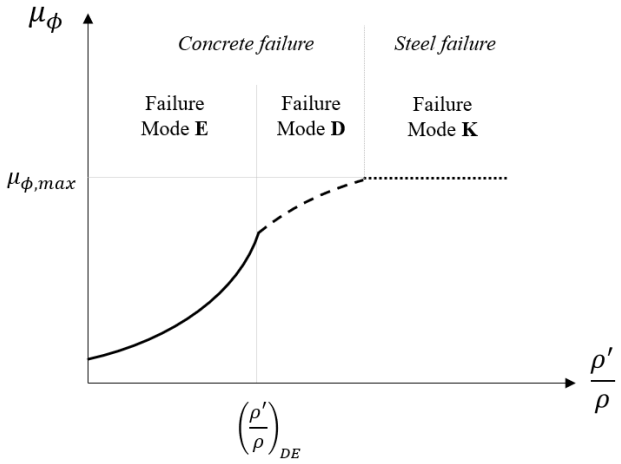

Fig. 2.16 Scheme of the proposed simplified formulation for the evaluation of ultimate curvature and curvature ductility capacity of double reinforced concrete beam sections

The proposed formulation can be effectively used in design practice, to perform local ductility design calculations or for estimating the ultimate deformation capacity of double reinforced concrete beams. Furthermore, the analytical formulations for the estimation of the ultimate curvature can be useful for the validation of numerical programs which calculate RC elements deformation capacity.

2.7 Discussion

The work presented in this chapter retraces, analyses and extends the classical analytical formulations for the calculation of the yielding curvature, ultimate curvature and curvature ductility for doubly reinforced concrete beams. The innovative contributions contained in the presented work consist in the comprehensive analysis of the yielding and failure conditions of beam sections, considering all the different possible ways in which they can occur. Moreover, in addition to the failure modes usually considered by the classical formulations, in this case failure modes that consider the spalling of the concrete cover in the compressed zone of the section are also analyzed.
The adopted approach has made it possible to derive the analytical expressions which define the boundaries between each yielding (failure) mode. By graphically representing these conditions, it was possible to obtain domains associated with each mode, which make it possible to determine immediately how the section reaches the yielding (failure) condition. This result is a relevant step in the context of pursuing objective ***O1*** presented in chapter 1. In fact, being able to identify the cases in which a certain yielding (failure) mode occurs allow also to define the range of validity of calculation approaches which assumes the occurrence of such yielding (failure) condition. Moreover, in addition to the limit conditions between different yielding (failure) modes, analytical expressions were also obtained for the calculation of curvature values associated to each of those yielding (failure) conditions.

Through a series of parametric analyses performed using the formulations which compose the proposed framework, it was possible to draw the following observations:

- The yielding condition occurs in the majority of practical situations by means of the yielding of bottom (tension) steel. However, the neutral axis depth at yielding can vary significantly, especially as a function of the mechanical reinforcement ratio ω and the ratio c/H. Simplified approaches, which assume a priori a constant value of the neutral axis depth at yielding, do not always result in safe-side estimations of curvature ductility of the section;
- The way in which the ultimate condition of the section occurs is highly variable; however, for sections with usual characteristics, concrete-side failures are predominantly encountered, with the bottom steel yielded in tension. The top steel may be either elastic or yielded in compression. By considering also possible failure modes involving concrete cover spalling at failure, it emerges that a steel-side failure mode can occur, which is reached during the spalling process of the concrete cover in the compressed zone of the section;
- The configuration of the graphical failure mode domains also varies considerably, mainly as a function of the mechanical reinforcement ratio ω and the ultimate tensile steel strain ε_{su} that characterize the reinforcing steel. However, considering the usual values of the ratio ω used in design practice and common values of ε_{su} relative to undamaged rebars not subjected to buckling phenomena, it is possible to refer to a single particular configuration of the failure mode domains, i.e., *Type 1* configuration;
- Considering the concrete cover spalling, obtained capacity values of curvature capacity and ductility are even double those obtainable without considering the spalling, against a loss of strength of the section which is in many cases less than 15%. In reality, the amount of strength loss induced by cover spalling may in many situations be even much lower, if reinforcing steel is characterized by a sufficient hardening. The occurrence of a steel-side failure during the cover spalling process approximately defines the maximum value of the ultimate curvature that the section is able to develop.

On the basis of the above observations, a simplified and compact approach has been derived from the general analytical framework, for the evaluation of the ultimate curvature and curvature ductility of doubly reinforced concrete beam sections. This approach considers only the main yielding and failure modes occurring for sections with usual characteristics. Specific validity limits are defined for the proposed approach, though that it can be used for beams characterized by section layout and material properties usually adopted in the engineering practice. As a matter of fact, the proposed approach can be usefully employed in design calculations, to check the ductility capacity of doubly reinforced concrete beam sections.

3

Experimental tests on sound and corroded reinforced concrete beams

A friend of mine once said that there is no difference between theory and practice. There is one difference. Practice won't let you forget anything or leave anything out. In theory, problems are easily solved because you can leave something out.
Charles F. Kettering

In the last three decades, a large number of experimental campaigns has been conducted to investigate the behaviour of reinforced concrete beams affected by reinforcement corrosion. In many of them, however, several different consequences of rebar corrosion on the members response were addressed simultaneously, not always allowing for the independent analysis of single effects separately. Moreover, in most of the tests emphasis was usually put on the evaluation of strength capacity and failure mode, granting less attention to information useful for a detailed analysis of deformation capacity. In this chapter, results from a two-steps experimental campaign on corroded beams performed at Tor Vergata University in Rome are reported, which allows to analyze the structural response of corroded beams specifically focusing on the effects of high corrosion levels developed in the tensile longitudinal reinforcement. Moreover, in the tests performed in the second step of the campaign, particular attention was put in measuring information useful for a detailed analysis of sectional and member deformation capacity.

Research presented in this chapter is part of a broader work program driven by a joint collaboration of researchers from Tor Vergata University of Rome and IUAV University of Venice, focused on testing and modelling the structural performances of corroded reinforced concrete elements.

3.1 INTRODUCTION

Experimental testing has a fundamental role in the study of reinforced concrete structures, providing data for the understanding of their mechanical behaviour and getting information useful to calibrate and validate models for predictive simulations. The need for experimental data on structural behaviour is even more pronounced in the study of deteriorated structures, in which additional phenomena take place affecting the mechanical behaviour.

With this regard, in this chapter a set of experimental tests on corroded RC beams is reported, which focuses on the analysis of flexural behaviour in members affected by corrosion in the tensile longitudinal reinforcement. Results of the tests allow for the analysis of structural effects of corrosion and will also serve to provide data to evaluate the performances of modelling approaches proposed in Chapter 4.

The presented experimental research is part of a broader research program, driven by a joint collaboration between research groups of Tor Vergata University of Rome and IUAV University of Venice, focused on testing and modelling structural behaviour of corroded reinforced concrete elements. Collaboration involves the joint use of facilities provided by the two institutions as well as the collaboration of researchers in the planned activities of testing and modelling.

The presented research involved experimental tests on a set of doubly reinforced concrete beams which were tested at the "Laboratory for structural and material testing" at Tor Vergata University of Rome. In a first stage of the research, tests on a first series of specimens have been performed, to analyze the global response of corroded beams and to check the use of an innovative set of sensors for monitoring the structural behaviour. In this first stage, experimental research was carried out by the research group from Tor Vergata University of Rome and results of the test have been presented in the works by Di Carlo et al. [69], [70]. Subsequently, the testing setup has been updated and the adopted sensors and monitoring techniques have been specifically designed to allow for a detailed analysis of the crack pattern and for the measurement of parameters useful for deformation capacity assessment. The updating and redesigning phase particularly benefitted of a close interaction between the research groups from Tor Vergata University of Rome and IUAV University of Venice. A second series of tests have been then performed considering the updated setup, providing additional results and allowing for a better understanding of the comprehensive behaviour of the tested specimens. Results from the two series of tests can anyway be analyzed as a whole, in order to provide a larger set of data upon which getting information about the corrosion effects on the behaviour of concrete beams.

In this chapter, a brief overview of related experimental research done in the past is firstly provided, followed by a description of the experimental campaign reporting the setups and monitoring methodologies adopted in the two series of tests. At the end of the chapter, results for all the tested specimens are briefly analyzed, to understand the effects of increasing corrosion levels on the structural performances of corroded beams.

3.2 Review of related experimental research

Since the attention has been raised regarding the relevance of reinforcement corrosion effects on the structural performance of concrete structures, numerous investigations have been performed involving experimental tests to evaluate the response of corroded RC members. In particular, a significant number of experimental campaigns were conducted for studying the flexural response of corroded RC beams. In several of those tests, specimens were characterized by the presence of corrosion in all the reinforcement, aiming to represent a condition close to the one of real deteriorated structures. In other cases, damage was introduced only in specific beams components, in order to investigate the specific associated consequences on the structural behaviour.

A case of particular interest with regards to the flexural behaviour of corroded beams is the one in which corrosion is present only in the longitudinal bars on the tensile side of the beam, with the concrete cover in the compressed side not affected by splitting cracks and with the longitudinal reinforcement on the compressed side, as well as the stirrups, in sound conditions. Such a corrosion scenario represents a very convenient case for studying the impact of tensile tie deterioration on the beams response, without experiencing other influences due to deterioration of other member components. In order to obtain this corrosion condition, proper arrangements and particular care need to be taken when designing the specimens and the adopted artificial corrosion procedure. Some research works done in the past carefully designed experimental tests to actually obtain the aforementioned kind of damaged condition, with the aim to specifically study the influence of tensile longitudinal rebars corrosion on the flexural performance of RC beams. In order to have an insight about the main expected consequences, it is worth to recall some of the key obtained results.

In the work of Almusallam et al. [102] a series of one-way simply supported and uniformly loaded RC slabs were tested, after being subjected to an artificial accelerated corrosion obtained by means of a galvanic corrosion process. The specimens were casted without any stirrups or any longitudinal reinforcement on the compression side, so the only actual corrosion effects were located in the longitudinal reinforcement placed on the tensile side of the slabs. The support and loading configurations, as well as the employed amount of reinforcement, make the obtained results applicable also for the case of RC beams. During the corrosion process, the slabs remained in a tank with a 5% sodium chloride water solution while a constant current of 2A was applied between the reinforcing steel serving as anode and an external stainless-steel plate serving as cathode. Considering the actual amount of corroding reinforcement, such a current intensity may have induced a current density of about 19000μA/cm^2. Average mass loss ratio Δ_m of steel was measured after the tests, computing an average value for each specimen and obtaining results in the range spanning from $\Delta_m = 1.00\%$ to $\Delta_m = 75.00\%$. For all the corroded specimens, failure was identified with the occurrence of a relevant drop of strength associated to a loss of bond between the reinforcement and the surrounding concrete. Significant reductions of yielding strength, ultimate strength and deformation capacity were recorded for the corroded slabs, especially for the cases with higher average loss of mass.

An extensive experimental research program reported by Mangat and Elgarf [103] investigated the flexural behavior of corroded beams, the majority of which were casted without any stirrups and without any longitudinal reinforcement on the compression side. A four-points-bending loading scheme was adopted and proper arrangements were adopted to prevent the occurrence of shear failure, by applying tubular steel collars around the beams at the shear spans. The beams were corroded using a galvanic corrosion process during which they were placed in a plastic tank with a 3.5% sodium chloride water solution. The water level was adjusted to exceed a bit the level of the longitudinal bottom reinforcement. A current with density varying between 1000μA/cm^2 to 4000μA/cm^2 has been impressed between the reinforcing steel acting as anode and an external steel bar used as cathode, aiming to obtain average percentage reductions of bar diameter spanning from $\Delta_{\phi_0} = 1.25\%$ % to $\Delta_{\phi_0} = 10.00\%$. These values would correspond to average relative mass loss values spanning from $\Delta_m = 2.48\%$ to $\Delta_m = 19.00\%$, but actually obtained average mass losses were not measured after the tests. The uncorroded specimens failed for crushing of concrete in the compressed part of sections belonging to the central span of the beams. For the corroded beams, instead, failure condition was considered to have been reached when consequences of bond loss along the bars was observed, such as extensive spalling of the concrete cover at the tensile side of the beams. A nonlinear decreasing trend for peak strength was observed at increasing corrosion levels, with more pronounced reductions for beams with the higher values of theoretical average diameter loss. A strong reduction in the values of ultimate displacement reached by the beams was also recorded.

For all the specimens analyzed in the two aforementioned studies, corrosion in the longitudinal reinforcement has impaired the bond strength, ultimately leading to a drop of member strength which has been associated with the failure of the specimens. According to Almusallam et al. [102], the loss of bond is a result of the combination of a progressive degradation of the bars ribs and of the formation on the bars of corrosion products which can act as a lubricant between the steel and the surrounding concrete. For high corrosion levels, a complete delamination and spalling of concrete cover can even occur, after the formation of the longitudinal splitting cracks induced by the expansion of corrosion products. In such a situation, the bond between the reinforcement and the remaining surrounding concrete is almost completely lost and rebars can be treated as they would be fully exposed. To analyze this kind of situations, the approach presented by Cairns [104] can be adopted, which proposed an interpretation of the behaviour of beams with fully exposed reinforcement and presented a numerical analysis procedure used to predict the structural response of a series of tested specimens. In his work, it has been shown that the full loss of bond may indeed change the beam resisting mechanism and the associated failure mode, with a consequent possible change in the ultimate strength and deformation capacity. However, it is worth to emphasize that the change of resisting mechanism type from a beam-type to an arch-type not always results in a reduction of strength and/or deformation capacity of the members. In fact, for beams loaded in four-points bending in which the resisting mechanism moves to an arch-type one, the compressive strains in concrete increase in the sections of higher bending moment values, while in the zones close to the supports

an increase in neutral axis depth can occur, eventually leading to a reversal of the normal strain pattern. So, the failure mode and the peak strength of the specimen closely depends on the concrete compressive strength and ultimate strain, on the yielding strength of the reinforcing steel and on the residual cross-sectional area of rebars.
Another series of tests on corroded beams loaded in four-points bending have been reported in the work by El Maaddawy et al. [105], which presents the results of an experimental campaign conducted on specimens having the longitudinal tensile reinforcement corroded only in the central portion between the loading points. The tested beams were provided with longitudinal reinforcement also on the compression side and with stirrups. However, special care was taken to ensure that corrosion would develop only in the central portion of the longitudinal reinforcement placed on the tensile side of the beams. In particular, the stirrups were protected by painting them with an anti-corrosion epoxy resin and by wrapping stirrups corners with plastic tubes, so they would not be in direct contact with the longitudinal rebars. To avoid corrosion of the longitudinal reinforcement placed on the compressed side of the beams, two different concrete mixtures were used to cast the beams. The central span of the beam, for a height of 100mm measured from the bottom edge, has been casted adding to the mixture a percentage of sodium chloride equal to 2.25% of the cement weight. The remaining parts of the beams were casted using normal unsalted concrete. This way, the difference in concrete conductivity allowed for the development of corrosion only in the central part of the longitudinal reinforcement placed at the tensile side of the beams. The galvanic corrosion process was adopted, applying a constant current of 0.215A between the anode (made by the tensile longitudinal reinforcement) and the cathode (made by a very thin stainless-steel tube placed inside the beams at a certain distance from the tensile surface). Considering the actual amount of corroding reinforcement, a density current of about 450μA/cm^2 may have been obtained. During the corrosion process, the specimens were stored under a polyethylene encase and a moisture fog was continuously provided by means of sprayers. The gravimetric method was used to assess the corrosion level after the tests in terms of average mass loss ratio, obtaining values spanning between $\Delta_m = 8.9\%$ to $\Delta_m = 31.6\%$. Half of the beams were corroded without any load applied during the corrosion process. The remaining specimens were subjected to a service load during the corrosion process, whose value was equal to 60% of the estimated yielding load of the uncorroded specimens. For specimens with average relative mass loss lower or approximately equal to 15.00%, which could be herein regarded as low-to-mid corroded specimens, some differences have been noted in the evolution of the corrosion process for preloaded and non-preloaded specimens, which then affected their structural response. In particular, considering the same duration of the corrosion process, pre-loaded beams developed larger flexural cracks during the corrosion process, which facilitate the ingress of moisture and accelerated the corrosion in longitudinal rebars. These specimens experienced slightly higher average mass losses and presented lower values of yielding and ultimate strength than the corresponding non-preloaded beams. The results for these specimens confirm the observations provided by Ballim et al. [106] regarding the importance of providing a service load during the corrosion process in order to represent situations similar to those of real structures. On the other

hand, for specimens with average relative mass loss higher that 15.00%, herein regarded as highly corroded specimens, no correlation between strength reductions and presence of flexural cracks during the corrosion process was observed. This fact could suggest that for high corrosion levels, the ingress of moisture or chloride ions which sustain and enhance the corrosion process on the bars happens mainly through the large splitting cracks which open along the longitudinal rebars, making negligible the contribution of flexural cracks occurred due to the presence of the service load. Another significant difference between mid-corroded and highly corroded specimens regards their failure mode. Reported results seem to indicate that the uncorroded specimen and the mid-corroded ones failed by concrete crushing in the compressed part of the sections at midspan. Three out of four mid-corroded specimens shown displacement capacity larger than that obtained for the uncorroded case. The authors suggest that this fact may be due to the reduction of the cross-sectional area of the corroded tensile longitudinal reinforcement, which would have enhanced the ultimate curvature of sections in the central span of the beams [8]. For highly corroded beams, however, corroded rebars were characterized by the presence of pits, which led to the rupture of some of the steel rebars. In most of the cases, this latter kind of failure was associated with a strong reduction in both strength and deformation capacity of the corroded specimens. This behaviour was not observed in the other two previous mentioned works by Almusallam et al. [102] and Mangat and Elgarf [103] in which the failure was governed by the loss of bond, but it seems to have a much more critical impact on the deterioration of ductility performances of corroded beams.

In all the three aforementioned experimental campaigns the emphasis were put in obtaining information mainly about the evolution of corrosion-induced damage and the global behavior and failure modes of the corroded beams, while considerations about strength and deformation capacity were obtained simply by the analysis of force-displacement curves. A deeper understanding of the behaviour of corroded members during experimental tests can be obtained by monitoring also other useful parameters. A comprehensive review of traditional and emerging techniques for monitoring the response of RC structures during testing has been provided by Zarate Garnica et al. [107]. In particular, techniques which allow to monitor rotations, curvatures or strains are indeed very useful, since these parameters can be used for analyzing the deformation capacity of the members and relating it with deformation capacity of their sections and with material properties.

Some past experimental works performed on corroded beams with corrosion on all the reinforcement addressed more in detail the assessment of deformation capacity. In particular, the experimental works reported by Du et al. [108] and Ou et al. [50] adopted methodologies and sensor layouts which allowed to monitor shear deformations and average curvatures over selected beam portions, using properly designed grids of linear variable displacement transducers (LVDTs). In the work of Berrocal et al. [109] an estimation of plastic rotation capacity in corroded beams was provided, based on analytical calculations which made use of some experimentally measured parameters.

Practical difficulties in monitoring deformations may also arise in certain situations. The work of Ou et al. [50] reported that LVDT measures can become unreliable for

significant beam deformations, when extensive and widespread concrete cracking occurred in the zone of the surface upon which the LVDTs are installed. Another practical limitation regards the unemployability of strain gauges attached to reinforcing bars which would later experience corrosion, as reported by Fernandez et al. [110]. In fact, the corrosion process also affects the sensors, making them unable to provide reliable measures or even unable to provide any measure.

In the recent years, non-contact techniques have become popular for monitoring the response of structures during testing. Among these techniques, digital image correlation (DIC) is nowadays a widely adopted methodology to measure displacement and strain fields and to monitor processes involving large deformation and fracturing in structural components [111], [112], [113], [114]. This technique makes use of a series of pictures taken during the experimental test over a portion of the structure which includes the region of interest (ROI) that needs to be monitored. Suitable algorithms are then used to track the motion of the points contained in the ROI between one image and another, in order to provide an estimation of the displacement and strain fields. The earliest and most commonly used algorithms are those which perform *local* DIC [111], [115], considering a discretization of the ROI in groups of pixels called "subsets" (or "facets"). Another class of algorithms relates to *global* DIC methods, which have been developed later and require the definition of a set of nodes, similarly to a finite element discretization, to compute the displacement field [116], [115]. In the majority of cases, the application of a suitable speckle pattern on the monitored surface is needed, in order to allow for a satisfactory result of the correlation process. In general, the accuracy of the obtained measures depends on the pattern quality, on the camera resolution and on the adopted lens [107]. Developments achieved in the past years led to several improvements in the adopted algorithms [117] and allowed to better quantify the accuracy of the obtained results [118], [119], [120], [121], demonstrating that DIC can be effectively employed for analyzing displacement and strain fields in structural elements. These achievements, combined with the increased affordability of necessary equipment and availability of commercial DIC packages [118], made the use of DIC to become widespread in the structural testing of reinforced concrete elements, in particular for the analysis of the crack pattern and the detection of crack widths [122], [123], [124], [125], [126].

Only recently, some applications have been reported of the use of DIC for analyzing the structural response of corroded reinforced concrete elements. In the works of Nasser et al. [127] and Berrocal et al. [128] DIC has been adopted to track the evolution crack pattern in corroded beams and to get insights about the occurring failure mechanisms. Moreover, a detailed estimation for the width of corrosion-induced splitting cracks have been obtained by Berrocal et al. [128], using DIC results to create virtual gauges for getting the crack width at several locations on the beam surface. The same authors also emphasize that some difficulties may arise in using DIC to monitor the crack pattern evolution while the corrosion process is still taking place. In particular, the setup needs to be designed so that the surface to be monitored could be exposed to the camera and accessible all the time. In addition, since in the analyzed case the speckle pattern was drawn before the corrosion to start, it was noticed that stains due to the flow of corrosion

product out of the cracks may compromise the quality of the surface pattern and make some areas of the ROI not adequate to get results [128].
The brief overview of the aforementioned experimental research works allows to get some insights about some fundamental aspects of the behaviour of corroded members, especially regarding the consequences of corrosion of the longitudinal tensile reinforcement. In addition, a glance about the evolution of testing procedures and relevant monitored data considered in the experimental tests on corroded reinforced concrete elements has been provided, with a focus on non-contact techniques and in particular on DIC. This kind of approaches opened the opportunity for a more comprehensive monitoring the structural response, with a reduced effort and limiting costs. However, despite the efforts undertaken in the past research works, several aspects in the behaviour of corroded concrete structures are still to be studied and fully understood. Particularly, in order to obtain knowledge which would allow for the development of more accurate structural assessment approaches, fundamental mechanisms and consequences of corrosion effects on every single structural component need to be understood and quantified. With this aim, it could be foreseen a further need in the near future for experimental research on corroded concrete elements, but increasingly focalized on the study of specific aspects of the corrosion effects on the structural response.

3.3 Description of the experimental tests

3.3.1 Geometry and material properties

The experimental research reported in this chapter aims to provide a contribution in the understanding of corrosion effects on the structural behavior of reinforced concrete members. In particular, consequences of corrosion affecting only the longitudinal tensile reinforcement are specifically addressed, aiming at provide additional contributions to the knowledge about the effects of this corrosion scenario, which were already investigated in past experimental research works, for example by Almusallam et al. [102], Mangat and Elgarf [103] and El-Maaddawy et al. [105]. The experimental research presented herein involved eight specimens, all of them casted with the same geometry, reinforcement layout, steel type and concrete mixture. Only the corrosion amount in the longitudinal tensile reinforcement is varied, allowing for specifically studying the consequences of increasing corrosion level on the structural response. The beams were designed so that in an uncorroded condition they would be characterized by a ductile failure due to concrete crushing, with a very large deformation capacity.
The beams have a total length $L_{tot} = 3.7m$ and a cross section characterized by width $b = 20cm$ and height $h = 30cm$. Bottom and top longitudinal reinforcement are both made by two rebars of $20mm$ diameter, so total cross-section areas of reinforcements are $A_s = A'_s = 6.28cm^2$. These values lead to equal values for reinforcement ratios $\rho = A_s/(d \cdot h)$ and $\rho' = A'_s/(d \cdot h)$, which are $\rho = \rho' = 1.05\%$. So, the ratio ρ'/ρ between cross-sectional areas of top and bottom longitudinal rebars is equal to 1. Longitudinal rebars are bent at $90°$ at both beam ends, to improve the anchorage effectiveness.

Transverse reinforcement consists of $8mm$ diameter stirrups with two vertical and horizontal legs. Stirrups spacing is $20cm$ in the central portion of the beam, while it is $10cm$ in the shear spans. A net cover of $2cm$ was adopted, measured between the stirrup boundary and the section edges. The conventional value of concrete cover c usually employed in sectional analysis refers to the distance between the longitudinal rebars' axis and the edge of the section and in this case is then equal to $c = 3.8cm$. Geometry of the specimens are illustrated in Fig. 3.1.

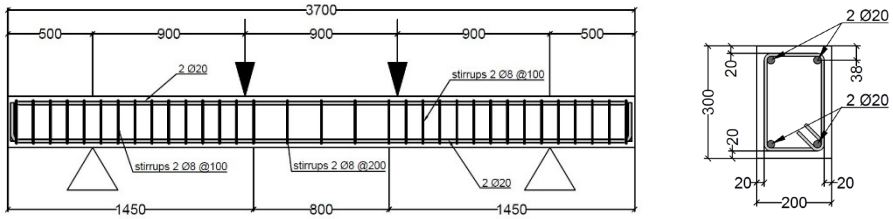

Fig. 3.1 Geometric characteristics of the beams (measures in [mm]): (a) Reinforcement location and spacing; (b) Section characteristics (Adapted from Di Carlo et al. [69])

The beams were tested with a four-points-bending scheme, with a total clear length between supports equal to $L = 270cm$ and the two loads applied at the thirds of the clear length, obtaining shear spans and constant moment zone having the same length, equal to $a = 90cm$. The obtained ratio between the shear span length and the effective section height is $a/d = 3.44$. An illustration of the loading scheme is also provided in Fig. 3.1.
Longitudinal and transverse reinforcements were made of hot rolled Tempcore® ribbed steel rebars with a characteristic yielding strength at least equal to $f_{yk} = 450MPa$ and having values of the other mechanical properties greater or equal to the minimum standards reported for steel rebars of class "C" defined in the Annex C of Eurocode 2 – Part 1-1 [129]. Tensile tests have been performed on three samples of rebar portions in sound conditions. Obtained yielding and peak loads N_y and N_t, as well as yielding and peak tensile strengths f_y and f_t, are reported in Table 3.1. Stress values for f_y and f_t have been calculated from the corresponding loads using the nominal diameter of the rebars, which was equal to $\phi_0 = 20mm$ for all the tested bars.

Table 3.1 Mechanical characteristics of reinforcing steel obtained from tensile testing of rebars

Sample	ϕ_o **[mm]**	N_y **[kN]**	N_t **[kN]**	f_y **[MPa]**	f_t **[MPa]**
Sample S1	20	160.8	200.7	512	639
Sample S2	20	158.0	196.0	503	624
Sample S3	20	158.7	196.7	505	626
Average	-	159.2	197.8	507	630
Std. Dev.	-	1.2	2.1	3.9	6.6

The mixture for the employed concrete was designed by a local industrial manufacturer, requiring performances greater or equal to those associated to the strength class C35/45 defined in the standard EN 206-1 [130]. Compression tests have been performed on four cubic samples with edge size of 100mm, according to instructions defined by the standard EN ISO 1920-3 [131] and EN ISO 1920-4 [132]. Values of cubic compressive strength $f_{c,cube,100}$ obtained for the 100mm-sized cubes are reported in Table 3.2.

Table 3.2 Mechanical characteristics of concrete derived from compression tests on cubic samples

Sample	Age [d]	$f_{c,cube,100}$ [MPa]	$f_{c,100}$ * [MPa]	$f_{c,cube,150}$ ** [MPa]	$f_{c,150}$ *** [MPa]
C1	158	57.4	49.0	55.2	46.9
C2	272	54.1	45.9	52.0	43.9
C3	357	52.1	44.0	50.1	42.2
C4	619	60.7	52.0	58.3	49.8
Average	-	56.1	47.7	53.9	45.7
Std. Dev.	-	3.3	3.1	3.1	2.9

*Calculated using eq. (2.3); **Calculated using eq. (3.2); ***Calculated using eqs. (3.2) and (2.3);

In many applications, though, the cylindrical compressive strength is required. The relation between the cubic and the cylindrical compressive strength depends on many factors, as the aspect ratio of the cylinder, the concrete strength, the aggregate grading and the moisture conditions at the time of casting. To get an estimation of the cylindrical compressive strength f_c the formulation proposed by L'Hermite [133] can be adopted as reported in eq. (3.1) and plotted in Fig. 3.2a, which is valid for cylinders with a height-to-diameter ratio equal to 2.

$$f_c = f_{c,cube} \cdot \left[0.76 + 0.2 \cdot \log_{10}\left(\frac{29}{568} \cdot f_{c,cube}\right)\right] \qquad \text{with } f_{c,cube} \text{ expressed in [MPa]} \qquad (3.1)$$

In some cases the values of concrete compression strengths evaluated on cubes or cylinders of other sizes are required. In order to calculate cubic compressive strength $f_{c,cube,dc}$ associated to a generic cube size d_c, the formulation reported by Neville [134], [135] plotted in Fig. 3.2b can be used. A mathematical expression for this formulation, derived from the graph of Fig. 3.2b, is expressed by eq. (3.2).

$$f_{c,cube,d_c} = f_{c,cube,150} \cdot [1.12 - 0.0008 \cdot d_c] \qquad \text{with } d_c \text{ expressed in [mm]} \qquad (3.2)$$

In Table 3.2, all calculated values of the cubic and cylindrical compressive strength for the tested samples are also reported.

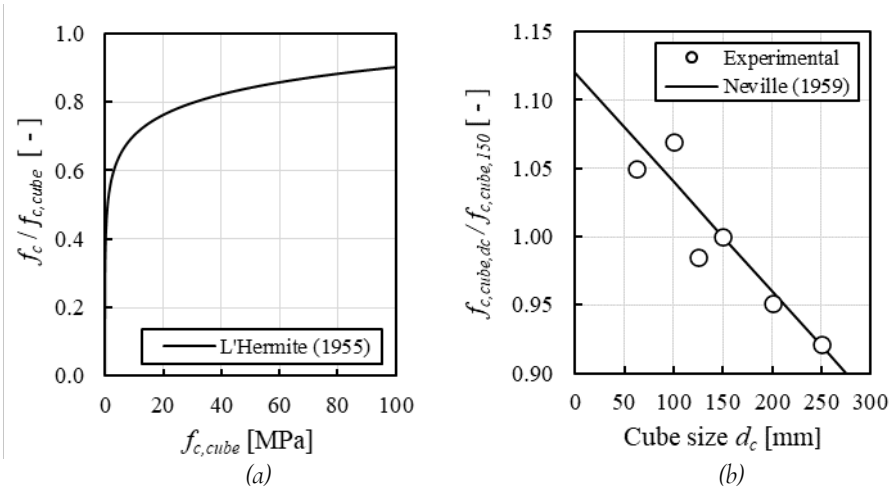

Fig. 3.2 (a) Relation between cylindrical and cubic compressive strength according to L'Hermite [133]*; (b) Compressive strength of cubes of different size (adapted from Neville* [135]*)*

3.3.2 Corrosion process

The reported experimental campaign was aimed at studying the effect of different corrosion levels on the structural response of RC beams. Among the eight considered specimens, two were left in uncorroded conditions, to be used as references. The other six specimens were subjected to an artificially accelerated corrosion process, designed with the aim of inducing corrosion only in the tensile longitudinal reinforcement. The corrosion was obtained by means of a galvanic corrosion process, made by passing a direct current between the bottom longitudinal rebars of the beams, acting as anode, and an external steel bar or plate, acting as a cathode. Despite the impressed current was directly passed only to the longitudinal tensile reinforcement, special care have been taken to avoid corrosion in the other rebars. In particular, the stirrups and the longitudinal reinforcement on the compressive side of the beams were protected with an epoxy paint layer, as shown in Fig. 3.3.

Fig. 3.3 Details of reinforcement used in the tested beams, highlighting the stirrups and compressive longitudinal rebars which were epoxy painted (From Di Carlo et al. [69]*)*

The external steel bar and the corroding beams were placed in a pool containing a 3% sodium chloride saline solution. The water level in the pool was made to reach half the height of the beams. Before the start of the corrosion process, the beams were left for at least 2 days in the saline solution, allowing chloride ions to penetrate inside the concrete cover and to reach the bottom longitudinal reinforcement in order to facilitate the corrosion process. An illustration of the setup used for the corrosion process is provided in Fig. 3.4.

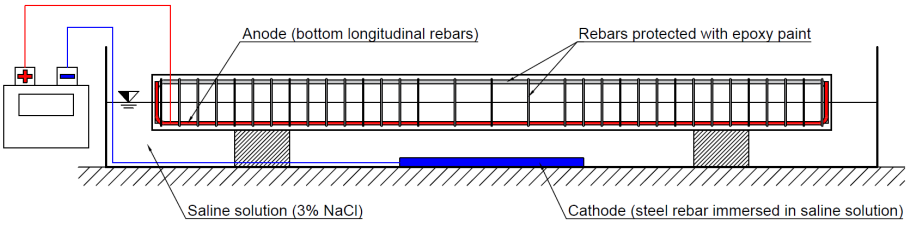

(a)

(b)

(c)

Fig. 3.4 Setup for artificially accelerated corrosion process (a) Scheme of the setup; (b) Power supply units; (c) Pool used for the accelerated corrosion process (Adapted from Di Carlo et al. [69], [70])

To quantify the corrosion level, one of the most commonly used parameters is the average mass loss ratio Δ_m, defined by the ratio between mass loss m_{loss} , i.e., the mass of the amount of steel which dissolve and forms rust, and the original steel mass m_0, as expressed by eq. (3.3):

$$\Delta_m = \frac{m_{loss}}{m_0} \tag{3.3}$$

In order to get an estimation of the mass loss generated during a galvanic corrosion process, the Faraday's law is usually employed [136], as reported in eq. (3.4):

$$m_{loss}\,[g] = \frac{I_{corr}[A] \cdot t_{corr}[sec] \cdot m_{mol}[\frac{g}{mol}]}{Val[\ ] \cdot C_F[\frac{C}{mol}]} \tag{3.4}$$

where the term I_{corr} is the current intensity, t_{corr} is the duration of the corrosion process, m_{mol} is the molar mass of the corroding metal ($m_{mol} = 55.845\,\frac{g}{mol}$ for iron), Val is the metal valence ($Val = 2$ for iron in the anodic reaction) and C_F is the Faraday's constant ($C_F = 96485.3365\,\frac{C}{mol}$).

The effectiveness of Faraday's law in predicting corrosion-induced mass loss of bare steel elements have been thoroughly verified. On the other hand, a satisfactory accuracy in its use for predicting corrosion levels in steel bars embedded in concrete may not always be guaranteed and some past research studies aimed to investigate this aspect. In the work of El-Maaddawy and Soudki [136] corrosion has been induced in rebar specimens embedded in concrete, considering different current intensities in the range 100 μA/cm^2 ÷ 500 μA/cm^2 and aiming to obtain percentage corrosion mass loss values in the range 4% ÷ 8%. The corrosion mass loss values predicted using the Faraday's law were in excellent agreement with the actual mass losses measured with the gravimetric method (i.e., weighting the corroded rebars extracted from the concrete specimens after the corrosion process), with an average difference of 4% between predicted and measured values. On the other hand, Malumbela et al. [137] analyzed data from a series of experimental tests conducted by various authors and found out that there seems to be a tendency for Faraday's law to overestimate the actual corrosion-induced mass loss, which is emphasized as the expected loss value increases. Nowadays, it is understood that actual mass loss for corroding steel embedded in concrete does not always follow Faraday's law. This result is attributed, in some unfavorable situations, to the fact that only a part of the impressed current oxidizes the anode creating rust, while the remaining part is consumed in competing reactions [138]. Another possible explanation can be regarded to the fact that the concrete cover delays the beginning of the corrosion process [139], so the difference between the predicted and measured mass loss may be dependent on concrete mixture and cover width.

In designing the artificial corrosion process, it is important to adopt an adequate current intensity for a sufficiently long period, in order to obtain the desired corrosion levels in the RC specimens to be studied. Accordingly, in case the Faraday's law is used to determine the required duration t_{corr} of the corrosion process, an empirical constant scaling factor λ_F can be introduced [140], as presented by eq. (3.5):

$$t_{corr}[sec] = \frac{\lambda_F \cdot Val[\ ] \cdot C_F[\frac{C}{mol}] \cdot m_{loss}\ [g]}{I_{corr}[A] \cdot m_{mol}[\frac{g}{mol}]} \tag{3.5}$$

The value to be used for the constant λ_F should be calibrated based on trial tests. However, values in the range $\lambda_F = 1.5 \div 2$ have been reported to provide satisfactory estimations of the mass loss [140], [141], [142]. Accordingly, for the presented experimental campaign the durations of the corrosion processes have been determined using eq. (3.4), with λ_F values taken among the aforementioned range.

3.3.3 First series of tests with original setup

The first part of the campaign involved experiments on six RC beams, two uncorroded and four corroded, whose results have been reported by Di Carlo et al. [69], [70]. In this stage of the campaign, particular attention was devoted to the calibration of the corrosion process and to the assessment of the effectiveness of the adopted sensor layout for monitoring the structural response. Two target values of average relative mass loss Δ_m were selected to be reached for the corroded beams, namely, $\Delta_m = 10\%$ and $\Delta_m = 20\%$, as indicated in Table 3.3. In the same table, actually obtained average corrosion levels are also reported.

The setup used for the first series of experimental tests is illustrated in Fig. 3.5. The beam was supported by two rolling cylinders with a fixed encase, which in turn were located above a wooden plank. The loads were applied by means of a system composed by two steel beams located on the specimen extrados and two high strength rebars, each one connected to a hydraulic jack and anchored on the concrete floor. Each jack had a maximum capacity of 325kN and was equipped with a load cell to measure the applied load. Potentiometers have been installed to measure the vertical displacement at supports, at loading points and at the midspan of the beam (see Fig. 3.5). Two LVDTs have been installed on one side of the beam, to measure the average strains in the upper part of the sections belonging the central span of the beam. Moreover, inclinometers and accelerometers placed in dedicated plastic casings were installed at five locations on the top of the beam. The aim for these latter sensors was to measure beam rotations and monitor modifications of dynamic behaviour of the beam during the test. However, data retrieved from accelerometers and inclinometers are to be processed by an external company and, at the time this dissertation is written, results have not yet been made available. Pictures of the testing setup are reported in Fig. 3.6. The testing protocol involved the loading of the beams controlling the vertical displacement at midspan. Some unloading and reloading cycles have been performed for some of the specimens, in order to check for possible stiffness or strength deterioration. Deflection of the beams were calculated removing the measured settlements at supports. Force-displacement curves have been retrieved, which express the total vertical load (sum of those measured by the two load cells) as a function of the midspan deflection. Response curves for uncorroded beams are plotted in Fig. 3.7.

Table 3.3 Corrosion levels and corrosion process for specimens tested in the first series of experimental tests

Specimen	Target Δ_m	Measured Δ_m
RC-1	0%	0.00%
RC-2	0%	0.00%
RC-C1	10%	7.55%
RC-C2	10%	13.12%
RC-C3	20%	17.85%
RC-C4	20%	22.94%

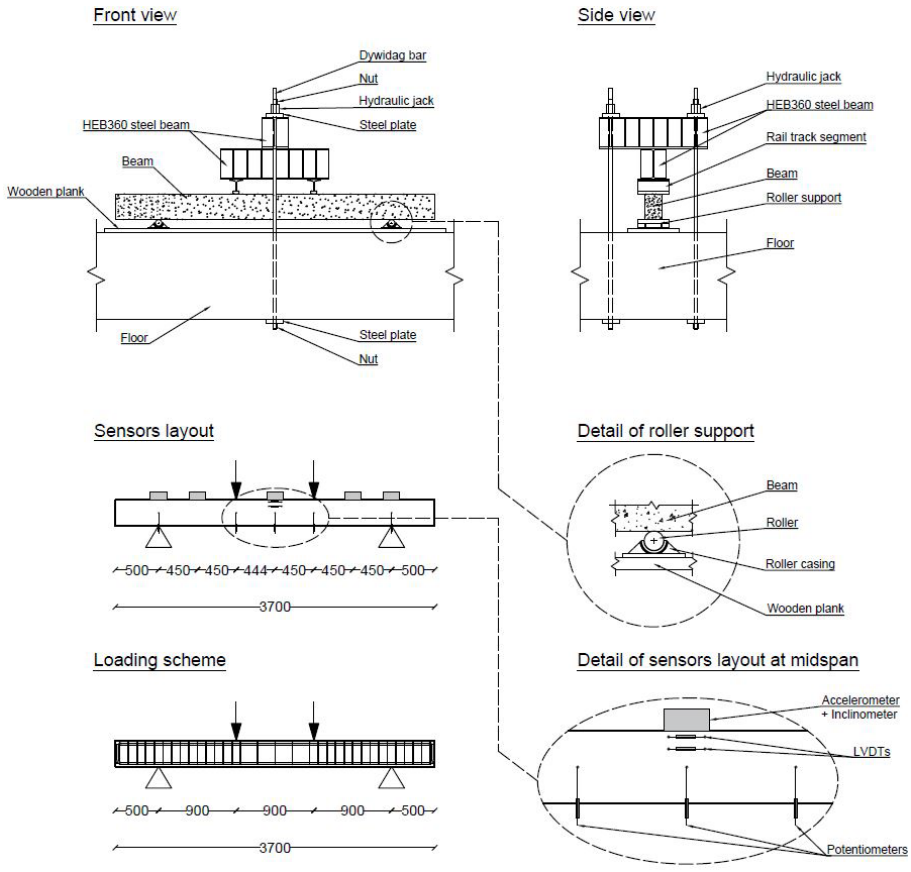

Fig. 3.5 Setup and sensor layout for the first series of experimental tests (Adapted from Di Carlo et al. [69])

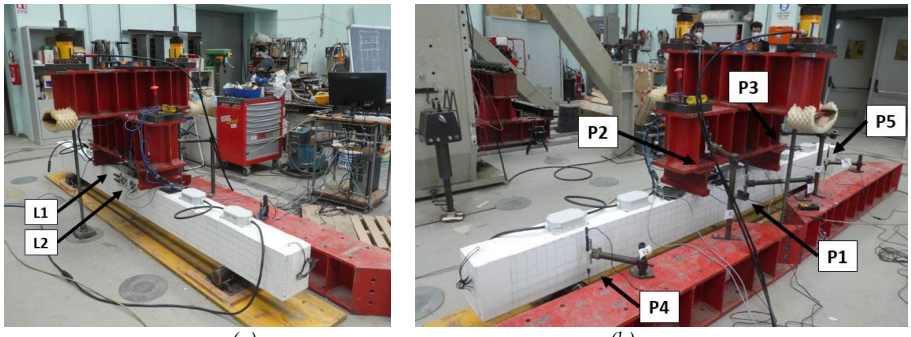

(a) *(b)*

Fig. 3.6 Pictures of the setup adopted for the first series of experimental tests (a) View of the side with LVDTs installed; (b) View of the side with potentiometers installed (From Di Carlo et al. [70])

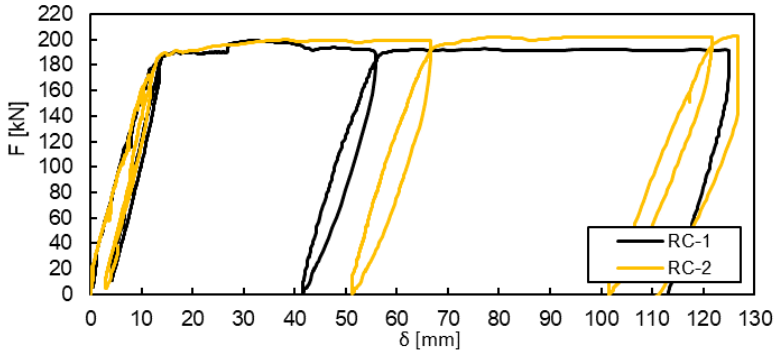

Fig. 3.7 Force-displacement curves for the uncorroded specimens (Adapted from Di Carlo et al. [69])

Both uncorroded specimens RC-1 and RC-2 reached a midspan deflection value approximately equal to 125mm and then were unloaded, terminating the tests. The force-displacement curves are characterized by an initial stiff branch up to flexural cracking, followed by a nearly linear post-cracking branch. Before the curves flatten due to the occurrence of bottom steel yielding in tension, midspan deflection started to increase slightly nonlinear, as a consequence of the development of shear deformations due to the opening of flexural shear cracks in the shear spans (Fig. 3.8a). The point at which yielding has been assumed to have occurred was identified by a quite significant tangent stiffness reduction. After that stage, one unloading and reloading cycle was performed. Subsequently, strength continued to slightly rise with the increases of deflection, possibly because of the reduction of neutral axis depth and of the hardening in tension of bottom steel. However, from a certain stage onwards, bending strength reached a constant value, despite the continuous increase of midspan deflection. This result could be explained by the fact that when crushing of the outer part of the concrete cover at midspan sections starts (Fig. 3.8b and Fig. 3.10a), neutral axis depth begins to increase again, causing a diminishing of the inner level arm associated to the resisting bending moment. This strength reduction balances the strength increase due to the hardening of the bottom steel, so that a constant bending strength is observed from a certain stage of the tests. After reaching this strength plateau, an additional unloading and reloading cycle was performed, and then the midspan deflection was increased till the maximum reached value. Despite extensive spalling of the concrete cover occurred in the compressed part of the sections at midspan (Fig. 3.8c and Fig. 3.10b), no strength reductions were observed for the uncorroded specimens.

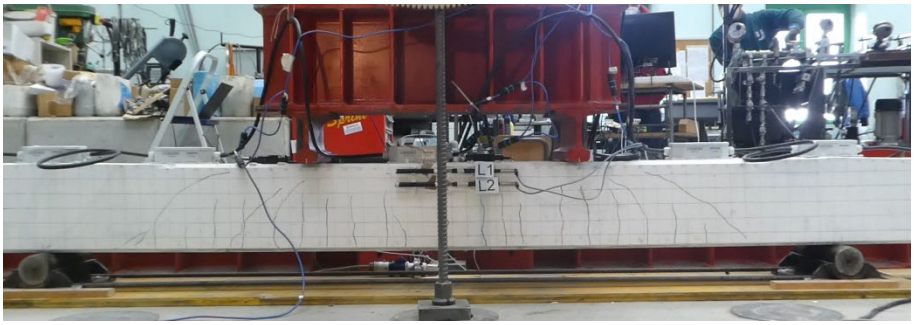

(a)

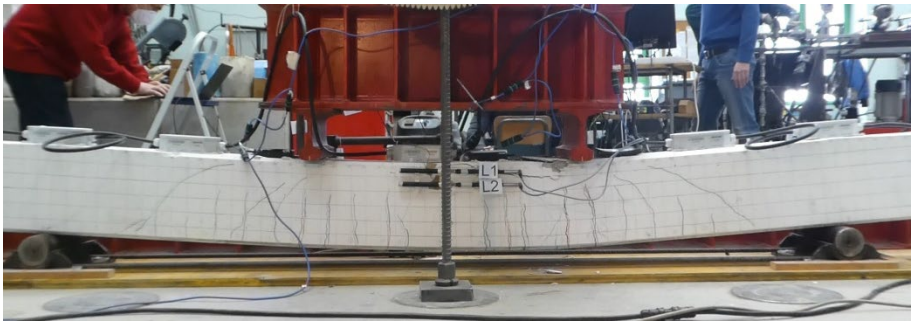

(b)

(c)

Fig. 3.8 Crack pattern and deformed configuration at different stages of the test for uncorroded specimen RC-2 (a) Unloaded after yielding; (b) Beginning of cover crushing; (c) After extensive crushing and spalling of the concrete cover (Courtesy of Prof. Z. Rinaldi and Prof. A. Meda, Tor Vergata University of Rome)

According to the conventional definition of ultimate displacement, based on the occurrence of a drop of strength in the force-displacement curve [99], a value for the ultimate deformation capacity of uncorroded specimens cannot be identified. However, it can be certainly pointed out that those beams demonstrated to have an extremely high ductility, evidenced by the fact that for an imposed displacement ductility demand $\mu_{\delta,d} > 12$ no actual strength reductions have been observed. Moreover, even if the tests would have continued reaching higher values of midspan deflection, non-linear geometry

effects due to the occurrence of large deformations may have started to be relevant, since the deformed configuration would have been quite different from the undeformed one. To analyze the behaviour of corroded specimens, it is necessary to consider their actual condition at the beginning of the tests, i.e., after the termination of the artificial corrosion process. In particular, corroded specimens exhibited a crack pattern characterized by longitudinal splitting cracks on the bottom face, left-side face and right-side face, which have been induced by the corrosion of the longitudinal bottom rebars. These cracks developed for all the longitudinal length of the beams and wide stains were present due to the flowing of corrosion products out of the cracks. Before the tests, specimens have been painted on all the surface but the cracked zones, in order to provide a clean base to draw a 5cm x 5cm squared reference grid. Force-displacement curves for the corroded beams of the first experimental series are provided in Fig. 3.9.

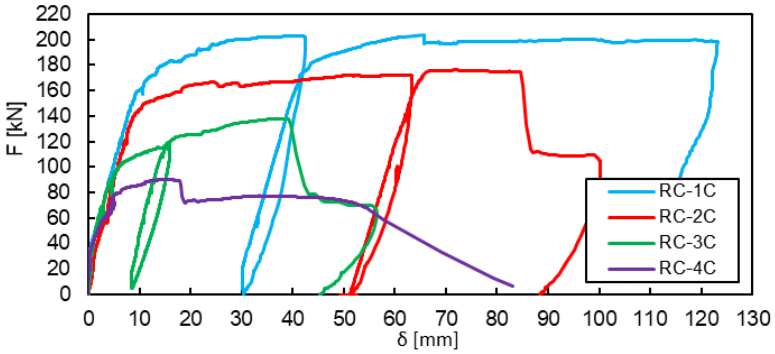

Fig. 3.9 Force-displacement curves for the corroded specimens tested in the first experimental series (Adapted from Di Carlo et al. [69])

The specimen RC-C1 has been the first corroded beam which was tested and served also for the calibration of the artificial corrosion procedure. The weighting of corroded rebars performed after the test led to an estimated global average mass loss ratio $\Delta_m = 7.55\%$. The recorded force-displacement response presents several similarities with those of the uncorroded beams. In particular, maximum bending strength is approximately the same as that measured for uncorroded specimens the test was continued up to reaching a deflection of about 120mm. Also in this case no reduction of strength has been observed, despite the occurrence of concrete crushing in the top cover at midspan (Fig. 3.10c). The main differences in the observed crack pattern consist in the fact that fewer flexural shear cracks developed in the shear spans. On the other hand, the main difference in the response curve is that from a certain point of the post-cracking branch, a gradual loss of stiffness can be observed, possibly caused by the combined action of longitudinal rebars yielding, shear deformations and additional deformation attributable to loss of bond in the corroded rebars. Because of this peculiar feature of the response curve, it is not easy to unambiguously identify a point of the curve associated to the stage of bottom rebars yielding.

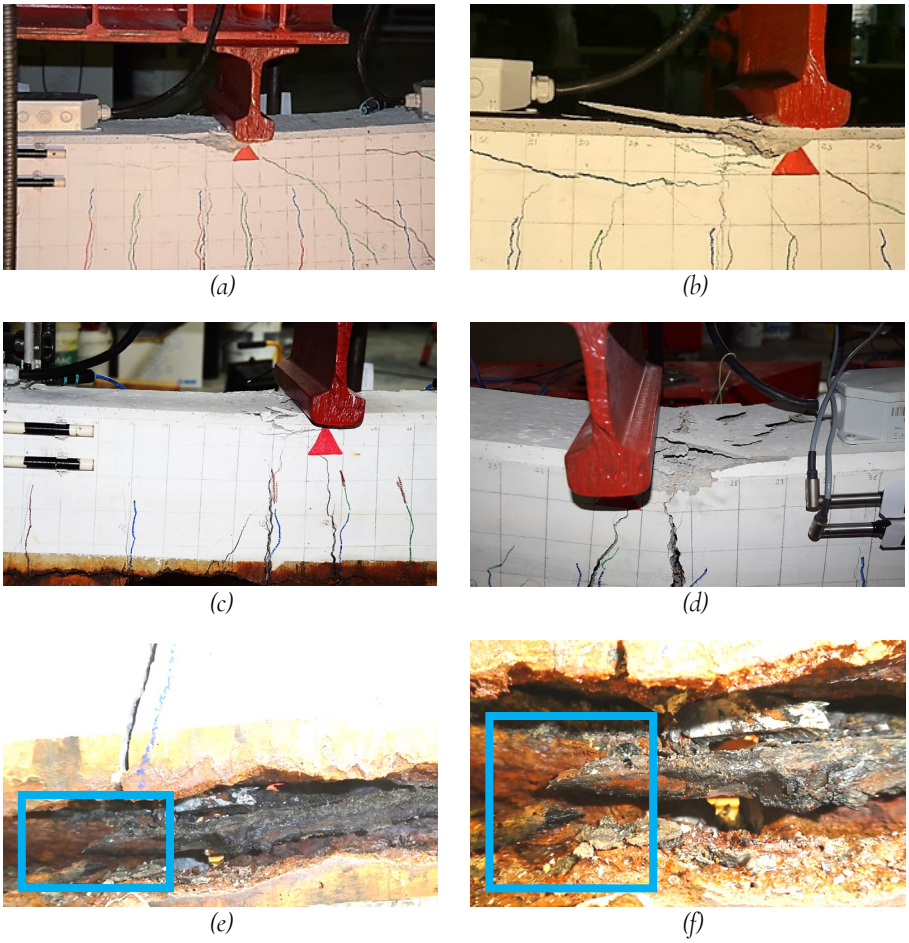

Fig. 3.10 Pictures of crack patterns and steel ruptures taken during the tests: (a) Beginning of concrete crushing in top cover of uncorroded specimen RC-1; (b) Concrete cover crushing and spalling in uncorroded specimen RC-2; (c) Beginning of concrete crushing of top cover in corroded specimen RC-C1; (d) Beginning of concrete crushing of top cover in corroded specimen RC-C2; (e) Fractured corroded steel rebar in corroded specimen RC-C3; (f) Fractured corroded steel rebar in corroded specimen RC-C4; (From Di Carlo et al. [69]*)*

The specimens RC-C2 was characterized by a global average mass loss ratio $\Delta_m = 13.12\%$. As for the case of beam RC-C1, the crack pattern was characterized by fewer inclined cracks in the shear spans. On the other hand, the response curve for this case presented some significant differences with respect to those obtained for the previously analyzed specimens, starting from the fact that the recorded maximum peak strength value has been appreciably lower. Furthermore, the most relevant difference was the occurrence of a sudden drop of strength observed in correspondence of a midspan deflection value of approximately 85mm. The occurrence of this abrupt loss of strength was identified as the failure stage of the beam. After a careful check of the specimen

conditions, which indeed shown crushing of top concrete cover (Fig. 3.10d), the occurrence of this drop of strength was attributed to a partial debonding and a loss of anchorage in one of the longitudinal bottom rebars. In particular, at the failure stage the splitting cracks which were present along the longitudinal bottom rebars opened significantly, reaching width values of several millimeters, and significant portions of the bottom concrete cover experiences spalling [70]. This kind of bond and anchorage failure characterized by a relevant drop of bending strength reminds the failures observed by Almusallam et al. [102] in corroded singly reinforced slabs.
Corroded specimens RC-C3 and RC-C4 presented higher values of global average mass loss ratio, respectively equal to $\Delta_m = 17.85\%$ and $\Delta_m = 22.94\%$. The response curves for these two specimens were both characterized by a peak bending strength and ultimate deformation capacity much lower than those observed for uncorroded beams. In particular, also in these cases a significant drop of strength was recorded at a certain stage of the test. However, in both these cases, the loss of strength was due to the rupture of one of the corroded longitudinal rebars. Some insightful information have been retrieved by an analysis of the crack pattern at the failure stages [70]. Beginning of concrete crushing in the compressed top cover has been observed in specimen RC-C3, while for specimen RC-C4 it seems that the failure occurred before the cover crushing could have begun. In both specimens, almost no shear cracks were present.
The analysis of crack pattern at failure and of the force-displacement curves allowed to recognize the failure mode of the tested specimens, as well as to get data about peak strength and displacement deformation capacity. By the time this dissertation is written, data recorded by the LVDTs have not yet been used in analyzing the behaviour of these tested beams. A preliminary survey of recorded data highlighted the presence of some disturbances, probably due to the development of extensive cracking in the zone where they were installed. To overcome this kind of issues, the employment of non-contact monitoring techniques such as DIC may represent an effective solution, allowing not only to easily monitor the crack pattern, but also to get extensive information on the displacement and strain fields during different stages of the tests. These considerations have been taken into account in the design of the second series of tests, in which a different sensors layout and DIC were used.

3.3.4 Second series of tests with updated setup

In the second part of the experimental campaign two additional RC beams were corroded and tested, in order to improve the understanding of the response of highly corroded beams, with special reference to deformation capacity in terms of member deflection and sections curvature. These additional tests allowed also to enlarge the database of experimental results, which has been then used to assess the performances of different analytical and numerical modelling strategies, as described in Chapter 4.
Theoretical target values of global average mass loss ratio Δ_m were selected equal to $\Delta_m = 15\%$ and $\Delta_m = 20\%$, as indicated in Table 3.4. This choice was done with the aim to obtain mid-to-high corrosion levels, which could result in extensive pitting phenomena on the corroded bars and consequently possible occurrence of rebars rupture. This kind of failure mode has in fact shown to be one of the most impactful of the reduction of

deformation capacity. Table 3.4 also reports the obtained average corrosion levels. The experimental setup and sensors layout used in the second series of experimental tests are illustrated in Fig. 3.11 and Fig. 3.12. In this case, a stiff steel frame equipped with a single hydraulic jack and a load transfer steel beam were used to apply the two vertical loads. Vertical displacements have been monitored at beam midspan and at loading points, by means of potentiometers.

Table 3.4 Corrosion levels and corrosion process for specimens tested in the second series of experimental tests

Specimen	**Target Δ_m**	Measured Δ_m
RC-C5	15%	22.72%
RC-C6	20%	27.52%

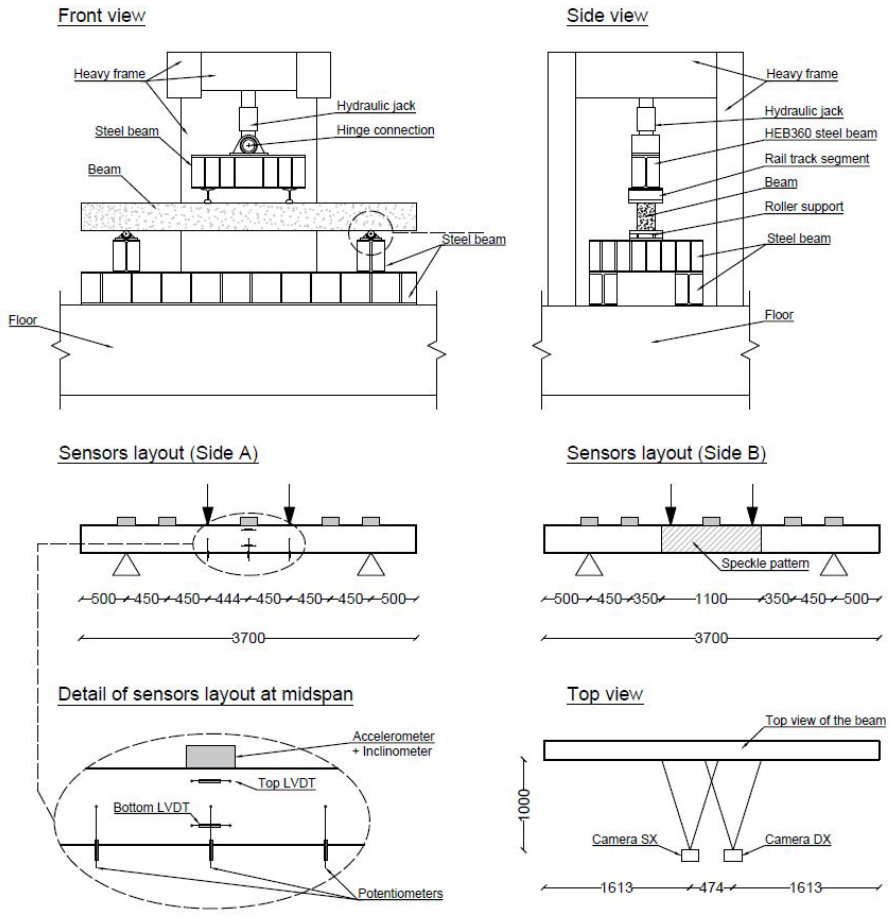

Fig. 3.11 Setup and sensor layout for the second series of experimental tests

(a) *(b)*

Fig. 3.12 Setup used in the second experimental series (a) Side with LVDTs; (b) Side with speckle pattern

One particular difference with respect to the sensors layout used in the first experimental series regards the position of the two horizontal LVDTs, which in this case have been installed at midspan respectively close to the top edge and to the bottom edge of the beam, as indicated in Fig. 3.11. This kind of LVDTs arrangement has been selected with the aim to obtain measures of average horizontal strains over a certain length of the beam midspan at different depths, so to being able to get an estimation of average curvature. The two LVDTs were positioned at depths equal to 5 cm and 22.5 cm from the beam top edge, respectively (Fig. 3.13a) and have different length at rest. For beam RC-C6, which was tested first, a length at rest equal to 150 mm has been adopted. Then, for the test of specimen RC-C5, the LVDTs were installed with a larger original length, equal to 250 mm, in order to get average strain measures over a larger portion of the central span.

In this second series of tests, DIC was also used for analyzing the structural response of corroded beams. Therefore, a suitable speckle pattern was created on one side of the specimens, involving only the central portion of the beams. The speckle pattern was created using an ad hoc developed procedure, which made use of spray paint applied through a 3D-printed plastic stencil with holes of random distribution and having diameter values between 0.5mm and 1.5mm Fig. 3.13b,c. Two camera were used, which were positioned at a distance of 1m from the beam lateral surface Fig. 3.13d. For the left side, a Lumix DC-TZ200 having a resolution of about 20 Mpx was employed, while for the right side has been adopted a Lumix DMC-TZ70 having a resolution of 12Mpx. Image correlation has been so performed separately for the pictures acquired by the two cameras. The software *Ncorr* [143] was employed to process the acquired images, which implements a local DIC algorithm. In processing the images, attention has been given in the choice of a proper subsets size. As in fact known, subsets should be as small as possible in order to increase accuracy of obtain displacement measurement. On the other hand, this requirement is in contrast with the fact that the subsets should also be as large as possible in order to encompass sufficient distinctive features in the pattern [112], [144]. A minimum size for the subset should be at least 3÷5 times the dimension of the speckles. Strain fields obtained from the DIC have been used to analyze the structural response and the failure modes experienced by the specimens.

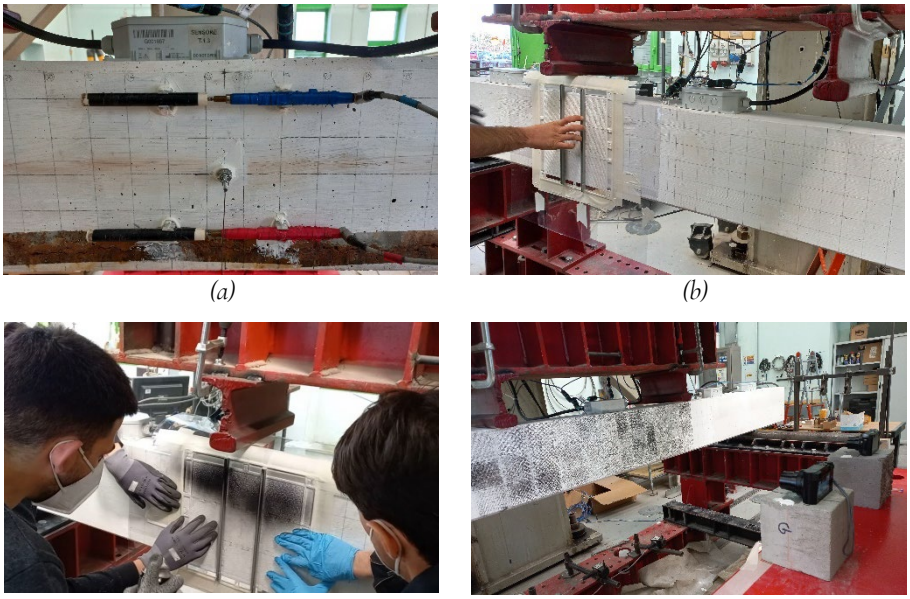

(a) *(b)*

(c) *(d)*

Fig. 3.13 Pictures from the setup used in the second experimental series (a) LVDTs installed at midspan in beam RC-C6; (b) Stencil used for generation of speckle pattern; (c) Creation of the pattern; (d) View of the complete speckle pattern for beam RC-C6 and location of the two cameras

As occurred for the corroded beams tested in the first experimental series, also these specimens presented extensive cracking already before being loaded, due to the presence of corrosion-induced splitting cracks formed along the longitudinal rebars at the bottom, left and right sides of the beams. Beams have been loaded monotonically and tests were terminated in both cases because of the occurrence of a significant strength drop. In Fig. 3.14 the force-displacement response curves are reported, for which the deflection values are those recorded at beams midspan. The corroded specimens RC-C5 and RC-C6 presented values of global average mass loss ratio respectively equal to $\Delta_m = 22.72\%$ and $\Delta_m = 27.52\%$. Force-displacement response of the two beams presents some similar global traits and are characterized by a similar sequence of occurred stages. A linear branch can be observed before the occurrence of flexural cracking, followed by a post-cracking branch which ends at the occurrence of yielding in tensile steel rebars. After yielding, the strength increases till reaching a peak. Then, a slightly softening branch follows, possibly caused by the beginning of crushing in the top cover.

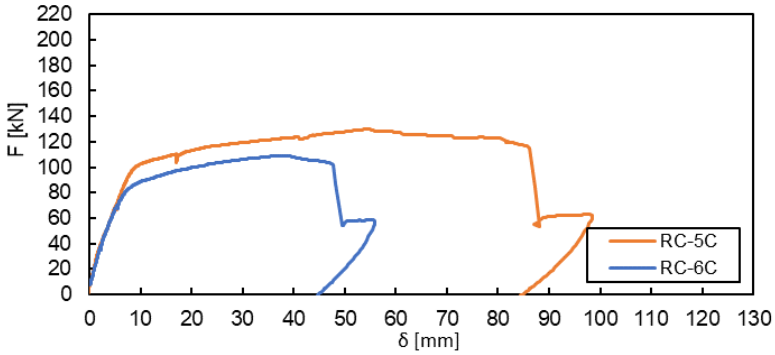

Fig. 3.14 Force-displacement curves for the corroded specimens tested in the second experimental series

For both the specimens, at a certain stage of the post-peak branch an abrupt drop of strength can be observed, associated to the rupture of one of the corroded longitudinal bottom rebars. The tests were interrupted shortly afterwards the occurrence of such strength drop. Pictures illustrating the deformed configuration and crack pattern at failure are reported in Fig. 3.15 and Fig. 3.16, for specimens RC-C5 and RC-C6 respectively. In Fig. 3.17 and Fig. 3.18 are then reported pictures illustrating details of the specimens at failure, including rupture of steel rebars. During the test of both specimens, widening of longitudinal splitting cracks was observed, which in the end resulted in spalling of the bottom cover at certain location of the beam central portion. Partial loss of bond along the longitudinal reinforcement may have occurred, contributing to larger deflections with respect to those associated to the pure flexural mechanism which assumes plain section behaviour. In addition, also in these cases almost no shear cracks were present, as was observed for specimens RC-C3 and RC-C4 of the first experimental series. Accordingly, shear deformations are not expected to have contributed significantly to the beam deflections.

The absence of flexural shear cracks in beams with increasing corrosion level can be explained considering two concurring causes. First, since the bending strength is much lower than the value recorded in uncorroded specimens, but the shear strength may not be so much reduced as well, the actual applied loads may have been much lower than those necessary to generate shear cracking. In addition, corrosion-induced partial loss of bond along the longitudinal rebars could have modified the load transfer mechanism and inhibited the development of shear cracks, as described by various authors [145], [146], [147].

(a)

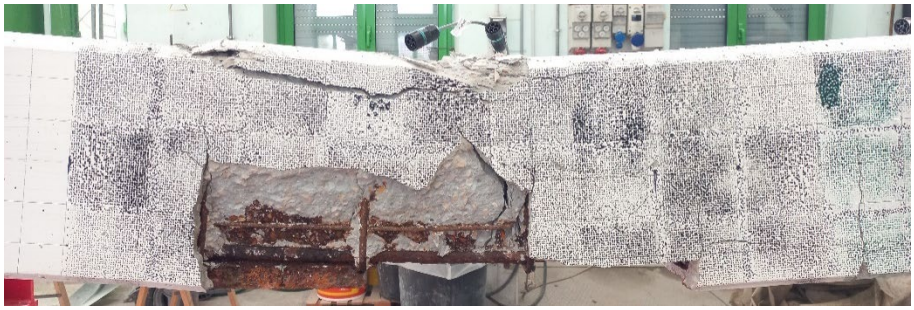

(b)

(c)

(d)

Fig. 3.15 Pictures of deformed configuration and crack patter at failure for beam RC-C5 (a) Side with speckle pattern; (b) Side with speckle pattern (Zoom); (c) Side with LVDTs; (d) Side with LVDTs (Zoom)

(a)

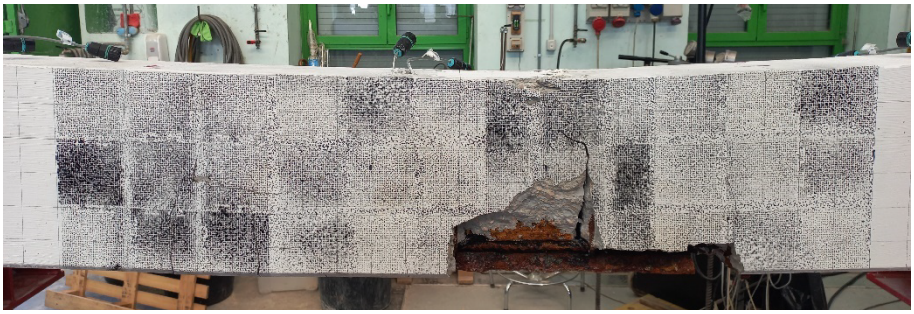

(b)

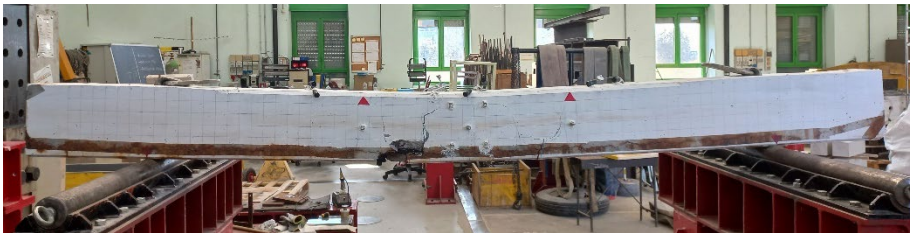

(c)

(d)

Fig. 3.16 Pictures of deformed configuration and crack patter at failure for beam RC-C6 (a) Side with speckle pattern; (b) Side with speckle pattern (Zoom); (c) Side with LVDTs; (d) Side with LVDTs (Zoom)

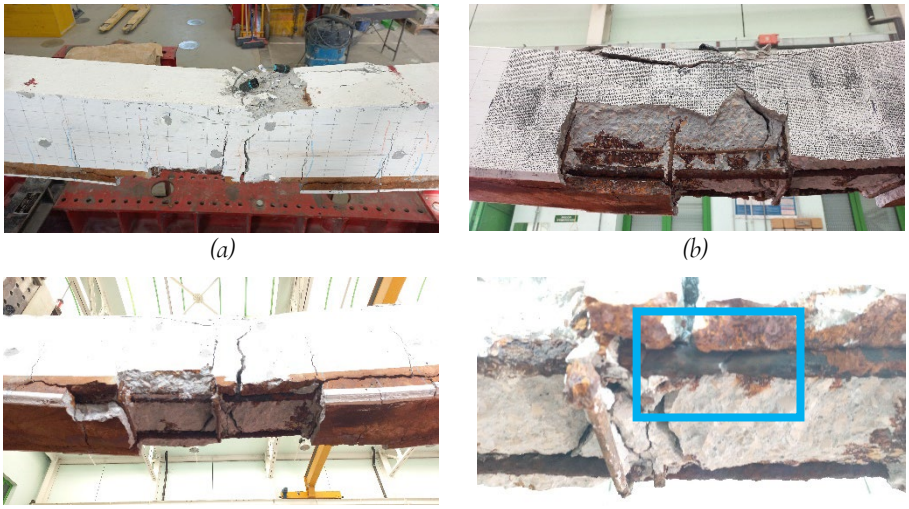

(a) (b)

(c) (d)

Fig. 3.17 Details of failure condition for specimen RC-C5 (a) Top view with visible signs of the beginning of top cover spalling; (b) View of the side with speckle pattern, with visible spalling of the lateral cover; (c) Bottom view of the beam, with extensive spalling of bottom concrete cover; (d) fractured corroded steel rebar

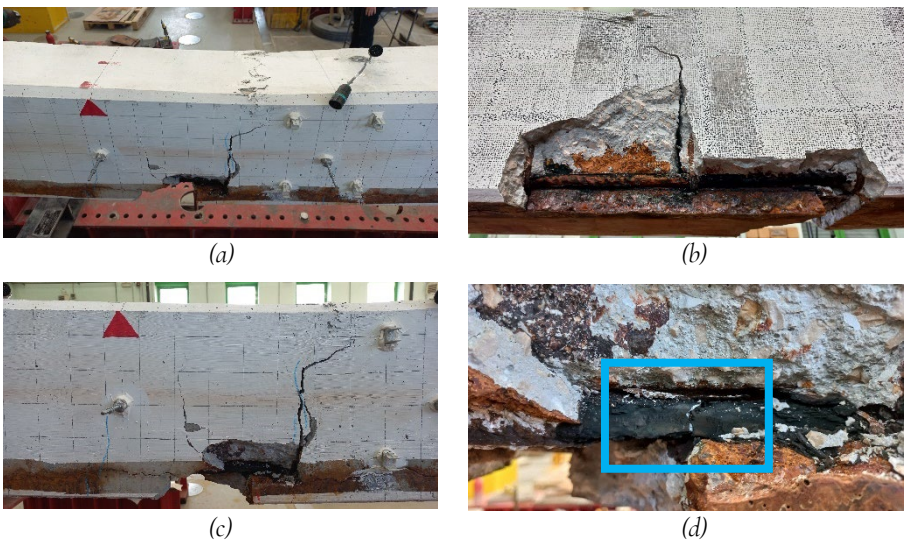

(a) (b)

(c) (d)

Fig. 3.18 Details of failure condition for specimen RC-C6 (a) Top view with very little signs of the beginning of concrete crushing; (b) View of the side with speckle pattern, with visible spalling of the lateral cover; (c) View of the side with LVDTs, with a visible main flexural crack which developed right in the zone with LVDTs; (d) fractured corroded steel rebar

Results of DIC processing are presented in Fig. 3.19 and Fig. 3.20 for specimens RC-C5 and RC-C6 respectively, plotting horizontal strain fields obtained for the monitored ROIs on one side of the beams at different stages of the structural response. In particular, stages corresponding to flexural cracking, yielding of the longitudinal bottom reinforcement, and peak strength reached by the member are considered. The overlapping area between the ROIs of the two employed cameras is represented with a white dotted rectangle and has a length of approximately 50 cm. The vertical red dotted line superimposed to the strain fields indicates the section at which rebar rupture was observed during the tests. DIC results indeed allow for a quite well measurement of relatively large strain values, while for low strains (e.g., in the range ±2‰) a significant noise affects the data. Because of this, at the cracking stage the depth of the neutral axis is hard to be identified clearly, although tensioned and compressed zones can be somehow recognized (Fig. 3.19a, Fig. 3.20a). For beam RC-C5, several flexural cracks characterize the crack pattern at the yielding stage (Fig. 3.19b), while only few of them experienced large localize deformations after the yielding stage. So, it can be seen how at the stage corresponding to member peak strength large deformations are concentrated only in a few main cracks (Fig. 3.19c). For beam RC-C6, which is characterized by a quite higher corrosion level, the crack pattern at yielding already presents just few, well-spaced, flexural cracks (Fig. 3.20b) and remains quite similar as the structural response evolves till the stage associated to peak strength, besides the widening of the already present cracks (Fig. 3.20c). It is worth to notice that, for both the analyzed beams, the section at which steel rupture occurred was located quite close to the main flexural crack which evolved after the yielding stage.

Concerning the overall structural response, it is relevant to highlight differences observed between the crack patterns obtained for the considered highly corroded beams and those obtained for uncorroded specimens [70], for which more cracks close-spaced cracks developed (e.g., see Fig. 3.8 to note the evolution the crack pattern observed in uncorroded specimen RC-2). As mentioned before, these differences can be attributed to the non-uniform distribution of cross-section properties along the beam axis in highly corroded specimens, which fosters the phenomenon of localization of deformations. Such differences have also implications on the proper modelling choices which should be adopted for the structural analysis of the considered beams, as will be discussed in the next chapter.

Measures recorded by LVDTs installed at beams midspan have been analyzed in order to get information on average strain and curvature values. In the following, only results for specimen RC-C5 are illustrated and analyzed. In fact, results for specimen RC-C6 have not been considered in the analysis, since data from the bottom LVDT showed a peculiar unregular trend after the yielding stage and may not be reliable. A possible cause can be found in the crack pattern which developed at beam midspan, in the zone between the two ends of the LVDT sensors (Fig. 3.16d). It can be seen that, in specimen RC-C6 no main flexural cracks developed among LVDTs length. So, deformations localized outside the portion where LVDTs were installed and recorded average strains do not increased so much after the yielding stage.

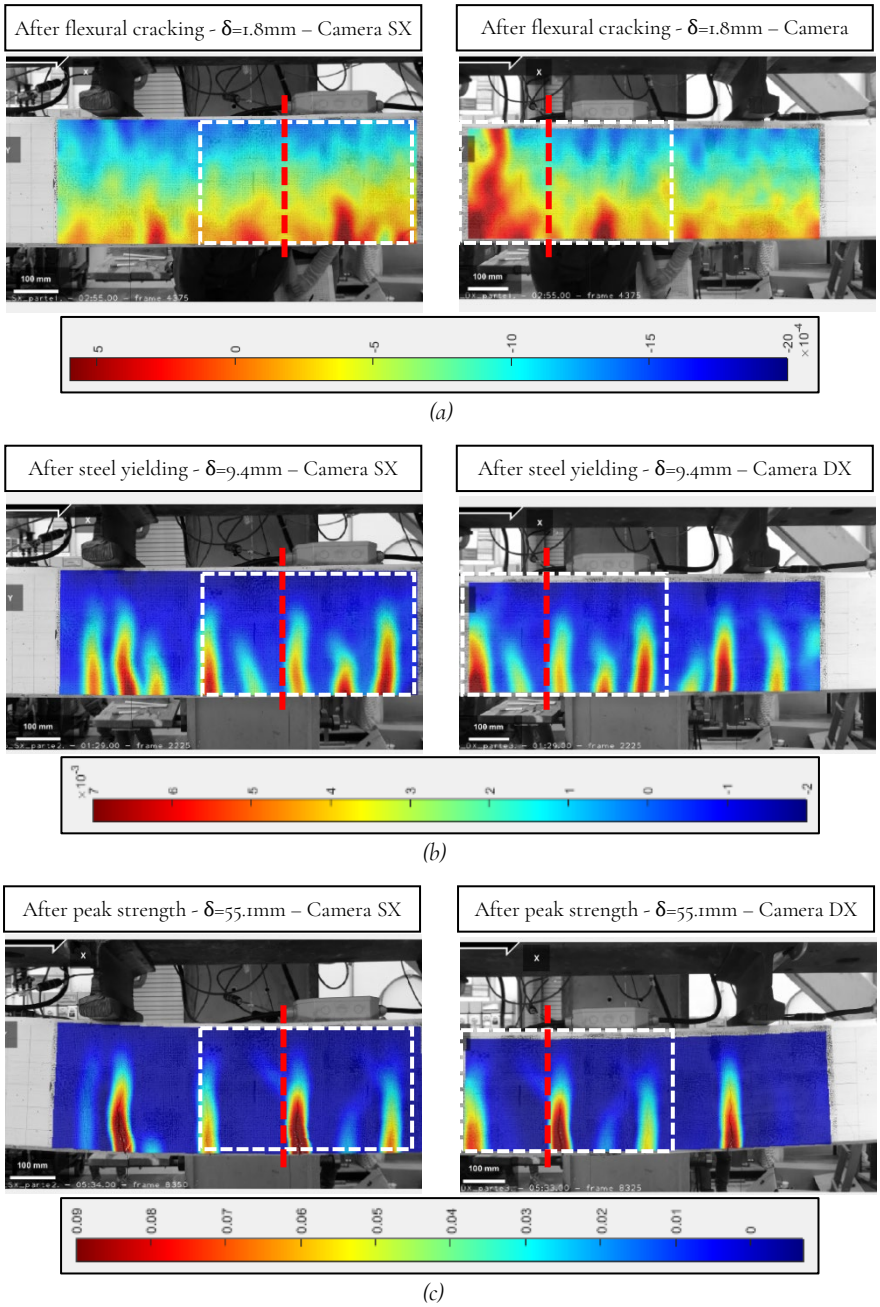

Fig. 3.19 Contour of horizontal strains on the concrete surface monitored obtained with DIC for beam RC-C5, at different stages of the loading process (a) At flexural cracking; (b) At yielding of longitudinal bottom rebars; (c) At the stage associated to the peak strength of the force-displacement curve.

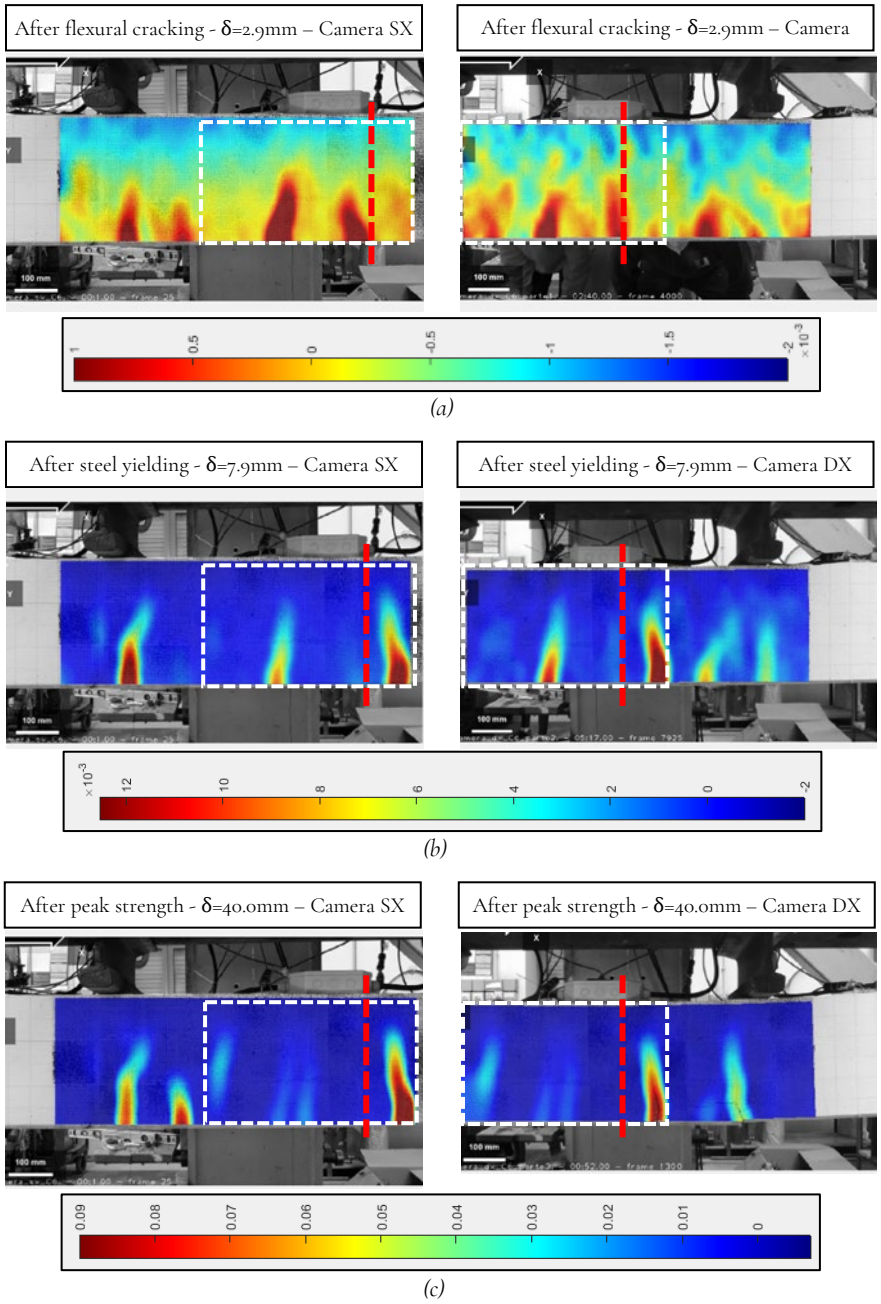

Fig. 3.20 Contour of horizontal strains on the concrete surface monitored obtained with DIC for beam RC-C6, at different stages of the loading process (a) At flexural cracking; (b) At yielding of longitudinal bottom rebars; (c) At the stage associated to the peak strength of the force-displacement curve.

For beam RC-C5, conversely, the main flexural crack formed and evolved right in the portion where LVDTs were installed. Graphs of average concrete strains at midspan for this specimen are reported in Fig. 3.21. Strains are plotted against the total applied load, i.e., the sum of the two punctual loads, in order to allow for an easy analogy with force-displacement curves reported in Fig. 3.14. The top LVDT recorded an average negative (compressive) strain increasing in modulus with the increase of applied load, up to a load of about 100kN. Then, a reversal in the trend is observed and positive (tensile) strains have been recorded. The bottom LVDT recorded positive (tensile) strains which, after a short nearly-linear initial branch, increased non-linearly with the increase of the applied load. Concerning the stages of the response prior to yielding, the difference between the relatively small intensity of negative (compressive) strains recorded by the top LVDT compared to the larger positive (tensile) strains provided by the bottom LVDT (Fig. 3.21b) can be explained by the decrease in neutral axis depth occurred after flexural cracking. After reaching the stage of rebars yielding, strains recorded by the bottom LVDT started to increase significantly, up to the last measured value approximately equal to 51‰ (Fig. 3.21a). Using values of average strains recorded by LVDTs, the average concrete strain at the depth of the bottom longitudinal reinforcement has been derived, as depicted in Fig. 3.22a. It needs to be emphasized that such strain measure may not be actually representative of the strains experienced by the bottom longitudinal steel rebars, since partial debonding due to corrosion may have compromised the validity of plain sections hypothesis. If so, the actual values of strain on the steel rebars may be quite lower than that derived for the concrete at the same depth.

An estimation of the average curvature at midspan has also been provided, using average strains values recorded by LVDTs. Obtained curvature values are plotted against the total applied load in Fig. 3.22b. Despite the quite high corrosion level achieved by the specimen, the derived value for ultimate average curvature at midspan appears not so low. This can be due, as mentioned above, to the fact that the used average strain values have been measured on concrete. So, the ultimate strain evaluated on concrete at the depth of longitudinal bottom steel may be quite higher than the actual strain acting on steel rebars, so leading to a high value of calculated ultimate curvature. Moreover, it is not surprising that despite such value of ultimate curvature, the ultimate member deflection would be quite low. In fact, this happens because large inelastic deformations concentrate only in very short lengths along the beam axis, straddling the major flexural cracks.

Other methods could be adopted in further future analyses of the presented tests to measure average curvatures at beams midspan [148]. In particular, curvatures could be obtained by double-differentiating the deflection distribution along the beam axis. The latter can be approximated with a parabolic law, defined using vertical deflection values measured at three locations along the beam axis (midspan and loading points). As an alternative, the deflection distribution can be derived from DIC data. A possible method to estimate curvature at various sections would involve the use of horizontal strains retrieved from the strain fields provided by DIC. However, it needs to be stressed that it may be difficult to limit noise present in strain fields obtained from DIC, especially for stages corresponding to the initial part of the structural response.

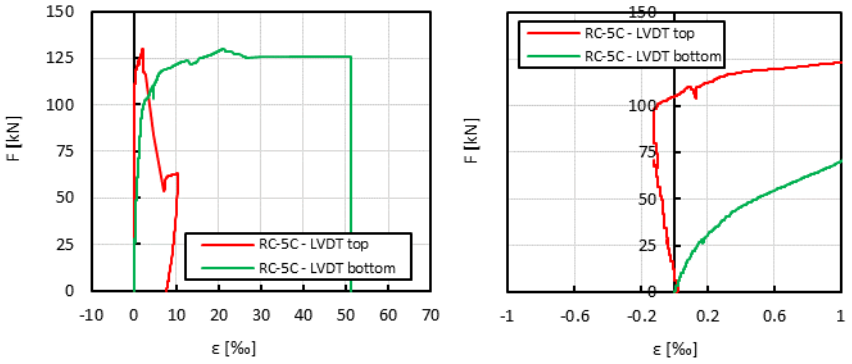

Fig. 3.21 Average strains obtained from LVDT data and calculated average curvature for beam RC-C5 (a) Average concrete strains recorded; (b) Average concrete strains recorded (Zoom);

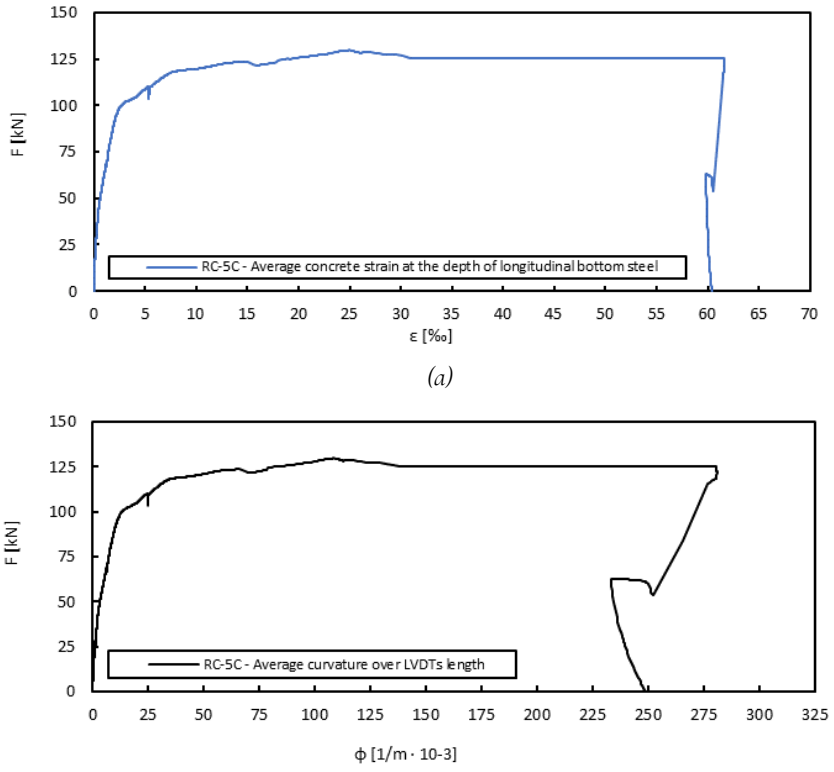

Fig. 3.22 Average strains and curvatures derived from data measured from LVDT for beam RC-C5 (a) Average concrete strain at the depth of the longitudinal bottom rebars ($d = 262mm$), derived using average concrete strain values measures at depths of installed LVDTs (b) Average curvature over the portion at midspan where LVDTs are installed, calculated using average concrete strains values measures with LVDTs

3.4 Analysis of results

3.4.1 Corrosion level

After the tests, the specimens have been demolished and the bottom longitudinal rebars have been extracted. Each bar has been spliced in 5 pieces, obtaining three straight segments of 1000mm length and two rebar portions which include the 90° bended bar ends (Fig. 3.23a,b). Average mass loss has been evaluated using the gravimetric method, i.e., weighting the corroded rebars and comparing their weight with that of an uncorroded bar. As can be seen in Fig. 3.23a, the locations of the three straight segments approximately coincide with the left shear span, the constant moment zone and the right shear span, respectively. Average values of mass loss ratio have been calculated for every segment of each corroded rebar, and results are presented in Table 3.5. In addition, other values of average mass loss ratio are provided, which were computed considering the average value on left and right rebars, or the average value on all the three segments. The first aspect worth noting from Table 3.5 is that average mass loss is far from being uniform, both along the beams and comparing the two rebars. This leads to the fact that average mass loss computed considering all the corroded rebars in a beam is quite different from that computed considering only one bar segment. In all corroded rebars but the right bar of beam RC-C2, the higher values of average mass loss are those obtained for the central segments (T2 in Fig. 3.23a).

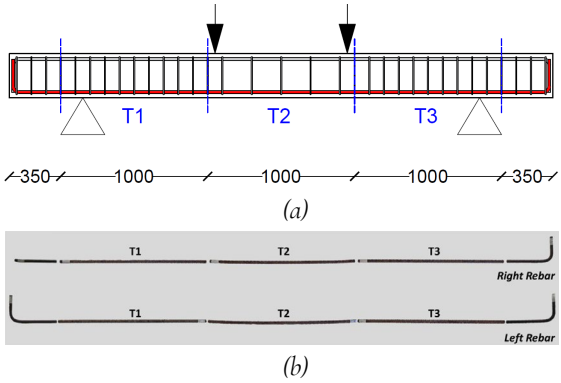

Fig. 3.23 Evaluation of average corrosion-induced mass loss (a) Definition of segments along the length of the longitudinal rebars; (b) Splitting of each corroded rebar in five portions, including three straight 1000mm segments to be used for mass measurement (image associated to beam RC-C1, from Di Carlo et al. [70]*)*

As a matter of fact, in beams which experienced failure by steel rupture, the fracture of one of the corroded rebars occurred in all cases in the central part of the beam. The maximum value of average percentage mass loss, equal to 46.72%, has been recorded for central segment of right rebar in specimen RC-C4. Overall, obtained values of the average mass loss ratio may seem quite high. However, such values may be reached in several cases in real structures, especially in environments with high concentrations of chloride ions, or in cases when corrosion process is fostered by the presence of other deterioration phenomena (e.g., extensive cracking due to ASR).

Table 3.5 Average percentage mass loss values obtained considering different portions of the corroded rebars for the computation of the average [149]

Specimen	Rebar	Average in segment T1	Average in segment T2	Average in segment T3	Average in all segments
RC-C1	SX	7.17	8.69	4.44	6.77
	DX	8.78	10.00	6.25	8.34
	Average	7.98	9.35	5.35	7.56
RC-C2	SX	9.48	13.62	4.84	9.31
	DX	23.03	18.67	9.07	16.92
	Average	16.26	16.15	6.96	13.12
RC-C3	SX	20.88	23.51	19.15	21.18
	DX	13.30	20.17	10.08	14.52
	Average	17.09	21.84	14.62	17.85
RC-C4	SX	15.52	20.93	12.36	16.27
	DX	28.62	46.72	13.50	29.61
	Average	22.07	33.83	12.93	22.94
RC-C5	SX	18.96	29.83	22.78	23.86
	DX	18.56	29.24	16.94	21.58
	Average	18.76	29.53	19.86	22.72
RC-C6	SX	25.20	33.47	25.34	28.00
	DX	27.14	32.66	21.29	27.03
	Average	26.17	33.06	23.32	27.52

3.4.2 Structural response

The specimens tested in the described experimental campaign differ each other only for the achieved corrosion level. It is then of great interest to compare the response of all the tested beams, in other to understand how the corrosion level affected their structural performances. With this aim, Table 3.6 summarizes the observed specimens conditions at the end of the tests, highlighting aspects related to the overall structural response, crack pattern and failure mode. In addition, in Fig. 3.24 the force-displacement curves for all the specimens are reported for comparison.

Table 3.6 Summary of condition of the specimens at the end of the tests

Specimen	Conditions at test end
RC-1	Extensive spalling of top concrete cover, tensile rebars yielded, presence of flexural crack and flexural shear cracks
RC-2	Extensive spalling of top concrete cover, tensile rebars yielded, presence of flexural crack and flexural shear cracks
RC-C1	Extensive spalling of top concrete cover, tensile rebars yielded, presence of flexural crack and few flexural shear cracks, delamination and spalling of the bottom concrete cover
RC-C2	Crushing and beginning of spalling of top cover, tensile rebars yielded, flexural cracks and few flexural shear cracks, extensive spalling of the bottom cover and associated loss of bond in longitudinal bottom rebars. Debonding close to one support and loss of anchorage in one of the longitudinal corroded rebars has been evidenced.
RC-C3	Crushing and beginning of spalling of top cover, tensile rebars yielded, flexural cracks and very few flexural shear cracks, localized spalling of the bottom cover. Rupture of one of the longitudinal corroded rebars has been evidenced.
RC-C4	Almost no crushing of top cover, tensile rebars yielded, flexural cracks but no flexural shear cracks, localized spalling of the bottom cover. Rupture of one of the longitudinal corroded rebars has been evidenced.
RC-C5	Crushing and beginning of spalling of top cover, tensile rebars yielded, flexural cracks but no flexural shear cracks, localized spalling of the bottom cover. Rupture of one of the longitudinal corroded rebars has been evidenced.
RC-C6	Almost no crushing of top cover, tensile rebars yielded, flexural cracks but no flexural shear cracks, localized spalling of the bottom and side cover. Rupture of one of the longitudinal corroded rebars has been evidenced.

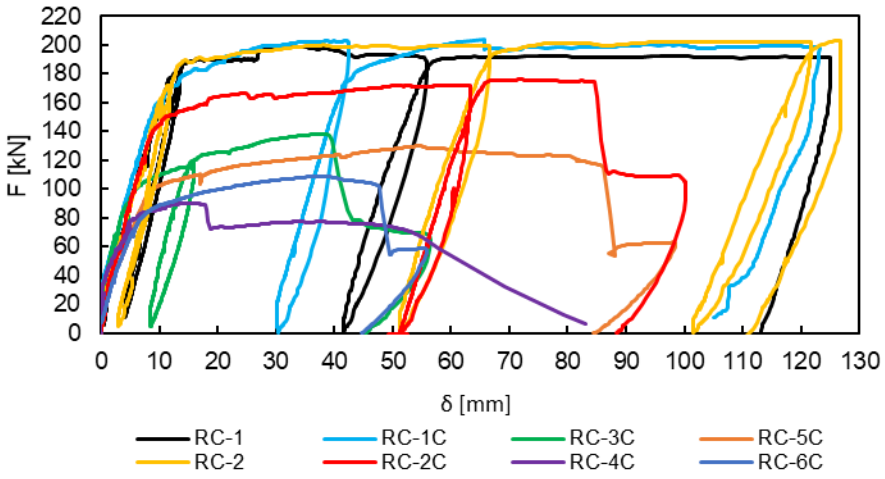

Fig. 3.24 Comparison of force-displacement curves for all the tested specimens

In order to better analyze the structural behaviour of the beams, it is also useful to extract some relevant parameters from the force-displacement curves, namely:

- F_y Strength at yielding
- δ_y Mid-span deflection at yielding
- F_{peak} Maximum strength
- δ_{peak} Mid-span deflection at maximum strength
- F_u Strength at failure
- δ_u Mid-span deflection at failure

In the present work, the yielding point for a response curve (δ_y , F_y) is identified as the point at which the linear or nearly-linear post-cracking branch ends. The point at maximum strength $(\delta_{peak} , F_{peak})$ is identified as the curve point associated to the maximum strength value achieved. Failure point, having coordinates (δ_u , F_u) is identified as the point where an abrupt and significant drop in strength is observed. In Table 3.7 values for the abovementioned parameters are reported, as retrieved from the response curves shown in Fig. 3.24.

Table 3.7Relevant parameters of capacity curves for sound and corroded beams

Specimen	F_y [kN]	δ_y [mm]	F_{peak} [kN]	δ_{peak} [mm]	F_u [kN]	δ_u [mm]
RC-1	188	14.4	199	32.8	-	-
RC-2	185	13.1	203	126.8	-	-
RC-C1	160	9.9	204	65.7	-	-
RC-C2	140	8.7	176	72.3	175	84.5
RC-C3	100	5.8	138	37.2	138	39.1
RC-C4	77	4.5	90	14.4	89	17.8
RC-C5	97	8.1	130	54.9	115	86.0
RC-C6	84	7.7	109	38.6	102	47.6

In Table 3.7 it can be noticed that the point of failure is not reported for beams RC-1, RC-2 and RC-C1. In fact, for these specimens the tests did not show any drop of strength. It is also relevant to observe that the point of peak strength in beam RC-2 is associated to the maximum achieved deflection. It can be instead observed that in corroded beams which experienced a drop of strength, the point of failure is always slightly ahead than the point of peak strength (see Table 3.7). Focusing on the results obtained for corroded specimens, it can be seen from Fig. 3.24 and that an increase in corrosion-induced mass loss reflects in a reduction of the bending strength. This is quite an obvious observation, since a reduction in cross-sectional area of bottom longitudinal reinforcement directly affects the yielding and peak bending strengths of the specimens. In particular, comparing value of yielding strengths F_y from Table 3.7 with values of average mass loss ratio in the central segment T2 reported in Table 3.5, it can be clearly seen a trend for which increasing mass losses lead to lower strengths.

Another commonly reported consequence of increasing corrosion levels regards reductions of deformation capacity. Such a reduction can indeed be observed in Fig. 3.24. However, it would be important to stress out that reduction in deformation capacity is the result of a combination of two consequences of corrosion: i) the first one is the occurrence of a change of the failure mode, for example moving from a "concrete failure" associated to a drop of strength due to extensive spalling of the top cover, to a "steel failure" associated to a drop of strength due to rupture of a rebar, caused by achievement of the apparent ultimate tensile strain; ii) the second one deals with the fact that the newly achieved failure mode would lead to a deformation capacity lower than the original one. This kind of mental exercise may seem worthless, while in reality it is of key importance in analyzing the response of corroded beams. In fact, since corrosion effects can modify the failure mode of the beams in many ways, it is not assured that the newly achieved failure mode would be associated with a lower deformation capacity.

Among the six corroded beams tested, five shown a reduced deformation capacity with respect to the uncorroded specimens. For beams RC-C3, RC-C4, RC-C5 and RC-C6 the failure was induced by a rupture of one steel rebar in the central part of the beam. Due to the presence of pits on the corroded rebar, stress concentration developed. This in turn led to strain concentration, i.e., the development of very high strains in a short length of the bar, whose value depends on the length of the pits. When the strains reached the ultimate tensile strain of the steel, fracture of the rebar occurred. For beam RC-C2, the failure was induced by a loss of anchorage in one of the longitudinal bottom rebars. In order to this having occurred: i) the steel rebar ought to have been completely corroded somewhere around the zone close to the support, before the 90° bended segment, and ii) the bond between steel and concrete ought to have been completely lost, especially along rebar portion close to the support. An analysis of the condition of the extracted corroded bars shown that these conditions may have been actually occurred. Comparing the drop of strength observed in beam RC-C2 with those of the other beams experiencing it, one cannot help but notice that there is a clear similarity, so that without knowing anything about the crack pattern and about what occurred in the tests, one might say that all those beams experienced the same kind of failure mode. As a matter of fact, it makes sense that drop of strength for beam RC-C2 would be similar to those for the other beams. In all the cases, in fact, member strength drop is associated to a loss of strength in the tensile chord of the beam: in the case of beam RC-C2 it was due to the loss of anchorage of the bar, which became ineffective; in the other cases it was due to the rupture of the bar at midspan.

Another interesting aspect worth noting regards the fact that also the failure modes involving rupture of the steel bar at midspan are different from each other. In fact, while for beams RC-C3 and RC-C5 the steel rupture occurred after the crushing and spalling of the top concrete cover has begun, in specimens RC-C4 and RC-C6 signs of top cover crushing were few or totally absent. In these latter cases then, the deformation capacity of concrete in compression has not been exploited.

3.5 Discussion

The results presented in this chapter allowed to get some insights on the structural behaviour of corroded RC beams. Some considerations are proposed in the following. In the presented research work the adopted setup and sensors layout were chosen in order to get data useful to analyze the deformation capacity of the studied beams. In particular, sensors to measure displacement, curvatures and strains were adopted. LVDT sensors were used to monitor average curvature at midspan, while DIC was employed to get information about the crack pattern and the strain fields developed on the beam side. Moreover, inclinometers were installed at different locations along the beam, in order to provide data about rotations.

The obtained and already processed data proved to be useful in the analysis of structural behaviour of the beams. In particular, LVDT measures were used to estimate average curvatures at midspan, while DIC allowed to accurately study the crack pattern evolution analyzing localization of deformations and to check for the possible presence of shear cracks. By the time this dissertation is written, the processing of the DIC results is still currently ongoing and further even better results could be obtained by the analyses, considering for example other choices of the adopted choices and parameters. Data from inclinometers are also currently being processed.

Some critical aspects in measuring deformation capacity for the studied beams may be recalled. As an example, in corroded beams which experienced steel rupture at midspan, it is not easy to get an effective measure of the curvature of the section which experiences failure. In fact, due to the presence of pits, the residual cross-sectional area of the bars is not uniform and so is the flexural stiffness of the sections at midspan. Accordingly, an average measure of curvatures encompassing a portion or even the whole constant moment zone of the beam may not be so representative of the curvatures developed by the very single section which experience steel rupture.

Another relevant aspect regarding the available data retrieved from the test is that the steel rupture occurred only at midspan or at the anchorage of the rebars. As a matter of fact, it would have been also interesting to be able observe steel rupture occurring in the plastic hinge zones of the shear spans. In such a case, it would have been possible to analyze the ultimate condition in the plastic hinge, whose behaviour is highly relevant for the study of corroded members response, for example in structures subjected to seismic actions.

Some considerations can be drawn regarding the accelerated corrosion process used and the procedure adopted to measure corrosion levels. It is indeed true that artificially accelerated corrosion leads to corrosion effects which may be different than those obtained from natural corrosion. However, Du et al. [108] pointed out that these differences are much more related to the magnitude of the effects, rather than on the kind of effects, so that corrosion effects on structural performances are of the same types. Insights about structural response of corroded beams achieved by analyzing the response of specimens which experienced accelerated corrosion procedures may then be in any case useful to understanding and analyzing the behaviour of real structures in deteriorated conditions.

A particular attention should then be given to the definition of corrosion levels achieved by the beams, which is particularly relevant for the research presented in this dissertation since it provides a necessary information to simulate the response of the studied specimens. As a matter of fact, the more accurate could be the information on residual area distribution along the rebar, the better it would be for a proper modelling of the structural response of the corroded specimens. By the time this dissertation is written, analysis of the distribution of residual diameter values along the corroded bars is currently ongoing, though not yet fully completed. Such an information will for sure prove to be useful to model the characteristics of rebars in analytical and numerical simulations of studied specimens. On the other hand, it is worth to recall that in practice only a rough estimation of the average corrosion level is usually available for real deteriorating structures. So, it appears also interesting to check the results obtainable with analysis approaches which use as an input a less refined estimation of the corrosion level in terms of average mass loss ratio. This latter aspect will be explored and investigated in the next chapter.

4

Performance assessment of practice-oriented modelling approaches for the analysis of sound and corroded reinforced concrete beams

I can live with doubt and uncertainty and not knowing. I think it's much more interesting to live not knowing than to have answers which might be wrong.
Richard P. Feynman

Performance-based approaches for the structural assessment are nowadays widely employed in engineering practice. Accordingly, suitable tools for estimation of structural performances of reinforced concrete members are needed, especially in terms of deformation capacity and ductility. In this chapter, analytical and numerical approaches for modelling the response of concrete beams are used to simulate the response of sound and corroded beams which was tested in the experimental campaign reported in Chapter 3. Attention is first put on checking the effectiveness of the proposed approaches in modelling the response of the tested beams. In combination, considerations about the modelling choices for representing the mechanical characteristics of corroded steel rebars are formulated, focusing on the approaches currently suggested to be used in engineering practice.

4.1 Introduction

Modelling approaches which can effectively and accurately represent the non-linear response of reinforced concrete (RC) members are strongly needed in nowadays engineering practice, in which performance-based design and assessment are paving their ways towards a widespread adoption [150], [151], [28]. In the assessment of structural performance of existing RC members, one relevant aspect to be considered regards the effects of deterioration mechanisms on the structural response. In particular, among the various degradation mechanisms, corrosion of reinforcement embedded in concrete is one of the most relevant and widespread [152] and also one of the most impactful on the structural behaviour of RC elements. Main effects include modifications of reinforcement geometry and mechanical characteristics, as well as of the behaviour of the surrounding concrete and of the steel-concrete interface [51], [52], [153]. Regarding main consequences at the member level, they involve the possible change of resisting mechanism and failure mode, often associated to reductions of strength and deformation capacity [46], [54].

For the assessment of RC members affected by degradation processes, a strategy often adopted in practice involves the use of modelling and calculation approaches originally developed for the analysis of undamaged structures, extended for taking into account of degradation effects just by adopting modified values of geometrical and/or material parameters which influence the structural response. However, some concerns have been raised regarding the validity and suitability of such approach, since it may not always represent an effective solution [59]. As an example, modelling procedures originally developed for the analysis of undamaged members, may not always be suitable to be used for damaged ones, since some of the hypotheses upon which those approaches were based may not be guaranteed anymore in the case of deteriorated structures. As a matter of fact, some care should always be taken when using models which were developed for undamaged members. The adopted analysis procedures should be first validated to prove their suitability for modelling the response of deteriorated members. In addition, when enhancements of such procedures are proposed, they should be done properly accounting for the specific consequences induced by the considered deterioration phenomenon, e.g., reinforcement corrosion [60].

The research presented in this chapter aims at evaluating the predictive performance of some practice-oriented modelling approaches herein adopted for the assessment of structural response of corroded RC beams, with a particular emphasis on the evaluation of failure modes and deformation capacity.

In modelling the response of corroded RC elements, several consequences of the deterioration phenomenon should be considered. Focusing on those consequences which significantly affect the deformation capacity of RC sections, two are in particular worth to be mentioned: i) the spread of cracking in the concrete surrounding the corroded rebars ; ii) the loss of confinement effectiveness due to the corrosion of the stirrups [55]. In fact, in case of failure modes associated to concrete crushing, the two aforementioned corrosion consequences could strongly reduce the sectional deformation capacity since

they can compromise the strain deformation capacity of concrete in compression and foster the buckling of compressed longitudinal rebars.
However, an additional corrosion consequence which can strongly influence the sectional deformation capacity is the rupture of longitudinal steel rebars. As widely known, in fact, for members characterized by significant corrosion levels and presenting pitting along the rebars, a significant apparent reduction of ultimate steel strain in tension can occur because of stress concentrations along the bars [56], [57].
The research pursued in the present work focuses in particular on this latter aspect, analyzing cases for which sectional and member deformation capacity are compromised by the unforeseen occurrence of corroded rebars rupture. With this aim, the results obtained for the corroded beams tested at Tor Vergata University in Rome [69] presented in Chapter 3, can offer a valuable bundle of data for the analyses. In particular, the available data on geometry and material characteristics of the tested specimens allow them to be a suitable case study to be used for test and analyze the performances of practice-oriented modelling approaches for the structural assessment of corroded concrete members.
In the present chapter, approaches for analyzing the structural response at section and member levels are considered. In particular, the analytical formulations for failure mode domains described in Chapter 2 has been used for analyzing the sectional behaviour. Analytical and numerical approaches based also based on sectional analysis and curvatures integration have been considered for modelling member response of RC beams. The considered analysis strategies allowed to simulate the response of both sound and corroded RC beams presented in Chapter 3, in terms of failure mode and force-displacement response curves. To take into account corrosion effects in the adopted modelling approaches, a common strategy has been adopted involving the use of reduced values for of both cross-sectional area and ultimate tensile strain of corroded rebars.
Several aspects are investigated in this chapter, with the goal of pursuing research objective ***O2*** described in Chapter 1. The first aim of the research is to check the capability of the considered approaches in correctly modelling the response of corroded members. The considered modelling strategies, based on sectional analysis, are indeed of a low level-of-approximation (LoA) type commonly employed in engineering practice to analyze the response of sound RC members, so the analysis of their modelling performances is of great interest. The second aim of the proposed work is to investigate how different modelling choices of the residual mechanical properties of the corroded rebars affect the member response of corroded RC beams. To doing so, variability in methods used for representing the residual cross-sectional area and the ultimate tensile strain of corroded rebars is considered. The third and last aim of the proposed investigation regards the understanding of the role of corrosion level quantification. In particular, it has been taken advantage from the fact that for the studied beam members, the average mass loss ratio has been calculated in different ways, as shown in Chapter 3. Accordingly, different values of mass loss ratio can be used as input in the herein adopted structural analysis procedures, depending on whether a coarser or a more refined description of the corrosion level wants to be used. In this sense, this aspect resembles again the choice between low or high LoA approaches, in which the input material

parameters can be defined with different degrees of refinement. The influence of the mass loss ratio definition on the obtained simulated response is studied in this chapter and some considerations are proposed regarding common mass loss ratio definitions used in the engineering practice. The performed analyses are presented mimicking the order followed in Chapter 3 for describing the experimental tests, as it is also convenient for the illustration of the obtained results. Accordingly, the analyses on uncorroded beams are presented first, whose results serve as reference for subsequent ones. Then, analyses performed on corroded beams from the first and the second experimental campaign are reported, whose results are particularly useful to address the abovementioned aims of the research work. Summary of main findings are reported at the end of the chapter.

4.2 Modelling materials behaviour

The adopted modelling strategies for RC beam elements are based on the response at sectional level. Accordingly, a description of the constitutive behaviour for concrete fibers and for steel rebars is required. As highlighted by Fardis [4], the constitutive laws for describing the mechanical behaviour of materials in analyses of RC members aimed at studying their inelastic behaviour should be chosen of a suitable type, in order to accounting for material non-linearities and possible effects due to cyclic loading. As an example, in Fig. 4.1 are illustrated material cyclic constitutive laws which can be used in the analysis of RC members. In particular, in Fig. 4.1a a cyclic constitutive law for concrete based on the formulation by Popovics [154] is depicted, while in Fig. 4.1b, as an example of constitutive law for steel, a Menegotto-Pinto [155], [156] cyclic law is illustrated, which allows to model cyclic behaviour of rebars also accounting for the Bauschinger effect. It is worth noting that this kind of law for reinforcing steel is not directly provided with a limitation on deformation capacity. So, a check always needs to be done in post-processing the analyses results, to assess whether defined values of ultimate steel strain have been achieved.
In the case an RC member is affected by corrosion of the reinforcements, its structural response is affected in many ways. In such a situation, some proper arrangements may be needed to model its structural behaviour, involving a modified description of geometric and material properties.

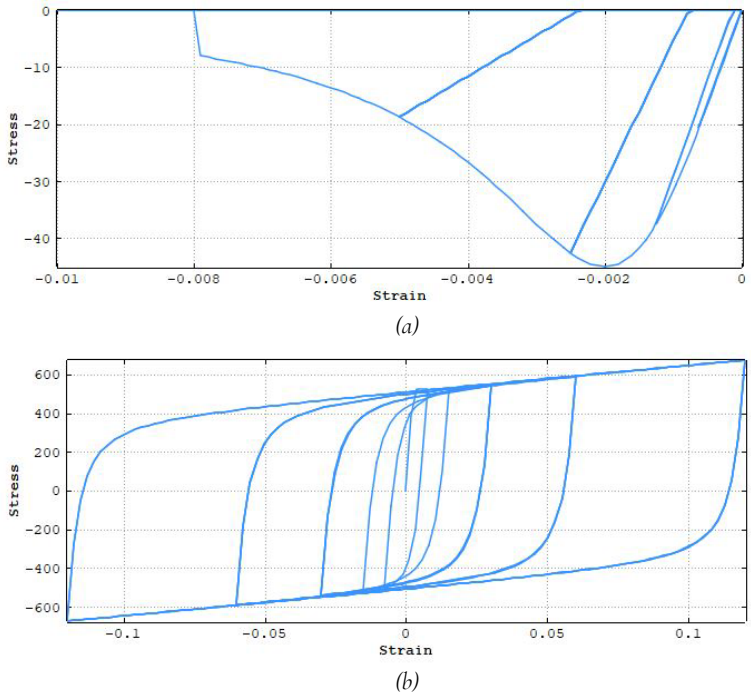

Fig. 4.1 Cyclic uniaxial constitutive laws for (a) Unconfined concrete in compression; (b) reinforcing steel

In particular, as well known [157], [158], the consequences of corrosion at the material level can be summarized as follows:

- *Effects on reinforcing bars*:
  The primary effect on steel rebars regards the non-uniform reduction of cross-sectional area [159], due to the transformation of iron in corrosion products, Fig. 4.2a. This reduction of area has in turn two additional consequences which affects the mechanical behaviour of steel rebars. The first consequences is that the stress-strain response of every corroded section of a bar may change and be different, due to the removal of a portion of its section. This is due to the fact that, depending on the manufacturing process, the material composing a rebar cross-section is not uniform on it (see e.g., Caprili et al. [160], Haefliger et al. [161], Haefliger et al. [162]). Accordingly, the removal of a portion of cross-section will modify the average global phenomenological stress-strain behaviour of the cross-section itself. The second consequence of rebar area reduction is related to the fact that the loss of cross-sectional area is non-uniform also along the rebar longitudinal axis, see Fig. 4.2b. This implies: i) that the average global phenomenological stress-strain behaviour of the cross-section changes along the rebar; ii) that highly localized reductions of cross-sectional area along the bar may induce stress concentration caused by axial equilibrium requirements, which in turn would lead to high strain

concentrations [57]. This way, an ultimate tensile strain value may be reached in a pit with a very short length, far before than it is reached on all the other nearby sections. This can lead to the rupture of the steel rebar.

- *Effects on concrete*:
  The development of corrosion products around corroded bars generates an increasing pressure on surrounding concrete, which leads to the formation and evolution of splitting cracks that start from the steel-concrete interface and spread radially, Fig. 4.2c. These can occur in all the reinforcement affected by corrosion, being it composed by longitudinal rebars and/or stirrups. This widespread crack pattern has the global effect of reducing the compression strength of concrete in such cracked zones. Moreover, the evolution of splitting cracks may result in local spalling of the concrete cover, Fig. 4.2d.

- *Effects on bond between steel and concrete:*
  The formation of corrosion products around the corroded rebars modifies the bond between the steel and the surrounding concrete, due to the occurrence of different phenomena. The formation of corrosion product, at the very beginning lead to an increase in bond between steel and concrete, till the corrosion level is quite low. On the other hand, when splitting cracks start to spread and the steel rebars lose a significant amount of cross-sectional area, the bond between steel and concrete significantly reduces. This is caused by the combination of several phenomena: i) the lubricating effect of corrosion products at the steel-concrete interface; ii) the significant reduction of rebar cross-section, which compromise the mechanical bond provided by the ribs of the bar(Fig. 4.2e); iii) the possible delamination or spalling or the concrete cover which can develop as splitting cracks evolve.

In the present work, not all the aforementioned corrosion effects were taken into consideration in the adopted modelling approaches. Regarding corrosion effects on concrete, the corrosion damage observed in the case study beams described in Chapter 3 may offer some insight. In particular, the concrete in the compressed part of the sections, i.e., the top part, was not affected by corrosion effects in any specimen and so remained in sound conditions. On the other hand, the concrete on the bottom part of the corroded beams experienced extensive splitting cracks and localized spalling, so indeed it experienced the effects of corrosion. However, the contribution that concrete in the bottom part of the sections provides to the global response of the beam members is pretty negligible, whether or not corrosion effects are considered.

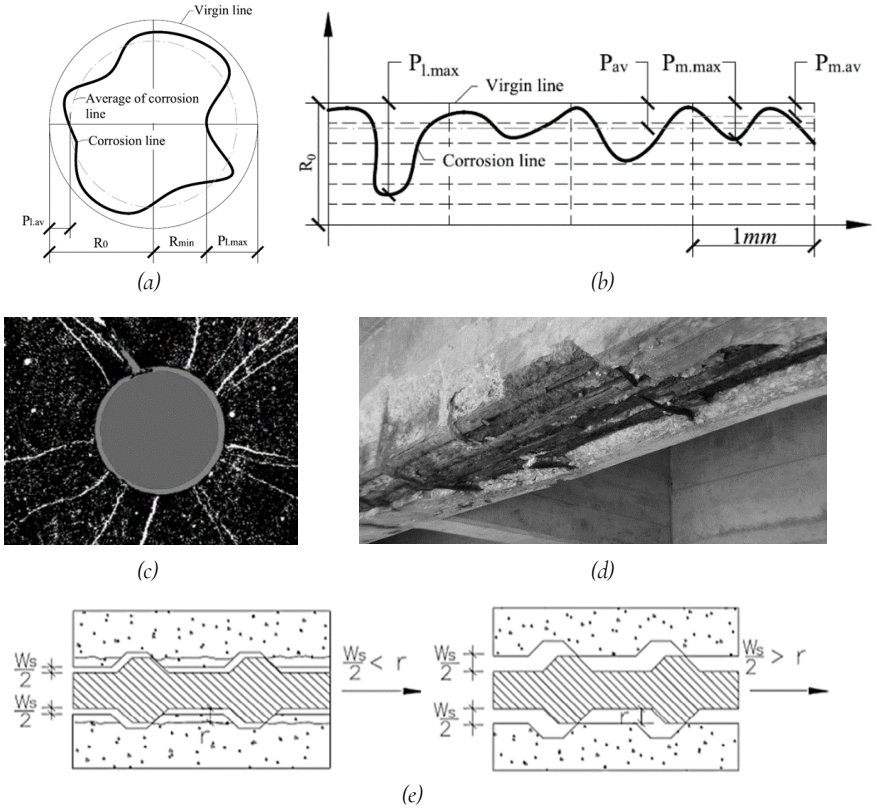

Fig. 4.2 Basic consequences of corrosion which can affect the structural behaviour of RC members (a) Non-uniform reduction of residual rebar radius (Adapted from Zhao et al. [163]*); (b) Non-uniform distribution of pit depth along the corroded rebars (Adapted from Zhao et al.* [163]*); (c) Development of radial splitting cracks in concrete around corroded rebars, due to the increase in pressure generated by the increase of corrosion products (Adapted from Savija et al.* [164]*) : (d) Spalling or delamination of the concrete cover (Adapted from Namita* [165]*); (e) Loss of mechanical bond in corroded ribbed rebars (Adapted from Plizzari et al.* [166]*).*

This is obviously due to the fact that concrete at the bottom part is subjected only to tensile strains, due to the low depth of the neutral axis. For these reasons, the corrosion effects on concrete has been chosen not to be modeled in the present investigation.
Regarding the modifications of steel-concrete bond induced by corrosion, a different perspective has been taken, which although led to the choice of not accounting for such changes. In fact, recalling that one of the goals of the proposed investigation is to check the performances of modelling approaches commonly adopted in engineering practice, modelling choices were restrained by the capabilities of the considered analysis approaches, which plain sections hypothesis and so perfect bond. Indeed, neglecting possible loss of bond due to rebar corrosion is a very strong hypotheses, and this aspect needs to be kept in mind while considering the obtained modelling results.

On the other hand, the focus of the present study has been very placed on modelling the corrosion effects on the behaviour of reinforcing steel. This has been accomplished by modelling a reduced value of cross-sectional area of the corroded bars, as well as by using a reduced value of their ultimate tensile strain. Although this kind of approach cannot model explicitly all the corrosion effects on steel mentioned in the list above, it has been chosen since it reflects one of the choices which are most commonly suggested to be adopted in engineering practice [158], and so it appears indeed useful to check its effectiveness.
The procedure adopted for calculating the residual area and ultimate tensile strain of the corroded steel can be summarized as follows:

1. Definition of the average corrosion mass loss ratio Δ_m
2. Calculation of an average uniform corrosion penetration x, using the average corrosion mass loss ratio Δ_m
3. Evaluation of a maximum pit depth p, also referred as maximum corrosion penetration, using the uniform corrosion penetration x amplified by a proper pitting factor α
4. Calculation of the minimum value of residual cross-sectional area of the corroded bar, using the maximum pit depth p_{max} and a suitable model for describing the shape of the residual portion of the cross-section
5. Calculation of the apparent residual ultimate tensile strain of the corroded bar, using a proper phenomenological formulation

As defined in Chapter 3, the average corrosion mass loss ratio can be expressed as:

$$\Delta_m = \frac{m_{loss}}{m_0} \tag{4.1}$$

Where the term m_{loss} is the mass loss value for the considered bar or bar segment and m_0 is its mass value in sound conditions.
The average uniform corrosion penetration x can be then calculated using the expression:

$$x = \frac{\phi_0}{2} \cdot \left(1 - \sqrt{1 - \Delta_m}\right) \tag{4.2}$$

Where ϕ_0 is the original diameter that the considered rebar had when it was in sound conditions. The evaluation of the maximum penetration depth p is then simply done using relation (4.3), where α is a properly chosen pitting factor:

$$p = \alpha \cdot x \tag{4.3}$$

Precisely because of its simplicity, it is worth to make a few remarks regarding eq. (4.3). By expressing the maximum corrosion penetration p_{max} with the previous relation, it

means to assume that a correlation exists between the maximum pit depth and a measure of the average corrosion level of the bar or bar portion. The pitting factor α should then be representative or the variability of the pitting depth along the bar. Two aspects are however worth to be mentioned, with reference to the above hypotheses. First, the corrosion level defined by means of a value of the average mass loss ratio can be calculated in several different ways depending on how the average is computed, as shown in Chapter 3. In addition, the value of the pitting factor α is traditionally suggested to be assumed equal to 10 [158], [167], but this assumption may be not so suitable for all corrosion levels. Values of experimentally observed pitting factors have been reported to be in the range 4 ÷ 8 for natural pitting corrosion and in the range 5 ÷ 13 for artificially accelerated pitting corrosion [168]. Recently, some research works proposed definitions of the pitting factor as a function of the corrosion level, as for example in the work of Zhao et al. [163] in which the pitting factor is suggested to non-linearly decrease with the increase in average mass loss ratio.

In the present study, different values of the pitting factor have been tested, taking as a reference the suggested values of 10. The results offered some useful insights on the proper values of the pitting factor to be adopted in the analyses of corroded RC members.

For the determination of the minimum residual cross-sectional area of corroded rebars, many models have been proposed in literature. In the present work, two of the models traditionally suggested to be used in the assessment practice have been tested, namely, the model from Rodriguez et al. [159] and the model from Val and Melchers [169]. In the model from Rodriguez et al. [159], the minimum residual area $A_{res,min}$ is computed as if the remaining cross-section would be circular-shaped, as illustrated in Fig. 4.3a and described by eq. (4.4):

$$A_{res,min} = \frac{\pi \cdot (\phi_0 - p)^2}{4} \tag{4.4}$$

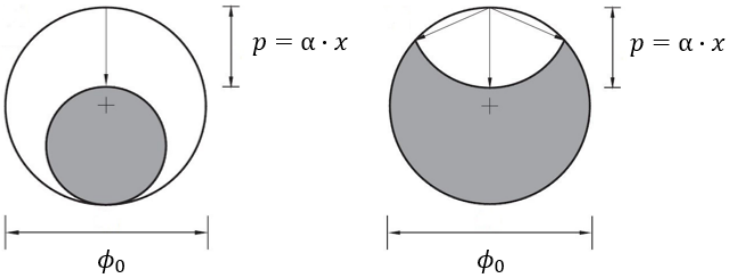

(a) *(b)*

Fig. 4.3 Models for the shape of residual cross-section (a) From Rodriguez et al. [159]*; (b) From Val and Melchers* [169]

In the model from Val and Melchers [169] the minimum residual area is computed considering a single hemispherical pit affecting the cross-section, as illustrated in Fig. 4.3b. The associated minimum residual area can be evaluated using eq. (4.5):

$$A_{res,min} = \begin{cases} \frac{\pi \cdot {\phi_0}^2}{4} - A_1 - A_2 & if \quad p \le \frac{\sqrt{2}}{2} \cdot \phi_0 \\ A_1 - A_2 & if \quad \frac{\sqrt{2}}{2} \cdot \phi_0 \le p \le \phi_0 \\ 0 & if \quad \phi_0 \le p \end{cases} \tag{4.5}$$

where:

$$A_1 = \frac{1}{2} \cdot \left[\theta_1 \cdot \left(\frac{\phi_0}{2} \right)^2 - a \cdot \left| \frac{\phi_0}{2} - \frac{(p)^2}{\phi_0} \right| \right] \tag{4.6}$$

$$A_2 = \frac{1}{2} \cdot \left[\theta_2 \cdot (p)^2 - a \cdot \frac{(p)^2}{\phi_0} \right] \tag{4.7}$$

$$a = 2 \cdot p \cdot \sqrt{1 - \left(\frac{p}{\phi_0} \right)^2} \tag{4.8}$$

$$\theta_1 = 2 \cdot arcsin\left(\frac{a}{\phi_0} \right) \tag{4.9}$$

$$\theta_2 = 2 \cdot arcsin\left(\frac{a}{2 \cdot p} \right) \tag{4.10}$$

Both the reported models base the evaluation of the minimum residual cross-sectional area on the maximum pit depth p, as expressed from eq. (4.3). In Fig. 4.4a, the variability of the residual-to-sound cross-sectional area with the ratio p/ϕ_0 is presented.
Clearly, the model from Rodriguez et al. [159] provides more severe estimations of the minimum residual cross-sectional area of corroded rebars. Tracing back the dependence of the maximum pit depth on the average mass loss ratio, graphs of Fig. 4.4b,c can be proposed, which highlight the variability of the residual-to-sound cross-sectional area due to variations of the mass loss ratio and of the pitting factor.
Regarding ultimate tensile strain of rebars, its reduction due to corrosion results from the interaction of different phenomena, as mentioned before. Herein, this reduction is modeled in a phenomenological way, considering simplified models which use as input only the minimum residual-to-sound cross-sectional area ratio of the corroded bars.

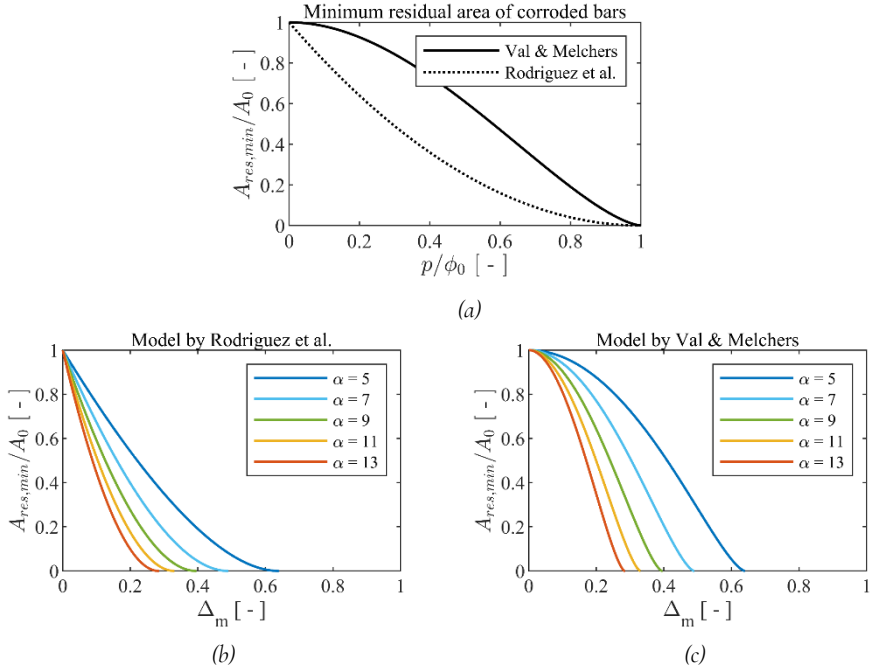

Fig. 4.4 Comparison of models for the shape of residual cross-section (a) Variability of residual-to-sound cross-sectional area with the ratio p/ϕ_0; (b) Variability of residual-to-sound cross-sectional area with the relative mass loss Δ_m, considering the model from Rodriguez et al. [159]*; (c) Variability of residual-to-sound cross-sectional area with the relative mass loss Δ_m, considering the model from Val and Melchers* [169].

In particular, the considered models are those from Coronelli and Gambarova [51] (expressed by eq. (4.11)), Biondini and Vergani [170] (expressed by eq. (4.12)), and Finozzi et al. [56] (expressed by eq. (4.13)).

Coronelli and Gambarova [51]

$$\varepsilon_{su,\ corr} = \varepsilon_{sy} + \left(\varepsilon_{su} - \varepsilon_{sy}\right) \cdot \left[1 - \frac{1-\left(\frac{A_{res,\ min}}{A_0}\right)}{\alpha_{pit}^{max}}\right] \tag{4.11}$$

Biondini and Vergani [170]

$$\varepsilon_{su,\ corr} = \begin{cases} \varepsilon_{su} & if\ 1 - \left(\frac{A_{res,\ min}}{A_0}\right) \leq 0.016 \\ \varepsilon_{su} \cdot 0.1521 \cdot \left[1 - \left(\frac{A_{res,\ min}}{A_0}\right)\right]^{-0.4583} & if\ 1 - \left(\frac{A_{res,\ min}}{A_0}\right) > 0.016 \end{cases} \tag{4.12}$$

Finozzi et al. [56]

$$\varepsilon_{su,\ corr} = \varepsilon_{su} \cdot e^{-0.032 \cdot 100 \cdot \left(\frac{A_{res,\ min}}{A_0}\right)} \tag{4.13}$$

In Fig. 4.5a comparison between the aforementioned models is proposed, in which the ratio between residual and sound ultimate tensile strain is plotted against the residual-to-sound cross-sectional area ratio, considering a sound value of the ultimate tensile strain of the rebars equal to $\varepsilon_{su} = 120‰$. The parameter α_{pit}^{max} in eq. (4.11) can assume values in the range 0 ÷ 0.5 and it controls the slope of the linear law proposed by Coronelli and Gambarova reported in Fig. 4.5. In all the calculations performed throughout the present work, a value $\alpha_{pit}^{max} = 0.5$ has been assumed.

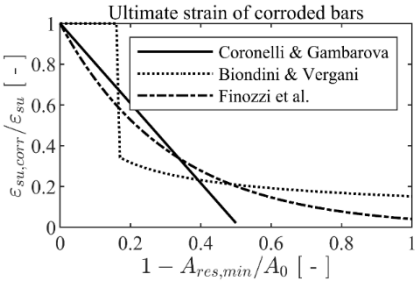

Fig. 4.5 Comparison of models for the residual ultimate tensile strain of corroded rebars, as a function of the residual-to-sound cross-sectional area ratio. Curves have been obtained considering a sound value of the ultimate tensile strain of the rebars equal to $\varepsilon_{su} = 120‰$.

In Fig. 4.6 the residual ultimate tensile strain for the corroded rebars is plotted for the three adopted models, considering various values of the sound ultimate tensile strain. Indeed, it can be appreciated the variability of results which are obtained by varying this latter parameter.

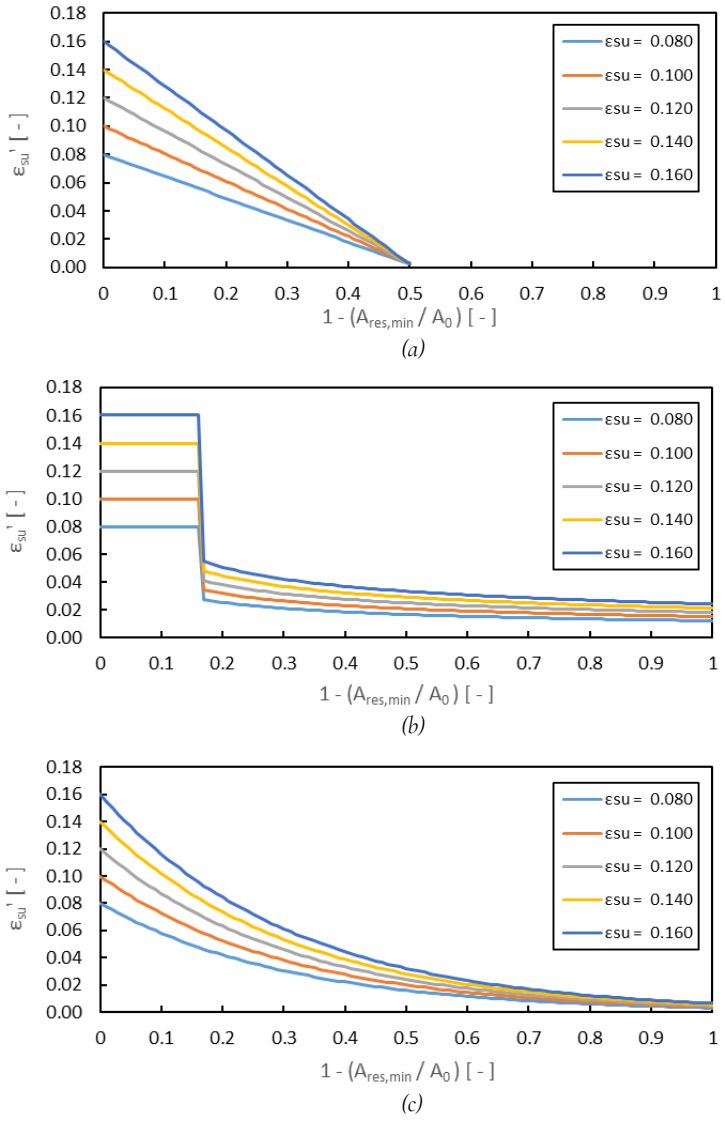

Fig. 4.6 Influence of the original sound value of ultimate tensile strain on its residual counterpart for corroded rebars, considering (a) Model from Coronelli and Gambarova [51]; *(b) Model from Biondini and Vergani* [170]; *(c) Model from Finozzi et al.* [56].

4.3 MODELLING RESPONSE OF UNCORRODED BEAMS

4.3.1 PREMISE

The studied uncorroded beams are the specimens RC-1 and RC-2 of the experimental campaign presented in Chapter 3. For both the specimens the test continued up to the reaching of a quite high value of the target midspan deflection, corresponding to a displacement ductility demand higher than $\mu_{\delta,d} = 12$. Despite extensive damage including spalling of the concrete cover in the constant moment zone was observed, no reduction of the bending strength was observed. The experimental results for the uncorroded beams served as references in the performed analyses to check the capabilities of the adopted modelling strategies to correctly predict the response of uncorroded members.

In the analyses presented in this chapter, the following material properties have been adopted: concrete compressive strength $f_c = 45MPa$; concrete tensile strength $f_{ct} = 2MPa$; steel elastic modulus $E_s = 206000MPa$; steel yielding strength $f_y = 520MPa$; steel hardening ratio $r_E = 0.0065$; ultimate tensile strain of sound rebars $\varepsilon_{su} = 120‰$.

4.3.2 MODELLING SECTION FAILURE MODE

The analytical failure mode domains proposed in Chapter 2 are herein used to analyze the section failure mode for the uncorroded specimens. Two types of graphs are built: i) domains obtained considering as ultimate condition for concrete that of the beginning of spalling (i.e., $\varepsilon_c = \varepsilon_{sp}$ on the outer fiber of concrete cover), see Fig. 4.7b; ii) domains obtained considering as ultimate condition for concrete that of core crushing (i.e., $\varepsilon_c = \varepsilon_{cu}$ on the outer fiber of concrete core), see Fig. 4.7c. Using these graphs, it is respectively possible to determine: i) whether the section reaches failure before or after the onset of cover spalling; ii) which is the section failure mode.

Regarding the adopted material constitutive laws, the developed formulation for failure mode domains described in Chapter 2 adopts a parabolic law followed by a linear softening branch for concrete, and elasto-plastic law for reinforcing steel, respectively illustrated in Fig. 4.8a and Fig. 4.8b. In the employed analytical formulation described in Chapter 2, tensile strength of concrete is neglected. The strain at peak compressive strenght is assumed equal to $\varepsilon_{c0} = -2‰$. The concrete law has been calibrated in order to provide a softening branch which reproduces the post-peak branch of the law from Popovics [154]. In the application of failure mode domains formulation, the beginning of spalling of compressed unconfined concrete has been assumed to occur at a strain value $\varepsilon_{sp} = -4‰$, according to Kent and Park [89] and Park and Ruitong [88]. Value of concrete ultimate strain in compression is taken equal to $\varepsilon_{cu} = -8‰$.

The graphs of failure mode domains for the undamaged beams are depicted in Fig. 4.9. They refer of course to both the uncorroded specimens RC-1 and RC-2, since they have identical section layout. In particular, Fig. 4.9a illustrates the domains configuration obtained considering the beginning of spalling as limit condition for concrete. The condition provided is of type "D", indicating that according to the model the beginning of concrete cover spalling (i.e., $\varepsilon_c = \varepsilon_{sp}$) can be effectively reached by the beam section,

with bottom steel yielded in tension and top steel elastic. Indeed, the beginning of spalling has been observed in the tests. For the domains configuration obtained considering the core crushing as ultimate condition for concrete, Fig. 4.9b, the predicted failure mode for the beam section is of type "D", indicating a failure by crushing of the core concrete with the bottom steel yielded in tension and the top steel elastic.

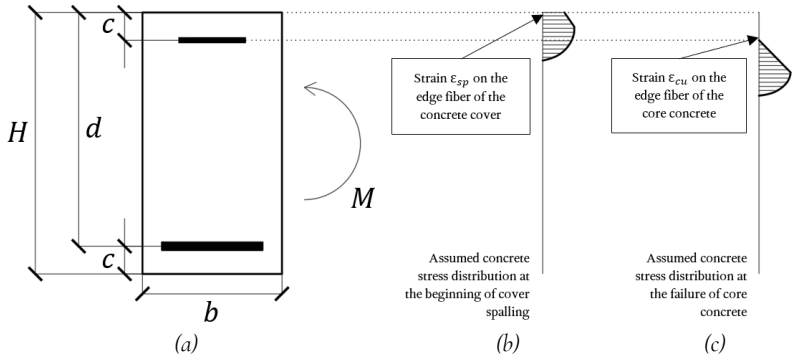

Fig. 4.7 (a) Considered section layout; (b) Concrete stress distribution at beginning of cover spalling; (c) Concrete stress distribution at failure of core concrete

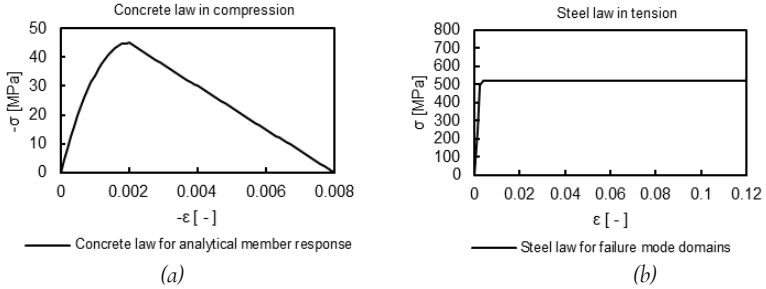

Fig. 4.8 Constitutive laws used for the analysis of the studied beams using the failure mode domains formulation proposed in Chapter 2 (a) Unconfined concrete; (b) reinforcing steel

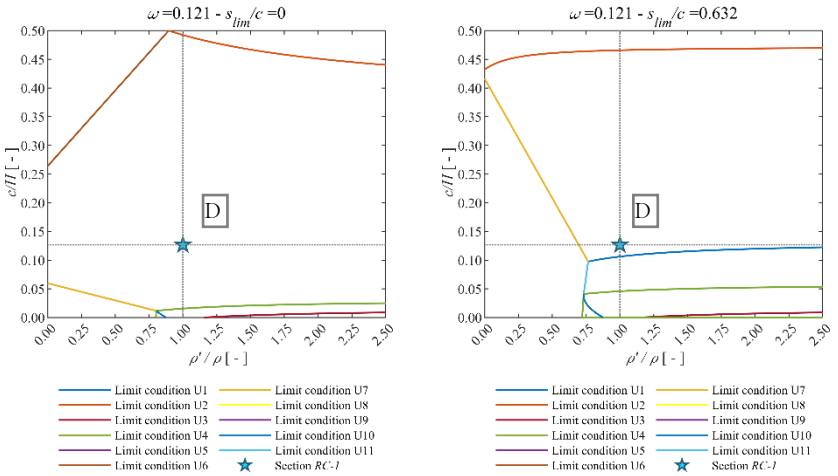

Fig. 4.9 Domains for the identification of the ultimate condition of the uncorroded beams (a) Limit for concrete set at beginning of cover spalling (i.e., $\varepsilon_c = \varepsilon_{sp} = -4‰$ at the outer fibers of the cover); (b) Limit for concrete set at crushing of core (i.e., $\varepsilon_c = \varepsilon_{cu} = -8‰$ at the outer fibers of the core).

The provided ultimate conditions for the two investigated stages suggest that the beam sections should be able to reach the stage of onset of cover spalling and then continue the loading process till a complete crushing of the core concrete would determine the ultimate condition for the member. This type of predicted failure mode is in good agreement with the response observed in the tests.

4.3.3 Modelling member response

Analytical modelling

A first step in analyzing the global member behaviour of uncorroded beams has been performed using an analytical approach for the estimation of the force-displacement response curve. This approach is described in detail in Appendix C and is based on integration of curvatures along the beam axis. The calculations have been performed using the hypothesis that the deformed configuration is not so different from the undeformed one, i.e., geometric non-linearities have not been considered. The scheme for the loading and boundary conditions which has been initially used is presented in Fig. 4.10a. Side appendices as well as the self weight of the beam were taken into account. According to the adopted loading and support conditions, the section at beam midspan is the one subjected to the highest value of bending moment. As a consequence, the section at midspan would be the first one to reach failure.

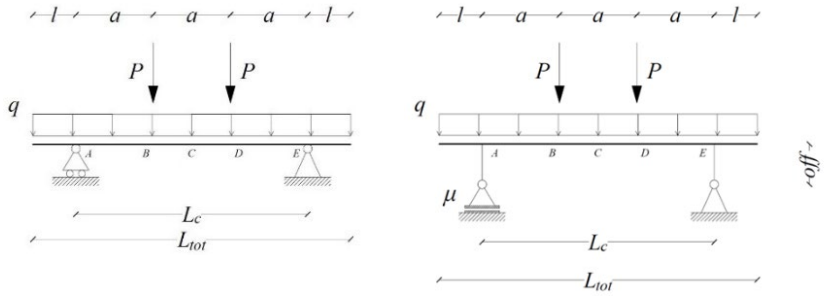

(a) (b)

Fig. 4.10 Schemes for the analysis of the studied beams (a) Basic reference scheme; (b) Scheme enhanced for considering friction and offset at supports

The member response can be described considering a series of consecutive stages for the section at midspan, corresponding to increasing values of member deflection at midspan. Four stages corresponding to significant conditions for the flexural behaviour of midspan section were considered, namely: i) flexural cracking; ii) flexural yielding; iii) onset of concrete cover spalling; iv) flexural failure. For the evaluation of the three latter conditions, the adopted procedures were inspired by approaches for estimating the yielding and failure conditions described in Chapter 2. An additional possible stage has also been taken into account, corresponding to the occurrence of shear cracking in the shear spans.

To summarize, the member response has been modelled considering a total of five possible different stages for the sectional behaviour of the section at beam midspan. Concerning the material constitutive laws, the concrete has been considered as unconfined and modeled with the same constitutive law adopted in section 4.3.2. For modelling reinforcing bars behaviour, a law composed by an initial elastic branch followed by a linear post-yielding branch with hardening has been employed, using a hardening ratio $b = 0.065$. For the sake of completeness, the adopted constitutive laws are depicted in Fig. 4.11.

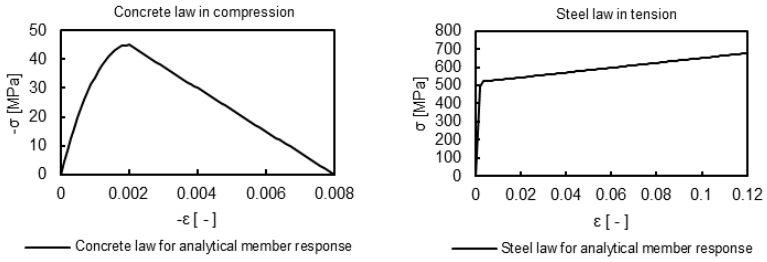

(a) (b)

Fig. 4.11 Constitutive laws used for the analytical calculation of the member response using the procedure described in Appendix C (a) Unconfined concrete; (b) reinforcing steel

By using the procedure described in Appendix C the analytical estimation of force-displacement curve for the uncorroded members have been obtained, which are presented in Fig. 4.12 together with the experimental response curve recorded for beam RC-2, provided for comparison. The obtained analytical response contains all the possible stages considered in the analysis. Flexural cracking is followed by the occurrence of shear cracking in the shear spans, which occurs before the yielding of the bottom reinforcement. After the yielding, the midspan section reaches the onset of compressed concrete cover spalling, and then continues to deform till its ultimate condition.
In the performed calculation, the ultimate stage is associated to a failure mode for the midspan section of type "D" according to the classification proposed in Chapter 2, i.e., a concrete core failure with bottom steel yielded in tension and top steel elastic. The calculated deformation capacity of the beam is quite higher than the maximum target deflection adopted in the experiments. It is possible that the actual ultimate deformation capacity of the tested uncorroded beams were higher than the maximum achieved deflection, since no strength drop has been recorded in the tests.

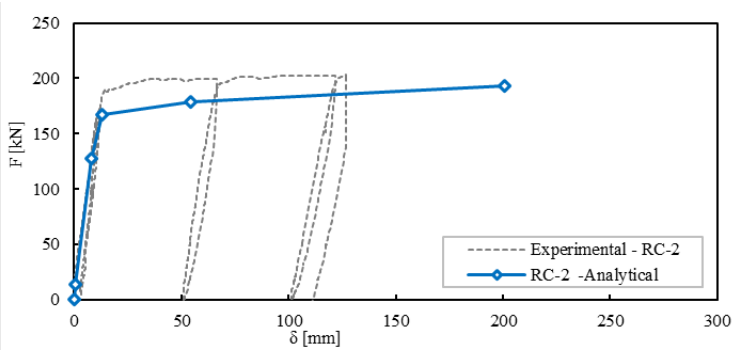

Fig. 4.12 Analytical response obtained for the uncorroded beams neglecting friction at supports

Some considerations are worth to be done also regarding the calculated bending strength of the uncorroded specimens. In fact, the obtained simulated response presents a bending strength which is significantly lower than that measured in the experiments, for both the yielding stage and the stage of onset of cover spalling. This discrepancy may be attributed to simplifications adopted in the modelling procedure, or in differences between assumed and actual values of material properties. However, the values adopted in the analysis for both concrete strength and steel yielding strength are equal or even higher than those experimentally measured and reported in Chapter 3. So, an additional possible explanation may be related to some phenomena which contributed to increase the experimentally measured strengths. Among various causes, one of the options relies on the possible presence of friction at supports and at loading points, which may have influenced the response of the tested specimens. Actually, for experimental tests performed by Rodriguez et al. [159], the Authors reported that in order to correctly compare measured and calculated strengths it has been necessary to take into account effects due to friction between the specimens and the supports, which had influenced

the structural response. In the present case, possible effects due to friction at the supports were introduced in the adopted modelling approach, by modifying the support scheme as depicted in Fig. 4.10b. In particular, a vertical support with horizontal friction was introduced at one of the support points of the beam. Moreover, offset between the actual position of the support and the beam axis was modeled, assuming it equal to half the beam height, i.e., $off = \frac{H}{2} = 150mm$. This choice of course does not aim to replicate the actual physical condition as it was for the beams tested with the adopted experimental setup, since, for example, no friction effect has been computed at the loading points. The adopted arrangements are rather a tentative to take into account of the overall friction effects in a simplified phenomenological way.
The introduction in the calculation scheme of both a non-null friction coefficient μ and of an offset off of beam axis generates a compressive axial load N acting in the beam central span, which can be expressed as:

$$N = \mu \cdot P \tag{4.14}$$

The resisting bending moment $M_{R,c}$ at midspan obviously benefits from the introduction of a compressive axial load, increasing depending on the load amount:

$$M_{R,c} = M_{R,c}(N) = M_{R,c}(\mu) \tag{4.15}$$

Moreover, the acting bending moment at midspan $M_{E,c}$ experiences an increase due to the combined effect of the offset and the axial load.
It can so be expressed as:

$$M_{E,c} = P \cdot (a - \mu \cdot off) + q \cdot \left(\frac{3}{2} \cdot a + l\right) \cdot \left(\frac{3}{4} \cdot a - \frac{1}{2} \cdot l - \mu \cdot off\right) \tag{4.16}$$

Accordingly, the total load F due to concentrated forces P can be expressed in turn as a function of the bending moment at midspan $M_{E,c}$ as follows:

$$F = 2 \cdot \frac{M_{E,c} - q \cdot \left(\frac{3}{2}a + l\right) \cdot \left(\frac{3}{4}a - \frac{1}{2}l - \mu \cdot off\right)}{a - \mu \cdot off} \tag{4.17}$$

Different values of the friction coefficient have been considered and an illustration of the obtained response curves are provided in Fig. 4.13. As can be seen, the introduction of friction effects in the modelling approach indeed allows to obtain higher bending strengths, comparable with those observed experimentally. As the friction coefficient increases, so does the axial load generated in the span of the beam between the two supports. Accordingly, the bending strength of the midspan section increases, leading to a higher member strength. Moreover, with higher axial load the section failure modes changes, so that for values of friction coefficient equal to or higher than $\mu = 0.4$, failure mode "E" is achieved instead of "D". It can also be seen that, since the shear cracking strength also increases with the axial load, the shear cracking occurs for higher and higher values of applied force, until it is no longer taken into account, as the level of applied load required to generate the shear cracking becomes greater than the load that induces yielding of the bottom reinforcement. Considering the values for material parameters reported in section 4.2, the best fit with the experimental results is obtained considering a friction coefficient $\mu = 0.3$.

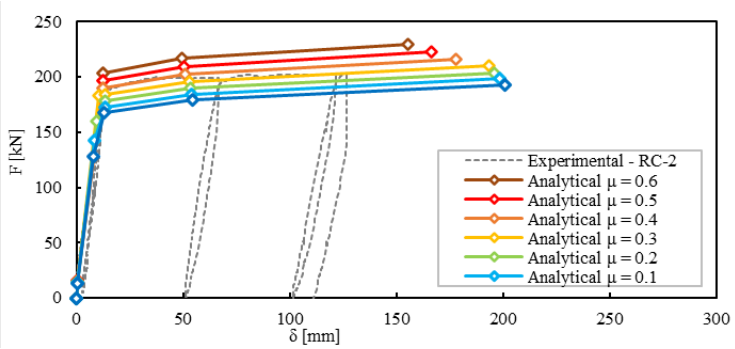

Fig. 4.13 Analytical response for uncorroded beams considering different values of the friction coefficient

Of course, by adopting different values for material properties or different calculation schemes other than that reported in Fig. 4.10b, different optimal values for the friction coefficient may be found. In particular, the optimal value of the friction coefficient increases by increasing the steel yielding strength, the amount of bottom longitudinal reinforcements, the offset at supports and the length of the side appendices of the beam. On the other hand, the optimal value of the friction coefficient would decrease by increasing the self-weight of the beam. The considered analytical modelling strategy is indeed useful to provide a first glimpse on the behaviour of the analyzed uncorroded beams.

Although, some of its characteristic features may also result in some limitation of its application, for example in case more complex material constitutive laws would be needed to be adopted, or in case the modelling of cyclic response of the specimens would be wanted to be addressed. In order to overcome these and other possible issues, numerical modelling approaches based on finite element analyses can be adopted.

Numerical modelling

In the present research, a numerical modelling strategy which makes use of fiber-based modes has been adopted. This kind of modelling strategy has been chosen for two main reasons. The first deals with the fact that such an approach would constitute a natural and more powerful extension of the previously adopted analytical procedure for modelling members response. The second reason lays on the fact that since these numerical approaches are widely employed in engineering practice, it is useful to test their capabilities as predictive tools, using the available experimental data for comparison. In this work, numerical simulations have been performed using the OpenSees framework [71] within the environment provided by the pre- and post-processing software STKO [72]. The beam members were modelled using displacement-based fiber beam-column elements, so that the structural behaviour is directly dependent on the behaviour of the beam sections. Shear deformations have been not computed in the adopted numerical approach.

Concerning the material constitutive laws, models depicted in Fig. 4.1 were used. In particular, to model concrete the uniaxial material *Concrete 04* has been used, which is

based on the Popovics law [154] for the behaviour in compression. In addition, to model the behaviour of concrete in tension, the same elastic modulus derived from Popovics law [154] in compression has been used. After the reaching of peak tension strength, a negative exponential law was employed so that a residual strength $f_{ctu} = 0.2MPa$ would be developed at an ultimate strain equal to $\varepsilon_{ctu} = 0.0005$. For steel rebars the uniaxial material *Steel 02* has been used, which implements the Menegotto-Pinto law [155] in the version proposed by Filippou et al. [156].

The analysis with monotonic loading has been performed by imposing a displacement history for the beam midspan to follow. To model the effects of friction at one of the supports, the support scheme represented in Fig. 4.10b was used, also considering the offset as previously done for the analytical calculation. A special boundary element has been used to model the friction support, i.e., the *implex-contact3D*, available in the STKO [72] library. In Fig. 4.14 the numerical response for uncorroded beams is presented, as obtained using a value equal to $\mu = 0.3$ for the friction coefficient.

The analysis was performed imposing the achievement of a very high deflection value at beam midspan, equal to $300mm$, in order to assess the numerical response of the beam at high imposed deflections. The obtained response curve is in agreement with that retrieved using the analytical calculation.

As mentioned before, the target displacement for the numerical analysis was intentionally chosen as quite large. It can be seen from Fig. 4.14 that no drop of strength is highlighted, even for very large values of midspan deflection. This behaviour can be explained considering the reinforcement layout of the beam sections and the adopted material properties. When the neutral axis depth increases due to concrete crushing and spalling in the compressed part of the midspan sections, the compressive strains on the top longitudinal reinforcement increase too. For very large curvatures, the concrete cover acts as completely spalled and the core concrete too experiences crushing. After core concrete fibers reach the ultimate concrete compressive strain, the contribution to the section equilibrium provided by the concrete starts to become negligible. This means that axial equilibrium of the section and bending strength are provided only by the top and the bottom reinforcements.

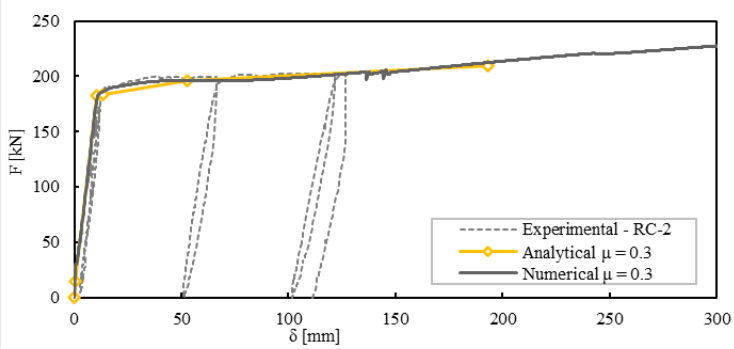

Fig. 4.14 Numerical and analytical response for the uncorroded beams, considering friction with $\mu = 0.3$.

The top reinforcement alone acts as the compressive chord of the section, while the bottom reinforcement behaves as the tensile chord. When then both the reinforcements are yielded, the section can continue to increase its bending strength due to steel hardening. Based on the adopted constitutive law, this behaviour can continue indefinetely till steel does not reach its ultimate tensile strain, so the strength could continue to increase while the deflection increase. In reality, such a condition often cannot take place, due to the occurrence of phenomena not considered by the model, e.g., buckling of the compressed reinforcement. In practice, when the outer fiber of the core concrete reaches its ultimate compressive strain, the section is considered to have reached an ultimate condition, even if no drop of strength is recorded.
For a more comprehensive analysis of the obtained numerical response, Fig. 4.15 presents a comparison with both the uncorroded beams RC-1 and RC-2, considering friction at supports. Despite the slightly differences between the two experimental curves, their peak strength is similar, as reported in Chapter 3.
A more detailed analysis of the combined effects of friction and tensile strength of concrete is proposed in Fig. 4.16, with particular regards to the early stages of the specimen response. The numerical response obtained neglecting both friction and concrete tensile strength is illustrated in Fig. 4.16a. It can be seen that, besides underestimating the experimental response in the initial branch, the stiffness of the numerical response is quite similar with the experimental one observed for the unloading and reloading branches, being representative of the member stiffness in a cracked condition. By introducing a value $f_{ct} = 2MPa$, Fig. 4.16b, the flexural cracking strength is quite well represented, while the post-cracking response is still underestimated.

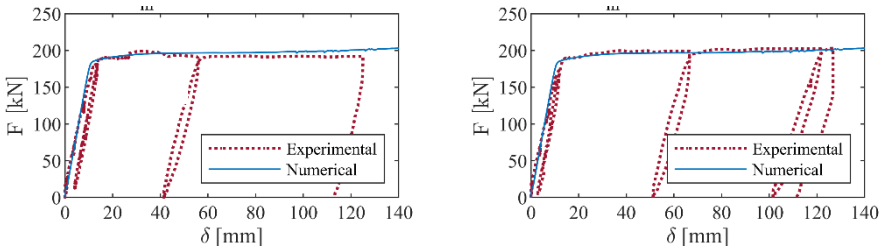

Fig. 4.15 Numerical force-displacement curves for uncorroded specimens obtained according to the scheme of Fig. 4.10b, i.e., considering friction and offset. Friction coefficient $\mu = 0.3$ (a) Beam RC-1; (b) Beam RC-2

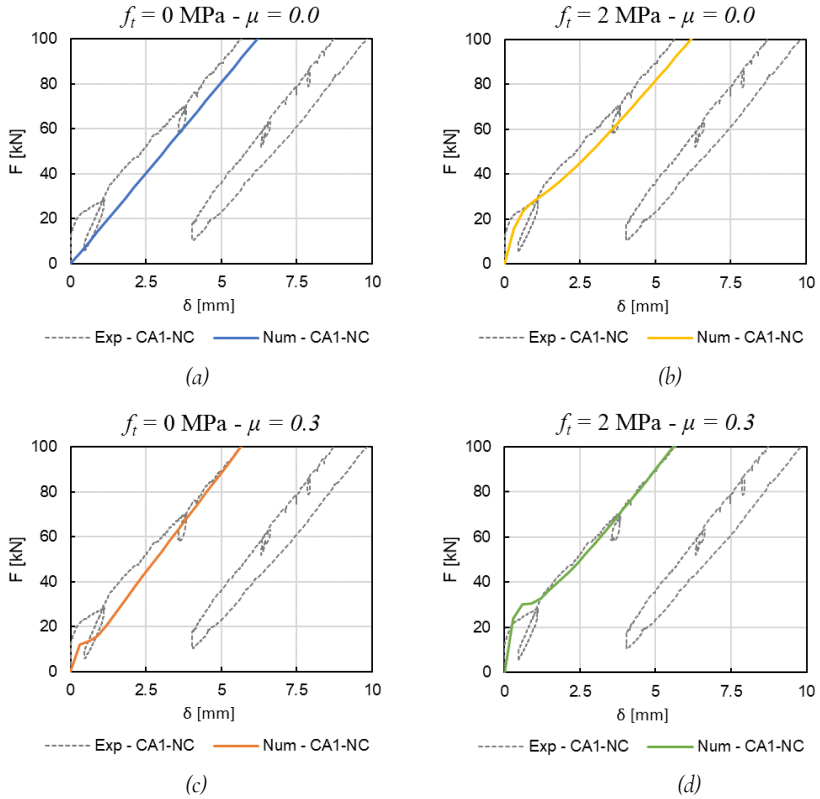

Fig. 4.16 Effect of concrete tensile strength and support friction on the early stages of simulated responses (a) Response neglecting tensile strength and friction; (b) Response considering only the tensile strength of concrete, with $f_{ct} = 2MPa$; (c) Response considering only friction with $\mu = 0.3$; (d) Response considering $f_{ct} = 2MPa$ and $\mu = 0.3$. In all cases the following values for other material parameters have been used: $f_y = 520MPa$, $f_c = 45MPa$, $f_t = 650MPa$, $E_s = 206000MPa$, $\varepsilon_{su} = 120‰$.

It interesting to note in Fig. 4.16c that the introduction of the arrangements adopted to consider friction effects produces a double consequence: i) the tangent stiffness of the curve increase as the load increase, due to the presence of friction at the support; ii) the initial stiffness is quite high, till to the achievement of a certain load value, corresponding to cracking strength of the compressed RC section with axial load. This latter consequence is due to the use of a non-null value of the friction and of the offset at the supports. In fact, the combined presence of the offset and of the friction induces an additional contribution to the resisting bending moment, which needs to be first overcome in order for the friction support to start sliding horizontally. The response obtained considering both the friction effects and the tensile strength of concrete is then presented in Fig. 4.16d. It can there be seen that the post-cracking branch of the experimental response is very well represented by the curve obtained by numerical analysis. The chosen optimal values for the friction coefficient and for the concrete tensile strength of uncorroded beams are of course dependent on the choices made in

assuming the values for other relevant material parameters involved. Moreover, the overall numerical response illustrated in Fig. 4.15 may vary significantly with the variation of some material parameters.

In order to analyze this aspect, a sensitivity analysis has been performed to assess the influence of the variability of different parameters on the numerical response obtained for the uncorroded beams. In particular, in Fig. 4.17a the effects of variability of steel yielding strength are addressed, showing that the bending strength of the specimen increases with an increase in steel yielding strength.

This increase in strength appears to be related to all the stages of the response, since the post-yielding branches of the various curves are almost vertically translated one to the other. On the other hand, variability of the concrete compressive strength would result in a very slight variation of the response curve, as illustrated in Fig. 4.17b. The most relevant influence is on the peak strength, which is slightly increased as the concrete compressive strength increases. It can also be appreciated that for high values of the concrete strength, the numerical response is characterized by some oscillations after the point of peak bending strength is reached. This can be explained by the fact that when the outmost top concrete fibers of the section experience softening, the post-peak loss of strength is greater the higher is the compressive strength of concrete. Another parameter which can greatly influence the global numerical response is the hardening ratio $b = E_h/E_s$ of the reinforcing steel, defined as the ratio between the post-yielding tangent modulus E_h and the initial tangent modulus E_s, i.e., the Young's modulus of the reinforcing steel. The effects of variability of this parameter are represented in Fig. 4.17c. Indeed, it can be seen that the post-yielding branch of the response tends to increase its slope the higher the hardening ratio. In the cases of low or even null hardening ratio, the response shows a post-peak softening branch, which eventually reaches a plateau at high deflection values. This phenomenon is due to the loss of strength induced by the crushing and spalling of the concrete cover, numerically simulated by the softening experienced by the most compressed concrete fibers of the section.

In the cases with higher hardening ratio, this loss of strength is instead compensated by the increase in bending strength provided by the hardening of the bottom steel and the subsequent increase in compressive stress in the elastic top steel. If steel hardening is non-null, then at further stages of the response when both the top and bottom reinforcement are yielded and the concrete contribution is not more relevant the bending strength of the section would continue to increase, as previously pointed out and shown in Fig. 4.14.

The last parameter considered for the sensitivity analysis is the friction coefficient, whose influence on the simulated member response is shown in Fig. 4.17d. The results are indeed similar to those obtained for the analytical modelling, as reported in Fig. 4.13. Higher values of the friction coefficient provide higher values of the bending strength of the member, due to the combined effect of increase of the axial load and increase in the bending moment contribution due to the offset. In this sense, the overall effect of the introduction of friction may seem similar to that of an increase in yielding strength of the steel.

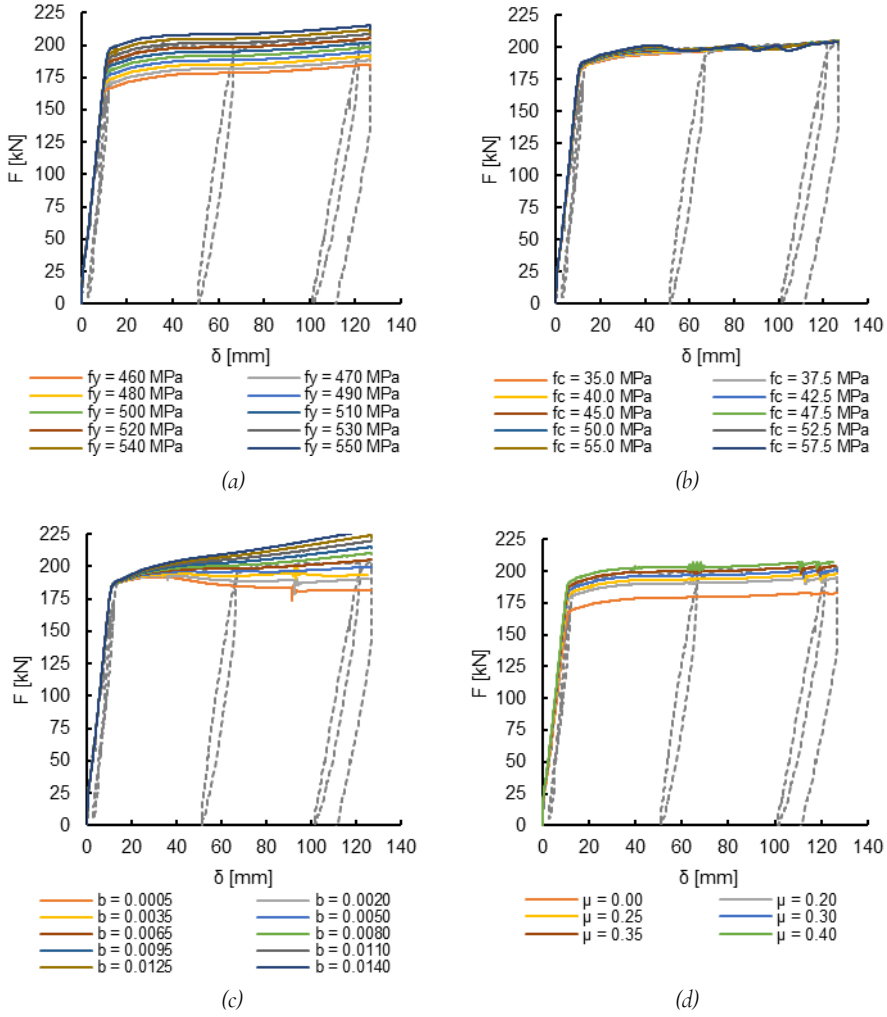

*Fig. 4.17 Sensitivity analysis for assessing the influence of different parameters on the numerical response obtained for uncorroded beams (a) Influence of steel yielding strength; (b) Influence of concrete compressive strength; (c) Influence of steel hardening, expressed as ratio **b** between post-yielding and elastic tangent modulus; (d) Influence of friction coefficient applied at the support.*

However, an additional different effect is observed due to the introduction of friction, namely, a progressive increase in tangent stiffness in the branch of the response after the flexural cracking but prior to reinforcement yielding. In fact, as already mentioned, the post-cracking stiffness of the member tends to increase while the applied load increases, due to the presence of friction at the support.

A last aspect worth to be addressed regards the capability of the adopted numerical modelling strategy to represent the behaviour of the tested specimens under cyclic

loading. In order to model the unloading and reloading branches which the uncorroded beams have undergone during the experimental tests, a suitable strategy for the application of loads was adopted in the numerical analyses. In particular, every loading and unloading branch has been simulated as an individual part of the analysis. The loading branches were modeled setting the target deflection to be reached by the midspan section of the beam, i.e., adopting a so called "displacement controlled" loading approach. Conversely, for the unloading branches the analyses were run setting that the recorded total applied force would decrease till reaching a zero value, so adopting a "force controlled" loading approach. These choices appear suitable for reproducing the cyclic response of the tested beams, since they aim to resemble the choices made governing the actuator during the tests. The numerical responses considering the cyclic loading are reported in Fig. 4.18. The material parameters and friction coefficient are the same as used for obtaining the results presented in Fig. 4.15.
Slightly differences between numerical responses obtained for beams RC-1 and RC-2 are of course due solely to the differences in the imposed displacement histories. It can be seen that not only the peak strength but also the unloading and reloading branches are well captured by the numerical response.

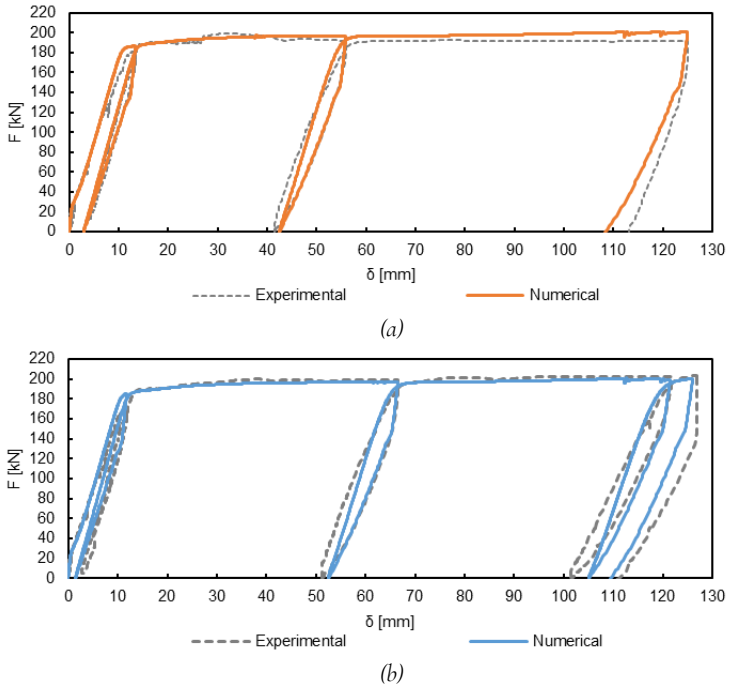

Fig. 4.18 Cyclic numerical response for uncorroded beams, considering $f_y = 520MPa$, $f_c = 45MPa$, $f_t = 650MPa$, $E_s = 206000MPa$, $\varepsilon_{su} = 120‰$, $f_{ct} = 2MPa$ *and* $\mu = 0.3$ *(a) Beam RC-1; (b) Beam RC-2.*

It is particularly significant to highlight that in the unloading branches, the double-sloped trend is quite well captured, i.e., a clear change of stiffness in the unloading

branch is observed in the numerical responses, as reported in the experimental ones. In the numerical response curves, this behaviour results from the combined introduction of the friction and offset at the support. In fact, as the unloading phase starts, the support does not immediately start to slide back to its rest position, due to the opposing effect provided by the friction.
Of course, it is also important to point out that, since direct experimental information on friction at the supports and at loading points are lacking, it is not possible to assure that the underlying mechanisms occurred in the reality are similar to those implemented in the adopted modelling strategy. It is only possible to observe that the overall global response is well reproduced by the adopted model.

4.4 Modelling response of corroded beams from the first experimental series

4.4.1 Premise

Some of the modelling approaches adopted in the previous section for the analysis of uncorroded specimens have then been adopted for modelling the response of corroded beams tested in the first experimental series described in Chapter 3. This way, the possibility to extend the validity of those models also for the simulation of corroded RC members has been assessed. Based on the obtained results, considerations about modelling performances have been formulated and possible insights for their enhancement are proposed. The sections geometry and material properties of concrete were the same used for the analyses performed on uncorroded members. Regarding the description of characteristics of bottom longitudinal reinforcement, models and formulations recalled in section 4.2 have been adopted.

4.4.2 Modelling section failure mode

The analytical failure mode domains formulated in Chapter 2 and used for the study of uncorroded beams are herein proposed to analyze the failure mode in sections of corroded members. The corrosion level in longitudinal bottom rebars was expressed in terms of mass loss ratio Δ_m calculated as average on the whole beams. As a consequence, the same value of mass loss ratio was assigned to both the longitudinal rebars. The traditionally suggested value for the pitting factor $\alpha = 10$ was adopted [158], [167], while the Val and Melchers model [169] was used to compute the minimum residual cross-sectional area of corroded bars. For the computation of the residual ultimate tensile strain of corroded reinforcement, the model from Finozzi et al. [56] has been adopted. The obtained graphs of failure mode domains are illustrated in Fig. 4.19, Fig. 4.20, Fig. 4.21 and Fig. 4.22, for beams RC-C1, RC-C2, RC-C3 and RC-C4, respectively.
Specimen RC-C1 is characterized by the lowest corrosion level among the corroded specimens and the domains configuration obtained considering the beginning of spalling as limit condition for concrete provides an ultimate condition of type "D", indicating that the beginning of concrete cover spalling (i.e., $\varepsilon_c = \varepsilon_{sp}$) can be effectively reached by the beam section, with bottom steel yielded in tension and top steel elastic.

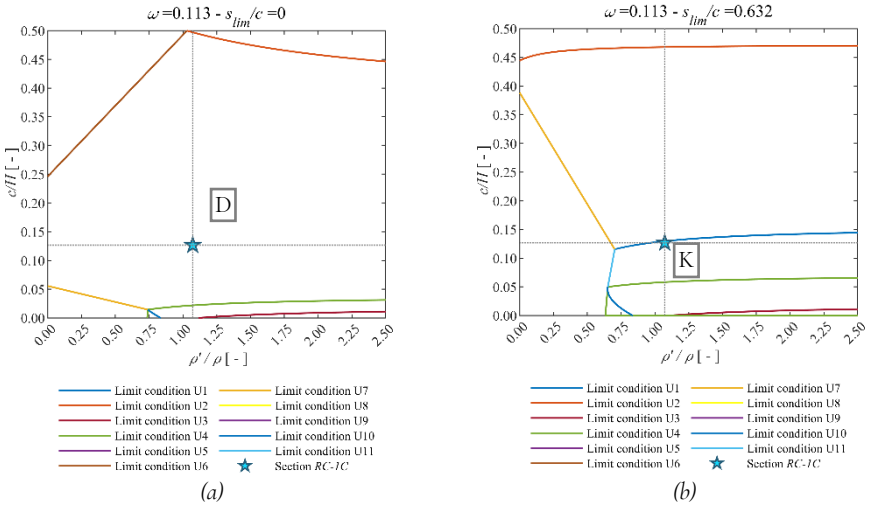

Fig. 4.19 Domains for the identification of the ultimate condition of corroded beam RC-C1 (a) Limit for concrete set at beginning of cover spalling (i.e., $\varepsilon_c = \varepsilon_{sp} = -4‰$ at the outer fibers of concrete cover); (b) Limit for concrete set at crushing of core (i.e., $\varepsilon_c = \varepsilon_{cu} = -8‰$ at the outer fibers of concrete core).

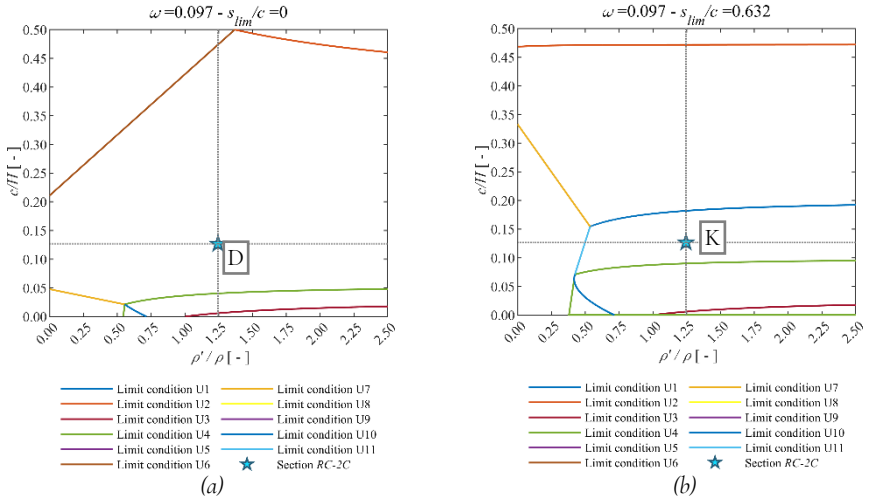

Fig. 4.20 Domains for the identification of the ultimate condition of corroded beam RC-C2 (a) Limit for concrete set at beginning of cover spalling (i.e., $\varepsilon_c = \varepsilon_{sp} = -4‰$ at the outer fibers of concrete cover); (b) Limit for concrete set at crushing of core (i.e., $\varepsilon_c = \varepsilon_{cu} = -8‰$ at the outer fibers of concrete core).

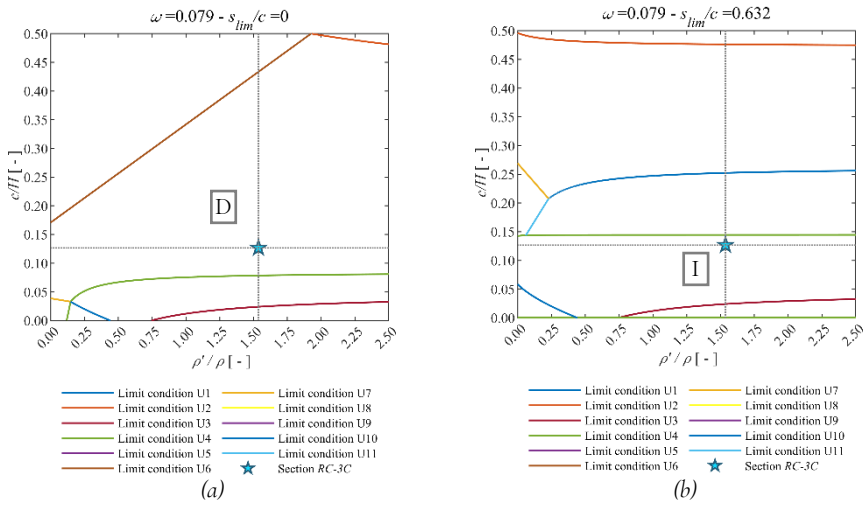

Fig. 4.21 Domains for the identification of the ultimate condition of corroded beam RC-C3 (a) Limit for concrete set at beginning of cover spalling (i.e., $\varepsilon_c = \varepsilon_{sp} = -4‰$ at the outer fibers of concrete cover); (b) Limit for concrete set at crushing of core (i.e., $\varepsilon_c = \varepsilon_{cu} = -8‰$ at the outer fibers of concrete core).

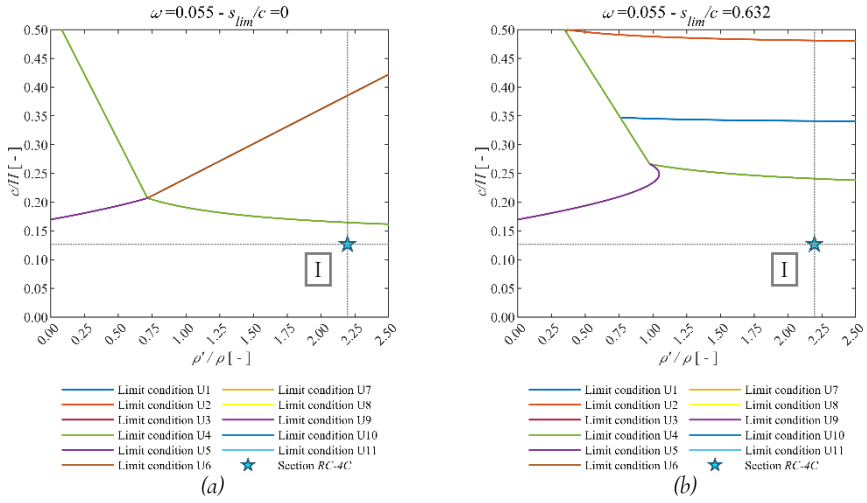

Fig. 4.22 Domains for the identification of the ultimate condition of corroded beam RC-C4 (a) Limit for concrete set at beginning of cover spalling (i.e., $\varepsilon_c = \varepsilon_{sp} = -4‰$ on the outer fiber of concrete cover); (b) Limit for concrete set at crushing of core (i.e., $\varepsilon_c = \varepsilon_{cu} = -8‰$ on the outer fiber of concrete core).

Accordingly, the analysis of failure domains suggests that specimen RC-C1 should have experienced a response characterized by the same stages of that observed for the uncorroded beams. In Fig. 4.20 the failure conditions predicted for beam RC-C2 are identified. The two identified conditions are respectively of type "D" and "K", for the two limit conditions set for concrete. This result indicates that, according to the model, the beam section would successfully reach the stage of the onset of cover spalling, but then would develop a failure due to steel rupture before the cover spalling process would have been completed. However, for beam RC-C2 it may be difficult to perform a straightforward comparison between the experimentally observed failure condition described in Chapter 3 and the flexural failure mode predicted by the models. In fact, the beam actually failed for a loss of anchorage in one of the longitudinal rebars, which was not at all related to the behaviour to the sections at midspan.
Domains for the ultimate conditions of beam RC-C3 are reported in Fig. 4.21, which indicates that the section would again develop a condition "D" considering the onset of spalling as limit condition for concrete. On the other hand, the failure condition of the section is identified as of type "I", i.e., due to bottom steel rupture with top steel elastic and the outmost concrete fiber in the range $-8‰ \leq \varepsilon_c \leq -4‰$. This combined information provided by the two graphs of Fig. 4.21 suggest that the beam section would start to experience crushing of the cover concrete, but soon after that the bottom reinforcing steel would reach its ultimate tensile strain. This behaviour is indeed quite similar to that observed in the experimental test of specimen RC-C3, for which the sections at midspan started to show crushing of the concrete cover, but soon after that the rupture of one of the corroded longitudinal rebars occurred.
Fig. 4.21 reports the graphs of domains for the identification of ultimate conditions for beam RC-C4. In this case, both the graphs indicate the achievement of the ultimate condition "I", meaning that the section would reach the failure by means of the rupture of the bottom longitudinal reinforcement even before concrete cover spalling can start to develop. The observed experimental behaviour for specimen RC-C4 described in Chapter 3 indeed seems to confirm the behaviour predicted by the failure mode domains.
In Table 4.1 a comparison is provided between the failure modes predicted through the analysis of failure mode domains and the experimentally observed conditions at the end of the test as retrieved from the information provided in Chapter 3.
The values for average mass loss ratio reported in Table 4.1 are those obtained computing the average on the whole beams. Indeed, it can be seen that a good agreement exists between the predicted failure and the observed condition, save for specimen RC-C2 for which a reliable comparison cannot be performed.
Despite its simplicity, the proposed analytical approach based on failure mode domains can then be taken as a useful tool for analyzing the response of beam sections, both in sound and in corroded conditions.

Table 4.1 Overview of behaviour for corroded beams of the first experimental series with comparison between observed and analytically predicted failure modes obtained using analytical failure mode domains

Beam	Δ_m [%]	Experimentally observed ultimate condition	Analytically predicted sectional failure mode
RC-C1	7.55	Concrete crushing at midspan with tensile reinforcement yielded	Nearly contemporary core concrete crushing and rupture of tensile rebars, with compressive rebars elastic
RC-C2	12.13	Debonding close to one support and loss of end anchorage of one longitudinal bottom rebar	Rupture of tensile rebars after the reaching of ultimate concrete compressive strain in the outer fiber of cover, with compressive rebars elastic
RC-C3	17.85	Rupture of bottom steel rebars at midspan after the beginning of concrete cover spalling	Rupture of tensile rebars after the beginning of concrete cover spalling, with compressive rebars elastic
RC-C4	22.94	Rupture of bottom steel rebars at midspan before the beginning of concrete cover spalling	Rupture of tensile rebars before the beginning of concrete cover spalling, with compressive rebars elastic

4.4.3 Modelling member response

The next step in the analysis of corroded members has involved the use of the numerical procedure introduced in section 4.3 for evaluating the force-displacement response curves of RC beams. Such procedure has been employed in order to evaluate its applicability for the analysis of members affected by reinforcement corrosion.

First, analyses have been performed modelling the effects of corrosion on reinforcing bar in the same way done for the failure mode domains, i.e., a value $\alpha = 10$ has been selected for the pitting factor; the model from Val and Melchers [169] has been used for modelling the shape of the minimum residual cross-sectional area of corroded bars; the model from Finozzi et al. [56] has been adopted for evaluating their residual ultimate tensile strain of rebars. In this first stage of the analyses, the values of mass loss ratio evaluated as average on the whole beams were again employed.

Simulations for the four examined corroded beams have been initially performed considering both the cases in which friction at supports is neglected or considered. In considering friction, it may be reasonable to assume that similar friction effects can be computed for all uncorroded and corroded specimens, since the type of supports adopted in the experiments were the same for all the tested beams. So, for the case in which friction was modeled, a value $\mu = 0.3$ for the friction coefficient was adopted, as

it had been retrieved and validated for the uncorroded beams. Results of the simulations are reported in Fig. 4.23 and Fig. 4.24, from which it can be seen how the relevance of friction effects depends itself on the bending strength of the specimens, being the friction-induced axial load proportional to the amount of the vertical applied loads. Accordingly, the difference between graphs presented in Fig. 4.23 and Fig. 4.24 is more significant for specimens RC-C1 and RC-C2, rather than for specimens RC-C3 and RC-C4, since the former present a higher bending strength.

From Fig. 4.24 it can be seen that the bending strength of corroded specimens is quite well represented in the numerical response curves obtained considering friction. A decreasing trend of strength is coherently observed with increasing values of the average mass loss ratio. Moreover, the values of peak strength are very well caught, especially for beams RC-C3 and RC-C4 which experienced the higher corrosion levels. Conversely, with regards to ultimate deformation capacity a different result is observed. In fact, besides the case of specimen RC-C1, for which an actual measure of failure deflection cannot be defined since no drop of strength was recorded, the numerically predicted deformation capacity for all the other corroded specimens overestimates the experimental one.

These results offer the opportunity to make some preliminary considerations with regards to the first aim of the proposed investigation, described in section 4.1. The satisfactory modelling performances achieved in terms of residual strength prediction well justifies the adoption of the considered strategies for modelling the characteristics of corroded reinforcement.

Indeed, this result supports the validity of the use of the adopted approaches in the engineering practice, for the assessment of residual strength of deteriorating structures. On the other hand, the observed poor performances in the estimations of deformation capacity may find an explanation on the fact that the adopted approaches where mostly developed and tested with special reference to modelling residual strength of deteriorated members. As a matter of fact, the issue of estimating deformation capacity for corroded structures began to receive deserved attention much later [108], [50] than the issue of strength assessment [171], [172]. In this context, despite in the recent years significant advances have been made in the understanding and modelling the phenomena which reduce the deformation capacity of corroded RC members [57], [161], the translation of this knowledge into simple, effective and reliable approaches to be used in engineering practice still lacks.

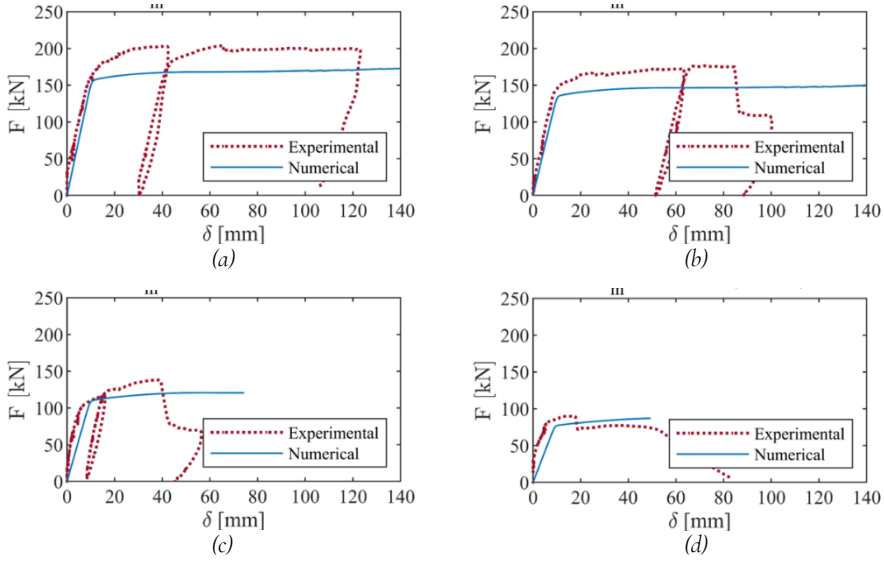

Fig. 4.23 Numerical response for corroded beams the first experimental series, obtained neglecting friction effects and considering a pitting factor $\alpha = 10$*, the Val and Melchers* [169] *model for the residual cross-sectional area of rebars and the model from Finozzi et al.* [56] *for the ultimate tensile strain of corroded bars.*

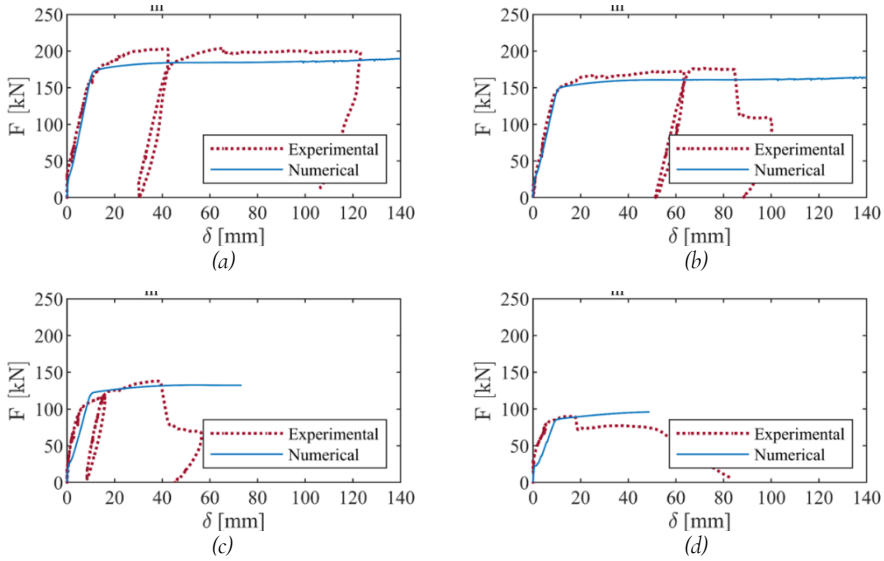

Fig. 4.24 Numerical response for corroded beams the first experimental series, obtained considering a friction coefficient $\mu = 0.3$*, a pitting factor* $\alpha = 10$*, the Val and Melchers* [169] *model for the residual cross-sectional area of rebars and the model from Finozzi et al.* [56] *for the ultimate tensile strain of corroded bars.*

4.4.5 First parametric analysis

The above considerations were of course drawn based on results obtained considering only some of the different possible choices with regards to the strategies for modelling characteristics of corroded steel. With the aim of expanding the database of obtained numerical results and of analyzing the influence on numerical response of different choices in modelling the characteristics of corroded reinforcement, a sensitivity analysis has been performed. Three modelling choices have been considered to be variable, namely: i) the choice of the pitting factor value; ii) the choice of the model for the shape of the residual cross-sectional area of corroded bars; iii) the choice of the model for the residual ultimate tensile strain of corroded bars. In Fig. 4.25 the different parameters and models considered in the sensitivity analysis are illustrated. The pitting factor has been made to vary in the range 5 ÷ 13, which is representative of values recorded in specimens which experienced accelerated corrosion [168]. The considered formulations adopted for modelling the shape of the residual cross-sectional area and the ultimate tensile strain of corroded bars have been presented in 4.2 and represent some of the models commonly suggested to be used in the engineering practice. The sensitivity analysis involved the simulation of beams RC-C3 and RC-C4, which actually experienced failure due to rupture of the reinforcement and so can be representative cases for the analyzed aspects.

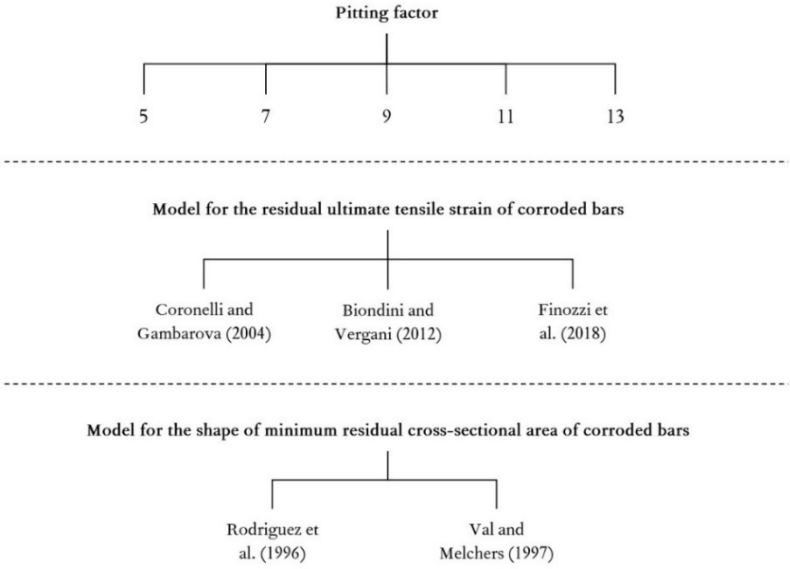

Fig. 4.25 Parameters and models considered in the first sensitivity analysis, performed for studying the influence of different choices for modelling the characteristics of corroded reinforcing bars on the deformation capacity of corroded beams obtained through the adopted numerical analysis procedure

Fig. 4.26 illustrates how the residual ultimate tensile strain for corroded bars vary with the variation of the pitting factor value and of the adopted models. A decreasing trend with increasing values of the pitting factor is clearly observed.

This variation is much more highlighted in the cases where the Val and Melchers [169] model is employed. On the other hand, when the model from Rodriguez et al. [159] is used, the decreasing trend is less pronounced since quite severe estimations of the residual cross-sectional area are obtained regardless of the adopted values for the pitting factor. The obtained values for the residual tensile strain reflect the behaviour observed in graphs of Fig. 4.4 and Fig. 4.6. For very low values of the residual cross-sectional area, such as those provided by the model of Rodriguez et al. [159] or those obtained with the model from Val and Melchers [169] for high pitting factors, some relevant phenomena can be observed. For both the models from Biondini and Vergani [170] and Finozzi et al. [56] the variability of ultimate strain is quite low, reflecting the behaviour illustrated in Fig. 4.6 for very low values of residual area. Conversely, for mid-to-low residual cross-sectional area the model from Coronelli and Gambarova [51] may return a null value of the residual ultimate strain, as occurs in most of the cases illustrated in Fig. 4.26c,d.

The comparison between the numerically simulated deformation capacity and the values observed in the experimental campaign for beams RC-C3 and RC-C4 is presented in Fig. 4.27, expressing the ratio $\delta_{u,model}/\delta_{u,exp}$ between numerical and experimental ultimate deflection values. A first glance at the graphs of Fig. 4.27 immediately highlights quite significant differences between the results obtained for beam RC-C3 and RC-C4. This fact may rise some attention, since the two specimens are characterized by not-so-different values of the global average mass loss ratio. However, such differences in the results can be easily explained considering that, for beam RC-C4, the locally-averaged mass loss ratio in the central portion of the beam (which governs the flexural strength and deformation capacity) is very much higher than the global average (see Table 3.5). Considering this, it appears that while for beam RC-C3 the corrosion level considered in the analyses was not so far from the actual one, for beam RC-C4 the computed corrosion level considered was way lower than the actual one, thus leading to the observed overestimation of the deformation capacity. This fact highlights the value of more locally defined information on the corrosion level to be used in the analyses. In the following, some observations are proposed regarding the difference in the results obtained using different models to describe the characteristics of the corroded steel.

Considering results obtained using the model from Val and Melchers [169] (Fig. 4.27a,b), it can be seen that the adoption of low-to-mid values for the pitting factor (i.e., values equal or lower than 9) leads in most the cases to an overestimation of the measured deformation capacity. Concerning the results obtained with the highest values of the pitting factor, different considerations can be done for the different used formulations for modelling the ultimate tensile strain of corroded rebars. In most the analyzed cases, the model from Coronelli and Gambarova [51] provided a null value of the ultimate tensile strain of the rebars, leading to an unacceptable result. It so appears that for mid-to-high corrosion levels, such as those observed in specimens RC-C3 and RC-C4, the model from Coronelli and Gambarova [51] needs to be adopted with some care, since it may provide quite severe underestimation of the deformation capacity. The model from Biondini and Vergani [170] provided ratio values always higher than the unity. For both the beams, the best results in terms of ratio of ultimate deflection have been achieved with the model from Finozzi et al. [56] using pitting factor $\alpha = 13$.

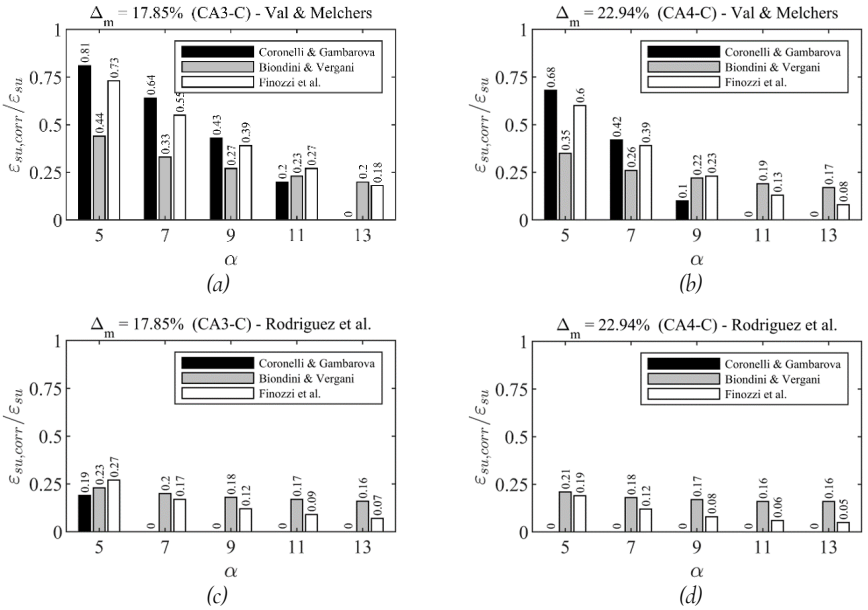

Fig. 4.26 Ratio between apparent ultimate tensile strain of corroded and sound steel rebars, for different models and values of the pitting factor, with $\varepsilon_{su} = 120‰$

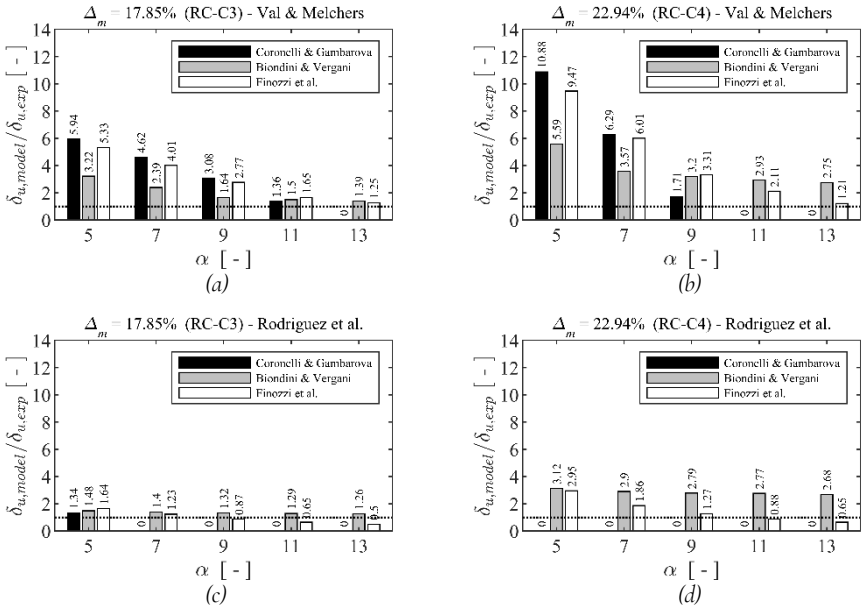

Fig. 4.27 Ratio between modelled and experimentally measured deformation capacity of corroded beams, for different models of ultimate steel strain and values of the pitting factor, with $\varepsilon_{su} = 120‰$

Considering the model from Rodriguez et al. [159] (Fig. 4.27c,d) much more severe estimations of the deformation capacity have been obtained, as expected. The use of the model from Coronelli and Gambarova [51] provided null values for ultimate deflection in most of the analyzed cases, even for the lowest values of the pitting factor. Results obtained with the model from Biondini and Vergani [170] show a quite good fit with the experimental ones in the case of beam RC-C3, while an overestimation of the capacity is observed for beam RC-C4. It can also be seen that for this model the deformation capacity ratio is very slightly dependent on the adopted values of the pitting factor, since for all the cases the residual cross-sectional area of the rebars is quite low due to the use of the model from Rodriguez et al. [159] (see Fig. 4.4). As a matter of fact, the residual cross-sectional area is so small that all the results belong to the last part of the law from Biondini and Vergani (see Fig. 4.6), where the variation of the ultimate tensile strain is almost negligible and a horizontal asymptote is being approached. Finally, the model from Finozzi et al. [56] provided in this case fairly good and safe-side estimations of the deformation capacity using mid-to-high values of the pitting factor.

The presented results showed how, even considering only corrosion effects on the characteristics of corroded rebars, a significant variability of results can be obtained by varying the adopted formulations and model parameters. Moreover, it has been shown that while traditionally suggested models for area reduction and values for the pitting factor can be adequate to predict residual strength of corroded members, they may not be as well suitable to simulate reduction of deformation capacity. With this regards, in the use of all the considered formulations for modelling ultimate tensile strain of corroded reinforcement, it appears clear that some care needs to be taken in choosing appropriate an value of the pitting factor and an appropriate model for the shape of the residual cross-sectional area, in order to obtain consistent results and to avoid gross under- or over- estimations of deformation capacity. First of all, regarding the area models it should be kept in mind the range of corrosion mass loss values upon which such models have been initially proposed and validated. As a matter of fact, beams RC-C3 and RC-C4 considered in the proposed analysis present quite high corrosion levels, and some doubts regarding the suitability of the model from Rodriguez et al. [159] may be raised. Secondly, from the general discussion of the obtained results it may seem to be suggested that in order to obtain good results for highly corroded beams, high values of the pitting factor (i.e., close to 13) should be adopted. This conclusion however, in the end it was proved wrong, or at least incomplete, after the examination of the results from the second parametric analysis, described in the next section.

4.4.6 Second parametric analysis

In order to address the third goal of the present investigation, declared in section 4.1, an additional aspect needs to be considered in the analysis of the results obtained from numerical simulations. In fact, all the previously presented results have been obtained defining the corrosion level by using average mass loss ratios computed as average on the whole beams. However, in several cases, it may be possible that more refined and local estimations of the corrosion level in terms of average mass loss would be available. In such cases, the consideration proposed above with regards to the use of the considered formulations and parameters values for modelling the characteristics of corroded reinforcement may not be still valid.
In order to provide some insights on this aspect, a set of analyses has been performed to study how the response obtained through the adopted numerical modelling procedure is influenced by the way with which the average mass loss is computed. To do so, it has been taken advantage from the fact that for the set of studied corroded beams the experimentally measured average mass loss has been computed in four different ways, defining the average mass loss at an increasingly local level (see Chapter 3). In particular, for the sake of clarity, it is worth to recall that the average mass loss had been computed as:

- Average on the whole beam (considering both the bars)
- Average on a single whole bar
- Average on a beam segment (considering both the bars)
- Average on a single bar segment

The beam segments have been defined in Chapter 3, dividing the clear length between the two supports in three segments of equal length.
The numerical simulations of the four beams of the first experimental series have been then performed considering the aforementioned four different ways of computing the average mass loss. In addition, the analysis of the influence of the way mass loss is computed has been performed considering also the variability of the pitting factor and of the formulation used to model the ultimate tensile strain of corroded bars. A summary of the variables considered in this second sensitivity analysis is given in Fig. 4.28. Values of the pitting factor in the range $5 \div 9$ were considered. This choice is motivated by the fact, observed in Fig. 4.26, that higher corrosion levels would require reduced pitting factor values to provide the same result in terms of deformation capacity.

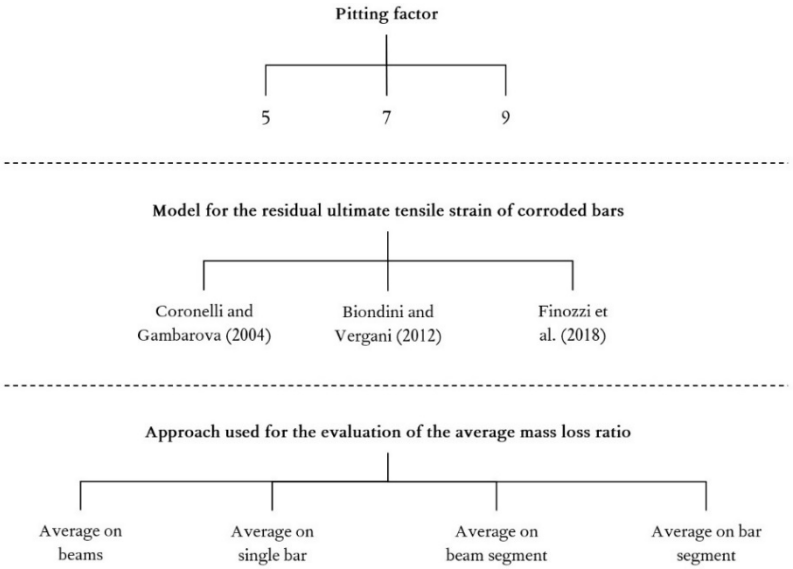

Fig. 4.28 Parameters and models considered in the second sensitivity analysis, performed for studying the combined influence of different choices for calculating the average mass loss and different choices for modelling the characteristics of corroded reinforcing bars on the deformation capacity of corroded beams obtained through the adopted numerical analysis procedure

The latter aspect is herein relevant, since more locally refined estimations of the corrosion level translates into higher maximum values of the average mass loss. In the performed analyses, characteristics of corroded rebars were modeled for each bar or each bar segment individually, depending on the chosen criteria for computing the average mass loss. Results of the sensitivity analysis in terms of force-displacement curves are reported for the four studied beams in Fig. 4.29, Fig. 4.30, Fig. 4.31 and Fig. 4.32. The three graphs reported in each figure refer to the three considered formulations used to model the ultimate strain of the corroded rebars. So, the curves presented in the three graphs of a figure are identical but for the value of the ultimate deformation capacity.
For the specimen RC-C1, whose results are reported in Fig. 4.29, no differences exist between the three presented graphs. This is due to the fact that in no one of the simulations the beam reached failure due to rupture of the reinforcement and so in all the cases the assigned target displacement was achieved. For all the numerical response curves a fairly good approximation of the experimental response is obtained, being the difference between the results quite slight. The greater difference in bending strength is recorded for the case of $\alpha = 9$ with the average mass loss computed on the bar segments, for which the numerically obtained bending strength is approximately 10% lower than the experimental one. Indeed, for corroded specimen RC-C1 the recorded peak strength is basically equal to that of the uncorroded specimens (see Chapter 3). Accordingly, any assumed reduction of cross-sectional area of bottom longitudinal rebars would result in an underestimation of the experimental measured strength.

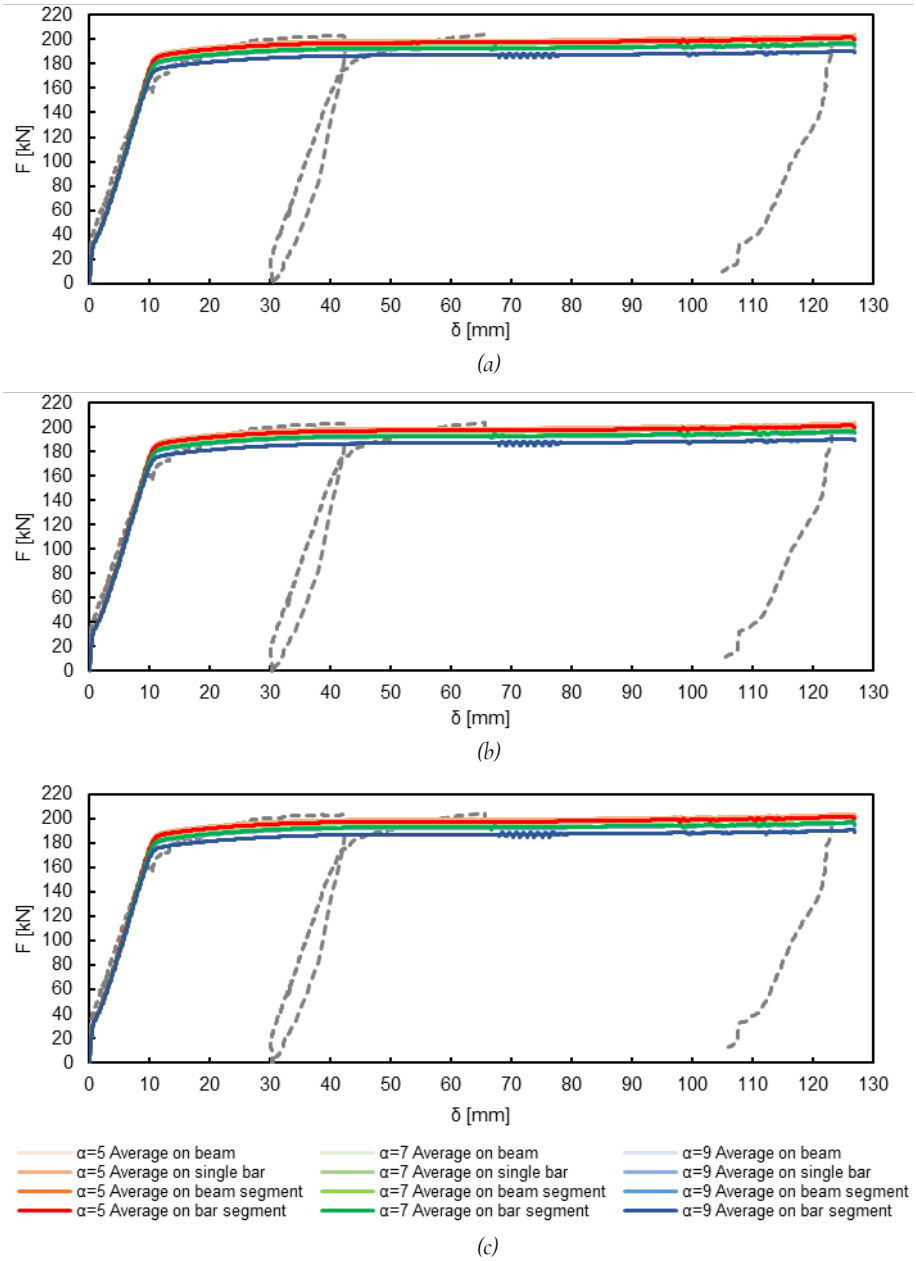

Fig. 4.29 Influence of type of average mass loss calculation and pitting factor assumption on the numerical response for beam RC-C1, obtained using Val and Melchers [169] *model for residual cross-sectional area of rebars and different models for ultimate tensile strain of corroded rebars: (a) Coronelli and Gambarova* [51]*; (b) Biondini and Vergani* [170]*; (c) Finozzi et al.* [56]

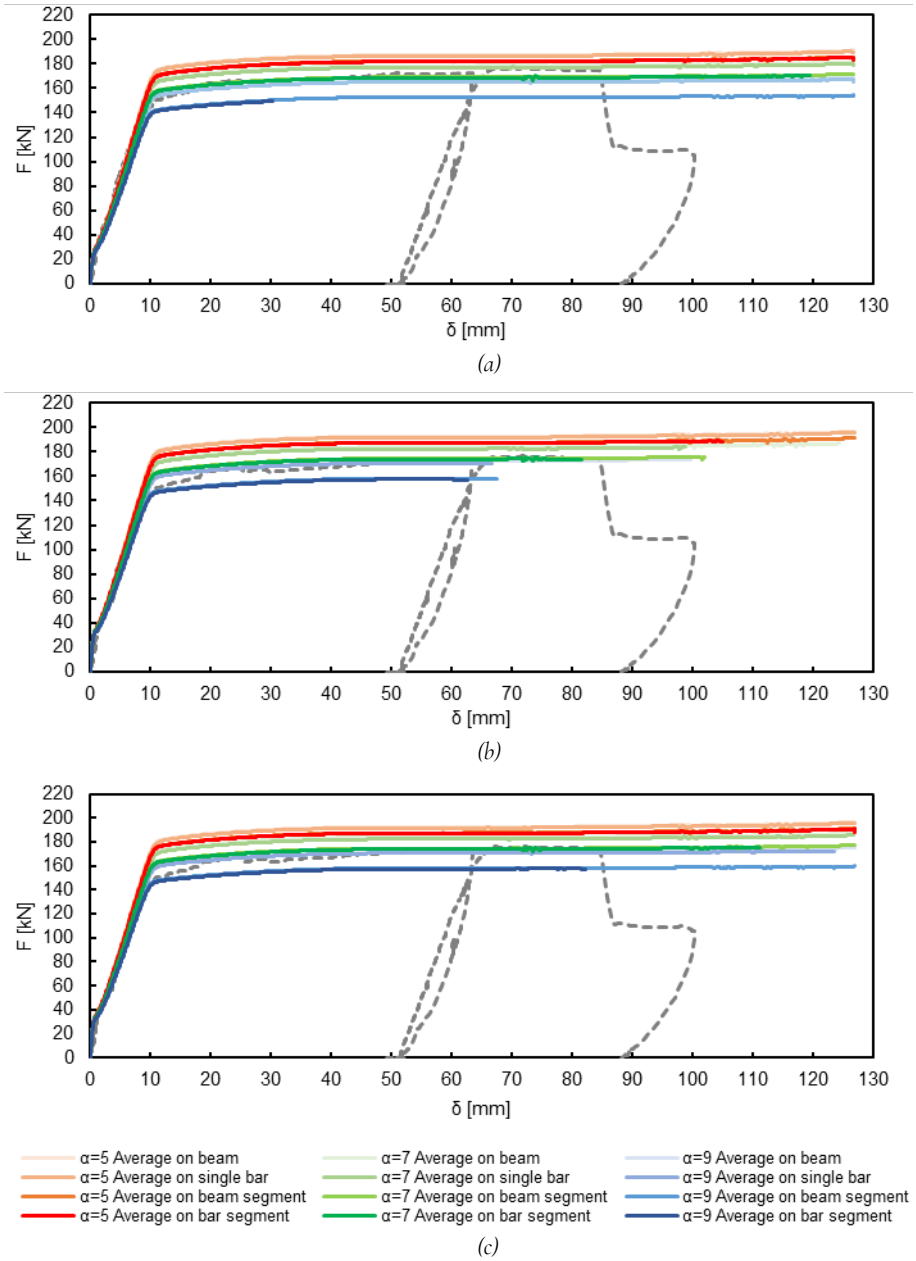

Fig. 4.30 Influence of type of average mass loss calculation and pitting factor assumption on the numerical response for beam RC-C2, obtained using Val and Melchers [169] *model for residual cross-sectional area of rebars and different models for ultimate tensile strain of corroded rebars: (a) Coronelli and Gambarova* [51]*; (b) Biondini and Vergani* [170]*; (c) Finozzi et al.* [56]

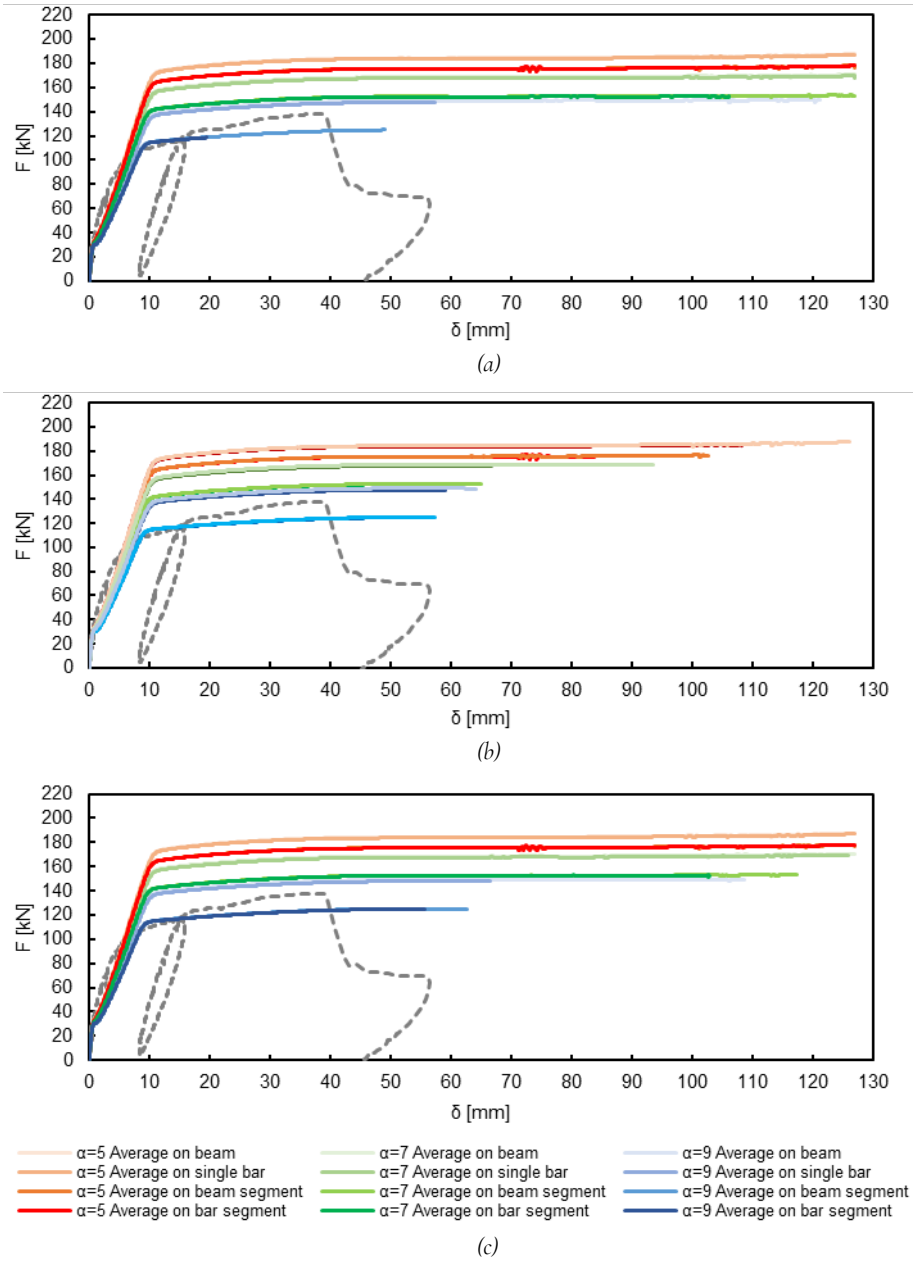

Fig. 4.31 Influence of type of average mass loss calculation and pitting factor assumption on the numerical response for beam RC-C3, obtained using Val and Melchers [169] *model for residual cross-sectional area of rebars and different models for ultimate tensile strain of corroded rebars: (a) Coronelli and Gambarova* [51]*; (b) Biondini and Vergani* [170]*; (c) Finozzi et al.* [56]

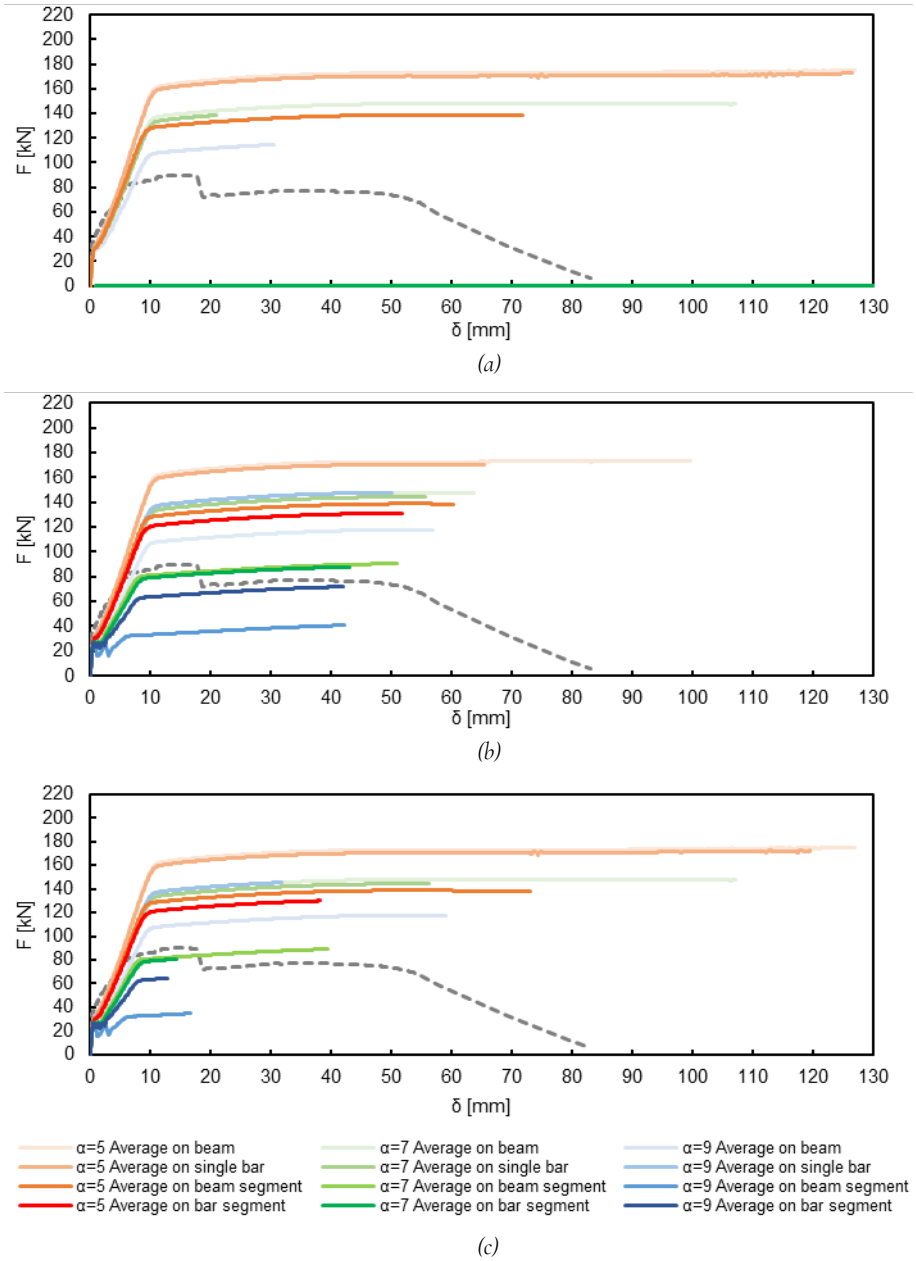

Fig. 4.32 Influence of type of average mass loss calculation and pitting factor assumption on the numerical response for beam RC-C4, obtained using Val and Melchers [169] model for residual cross-sectional area of rebars and different models for ultimate tensile strain of corroded rebars: (a) Coronelli and Gambarova [51]; (b) Biondini and Vergani [170]; (c) Finozzi et al. [56]

In Fig. 4.30, which reports results obtained for beam RC-C2, differences between the three graphs and between the various curves associated to different simulations start to be more appreciated. The best results in terms of prediction of the residual bending strength are obtained with the pitting factor $\alpha = 7$ considering the mass loss computed on the beam segments and on the bar segments. With the aim of commenting the results in terms of deformation capacity estimations, some premises are necessary. In all the performed simulations which shown a failure due to steel rupture, the achievement of the ultimate tensile strain of corroded reinforcement occurred in the central span of the beam, and in particular in the zone between the two loads. On the other hand, in the experimental test, the failure of the specimen was triggered by a loss of anchorage in one of the corroded longitudinal rebars, probably induced by severe pitting developed in the rebar in the zone of the anchorage, coupled with a complete loss of bond along the bar itself. Then, it clearly appears that even if the numerical response would provide the same ultimate deflection than that recorded in the experiment, the underlying modeled failure mechanism would be significantly different. So, a proper comparison of the obtained results in terms of deformation capacity appears difficult to be performed. In addition, the possibility of analyzing the experimentally observed behaviour of specimen RC-C2 using the results provided by the adopted numerical modelling strategy may be arguable. In fact, it is unequivocal that at some point of the test, somewhere prior to failure, extensive and spread loss of bond along the bottom longitudinal rebars occurred, having possibly changed the resisting mechanism of the beam from a bending-type mechanism to an arch-type mechanism. In such a situation, plain section hypothesis does not hold anymore ad so the deflections computed within the adopted modelling strategy would be no more directly comparable with those measured in the test, since no loss of bond is considered in the analyzed modelling procedure. For the sake of completeness, a comment on the numerically obtained deformation capacity values for beam RC-C2 is anyway provided, with the aim of analyzing the effects of the adoption of different modelling choices. Considering the results obtained with models from Coronelli and Gambarova [51] and from Finozzi et al. [56], steel ruptures occurred almost only considering average mass loss computed on the single bar segments. On the other hand, considering the model from Biondini and Vergani [170] quite low values of ultimate tensile strain for steel were obtained for both the cases of average mass loss computed on bar segments and beam segments, so resulting in reduced deflection capacity in several cases, especially for pitting factor values equal to 7 and 9.

In Fig. 4.31 numerical response curves obtained for specimens RC-C3 are illustrated. In this case, reduced deformation capacity due to steel ruptures are visible in all the three graphs associated to the models for calculating the ultimate tensile strain. Moreover, differences between various numerical response curves are more pronounced, due to the relevant reductions in bending strength associated to the cases with high pitting factors and high values of locally estimated average mass loss. The curves are almost grouped in couples of two types: i) curves for average mass loss computed on the whole beams present almost the same bending strength of curves for average mass loss computed on single bars; ii) curves for average mass loss computed on the beam segments present almost the same bending strength of curves for average mass loss computed on bar

segments. Besides, the two curves with approximately equal bending strength usually shown slightly different ultimate deflections. This behaviour is due to the fact that in the central segment of the beam RC-C3, i.e., where steel failure occurs in the simulations, the average mass loss for the left rebar is just slightly different from that obtained for the right one. Among the various analyzed combinations of variables, the best fit with experimental result is obtained with a pitting factor $\alpha = 7$, the model from Biondini and Vergani [170] and the average mass loss computed on the single bar segments.
To conclude the analysis, results obtained for specimen RC-C4 are examined considering the numerical response curves reported in Fig. 4.32. Trends similar to those observed for specimen RC-C3 can be noted, besides some relevant differences are present. For the model from Coronelli and Gambarova [51], many curves are not present since the model provided a null value for ultimate tensile strain of corroded bars. Moreover, in the case of specimen RC-C4 the difference in average mass loss computed for the left and the right rebars in the central segment of the beam is much more pronounced. This fact avoids the curves to be grouped in couples, as instead observed for beam RC-C3. Among the simulations performed for beam RC-C4, the best fit with the experimental force-displacement curve is obtained with the model from Finozzi et al. [56], a pitting factor $\alpha = 7$ and the average mass loss computed on bar segments.
The strong difference in average mass loss observed between the left and right rebars in the central portion of the beam RC-C4 may lead to some counterintuitive results. As an example, in Fig. 4.32c, the curve for $\alpha = 9$ and average mass loss computed on bar segments is characterized by a bending strength higher than that of the curve for $\alpha = 9$ and average mass loss computed on beam segments. Conversely, for the value of ultimate deflection, the order is reversed between these two curves. This is due to the fact that in the first case the total cross-sectional area is higher than that obtained in the latter one, since the corrosion on the two rebars is computed differently from each other and only in one of the them the area reduction is very high ($\Delta_m > 45\%$, see Chapter 3). For the very same reason, the ultimate tensile strain of the reinforcement is instead lower in the first case, justifying the lower ultimate deflection shown by the curve. Another example of a counterintuitive behaviour is observed in Fig. 4.32b in the curves obtained with $\alpha = 9$ respectively computing the average mass loss on beam segments and on bar segments. For the reason explained shortly above, in the first case the bending strength is actually higher than that observed for the latter one. However, the two curves show almost the same deformation capacity. This is due to the use of the model from Biondini and Vergani [173], which for very high corrosion level tends to approach an asymptotic minimum value for the ultimate tensile strain independent on the actual value of minimum residual cross-sectional area of the rebars. As a matter of fact, the beam RC-C4 represents a particular case since the local corrosion level for one the rebars in the central span of the beam is quite high. Actually, such value is much higher than those for which most of the adopted formulations to model the characteristics of corroded rebars were calibrated. So, despite results obtained for this case can indeed be considered as valuable, some care should be taken in generalize them to other situations.
Some results from the second sensitivity analysis presented just above may seem to provide contrary views to those obtained from the first sensitivity analysis, but actually

they do not. The newly provided results just allow to expand the previously conceived observations, adding insights regarding the effects of considering different ways for defining the average mass loss. In the first set of results emerged that the traditionally suggested value for the pitting factor $\alpha = 10$ may be actually too low to correctly represent the observed ultimate deformation capacity of corroded members. On the other hand, the second set of analyses allowed to clarify and point out that if very high corrosion levels are recorded or if more local and refined estimations of the average mass loss are adopted (which translate in higher values of average mass loss for the most corroded zones of the member), the traditionally suggested value or even lower values of the pitting factor may be more suitable to be used in order to obtain a predicted deformation capacity avoiding excessive under- or over- estimations.

4.5 Modelling response of corroded beams from the second experimental series

4.5.1 Premise

The results for the corroded specimens tested in the second experimental series, i.e., specimens RC-C5 and RC-C6, have been herein employed to verify and extend the observations and insights retrieved from the analysis of the first set of corroded specimens, presented in section 4.4. In particular, only some of the previously tested combination of models are adopted to represent the mechanical characteristics of corroded reinforcement, taking advantage of the insights obtained from the previously analyzed results.

4.5.2 Modelling section failure mode

In Fig. 4.33 and Fig. 4.34 are presented the graphs for the identification of ultimate condition in beams RC-C5 and RC-C6, respectively. The computations have been performed using the same modelling hypotheses adopted in section 4.4 for the corroded beams of the first experimental series. In particular, a pitting factor $\alpha = 10$ was used, together with the model from Val and Melchers [169] and the model from Finozzi et al. [56]. In first instance, average mass loss has been computed as average on the whole beams. Failure mode domains for beam RC-C5 presented in Fig. 4.33 both indicates a failure of type "I", suggesting that the beam would have reached rebar rupture when the cover spalling has not even started (i.e., the outmost compressed section fibers wouldn't have reached the strain ε_{sp}). For beam RC-C6, failure mode domains shown in Fig. 4.34 even suggest that the compressed concrete fibers wouldn't have reached the concrete strain at peak strength before the steel fracture occurred. Based on the analysis of experimental crack patterns described in Chapter 3, it is clear that predicted failure modes are slightly different than those actually occurred.

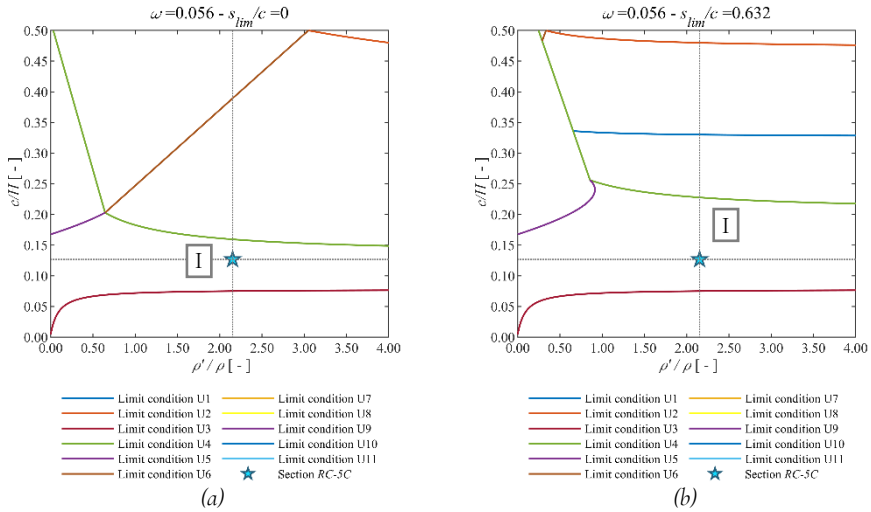

Fig. 4.33 Domains for the identification of the ultimate condition of beam RC-C5 (a) Limit for concrete set at beginning of cover spalling (i.e., $\varepsilon_c = \varepsilon_{sp} = -4‰$ on the outer fiber of concrete cover); (b) Limit for concrete set at crushing of core (i.e., $\varepsilon_c = \varepsilon_{cu} = -8‰$ on the outer fiber of concrete core). Results obtained considering a pitting factor $\alpha = 10$, the model from Val and Melchers [169], the model from Finozzi et al. [56], and computing the average mass loss as average on the whole beams.

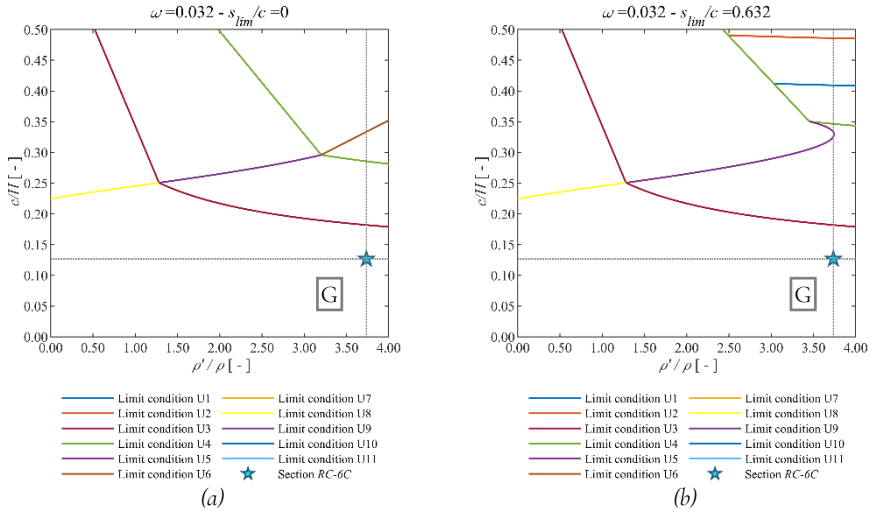

Fig. 4.34 Domains for the identification of the ultimate condition of beam RC-C6 (a) Limit for concrete set at beginning of cover spalling (i.e., $\varepsilon_c = \varepsilon_{sp} = -4‰$ on the outer fiber of concrete cover); (b) Limit for concrete set at crushing of core (i.e., $\varepsilon_c = \varepsilon_{cu} = -8‰$ on the outer fiber of concrete core). Results obtained considering a pitting factor $\alpha = 10$, the model from Val and Melchers [169], the model from Finozzi et al. [56], and computing the average mass loss as average on the whole beams.

4.5.3 MODELLING MEMBER RESPONSE

Numerical simulations of the force-displacement response for the two studied beams have then been performed. To model the characteristics of corroded rebars, the same modelling choices used for the computation of failure mode domains have been adopted. Force-displacement curves are reported in Fig. 4.35.

It can be seen that for both the specimens the numerical responses underestimate the experimental ones in terms of both peak strength and deformation capacity. Also the post-cracking stiffness appear to be quite lower than that observed experimentally, indicating that a possible cause of the observed results lay in a too severe and conservative estimation of the residual cross-sectional area of the rebars.

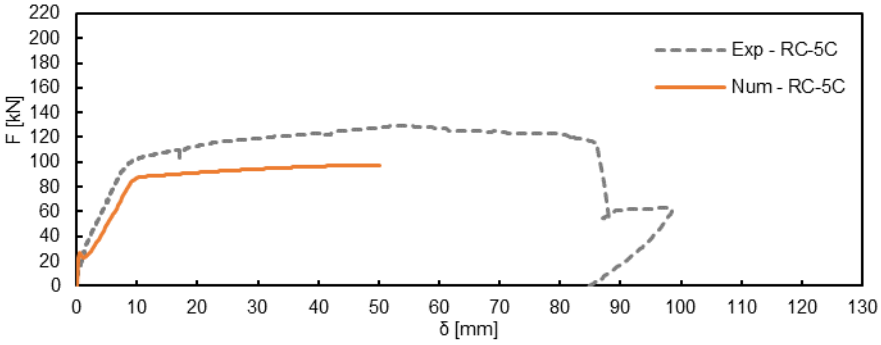

(a)

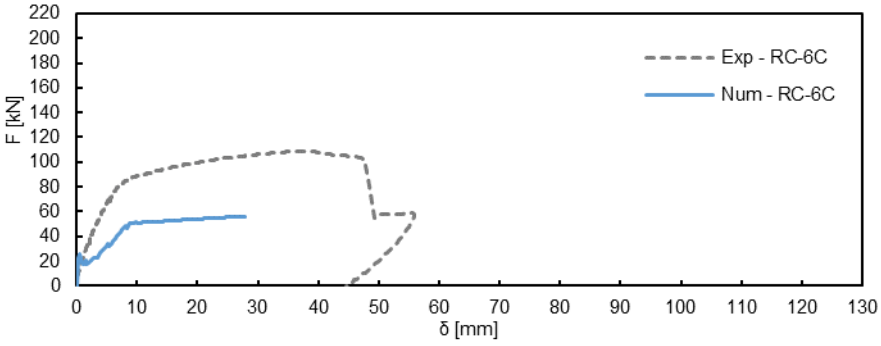

(b)

Fig. 4.35 Numerical response for corroded beams the second experimental series, obtained considering a friction coefficient $\mu = 0.3$, a pitting factor $\alpha = 10$, the Val and Melchers [169] model for the cross-sectional area of rebars and the model from Finozzi et al. [56] for the ultimate tensile strain of corroded bars.

4.5.3 Parametric analysis

In both the types of analysis considered, i.e., the analysis of the failure modes and the modelling of the response curves for the corroded beams, it appears that for the analyzed specimens the adopted modelling choices may not be the most suitable in order to achieve a correct representation of the experimentally observed response, since the obtained numerical results are characterized by a severe conservativism. As a matter of fact, the parametric analyses previously presented in section 4.4 shown that the choices for modelling corroded rebars traditionally suggested to be adopted in engineering practice may not always be a proper option, especially if the average mass loss value is particularly high. To further investigate this aspect, an additional parametric analysis was performed, taking advantage of the insights got from the results obtained for the first series of corroded specimens. In particular, a series of simulations varying the adopted pitting factor were performed. In this case, however, the considered average mass loss values were computed only as average on the single bar segments, as was described in Chapter 3. Among the available choices, this one provides the better description of the actual corrosion level along the bars. To model the shape of the residual cross-sectional area of the rebars, the model from Val and Melchers [169] was adopted. As a matter of fact, it has been shown in the previous paragraph that the model from Rodriguez et al. [159] leads to very severe estimations of the residual area in the case of quite high corrosion levels, such as those observed in the analyzed beams.

Numerical results are compared with the experimental response curves in Fig. 4.36 and Fig. 4.37, for beams RC-C5 and RC-C6 respectively. The trend already observed in section 4.4 regarding the behaviour of the different models for the evaluation of ultimate tensile strain is herein found again. For the highest pitting factor values, which correspond to lower values of residual cross-sectional area, the model from Coronelli and Gambarova provides null values of ultimate tensile strain of corroded bars, so many curves are actually not present in the graphs of Fig. 4.36a and Fig. 4.37a. On the other hand, the slightly variation of ultimate tensile strain with the corrosion level provided by the model from Biondini and Vergani [173] translates in a gradual variation of the beams deformation capacity. A more pronounced exponentially varying deformation capacity is obtained with the model from Finozzi et al. [56], as already observed in the previous section. With regards to the influence of the pitting factor values, the results observed in section 4.4 are herein found again and observable in a more detailed way.

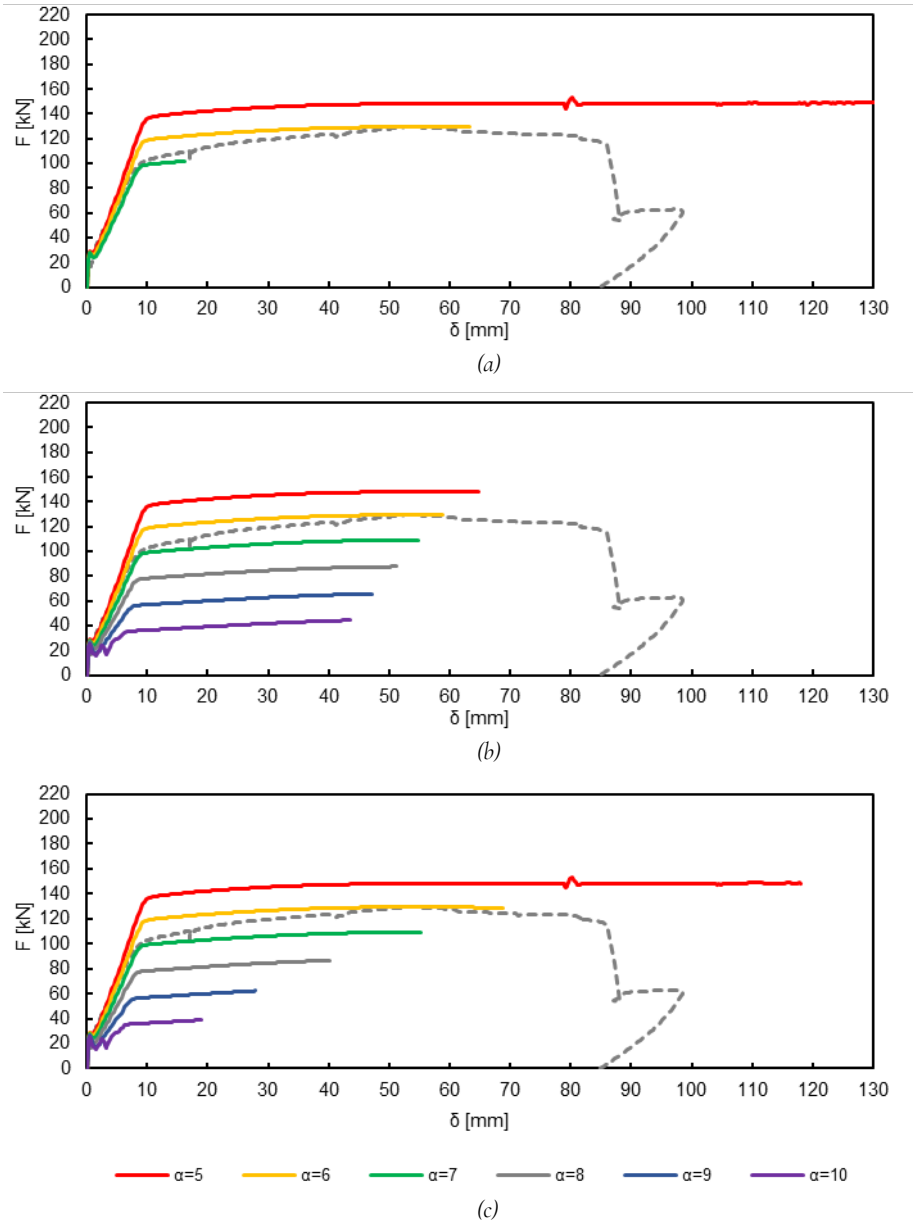

Fig. 4.36 Influence of pitting factor value on the numerical response for beam RC-C5. The results have been obtained considering the average mass loss ratios computed as average on single bar segments, using Val and Melchers [169] *model for residual cross-sectional area of rebars and different models for ultimate tensile strain of corroded rebars: (a) Coronelli and Gambarova* [51]*; (b) Biondini and Vergani* [170]*; (c) Finozzi et al.* [56]

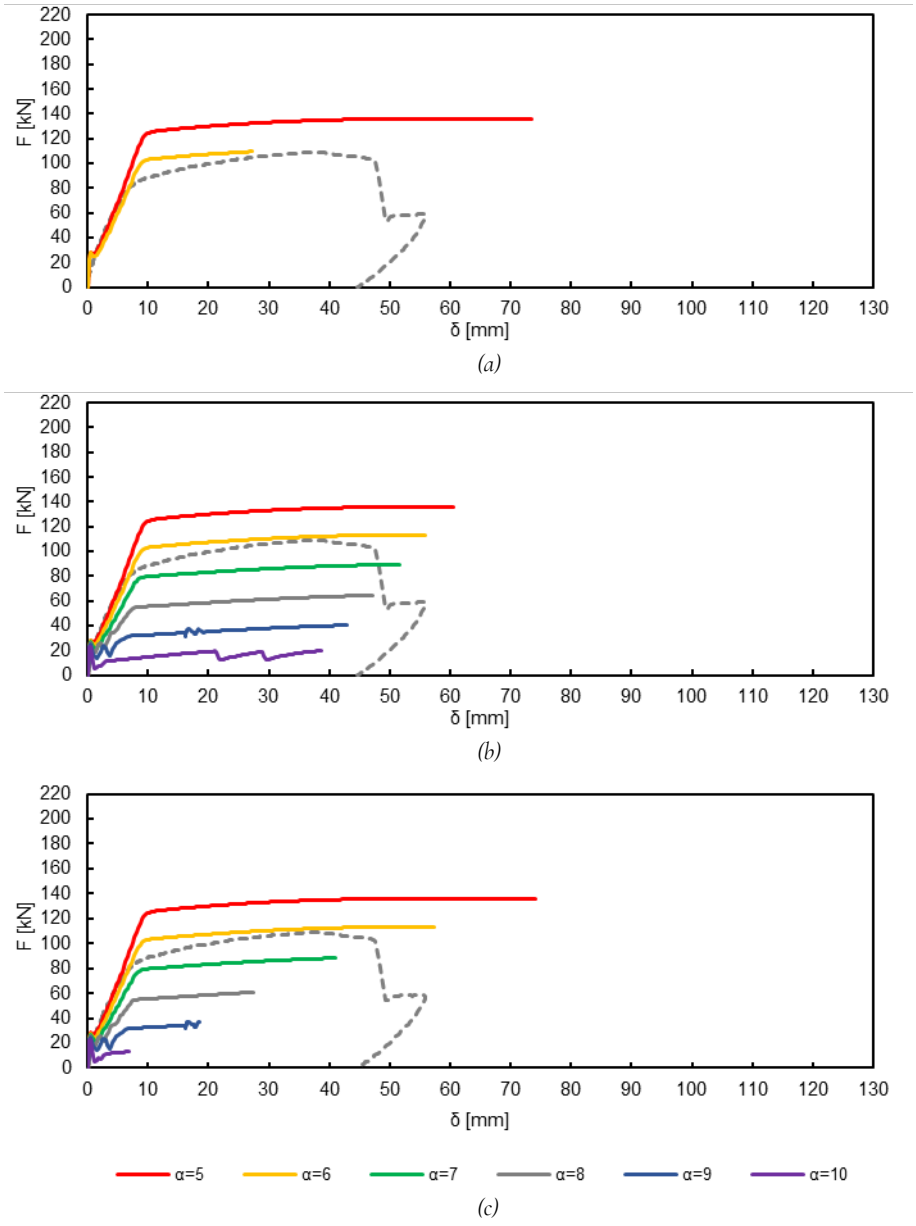

Fig. 4.37 Influence of pitting factor value on the numerical response for beam RC-C6. The results have been obtained considering the average mass loss ratios computed as average on single bar segments, using Val and Melchers [36] model for residual cross-sectional area of rebars and different models for ultimate tensile strain of corroded rebars: (a) Coronelli and Gambarova [8]; (b) Biondini and Vergani [37]; (c) Finozzi et al. [14]

Indeed, the adoption of a pitting factor $\alpha = 10$ leads to a severe underestimation of the structural performances. It is therefore highlighted again that when a more local description of the corrosion level is adopted, often leading to quite high values of the locally-averaged mass loss ratio, a more refined definition of the pitting factor is required in order to avoid excessive underestimation of both the bending strength and the deformation capacity of the members.
In both the analyzed cases, the best agreement between the experimental and numerical response curves is obtained using a pitting factor $\alpha = 6$. In order to make a counter-check and verify the predictive effectiveness of the analytical approach based on failure mode domains, the domains for ultimate conditions of beams RC-C5 and RC-C6 were recomputed using the average mass loss values computed on single bar segments and a pitting factor $\alpha = 6$. The newly obtained domains for the ultimate conditions are illustrated in Fig. 4.38 and Fig. 4.39, while a comparison of failure modes obtained with different modelling hypotheses is provided in Table 4.2.

Table 4.2 Overview of behaviour for corroded beams of the second experimental series with comparison between observed and analytically predicted failure modes obtained using analytical failure mode domains. Results obtained considering the model from Val and Melchers [169] *for the shape of residual cross-sectional area of bars and the model from Finozzi et al.* [56] *for the ultimate tensile strain of bars.*

Beam	RC-C5	RC-C6
Experimentally observed failure mode	Rupture of bottom steel rebars a bit after the beginning of concrete cover spalling	Rupture of bottom steel rebars just after the beginning of concrete cover spalling
Analytically predicted failure mode with $\alpha = 10$ and computing the average mass loss as average on the whole beams	Rupture of bottom steel rebars with top steel elastic and concrete fibers which do not have reached the strain at which cover spalling begins	Rupture of bottom steel rebars with top steel elastic and concrete fibers which do not have yet reached the peak concrete strength
Analytically predicted failure mode with $\alpha = 6$ and computing the average mass loss as average on bar segments	Rupture of bottom steel rebars with top steel elastic, after the beginning of concrete cover spalling	Rupture of bottom steel rebars with top steel elastic, just after the beginning of concrete cover spalling

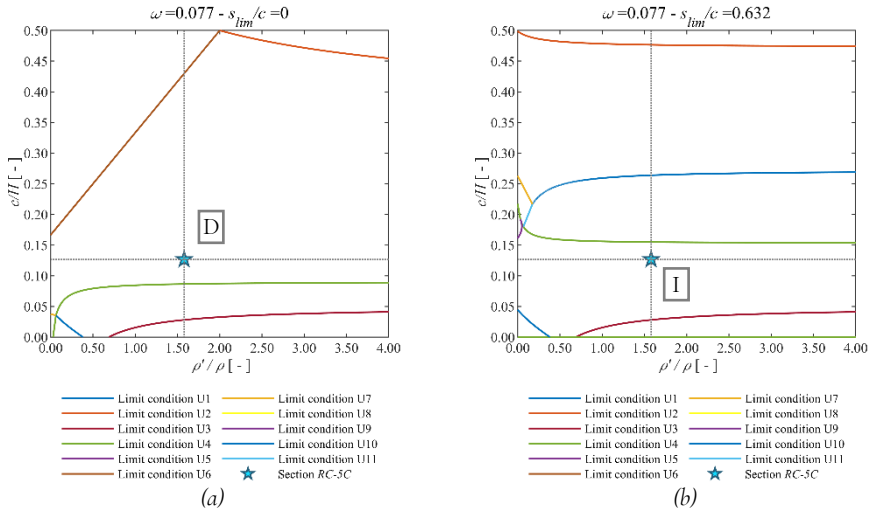

Fig. 4.38 Domains for the identification of the ultimate condition of corroded beam RC-C5 (a) Limit for concrete set at beginning of cover spalling (i.e., $\varepsilon_c = \varepsilon_{sp} = -4‰$ on the outer fiber of concrete cover); (b) Limit for concrete set at crushing of core (i.e., $\varepsilon_c = \varepsilon_{cu} = -8‰$ on the outer fiber of concrete core). Results obtained considering a pitting factor $\alpha = 6$, the model from Val and Melchers [169], the model from Finozzi et al. [56], and computing the average mass loss as average on the single bar segments

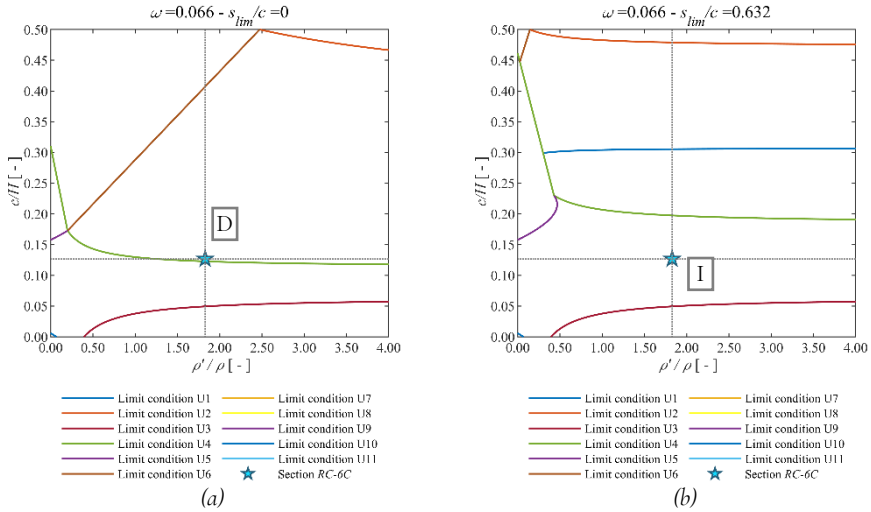

Fig. 4.39 Domains for the identification of the ultimate condition of corroded beam RC-C6 (a) Limit for concrete set at beginning of cover spalling (i.e., $\varepsilon_c = \varepsilon_{sp} = -4‰$ on the outer fiber of concrete cover); (b) Limit for concrete set at crushing of core (i.e., $\varepsilon_c = \varepsilon_{cu} = -8‰$ on the outer fiber of concrete core). Results obtained considering a pitting factor $\alpha = 6$, the model from Val and Melchers [169], the model from Finozzi et al. [56], and computing the average mass loss as average on the single bar segments

It can be seen that the domains obtained with the refined definition of the corrosion level and the adoption of a lower value of the pitting factor actually provides failure mode predictions which fit quite well with the observed experimental behaviour. This observation supports the effectiveness and usefulness of this modelling tool, which can be effective if a proper description of the mechanical characteristics of corroded steel is available to be used.

An additional in-depth study was carried out analyzing the numerical response obtained for beam RC-C5 by using a pitting factor $\alpha = 6$, and computing the average mass loss as average over the single bar segments. A first comparison in terms of average concrete strains at the depth of the bottom longitudinal reinforcements is provided in Fig. 4.40a. It can be observed that a good agreement exists regarding the behaviour prior to steel yielding. On the other hand, it can be noticed in Fig. 4.40a that the numerically estimated strain is quite lower than the experimental average measure, evaluated from LVDT data as described in section 3.3.4. This result can be attributed to two concurring causes. First, since the experimental strain values have been derived from the measures of bottom LVDT installed on the side of the beam, the actual strain values in the bottom reinforcement may have been lower than those computed from the LVDT measures, if slippage of rebars due to loss of bond would have occurred. Moreover, the ultimate tensile strain of rebars used in the numerical analyses may be lower than the actual ultimate strain of the corroded rebars in the studied specimen. In fact, just because the adopted modelling choices led to a satisfactory estimation of the residual strength it is not guaranteed that the same choices would also lead to a proper value of the residual ultimate strain of rebars.

The observed difference in the experimentally and numerically derived average ultimate steel strain, reflects in a perfectly analogous difference in terms of average ultimate curvature of the sections at midspan, as can be seen in Fig. 4.40b. This is due to the fact that since the sectional failure mode is related to steel rupture, the value of the ultimate curvature is actually directly depending on the ultimate tensile strain of the rebars. However, when the comparison is then observed in terms of midspan deflections, Fig. 4.40c, it can be seen that the numerically obtained ultimate deflection is in proportion less conservative than the average strain or the ultimate curvature. This fact can be explained considering the aspects discussed in the following.

In the experiment, large curvature values, close or equal to the ultimate curvature, developed only in localized zones in correspondence of the few main flexural cracks, leading to reduced ultimate deflection values for the members.

The reason for the occurrence of few and large-spaced flexural cracks in highly corroded beams have been already discussed in section 3.3.4. On the other hand, the used numerical modelling strategy assumed uniform sectional characteristics over the constant moment zone of the beams. Moreover, even if a refined discretization with a more local definition of corrosion level would be adopted, curvatures would be anyway obtained as smeared over beam portions associated to single gauss points. So, the adopted modelling strategy it is not able in any way to actually represent the localization of large curvatures occurring in the main cracks.

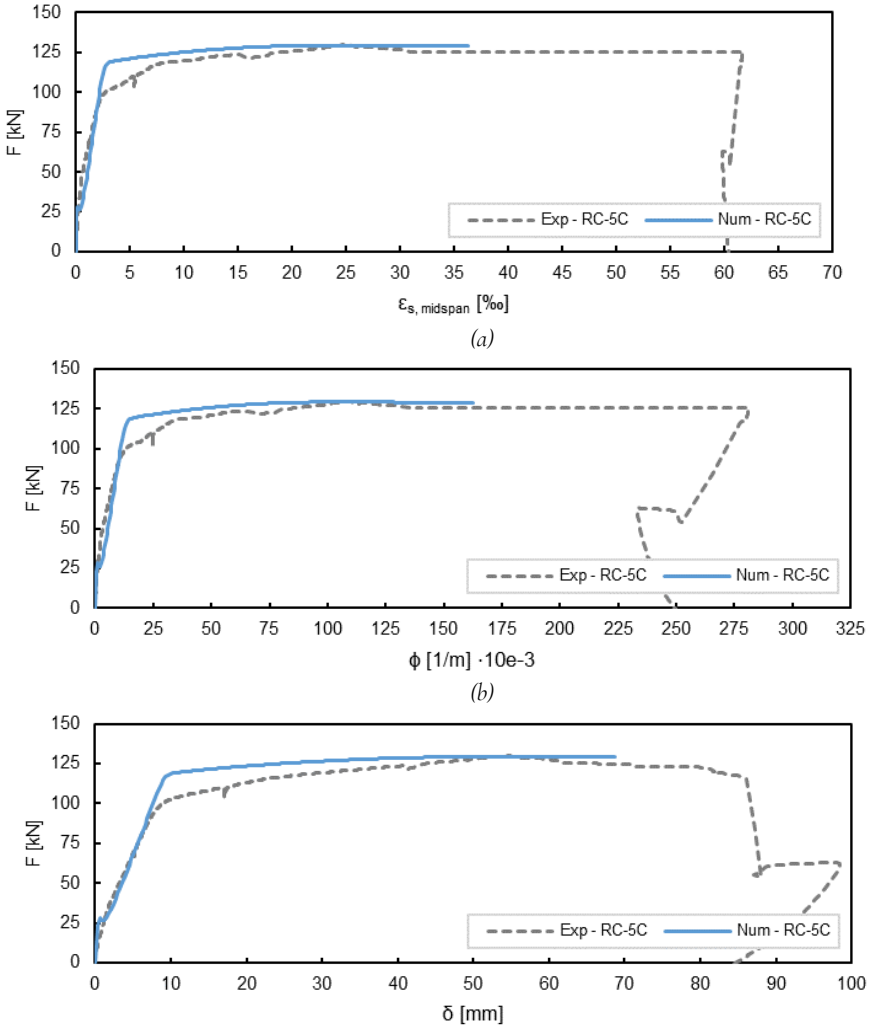

Fig. 4.40 Comparison of deformation parameters obtained for beam RC-C5 from the numerical simulations and from experimental data (a) Average concrete strain at the depth of the bottom longitudinal rebars, plotted against the total load. (b) Average curvature at beam midspan, plotted against the total load; (c) Midspan deflection, plotted against the total load. The numerical simulation have been performed considering a pitting factor $\alpha = 6$*, the model from Val and Melchers* [169]*, the model from Finozzi et al.* [56]*, and computing the average mass loss as average on the single bar segments.*

4.6 Discussion

In this chapter different practice-oriented modelling approaches have been analyzed and tested, with the aim of check their suitability for the structural assessment of RC beams affected by reinforcement corrosion. Particular attention was devoted to analyze the capability of the adopted modelling procedures to correctly predict the failure mode and the deformation capacity of corroded members. The data for sound and corroded beams tested in the experimental campaign described in Chapter 3 have been used to evaluate the predictive performances of the analyzed approaches.

The attention has been focused on the analysis of different formulations and parameters values commonly used to represent the mechanical characteristics of corroded reinforcement. With this regard, different aspects have been investigated, addressing the suitability of adopted models, the influence of different modeling choices and the influence of the way corrosion level is defined. The obtained results allowed to draw some considerations and to get some insights which may be helpful for a better use of the analyzed modelling procedures in the engineering practice.

First, it has been observed that by employing some of the traditionally suggested approaches, different modelling performance has been obtained with reference to the prediction of bending strength and deformation capacity of corroded members. It would make sense that the approaches traditionally suggested for modelling the mechanical characteristics of corroded reinforcement would provide fairly good predictions for strength estimation, while instead leading to rather poor estimations of deformation capacity. As a matter of fact, many of the analyzed models were developed focusing the attention on the aim of modelling structural performances mainly in terms of residual strength. Indeed there is a need for refined modelling procedures which allow a safe-side and reliable prediction of the deformation capacity, especially considering the importance of its evaluation in the seismic assessment of existing structures. Such approaches should however be sufficiently simple and direct so to be effectively helpful and employable in engineering practice.

Considering the effects due to the adoption of different formulations or parameters values to model the characteristics of corroded rebars, it has been shown that a great variability of the results can be found. Every model has its own peculiarities and should be used only being aware of the results that it may provide for different corrosion levels, also considering the field of validity for which the model was originally developed. One particular aspect which was investigated regards the adoption of suitable values for the pitting factor, also considering the combined influence of the variability in the other adopted models and the variability in the way the corrosion-induced average mass loss is computed. The observed results concerning the most suitable choices for the value of the pitting factor are quite in agreement with some recent findings from other authors. For example, Zhao et al. [163] proposed an analytical law for the pitting factor variation, which provides exponentially decreasing values as the average mass loss value increase. This trend may be interpreted under the hypothesis that as the average mass loss value increases, the corrosion penetration would become more uniform on the considered

rebar portion, moving to a condition close to that of generalized corrosion. Accordingly, the pitting factor would reduce by its definition.
The results obtained at the current stage of the research, although, do not yet allow to propose a new formulation for the calculation of the most suitable pitting factor value. Based only on the obtained results, a rule of thumb may be that if the mass loss is estimated more locally, a value of the pitting factor lower than the suggested value $\alpha = 10$ may be used in the portions of bars for which the locally calculated average mass loss is greater than the average mass loss computed on the whole beam. Ideally, if the mass loss would be computed for pieces of rebars approaching a zero length, then the pitting factor to be used of course would be unitary for all the pieces, no matter the value of their locally evaluated mass loss compared with the global average one. However, to suitably address the issue of assigning a pitting factor value on portions of rebars for which a local estimation of the average mass loss is available, statistical descriptions of the pit depth distribution dependent on the length of the bar portion should be made available. Further experimental campaigns on corroded bar segments aiming to provide a better understanding of the distributions of pit depth are indeed needed [174]. Alongside with this aspect, it would also be important to consider the possibility of contemporary formation of pits in adjacent rebars in the same beam section [175].
Recalling the research objective ***O2*** stated in Chapter 1, its core aim has been addressed by the presented investigations, highlighting some of the current limits to the applicability of the considered modelling strategies for the analysis of corroded RC beams. In particular, an obvious limitation of the adopted procedure regards the inability to consider effects due to reduction of bond between the rebars and the surrounding concrete. Although this limit can represent a serious drawback of the considered modelling strategies, other aspects can make them actually desirable for practical applications, i.e., their simplicity, speed and easiness to use in practice. Besides, future developments of the research could involve the enhancements of considered modelling strategies in order to possibly account for loss of bond, for example adopting approaches such as that proposed by Manfredi et al. [176].
Additional observations regarding other less obvious aspects which can be critical for the effectiveness of the studied models have also been formulated. One of them regards the fact that in the procedures traditionally suggested to predict the structural response of corroded members, the workflow to be used for the estimation of mechanical characteristics of corroded rebars appears to be a bit ill posed.
As an example, considering the procedure for the calculation of the residual cross-sectional area described in section 4.2, it has been seen that several steps need to be done, each of which requires the adoption of a specific model or of a value for some model parameter. It is quite obvious that the same final result can be obtained with different combination of these modelling choices. The real issue consists in the fact that in many cases there is no control or available insight on which choice of models is consistent and suitable to be used. In this context, the results and observations provided in this chapter may serve as a contribution useful to start filling this lack. Moreover, further experimental studies would be strongly needed to investigate the direct correlations which may be observed between the corrosion level and the minimum residual cross-

sectional area and pitting depth distribution of rebars. This kind of information would at least allow to discuss if some improvements may be introduced in the currently suggested workflow for the definition of mechanical characteristics of corroded rebars.
Reviewing the overall results currently obtained from the analyses of the studied corroded beams, several improvements can be suggested which may be part of further deeper investigations. In particular, some experimental results for the considered beams are currently still being analyzed, such as the detailed measure of residual area along the corroded rebars. Such information would offer the possibility to improve the numerical simulations and to test different modelling approaches. Other kind of data would also allow to improve the performed analyses. As an example, it would be very useful, when possible, to get experimental information about the value of ultimate tensile strain of the sound reinforcing bars, since it is a main parameter used in the assessment of deformation capacity in corroded members, as described in section 4.2. Moreover, knowing the ultimate tensile strain of the rebars would allow to compute also an estimation of the experimental value of the hardening ratio, which is a very impactful parameter in the assessment of the deformation capacity. In this context, it is also worth to point out that an important improvement in the presented modelling approaches would be to modify the formulation of failure mode domains presented in Chapter 2 in order to allow it considering steel hardening.
In the end, some more general insights for the improvement of assessment approaches for corroded members can be proposed. Considering that the corrosion level may be known or defined with different levels of approximation, a correspondingly framework for the structural assessment based on the level of approximation (LoA) approach may be developed. As an example, if the corrosion level is known in a roughly approximated way, then the pitting factor value, the residual area model and the model for definition of ultimate strain may be assumed in a very simplified way and in order to provide a safe-side estimation of the structural response. On the other hand, if the corrosion level would be described in a more local and refined way, better could be also done in the adopted modelling procedure, adopting more refined approaches. As an example, if the corrosion level would still be expressed in terms of average mass loss, but the average would be computed on small portions of bars, refined calculations could be adopted for the evaluation of the pitting factor, for example assuming its dependance on the mass loss ratio as suggested by Zhao et al. [163]. If an even more detailed description of the residual area along the bars would be available, then a detailed modelling approach could be implemented. In particular, an actual improvement of the calculation of the apparent residual ultimate tensile strain of the bars could be done using the approaches proposed by Chaoqun et al. [57] and Haefliger et al. [161]. The investigation of these possible improvements in the assessment procedures may be the aim of future further research.

5

Potential and limitations of the use of MT-DInSAR data as an aid to monitor deformation demands in structures subjected to ground settlements

Asking the right questions made me a scientist.
Isidor I. Rabi

Several urbanized areas in many countries all over the world are affected by ground movements and settlements, which can be triggered by several natural or man-made causes. The development of differential settlements in soil below building foundations may induce undesired effects on the above constructions, in terms of unforeseen deformation demands in structural members and development of extensive damage in infills and non-structural elements. Structural effects of differential ground settlements strongly depends on the spatial distribution and on the magnitude of the soil motions. Advances achieved in recent years by remote sensing techniques, and in particular in Multi – Temporal Differential Synthetic Aperture Radar Interferometry (MT-DInSAR) techniques for monitoring deformation of Earth's surface features, initiated the adoption of these tools in the field of civil structural health monitoring. This chapter analyzes whether and how MT-DInSAR data can be effectively adopted for monitoring ground and buildings settlements in order to improve estimations of deformation demands in structural members.

Research presented in this chapter has been developed in the context of a joint collaboration of researchers from CNR-IREA, IUAV University of Venice, Tor Vergata University of Rome and University of Naples "Federico II", performed among the research activities of the project DPC-ReLUIS 2019-2021 – Working Package 06 : "Structural health monitoring and satellite data"[74].

5.1 Introduction

Deformation demands in structural members induced by ground settlements may lead to structural consequences of various significance, ranging from minor damages up to the risk of collapse of constructions [177], [178]. The type and relevance of structural effects that may occur strongly depend on the structural typology considered [179], [180]. Focusing on RC frame structures, differential ground settlements can induce relevant distortions in beams at the foundation level and at upper storeys, as well as significant damages to possibly present infill walls or non-structural elements. Rotation demands in beams may in some cases be relevant, and they could become an issue for the structural safety of the building [34], [35]. Starting from the second half of the last century, much effort has been put on the development of tools for the estimation of structural response and associated damage induced by differential ground settlements. A first group of studies was devoted to provide qualitatively predictions of damages associated to deformation demands induced by differential ground settlements, leading to the development of empirical approaches to relate the distribution and amount of differential settlements of foundations to different levels of building structural damage [181], [182], [183]. An advancement has been subsequently made with the proposals of methods which make use of simplified mechanical-based models to represent the structural response, again allowing for a classification of damage level based on distribution and amount of differential settlements [184], [178], [185], [186]. Finally, more refined strategies for the estimation of structural response and damage due to foundation settlements have been proposed recently, [187], [188], [189], which adopt more sophisticated modelling strategies to simulate the structural behaviour, by means of analytical models or nonlinear finite element simulations.

Whatever the adopted approach, a key aspect in the structural assessment process is related to the determination of the actual intensity and spatial distribution of ground deformations, which strongly vary depending on the causing phenomenon. Actions causing differential foundations settlements can be of various kinds. They can be determined by natural causes, anthropic causes, or a combination thereof, and can have different extensions in space, from territorial to local, so involving several or single buildings. If the cause of the phenomenon is known and/or some of its characteristics can be assumed to be known (as for example in the case of tunnelling-induced settlements), simplified models may be available to obtain a rough estimation of the extent and amount of subsidence. However, the validity of such approaches is often quite unknown, considering the actual complexity of the three-dimensional ground deformations field and the possible effects occurring in urban areas due to the presence of adjacent applied loads [36]. Further investigations are often necessary to improve the information about the ground settlements field. In such situations, periodical and spatially distributed on-site monitoring of ground settlements may be necessary.

In this context, an aid could be provided by the recent advancements achieved in remote sensing techniques for monitoring deformations of objects on Earth's surface. In particular, Multi-Temporal Differential Synthetic Aperture Radar Interferometry (MT-DInSAR) techniques are nowadays capable of providing high-resolution, sub-centimeter

accuracy data to monitor deformations of ground and of constructions, over relatively wide urbanized areas [61], [190], [191]. The promising potentials of this class of techniques have rapidly attracted the attention of the scientific and technical civil engineering community over the last years, and several studies have been pursued to explore the uses of MT-DInSAR techniques in structural monitoring.
A first class of applications involves the use of remote sensing data to analyze the built heritage of urbanized areas at a relatively large scale, with the purpose of classification or detection of possible hazards [192], [193], [194], [195], [196], [197]. Several studies have also been performed specifically focusing on monitoring the ground and structures deformations with the aid of MT-DInSAR data at the scale of individual constructions. In particular, focusing on the applications performed on civil structures and infrastructures, various works have been proposed targeting buildings [198], [199], [200], [201], [202], dams [203], [204], [205] and bridges [206], [207], [208], [209], [210], [211], [212], [213], [214], [215], [62], [216], [217]. A relevant application which has also been recently proposed [67] involves the use of MT-DInSAR monitoring data to enhance the predictions provided by standard analytical models for the estimation of ground deformations due to tunnel excavations (e.g., to validate or update simplified models for determining ground settlements profiles, such as those based on greenfield assumption [218], by using ground deformation data obtained by MT-DInSAR procedures).
The goal of the research presented in this chapter is to analyzes potential and limitations of MT-DInSAR techniques to be used as an aid for the estimation and monitoring of structural deformation demands induced by ground settlements. In the following, a brief overview of the effects of differential settlements on RC frame buildings is presented, with special attention to aspects related to rotation and curvature demands at beam members. Then, a brief review of basic aspects concerning MT-DInSAR monitoring is provided, which is useful to highlight the key features of these techniques and to gain a more comprehensive understanding about their current limitations. Subsequently, relevant aspects for the use of MT-DInSAR data for structural monitoring applications at the single building scale are discussed. Some examples of applications are provided in order to demonstrate and emphasize some of the addressed aspects. At the end of the chapter, considerations and recommendations for the use of MT-DInSAR data in structural monitoring applications are proposed.

5.2 Deformation demand in structural members of reinforced concrete frame buildings subjected to differential ground settlements

In RC frame buildings, differential settlements of foundations induce additional stresses in beams and columns. Deformed configuration of the structure, obtained as a result of such foundation settlements, may be characterized by the spreading of flexural cracking, and eventually yielding, at member ends [179] as illustrated in the example provided in Fig. 5.1a [188]. Very often, damages of the main RC structural elements are anticipated by the development of clearly noticeable damages in infills or other non-structural elements [185]. As a matter of fact, several are the cases in which the amount of

differential settlements is sufficient to induce extensive damage to infills or non-structural elements, while at the same time it is too low to create serious issues to the main RC elements. Nevertheless, in some situations the settlements can be severe, as in the cases of a significant subsidence phenomena or of the failure of a foundation structure. In such scenarios, the deformation demands developed in the structural members can be severe too, and eventually lead to a partial collapse of the structure [177]. Considering beam members, the developed settlement-induced deformations are dependent on the motion of the two adjacent beam-column nodes, i.e., they can be determined as a function of the displacements and rotations of the two adjacent columns [219]. As an example, in Fig. 5.1b a simple ideal case is represented in which two columns of a RC frame, having distance L from each other, are experiencing different vertical displacements and so developing a differential settlement δ_d, which in turn induces bending and shear actions in the beams connecting the two columns.

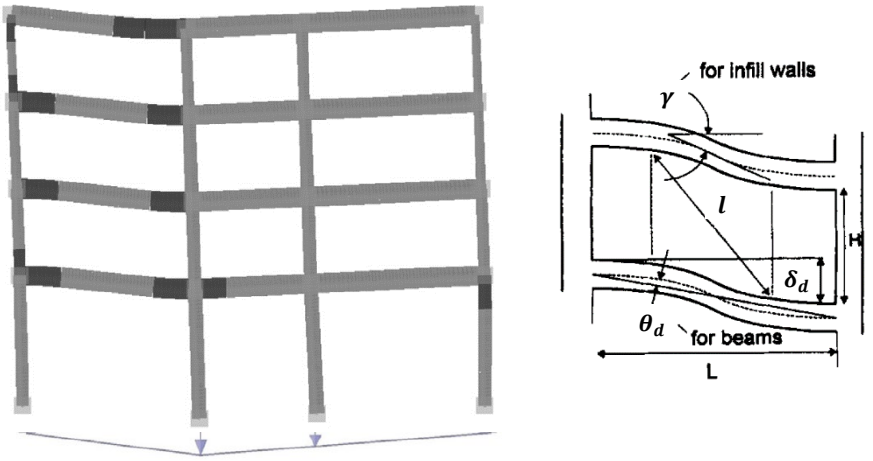

(a) (b)

Fig. 5.1 (a) Examples of deformed configuration for a RC frame subjected to differential ground settlements (Adapted from Fotopoulou et al. [188]*); (b) Simplified schematization of deformed configuration used to define chord rotation demand in beams between two columns of a RC frame subjected to differential ground settlements (From Boone* [185]*)*

For the ideal case reported in Fig. 5.1b, once the differential settlement δ_d is known, it is then possible to calculate the chord rotation demand θ_d for the beams, according to the expression:

$$\theta_d = \delta_d / L \tag{5.1}$$

As well know, the chord rotation demand in a RC member is accommodated by the development of flexural deformations, shear deformations and fixed-end rotations [4]. If the contributions of the two latter mechanisms would be neglected, it would mean to

hypothesizing that the whole chord rotation demand θ_d would be fulfilled only by flexural deformations of the member, so that it could be written as follows [4]:

$$\theta_d = \theta_y + (\phi_d - \phi_y) \cdot L_{pl} \cdot \left(1 - \frac{L_{pl}}{L}\right) \tag{5.2}$$

where the term θ_y indicates the chord rotation at flexural yielding of the end sections of the beam. According to the aforementioned hypotheses, the latter can be expressed as follows:

$$\theta_y = \frac{1}{3} \cdot \phi_y \cdot \frac{L}{2} \tag{5.3}$$

In equations (5.2) and (5.3) the terms ϕ_y and ϕ_d represent the yielding curvature and the curvature demand of the end sections of the beam, respectively. The term L_{pl} indicates the conventional plastic hinge length usually adopted in the calculation of curvature deformation capacity of RC sections [4].
In the context of a structural assessment, it can be also useful to express the deformation demand in terms of ductility. Based on the relations derived above, the chord rotation ductility demand $\mu_{\theta,d} = \theta_d/\theta_y$ can be calculated as:

$$\mu_{\theta,d} = 1 + (\mu_{\phi,d} - 1) \cdot \left[6 \cdot \frac{L_{pl}}{L} \cdot \left(1 - \frac{L_{pl}}{L}\right)\right] \tag{5.4}$$

where the term $\mu_{\phi,d} = \phi_d/\phi_y$ represent the curvature demand at beam ends. By inverting the previous equation, an expression to estimate such curvature deformation demand can be obtained:

$$\mu_{\phi,d} = 1 + \frac{(\mu_{\theta,d} - 1)}{\left[6 \cdot \frac{L_{pl}}{L}\left(1 - \frac{L_{pl}}{L}\right)\right]} \tag{5.5}$$

The term in squared brackets in the denominator assumes values in the range $]0; 1[$, so its variation has a great influence on the curvature demand $\mu_{\phi,d}$. Values of the ratio L_{pl}/L suggested to be used in engineering practice for beam sections properly designed to obtain a ductile behaviour are usually in the range $0.08 \div 0.10$, despite much lower values may be more appropriate to be used when significant localization of deformations are expected (see Appendix C, section C.4.3.2). For the sake to provide an example, by considering a value $L_{pl}/L = 0.09$ the term in squared brackets at the denominator of equation (5.5) assumes the value 0.5 and the curvature demand can be approximately estimated as:

$$\mu_{\phi,d} = 1 + \frac{(\mu_{\theta,d} - 1)}{0.5} \tag{5.6}$$

To gain some sensibility on the deformation demand obtainable through the aforementioned expressions, it is useful to consider a simple example. Let consider a 4m-long RC beam with end sections characterized by a yielding curvature $\phi_y = 0.01\, m^{-1}$. The corresponding beam chord rotation at yielding would be $\theta_y = 0.66\%$. By hypothesizing a differential settlement $\delta_d = 0.1m$, equation (5.6) would provide a curvature ductility demand $\mu_{\phi,d} = 6.5$, which can be a non-negligible portion of the total

curvature capacity, considering usual geometry and material parameters for RC beam sections. Of course, the previously reported formulations lead to a quite severe and safe-side estimation of the curvature demand, since in reality part of the chord rotation demand would be accommodated by means of shear deformations and fixed-end rotations, which have been neglected in the expressions (5.2) and (5.3).
Moreover, in a real condition the ground settlement field occurring at the base of the structure does not necessary lead to the simplified and ideal deformed configuration reported in Fig. 5.1b, e.g., rotations of beam-columns joints can occur. To analyze real scenarios, more advanced modelling methodologies need to be adopted to analyze the structural response and so determine the chord rotation demand at beams, as well as the other deformation parameters at various structural members. In particular, numerical simulations performed using nonlinear finite element analyses (NLFEA) can be a valuable tool to do so. Application of numerical analyses to study the response of RC buildings subjected to differential settlements have been proposed by several works. Negulescu et al. [187] performed parametric NLFEA on a one-bay one-story RC frame modeled using fiber-based beam-column elements and subjected to ground settlement at one of the column supports, varying the foundation type, the characteristics of the RC frame and the inclination and magnitude of the imposed ground settlement. Fotopoulou et al. [188] developed NLFEA of RC frame structures without infills, again modeled using fiber-based elements. Quasi-static time history of displacements were imposed at building supports, to simulate the differential settlements induced by ground liquefaction. The results showed development of significant inelastic deformation demand at beams ends. Lin et al. [35] and Desbrousses and Lin [34] performed NLFEA implementing nonlinearity of the structural behaviour using concentrated plastic hinges at the ends of beams and columns, defined according to FEMA 356 [220]. In some of the analyzed cases, failure occurred in column due to excessive tension axial load. Such a scenario not necessarily reflects the behaviour of a real structure. For this reason, in applying displacement histories at supports it may be suitable to monitor the vertical reaction of the supports at which an imposed displacement history is applied. In fact, depending on the foundation type, if the vertical reaction at one of the supports would become negative (i.e., the support would "pulling" the structure downwards), then the analysis should in some cases continue without imposing an a priori determined motion at that support. A structural modelling approach similar to that used in the latter study, i.e., making use of elements with concentrated plasticity to study RC frame buildings subjected to differential settlement, has then been adopted by Miano et al. [189], employing plastic hinge laws defined according to a model specifically derived for RC elements with plain rebars [221]. The analyses were performed imposing different settlement profiles with progressively increasing magnitudes at the base of the structures, also considering motions in the horizontal and inclined directions, in order to accounting for a wide range of possible settlements profiles, though not necessarily referring to a ground deformation phenomenon associated to a specific cause.
Indeed, since the settlements magnitude, direction and spatial distribution are the input information used in the structural analyses, they do have a significant impact on the results. Consequently, uncertainty in their definition leads to a corresponding

uncertainty in the simulated structural response, i.e., in the estimated deformation demand at structural members. A first step to reduce the uncertainty in the ground motion profile is the identification of the causes. Various phenomena can induce ground settlements below built structures, including soil consolidation, subsidence, tunnelling, excavations, landslides, earthquakes, seismic liquefaction, water seepages, etc. [85]. These different causes can lead to significantly different settlement profiles at buildings foundations, as shown in the example reported in Fig. 5.2 [185].

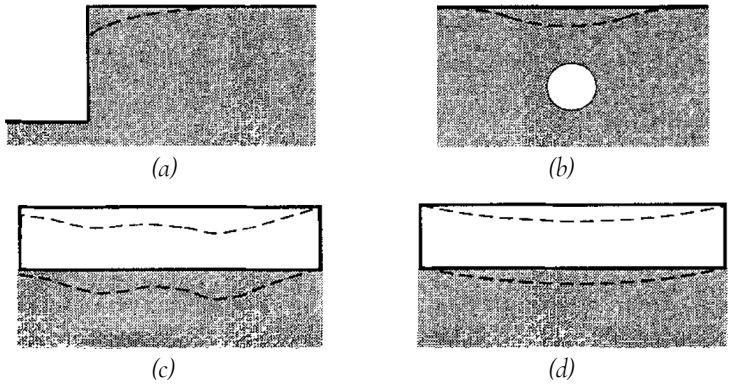

Fig. 5.2 Examples of ground deformation profiles associated to (a) Open cut excavations; (b) Tunnelling; (c) Building self-weight; (d) Beam analogy (From Boone [185]*)*

Moreover, even if the causing phenomenon is known, it is not straightforward to determine the ground deformation profiles affecting the structures. For some scenarios, simplified models have been developed to provide estimations of the ground settlement profiles and are widely used in practice [185]. As an example, for the case of tunnelling-induced settlements, Peck [222] proposed a simple model to describe a bidimensional ground settlement profile due to tunnelling, assuming that the greenfield settlements (i.e., undisturbed by the buildings) can be modelled as a Gaussian function, defined using few geometric characteristics of the tunnel and mechanical parameters of the soil. Such an approach is indeed based on several simplifications, first of all the fact that the real deformation phenomenon is three-dimensional [223]. By means of experimental tests on scaled model, Laefer et al. [36] showed that the adoption of the greenfield displacement profile may lead to relevant underestimations of the ground settlements below the buildings.

Considering the aforementioned aspects it appears clear that, in order to improve the definition of the ground settlements field occurring in a certain urban area, in situ measurements are usually very necessary, if not even mandatory, in practice. However, as anticipated in section 5.1, a different type of aid in this context could be gained through the exploitation of some specific remote sensing techniques, and in particular of the MT-DInSAR techniques. An insightful application of these techniques in a case in which tunnelling-induced ground settlements needed to be estimated has been proposed by Giardina et al. [66] and Macchiarulo et al. [67]. In their work, instead of the

usually adopted Gaussian distribution of settlement profile based on greenfield hypothesis, a modified Gaussian formulation was applied. Such modified formulation was obtained by using the values of ground deformation provided by MT-DInSAR data. This way, a better estimation of the actual ground deformation profile has been obtained, somehow taking into account of soil-structure interaction effects. This kind of remote sensing applications appear to be really promising, and can represent an effective aid for the estimation of the ground settlements field to be used as input in the analysis of the structural response of real buildings subjected to differential settlements. The exploitation of MT-DInSAR data to improve the knowledge about ongoing, or past, ground deformation processes are not restricted to the cases of tunnelling-induced settlements. In fact, this tool can be useful to monitor ground motion phenomena associated to several possible causes, so resulting in have a very broad field of applications. It is so that the exploitation of MT-DInSAR remote sensing techniques could be an effective aid in the analyses of deformation demand in structures subjected to differential ground settlements.

5.3 Summary about basics of MT-DInSAR monitoring

Differential Synthetic Aperture Radar Interferometry (DInSAR) is a satellite remote sensing technique which allows to extract information on the motion experienced by objects on the Earth surface, using radar images acquired by special classes of satellites. Radar satellite systems most commonly used for earth surface monitoring applications revolve around the Earth on near-polar orbits, performing trajectories slightly inclined with respect to the meridians (at angles of a few degrees), travelling half of their orbit from the north pole to the south pole (descending orbit, DES) and half from the south pole to the north pole (ascending orbit, ASC). As they fly along their orbit, the radar sensors mounted on the satellite emit electromagnetic signals towards the Earth surface and acquire the backscattered echoes, recorded as time delays and, therefore, as distances between the points on the ground and the sensor.

Fig. 5.3 shows as an example the scheme of the acquisition geometry of a radar satellite, which travels along the flight direction and sends electromagnetic signals that invest the earth's surface in an area, called antenna footprint, having a certain extent in the two directions parallel and orthogonal to the satellite's line of flight. The position of an object on the Earth surface can be located with reference to the satellite trajectory using a cylindrical coordinate system (x, r, θ).

The x coordinate is called azimuth, whose axis coincides with the satellite's line of flight, which forms an angle ϕ (called the heading angle) with the direction of the meridians. The coordinate r is called the slant range (or simply range) and represents the distance between the sensor and the ground point along the satellite line of sight (LOS), i.e. along the pointing direction of the radar in which the electromagnetic signals affecting the objects (targets) in the illuminated area are emitted and recorded. The ground projection of the range direction is called the ground range. The third coordinate θ, called off-nadir or look angle, is the angle formed between the vertical direction and the LOS, which varies depending on the type of satellite and its operating mode.

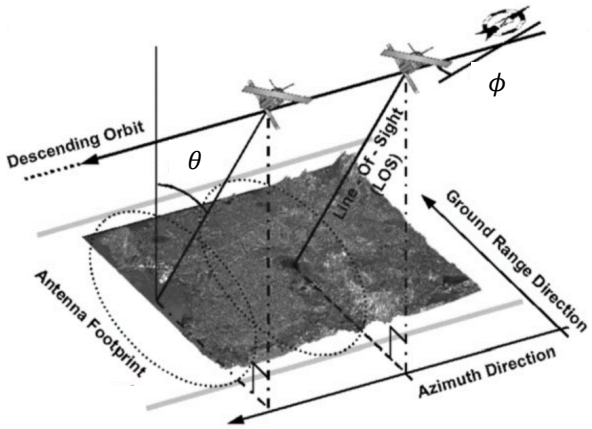

Fig. 5.3 Scheme of the acquisition geometry of a radar satellite (Adapted from Colesanti and Wasowsky [224])

The antenna footprint is characterized by a width in the ground range direction called the swath width. Usually provided values of the off-nadir angle θ refers to the center of the footprint. However, the variation of this angle, although directly related to the extent of the area covered in the actual measurement configuration, can be considered small enough so that the angle θ evaluated at the center of the scene can be sufficient to describe the acquisition geometry. In commonly used radar satellite systems, in order to improve coverage and resolution along the azimuth direction, the use of Synthetic Aperture Radar (SAR) systems has been introduced. This approach uses the movement of the antenna along the satellite's line of flight to improve spatial resolution in the azimuth direction, while leaving range resolution unchanged, using the concept of a "synthetic antenna", i.e., without increasing the size of the physical antenna.
By processing of the data detected by the antenna related to a certain area (this operation is sometimes referred to as focusing of the raw data [225]), a radar image is generated, consisting of pixels defined in the two directions azimuth and slant range, typically called radar coordinates. A SAR image is then represented, in digital format, through a matrix of $n \cdot m$ pixels in radar coordinates characterised by a modulus or amplitude E and a phase φ, which contain the information related to the signals backscattered from the scene on the ground. The combination of the motion of the satellites along their orbit with the rotational motion of the Earth around its axis makes it possible to obtain radar images of the same area at different time instants. The time taken by the satellite to revisit the same area is called the revisit time. The availability of more SAR images acquired over the same area at different times allowed for the development of DInSAR techniques for measuring deformations of objects on the Earth surface [75]. The DInSAR technique, by exploiting the phase difference between two satellite SAR images acquired by the satellite over the same area at different times (and also from two orbital positions which may be slightly different), allows to measure of the LOS component of the deformation of objects, Fig. 5.4.

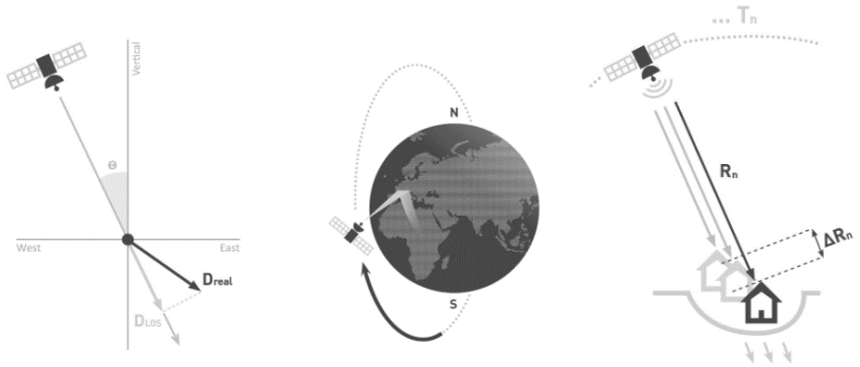

(a) *(b)* *(c)*

Fig. 5.4 Scheme of the basic principles of satellite radar interferometry a) Satellite line of sight and projection of a deformation vector of a point on the earth surface on the satellite line of sight; b) Orbit of the satellite; (c) Detection of ground and building deformations employing radar satellite images collected for the same area in different time instants (adapted from TRE Altamira [226]*)*

In order to implement this technique using a couple of SAR images, one of the two images is chosen as the reference and is called the master image (typically corresponding to the image acquired first in time), while the other is called the slave image. The time elapsed between the acquisitions of the two images is called "temporal baseline", while the distance between the two positions along the satellite's orbit during the two acquisitions is called "spatial baseline". The displacement measurements that can be obtained from interferometric analysis are differential not only with regards to time, but also with reference to spatial location. Displacements measured are in fact computed with respect to a time reference, being it the acquisition date of the chosen master image (Reference Date), and with respect to spatial reference, being it a pixel of the images (Reference Point) chosen in an area considered stable or of known deformation. The measured phase difference Δ_φ (also called interferometric phase) between the corresponding pixels of two acquired radar images is interpreted as a change in phase of the slave image with respect to the reference master image.
The phase difference Δ_φ between two SAR images gives rise to the so-called interferogram. The interferogram is a two-dimensional image in the range and azimuth plane represented with a series of fringes (as the interferometric phase is a wrapped phase), the values of which lie between $-\pi$ and $+\pi$, see Fig. 5.5.

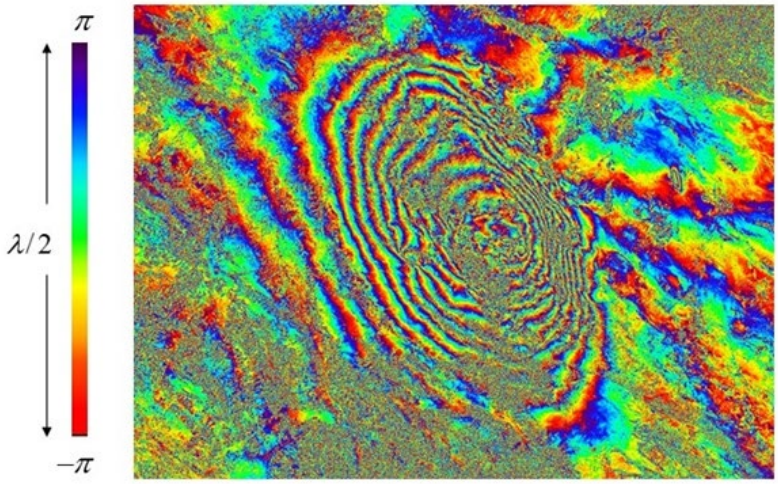

Fig. 5.5 Example of co-seismic interferogram related to the earthquake that struck the city of L'Aquila (Italy) on 6 April 2009 and obtained with COSMO-SkyMed SAR (adapted from ReLUIS [85]*)*

The phase difference Δ_{φ} is the sum of several phase contributions and can be expressed as follows:

$$\Delta\varphi = \Delta\varphi^{deformation} + \Delta\varphi^{topograpic} + \Delta\varphi^{atmospheric} + \Delta\varphi^{orbit} + \Delta\varphi^{noise} \quad (5.7)$$

where $\Delta\varphi^{deformation}$ is the deformation signal corresponding to the displacement that occurred between the two SAR acquisitions; $\Delta\varphi^{topograpic}$ is the topography component of the signal of the observed scene with respect to a global reference system and depends on the interferogram baseline and the elevation of the point; $\Delta\varphi^{atmospheric}$ is the signal due to possible atmospheric inhomogeneities between the two SAR acquisitions that introduce spurious delays in the signal; $\Delta\varphi^{orbit}$ represents the phase residuals due to the inaccurate knowledge of the orbits described by the satellite during the acquisitions; $\Delta\varphi^{noise}$ is the phase difference related to the decorrelation noise. This latter phenomena is due to both spatial decorrelation, caused by an excessive distance (i.e., spatial baseline) between the orbits travelled by the satellite during the two acquisitions, and to temporal decorrelation, caused by a change in the electromagnetic properties of the ground scene (e.g. due to weather events or to other changes in the scene) especially in the case of acquisitions far apart in time.

It is useful to provide some additional highlight to clarify the phenomena which generates the various phase difference contributions present in eq. (5.7). In particular, the presence of the topographic phase $\Delta\varphi^{topograpic}$ is due to the fact that in next image acquisitions the satellite does not retrace exactly the same trajectories on the orbit, the total phase difference $\Delta\varphi$ contains information on both the deformation of ground objects and the topography of the area [227].

In order to retrieve he phase component $\Delta\varphi^{deformation}$ associated with the deformation of the ground objects it is necessary to remove these other phase contributions from the

total interferometric phase $\Delta\varphi$. Dedicated procedures and algoritms are used to compute estimations of the additional contributions, in other to remove them from the total interferometric phase and so obtain the phase contribution $\Delta\varphi^{deformation}$ only related to the deformations. In particular, to evaluate the topographic contribution $\Delta\varphi^{topograpic}$ associated with the average topography of the scene, the following procedure is adopted. Taking into account the distance between the orbits actually travelled by the satellite during image acquisition (spatial baseline), the topographic phase is calculated for each point on the SAR reference grid from the sensor-target distance between the two images, estimated using knowledge of precise orbital information and an accurate external DTM. This phase information constitutes a so-called "synthetic interferogram". This phase contribution is then removed from the total phase $\Delta\varphi$. The result of this removal leads to the generation of the so-called "differential interferogram", i.e. a wrapped interferogram where the phase information for each pixel is mainly related to the deformations that occurred to the ground object during the time interval between the two acquisitions.
Assuming that there are no topographic phase residuals and that the phase contributions due to the atmospheric, orbit and noise contributions can be removed or neglected under appropriate considerations, the phase contribution $\Delta\varphi^{deformation}$ becomes known. This phase contribution would be then almost only associated to variation δ_{los} of the distance between the sensor and the target object on the ground measured along the satellite line of sight, developed in the time interval between the two acquisitions. In such a condition, the deformation phase could be expressed as follows:

$$\Delta\varphi^{deformation} = \frac{4\pi}{\lambda} \cdot \delta_{los} \tag{5.8}$$

where λ is the wavelength of the transmitted/received signal. By inverting equation (5.8), the expression for the estimation of the variation δ_{los} of the distance between the sensor and the target object on the ground measured along the satellite line of sight can be obtained:

$$\delta_{los} = \frac{\Delta\varphi^{deformation}}{2\pi} \cdot \frac{\lambda}{2} \tag{5.9}$$

It follows from equation (5.9) that a phase change of 2π, i.e., an entire interferometric fringe, corresponds to a displacement along the LOS of $\delta_{los} = \lambda/2$. In particular, since the values of phase $\Delta\varphi^{deformation}$ belong to the range $]-\pi;\ \pi]$, eq. (5.10) can be also interpreted in the version rewritten in the following:

$$\delta_{los} = \frac{\Delta\varphi^{deformation}}{\pi} \cdot \frac{\lambda}{4} \tag{5.10}$$

From eq. (5.10) it can be observed that the deformation δ_{los} directly retrieved from the interferometric phase $\Delta\varphi^{deformation}$ can have a maximum value of $\pm\lambda/4$. Actually, the real value of the deformation projected on the satellite line-of-sight may be quite larger than that threshold. In order to obtain the actual deformation value, a process called "phase unwrapping" is required to be performed on the interferometric phase calculated directly from the SAR image pairs, in order to recover the absolute phase change

(moving from the so-called "wrapped" interferometric phases to the "unwrapped" interferometric phases). In this way, it is possible to detect line-of-sight deformation values much larger than $\pm \lambda/4$. Beside this, the so retrieved deformation measure is still proportional to the wavelength of the radar signal. Accordingly, it can be observed that the accuracy with which surface displacements can be measured is equal to a fraction of the wavelength λ at which the SAR sensor operates. Being the sensor working in the microwave range, with wavelengths of typically a few centimeters, it can be realized that it is therefore possible to achieve accuracies on deformation measures of even a few millimeters.

Besides the accuracy of the deformation measures, another issue arises when it is needed to retrieve information regarding the three-dimensional components of the deformation measure for an object on the Earth surface. As a matter of fact, since the satellite sends and receives the microwave signals along the LOS, it only measures the component of the real displacement along the LOS. By decomposing the real displacement δ into its three Cartesian components δ_E, δ_N and δ_U (respectively along the East, North and Vertical directions), the measured displacement along the LOS can be expressed by the sum of the projections onto the LOS of the three Cartesian components of the real displacement. This can be stated as expressed by eq. (5.11), for the generic case of SAR images acquired from the ascending or descending (A/D) orbits:

$$\delta_{LOS_{A/D}} = \delta_E \cdot c_{E_{A/D}} + \delta_N \cdot c_{N_{A/D}} + \delta_U \cdot c_{U_{A/D}} \tag{5.11}$$

Where $c_{E_{A/D}}$, $c_{N_{A/D}}$, $c_{U_{A/D}}$ are the direction cosines of the angles $\alpha_{E_{A/D}}$, $\alpha_{N_{A/D}}$, $\alpha_{U_{A/D}}$, defined between the East, North and Vertical directions and the LOS direction, for the ASC and DES acquisition geometries respectively, as indicated in Fig. 5.6 and Fig. 5.7. These direction cosines represent the components of the unit vectors of the ASC and DES LOS directions, respectively indicated in Fig. 5.6 as $i_{LOS,A}$ and $i_{LOS,D}$, and they can be expressed, as widely known, as follows:

$$\begin{aligned} c_{E_{A/D}} &= cos\, \Phi_{A/D} \cdot sin\, \theta_{A/D} \\ c_{N_{A/D}} &= sin\, \Phi_{A/D} \cdot sin\, \theta_{A/D} \\ c_{U_{A/D}} &= cos\, \theta_{A/D} \end{aligned} \tag{5.12}$$

Range of values for direction cosines $c_{E_{A/D}}$, $c_{N_{A/D}}$, $c_{U_{A/D}}$ are reported in Table 5.1 considering the acquisition geometries of some radar satellites [228], [229]. These parameters are needed to retrieve information about the components δ_E, δ_N and δ_U of the actual deformation. This aspect can be addressed in different ways.

If the direction of the real displacement were known, and so would thus be its angle relative to the direction of the LOS, the determination of the intensity of the real displacement would be straightforward. Obviously, being χ the angle subtended between the actual deformation direction and the direction of the LOS, the intensity of the real displacement can be derived directly just using information obtained from one orbit:

$$\delta = \frac{\delta_{LOS_{A/D}}}{cos(\chi)} \tag{5.13}$$

However, this approach is almost never applicable in practice, as it is difficult to estimate or assume the exact direction of motion of an object (unless it is already being monitored with other instruments or techniques). On the other hand, if it is known at least the plane containing the real displacement vector (or, equivalently, any direction orthogonal to the real displacement vector), it is still possible to retrieve the intensity and components of the real displacement, if LOS deformations acquired from two different orbits (e.g., ASC and DES) are available for the object to be monitored.
Let consider any direction orthogonal to the real displacement vector (i.e. perpendicular to a plane containing the real displacement vector) This direction can be identified by the cosines of the angles $\alpha_{\perp}$, $\beta_{\perp}$ and $\gamma_{\perp}$ subtended between the direction orthogonal to the plane containing the real displacement vector and the Coordinate axes (East, North, Vertical). Once the real displacement vector has been decomposed into its three Cartesian components δ_E, δ_N and δ_U (East, North, Vertical), the sum of the projections of these components on the direction orthogonal to the real displacement must be zero.

Table 5.1 Sensitivity evaluation of the instruments in the different directions (From Talledo et al. [229])

Satellite	**ESR 1/2**	**ENVISAT**	**RADARSAT 1/2**	**COSMO-SkyMed**
Acquisition mode	Stripmap	Stripmap	Stripmap	Stripmap
Φ [°] *	8.5	8.5	8.6	7.86
θ [°] **	23	15 - 45	20-50	20-60
c_E [%]	0.386	0.256 – 0.699	0.338 – 0.757	0.339 – 0.858
c_N [%]	0.580	0.380 – 0.105	0.511 – 0.114	0.470 – 0.118
c_U [%]	0.921	0.966 – 0.707	0.939 – 0.643	0.939 – 0.500

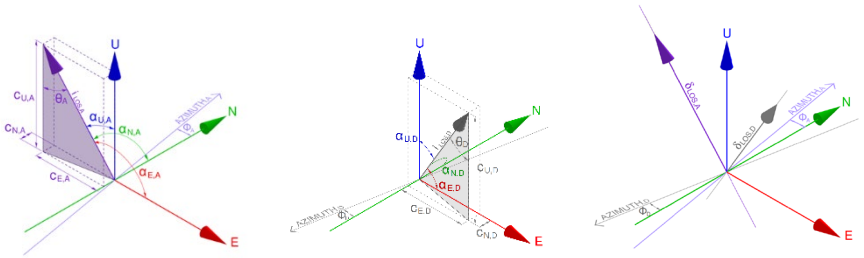

(a) *(b)* *(c)*

Fig. 5.6 Three-dimensional views of satellite acquisition geometry (a) ASC orbit; (b) DES orbit; (c) Superposition of LOS directions from ASC and DES orbits (adapted from Talledo et al. [229])

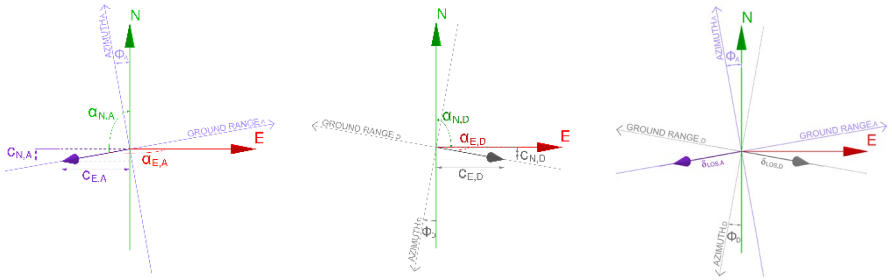

(a) (b) (c)

Fig. 5.7 Top views of satellite acquisition geometry (a) ASC orbit; (b) DES orbit; (c) Superposition of LOS directions from ASC and DES orbits (adapted from Talledo et al. [229])

This translate into the following equation:

$$\delta_E \cdot cos(\alpha_\perp) + \delta_N \cdot cos(\beta_\perp) + \delta_U \cdot cos(\gamma_\perp) = 0 \tag{5.14}$$

In order to calculate the components δ_E, δ_N and δ_U of the actual deformation vector, it is possible to set up a linear system with three unknowns and three equations, by using twice eq. (5.11), written for both the ASC and the DES orbit, and by adding eq. (5.14), as shown in the following:

$$\begin{cases} \delta_E \cdot c_{E_A} + \delta_N \cdot c_{N_A} + \delta_U \cdot c_{U_A} = \delta_{LOS_A} \\ \delta_E \cdot c_{E_D} + \delta_N \cdot c_{N_D} + \delta_U \cdot c_{U_D} = \delta_{LOS_D} \\ \delta_E \cdot cos(\alpha_\perp) + \delta_N \cdot cos(\beta_\perp) + \delta_U \cdot cos(\gamma_\perp) = 0 \end{cases} \tag{5.15}$$

The linear system proposed in eq. (5.15) can be rewritten in a compact way as follows:

$$\overline{\boldsymbol{T}} \cdot \overline{\boldsymbol{\delta}} = \overline{\boldsymbol{s}} \tag{5.16}$$

where:

$$\overline{\boldsymbol{T}} = \begin{bmatrix} c_{E_A} & c_{N_A} & c_{U_A} \\ c_{E_D} & c_{N_D} & c_D \\ cos(\alpha_\perp) & cos(\beta_\perp) & cos(\gamma_\perp) \end{bmatrix} \tag{5.17}$$

$$\overline{\boldsymbol{\delta}} = \begin{bmatrix} \delta_E \\ \delta_N \\ \delta_U \end{bmatrix} \tag{5.18}$$

$$\overline{\boldsymbol{s}} = \begin{bmatrix} \delta_{LOS_A} \\ \delta_{LOS_D} \\ 0 \end{bmatrix} \tag{5.19}$$

The need to define a plane containing the real displacement vector, or a direction orthogonal to it, leads to the fact that the approach described above requires more

information than just the data provided by the LOS deformations. However, it still represents a method which may be effectively adopted, depending on the object being analyzed. If, for example, the deformation of an object is impeded or can be assumed negligible along a certain direction, then the choice of the plane containing the real displacement vector may be quite straightforward. Another case in which complementary information about the deformation of an object are available is the one in which the investigate point is known to experience a rigid body motion.
On the other hand, in the absence of any helpful information regarding the direction of the real deformation vector, a simplification is adopted to solve the linear system (5.15) and to so retrieve the deformation components δ_E, δ_N and δ_U. Looking at the values of direction cosines reported in Table 5.1, it can be seen that for almost all the considered satellites and acquisition modes, the direction cosine $c_{N_{A/D}}$ assumes quite low values. So, the central terms in the first two rows of the system (5.15) may be assumed to be quite negligible:

$$\begin{aligned} &\delta_N \cdot c_{N_A} \approx 0 \\ &\delta_N \cdot c_{N_D} \approx 0 \end{aligned} \tag{5.20}$$

According to this observation, it appears that the solution of the linear system (5.15) would not be so much influenced if the following assumption would be introduced:

$$\delta_N = 0 \tag{5.21}$$

Actually, assuming the assumption stated by eq. (5.21) means to assume that the actual real deformation vector would be orthogonal to the North direction, i.e., belonging to the East-Vertical plane. Such a condition can also equivalently be expressed using eq. (5.14) adopting the following values for the cosine terms $cos(\alpha_\perp)$, $cos(\beta_\perp)$ and $cos(\gamma_\perp)$:

$$\begin{aligned} &cos(\alpha_\perp) = 0 \\ &cos(\beta_\perp) = 1 \\ &cos(\gamma_\perp) = 0 \end{aligned} \tag{5.22}$$

By introducing assumption (5.21) in eq. (5.15), a simplified version of the linear system is obtained, which is composed by two equations with the two unknowns δ_E and δ_N:

$$\begin{cases} \delta_E \cdot c_{E_A} + \delta_U \cdot c_{U_A} = \delta_{LOS_A} \\ \delta_E \cdot c_{E_D} + \delta_U \cdot c_{U_D} = \delta_{LOS_D} \end{cases} \tag{5.23}$$

For the sake of completeness, the solution of the system is provided herein:

$$\delta_E = \left(\frac{c_{U_A}}{c_{U_A} \cdot c_{E_D} - c_{U_D} \cdot c_{E_A}}\right) \cdot \delta_{LOS_D} - \left(\frac{c_{U_D}}{c_{U_A} \cdot c_{E_D} - c_{U_D} \cdot c_{E_A}}\right) \cdot \delta_{LOS_A} \tag{5.24}$$

$$\delta_U = \left(\frac{c_{E_D}}{c_{U_A} \cdot c_{E_D} - c_{U_D} \cdot c_{E_A}}\right) \cdot \delta_{LOS_A} - \left(\frac{c_{E_A}}{c_{U_A} \cdot c_{E_D} - c_{U_D} \cdot c_{E_A}}\right) \cdot \delta_{LOS_D} \tag{5.25}$$

The adopted assumption (5.21) is obviously a quite strong choice (except for some particular structures for which assumption (5.21) actually represents a condition close to

reality) and leads to an approximated result. However, it is worth to highlight that other options adoptable in trying to retrieve also the deformation component δ_N may not lead to adequate results. In fact, considering the LOS direction defined by the cosines whose values have been reported in Table 5.1, it can be understood that the accuracy in the deformation component along the North-South direction would be much lower than that for the other two components. Consequently, having to accept the limitations due to the satellites acquisition geometries, Consequently, having to accept the limitations associated with the acquisition geometries used by the satellites, it is usual to opt against estimating the North-South component. Based on these observations, the simplification introduced with eq. (5.21) is largely adopted in practice in order to obtain an estimation of the displacement components δ_E and δ_U.

The application of conventional two-images DInSAR technique, based on the analysis of individual interferograms is characterized by several limitations. Among them, one is related to the fact that using this technique, in many situations it can be difficult to effectively separate the phase contribution related to ground deformations from those related to errors in the DTM used for topographic phase compensation, errors due to inaccurate orbital information, and variations in atmospheric conditions between acquisitions, which are difficult to compensate for in the absence of reliable atmospheric models. In order to overcome the limitations of the conventional DInSAR techniques, the interest of the scientific community has increasingly focused on the development of advanced Multi-Temporal DInSAR (MT-DInSAR) techniques. Such approaches are based on the use of larger datasets, consisting of many (dozens, sometimes hundreds) of SAR images of the same area, which are used to produce differential interferograms then suitably combined to derive information on the evolution of surface displacements over time. Despite considerable algorithmic complexity and significantly longer computation times compared to classical DInSAR interferometric techniques, the adoption of MT-DInSAR approaches which make use of a large number of images and interferograms leads to considerable improvements in the accuracy of the deformation measures, thanks to the estimation of possible atmospheric contributions and topographic errors.

The results obtained from multi-temporal interferometric processing are the displacement time series for a set of pixels in the radar images which are coherent in the interferometric analysis. Coherent pixels are usually refereed as “persistent scatterers” (PS). Each PS is associated with a surface area or an object on the earth surface that depends on the resolution cell size of the SAR data. For each PS the spatial location is provided in terms of geographical coordinates (i.e., latitude and longitude) and elevation with respect to a global reference system. Also available for each PS are information for the identification of the components of the LOS vector. The displacement time series provided for each PS describe the LOS component of the displacement measured for the backscattering objects contained in the cell corresponding to associated pixels of the radar images. The displacement history refers to the date of the acquisition of the oldest image used, and to a reference point chosen among the PSs available in the scene. So, the deformation measures are relative in space and in time, being referred to a specific time instant and being defined with respect to the motion of the reference point. Since displacement time histories area available, for each PS a mean value of LOS deformation

velocity is also usually computed, as linear regression of the associated displacement time history. An example of LOS displacement time history obtained for a PS is presented in Fig. 5.8a. In Fig. 5.8b, an example of map reporting LOS mean deformation velocity values for each PS of a monitored area is provided. By accepted convention, positive values of LOS displacement or mean deformation velocity indicate PSs which are moving towards the satellite.

Different advanced multi-temporal satellite SAR interferometry techniques have been developed. Some of the most popular include the permanent scatterers (PSInSAR®) technique [230], the small baseline subsets (SBAS) technique [78], the SqueeSAR® technique [231] and the Stanford Method for Persistent Scatterers (StaMPS) technique [232]. A description of the characteristics of each technique goes beyond the scopes of the present work and it is not addressed herein. Information about characteristics of different multi-temporal DInSAR processing techniques can be found in [85].

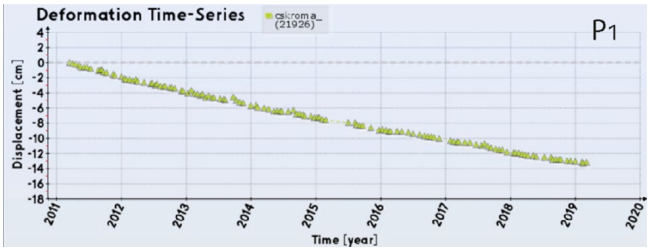

(a)

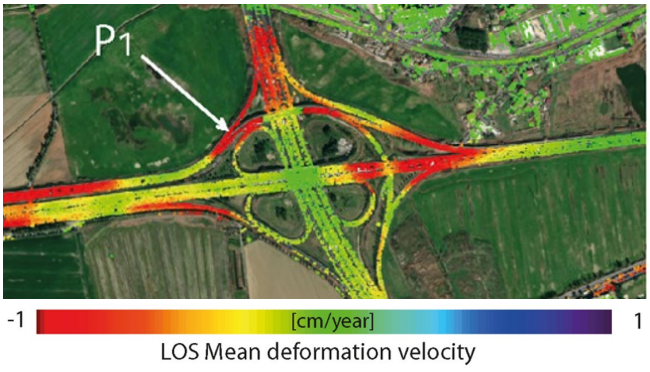

(b)

Fig. 5.8 (a) Example of LOS displacement time history for a persistent scatterer (PS); (b) Example of map reporting PSs present over an area, each one colored using a contour scale representative of the value of mean deformation velocity of PSs. Results have been obtained using COSMO-SkyMed images for the area of Rome (Italy) acquired in the period 2011-2019 processed by CNR-IREA with Small Baseline Subsets (SBAS) multi-temporal DInSAR technique (Adapted from Talledo et al. [229]*)*

5.4 Critical aspects for the use of MT-DInSAR data as an aid to monitor deformation demands in constructions

Among the possible uses of the MT-DInSAR data, one in particular is of interest to be exploited in the process of structural assessment of constructions, i.e., the use of those data to improve the estimations of ground motion characteristics to be employed for the evaluation of deformation demands in structural members. In this section, critical aspects relevant to that aim are addressed, highlighting major issues which currently limit the fully exploitation of this kind of use of MT-DInSAR data.

This first aspects worth to be mentioned regards the spatial distribution of PSs in areas of interest. Considering a map representation of PSs obtained with multi-temporal interferometric techniques at full spatial resolution, superimposed on an optical image or a cartographic map, it is possible to see that PSs are distributed on a sparse grid and densified in the vicinity of targets or anthropic structures, such as buildings and infrastructures. It is also quite common to observe some areas without PSs. In Fig. 5.9 is reported an example reported by Talledo et al. [229], which illustrates the distribution of PSs obtained from the ascending dataset (green PSs) and a descending dataset (red PSs) for an area of Rome (Italy), where it is possible to detect both areas characterised by a high density as well as with the absence of PSs. It should first be emphasised that the PSs of the two ascending and descending datasets are in general not coincident and that they may present significantly different spatial distribution, depending mainly on the different acquisition geometries of the satellites in the two orbits. In both Fig. 5.9a and Fig. 5.9b it can be seen that PSs are lacking both in several vegetated areas, as well as in some built areas. An emblematic case is the lack of PSs on the central portion of a bridge deck, visible in the upper central part of the scene.

The reasons behind the lack of PSs in certain areas are not always unambiguously identified. In some cases, the absence is presumably associated to the absence of sufficiently backscattering objects within the area of interest. This can be due in general to the presence of temporal decorrelation effects, as in the case of flat surfaces and vegetated areas. In other cases on the other hand, the absence of measurement points cannot be justified by those phenomena. It can be due, instead, to the fact that the algorithm used in the MT-DInSAR analysis may exclude PSs characterised by a highly time-variable deformation behaviour and consequently associated low values of the temporal coherence. This issue can occur for example in the presence of unexpected deformation effects, or in the case of structures subjected to heavy traffic loads, strong winds, sudden and relevant changes in temperature or secondary vibrational effects. Indeed, the lack of PSs associated to this latter aspect can be troubling when it occurs in civil infrastructures for which the monitoring of deformations is desired.

The analysis of MT-DInSAR data can be performed considering the PSs obtained for one orbit or for both the ascending and descending orbits. In general, the analysis of data obtained from the processing of a single orbit (ascending or descending dataset) can provide preliminary information in relation to ongoing deformation phenomena, although it is well known that it is not possible to draw definitive considerations from the deformation measurements of a single dataset.

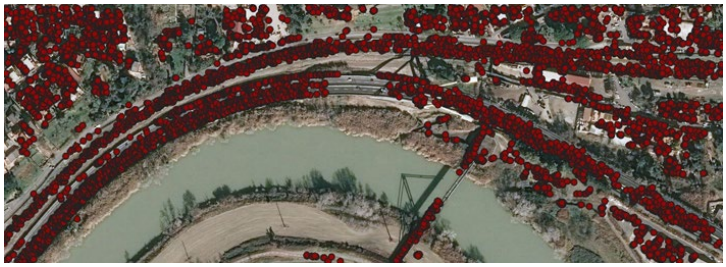

(a)

(b)

Fig. 5.9 Example of PSs spatial distribution related to: a) ASC (red points) and b) DES (green points) orbits (Adapted from Talledo et al. [229]*).*

In fact, the information from the MT-DInSAR data provide the displacement and mean displacement velocity components along the LOS. As a general rule, the more the direction of the real displacement (or mean deformation velocity) vector deviates from the LOS direction, the smaller the component measured by the satellite. In Fig. 5.10 examples are depicted showing different possible configurations of the real deformation vector with respect to the LOS. As a limiting condition, in the case of the direction of the real displacement (or mean deformation velocity) is perpendicular to the LOS, the component measured by the sensor is zero (Fig. 5.10c). For this reason, it is important to note that an indication of high displacement (or mean deformation velocity) along the LOS is a certain indication of an ongoing deformation process. On the other hand, a low value of LOS displacement (or mean deformation velocity) does not guarantee the absence of ongoing deformation phenomena. It is also interesting to note how the use of a single dataset can provide significant indications in order to determine the real displacement vector, when used in association with data from pre-existing studies or traditional monitoring techniques, such as optical levelling or GNSS measurements.
In particular, if the direction of real deformation is known, it is then possible to derive the intensity of the displacement along that direction, starting from the projection measured along the LOS, as expressed by eq. (5.13). In fact, for certain types of instability phenomena it can be assumed that the main component of deformation would assume a specific direction (e.g., in the case of subsidence phenomena, it may be assumed that the main direction of displacement is vertical). However, it is worth to underline that

caution needs to be taken in adopting this kind of assumptions and that the proper selected main deformation direction must be evaluated case-by-case.
If the MT-DInSAR data obtained from both the ascending and descending orbits are available for the studied area, then combination of those information is possible in order to improve the information on the deformation phenomena taking place. In particular, the observation of LOS mean deformation velocity values in the scene makes it possible to get some information on the deformation phenomenon. Let consider for example the case shown in Fig. 5.11a, for which a pure vertical motion is represented. In that case, the sign of the LOS mean deformation velocity of the two acquisition geometries would be concordant and, in the case the angle of incidence would be the same for both ascending and descending geometries, the modulus of the LOS mean deformation velocity vector along the LOS would be the same for the two cases. On the other hand, considering the case of a real mean deformation velocity having horizontal direction, shown in Fig. 5.11b, it can be observed that the LOS deformations for the two orbits would have discordant sign and, again, equal modulus in the case of an equal angle of incidence. This is due to the fact that in one geometry the sensor detects a motion towards the satellite, while in the other geometry it measures a motion away from the satellite.
In order to fully exploit the information achievable by the availability of MT-DInSAR data from both the ASC and DES orbits for a studied area, it is possible to adopt the procedures described in section 5.3 to evaluate the components of PSs deformations along the Vertical and East-West directions. However, as previously underlined, the PSs identified for the ASC and DES dataset are mostly non-coincident and present deformation time series defined by different time vectors. Spatial resampling techniques can be employed in order to obtain a set of spatially referenced points where information of LOS deformation is available for both ASC and DES orbit in order to perform subsequent combinations. The resampling and combination phases can be performed either in the raster or in the vector space.

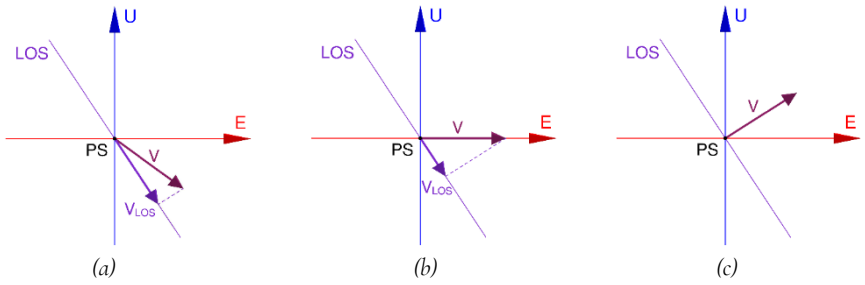

Fig. 5.10 Variability of the measured mean velocity component as a function of the direction of the real mean velocity: (a)-(b) Real velocity with component parallel to LOS; (c) Real velocity orthogonal to LOS (Adapted from Talledo et al. [229]*)*

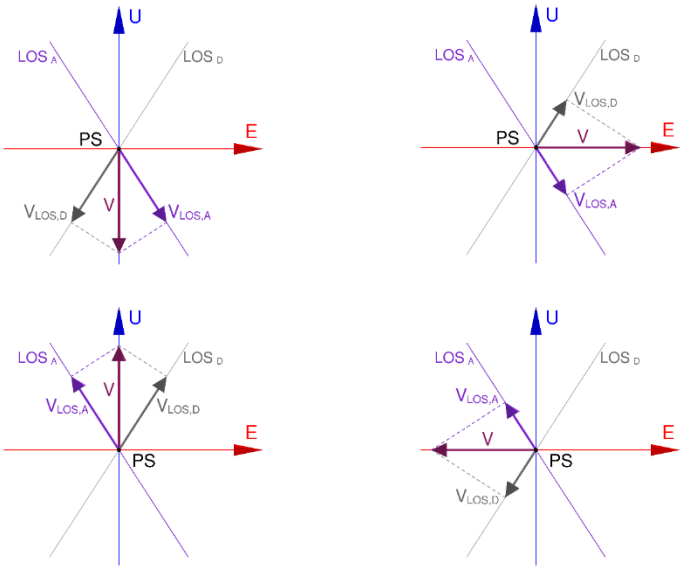

Fig. 5.11 Example of decomposition of the mean velocity vector of real displacement in ascending and descending geometry. a) Vertical velocity b) Horizontal velocity (Adapted from Talledo et al. [229])

The former ones, represented for instance by interpolation methods, requires different rasterization steps for the ASC and DES geometries. The latter techniques, for instance represented by nearest neighbors approaches [233], combine the ASC and DES datasets in the vector space.

Working with interpolation techniques has the advantage of providing continuous maps, although it is more difficult to account for the three-dimensional nature of the DInSAR data. On the other hand, working in vector space accounts easily for the actual 3D position of the points and easily permits the combination of displacement histories in order to compute Vertical and East-West components of displacement. However, with these latter approaches the number of PSs couples for which the combination can be performed can be limited, leading to a lower number of obtained points for which the Vertical and East-West components of displacement are available. In Fig. 5.12 is presented an example in which results of a spatial interpolation procedure are illustrated, followed by an evaluation of deformation components obtained by means of the eqs. (5.24) and (5.25). This application has been developed for the San Michele complex, a monumental building located close to the bank of the Tiber river in Rome, Italy. Details about the MT-DInSAR data and ancillary data used can be found in [234], [229]. The building geometry and the PSs obtained for the ASC (green) and DES (red) acquisition geometries are illustrated in Fig. 5.12a and Fig. 5.12b, respectively. In Fig. 5.12c and Fig. 5.12d are depicted the mean deformation velocity maps obtained for the building area, respectively for the ASC and DES datasets. It can be seen that in the South corner

of the building, negative mean deformation velocity values of approximately the same intensity are highlighted for both the acquisition geometries. After having performed the combination of deformation values, mean deformation velocity along the East-West and vertical direction has been obtained, as represented in Fig. 5.12c and Fig. 5.12d respectively. As expected, the results show a nearly vertical deformation trend for the South corner of the building.

In performing the combination of data from the two orbits, it is worth to recall that the MT-DInSAR data retrieved for the ASC and DES orbits are not referred to exactly the same time series. For this reason, in the case one of the approaches described in section 5.3 for combining the ASC and DES information wants to be adopted to retrieved displacement time-series of the Vertical and East-West components, a temporal resampling operation needs to be performed on the ASC and DES time series of the LOS deformation. The temporal resampling can be performed by the desired sampling frequency, chosen based on the specific desired application. Particular care should be taken because the displacement time series are differential, and temporally referred to the first acquisition.

When the beginning time of the resampled series is shifted in time for ASC and DES geometries, it is very important to trim the heading of the time series that starts first, in order to obtain the same starting time. This operation must be followed by the depuration of the cumulated displacement at the trimming point from the entire displacement time history. Once the ASC and DES resampled time series having the same sampling frequency and starting time are available, it is then possible to combine the displacement measures from ASC and DES geometries for each instant, so obtaining the time series for the deformation components along the Vertical and East-West directions.

An additional relevant aspect it is worth to be pointed out, regarding the use of deformation measures retrieved from displacement time series. From those measures, the total cumulative displacements undergone by different parts of the structures can be retrieved. These, in turn, could be adopted to compute the total differential ground settlements imposed to the structure, needed to compute the structural response and so evaluate deformation demands in structural members.

However, the cumulative displacements retrieved from the MT-DInSAR represent only the amount relative to the monitored period (defined by the first and last acquisition dates of the radar images used to produce the deformation time series). Therefore, if the studied construction has been built before the beginning of the time series, information on earlier deformation phenomena affecting the building needs to be gathered in order to use the MT-DInSAR cumulative displacement for structural assessment. As an example, the available time series can be possibly extended and adjusted with other MT-DInSAR time series relative to the area under investigation, obtained from earlier satellite missions.

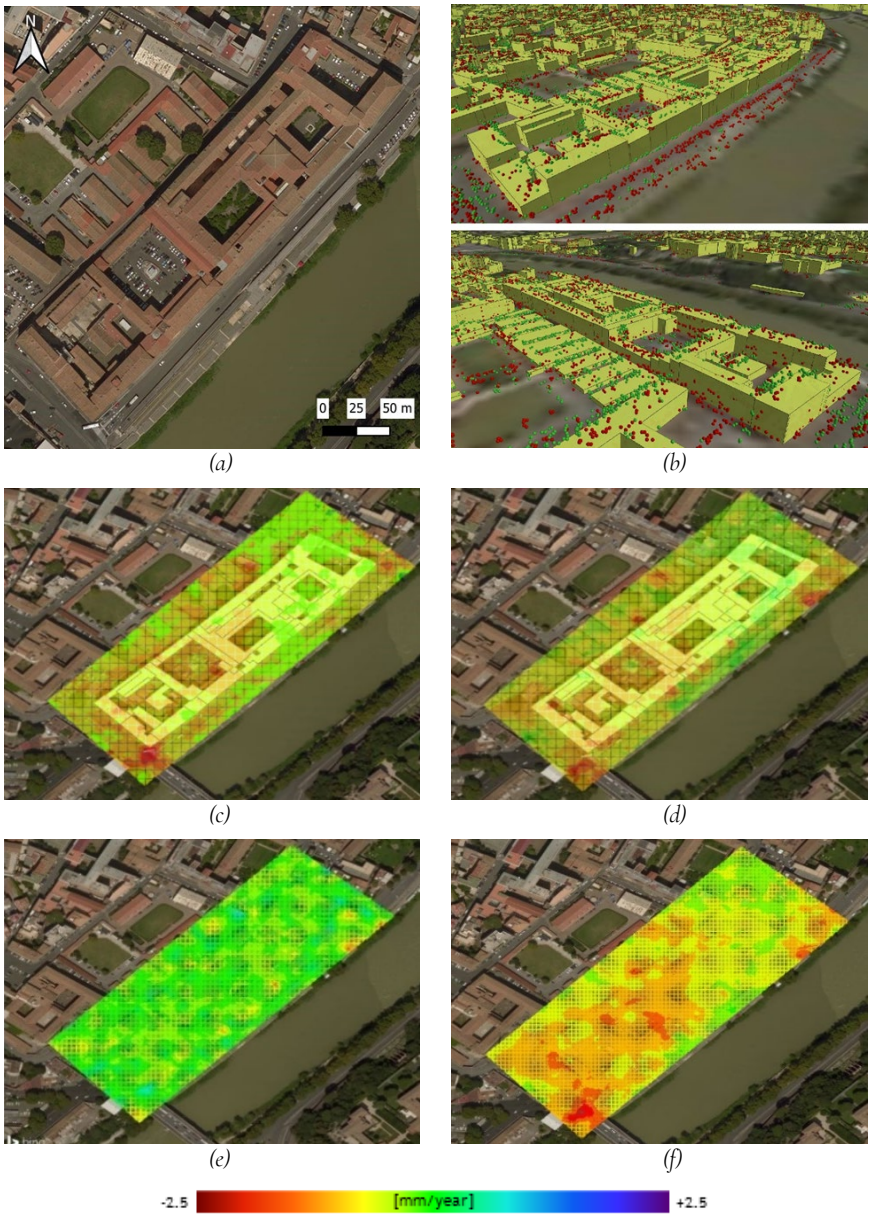

Fig. 5.12 Example of combination of ASC and DES data performed using LOS mean velocity values made available for points of a user-defined regular grid, resulting from the application of a spatial interpolation technique: (a) Top view of the studied building; (b) ASC (green) and DES (red) PSs in the zone of the studied building; (c) ASC mean LOS deformation velocity obtained for points of the regular grid, by means of spatial interpolation; (d) DES mean LOS velocity for points of the regular grid, obtained by means of spatial interpolation; (e) East-West velocity; (f) Vertical velocity (From ReLUIS [85] *and Talledo et al.* [229])

5.5 CURRENT LIMITATIONS AND POTENTIALS TO BE EXPLOITED

Based on the previously discussed aspects and examples, a summary of the most relevant potentials and of the current limitation of the use of MT-DInSAR data in structural monitoring applications as an aid for deformation demands monitoring in civil structures and infrastructures is proposed. The aim is to highlight relevant aspects which may be useful to trace future direction for both research and technical developments, the fields of processing techniques and procedures for DInSAR data adoption in structural health monitoring practices.
With regards to the key potentials which make the technique very attractive, the following aspects are worth noting:

- MT-DInSAR techniques can be a valuable tool for supporting the detection of building and infrastructure damages, as well as for structural monitoring processes;
- These techniques allow to carry out multiscale analysis, i.e., to use PSs data to perform an analysis at urban scale, in order to detect possible areas where instability phenomena are occurring, or at a single construction scale, for monitoring individual buildings and structures;
- Whenever the PSs density and distribution are adequate, these techniques do not require the installation of any ground instrumentation and can provide data over very large areas at a reduced cost;

As a matter of fact, some features proper of the MT-DInSAR monitoring technique can represent an issue which can limit the full potential exploitation of its use in structural monitoring practices. In the following, some aspects regarding these limitations are summarized:

- Improvements would be desirable regarding the accuracy of the PSs georeferencing, possibly exploiting the use of corner reflectors equipped with GNSS monitoring stations;
- The retrieved MT-DInSAR measurements allow to compute the vertical deformation for PSs of the studied area cumulated during the monitoring period. However, cumulated displacement measures can represent just a portion of the actual total deformation which affect ground around and below the studied structures and so may be not effective in correctly estimating actual values of structural deformation demands;
- In performing interpolation operations to study a single construction, it is necessary to account for the spatial correlation among PSs. As a matter of fact, it would be very helpful to have information about the structural behaviour of the building before performing the interpolation of PSs data, for a proper definition of the homogeneous portions of the structure in which a distinct spatial resampling can be done.

5.6 Discussion

In this chapter, main advantages and limitations of the use of MT-DInSAR data in the monitoring of structural and ground deformations has been discussed, highlighting the characteristics of the information obtainable through the use of one or two dataset (i.e., ASC and DES), as well as the cases in which it is necessary to use specific spatial and/or temporal resampling methodologies. As a matter of fact, the use of MT-DInSAR data to improve the definition of ground settlements profiles to be employed as input in structural analysis procedures does not seem so straightforward to be pursued, and advances aimed at solving some critical aspects are needed.

A relevant aspect worth to recall concerns the selection of the PSs to be considered in the analyses to be carried out. As a general rule, it is always advisable to use as many PSs as possible in order to minimize the uncertainties linked to the single data. However, the use of all the PSs available in the zone of interest may not always be the most appropriate choice. In fact, depending on the spatial correlation or decorrelation of deformation phenomena at ground and on the analyzed structures, PSs to be considered as representative of the deformation of the investigated object or area must be evaluated on a case-by-case basis (e.g., in the case of deformations of the deck of a bridge, which are not necessarily correlated with those of the ground below). This aspect needs to be considered when analyzing the applicability of different spatial resampling techniques, in order to avoid incurring in possible misinterpretations of a deformation phenomenon.

A further aspect of great importance, already mentioned throughout the chapter, is related to the fact that all deformation values obtained through MT-DInSAR techniques are differential and are therefore relative both in time (with respect to the initial instant) and in space (with respect to the reference point of the scene). As an example, cumulative values of ground or structural displacements obtained by MT-DInSAR time series are clearly relative to the monitoring period and do not refer to the entire past history of deformation phenomena affecting the building. As a consequence, they cannot be directly used as a measure of the actual displacement of the building, unless they are supplemented with detailed information on the deformation state of the building and the ground up to the initial instant of the MT-DInSAR time series. It is therefore always desirable to integrate information provided by MT-DInSAR data with other specific information that can be obtained from site investigation campaigns.

With regards to future improvements of the technique and of its use in the field of civil structural health monitoring, some suggestions can be provided. In first instance, the exploitation of most recent radar satellite constellations as well as up-to-date MT-DInSAR processing algorithms can be pursued, aiming at obtaining improved spatial resolution of PSs and accuracy in their spatial positioning, as well as better accuracy of deformation measures. Another relevant aspect which can be a field for further improvements regards the approaches for the reconstruction of the actual 3D deformation vector, using MT-DInSAR data obtained from different acquisition geometries and integrating them with other types of data, e.g., from GNSS monitoring.

6

Conclusions

Education is not the filling of a pale, but the lighting of a fire.
William B. Yeats

This chapter proposes a retrospective view on the research work presented throughout the dissertation, recalling the research objectives stated in Chapter 1 and summarizing the main findings and insights provided in the core chapters of the thesis. In addition, mention is made to some research aspects which have been addressed but not yet fully developed. In the end, considerations and suggestions for future research are given.

6.1 Introduction

The research works presented in this thesis addressed some specific aspects regarding the evaluation of deformation capacity and demand in beam members belonging to reinforced concrete (RC) structures. The attention has been devoted to the development and analysis of approaches which can be actually employed in the engineering practice, addressing aspects which are relevant both in the case of the design of new structures and in the assessment of existing ones. The research work has been driven by general research questions which address current relevant challenges in the field of structural assessment of RC structures. The identified questions inspired the pursuing of three more specific research objectives, which have been developed throughout the work.
The first goal, identified by objective ***O1***, addressed the analysis of deformation capacity and ductility in doubly reinforced concrete beam sections, by means of the development of an analytical framework which allows to study the yielding and failure modes of beam sections. The second objective ***O2*** focused on the assessment of the predictive performances of different modelling approaches for the analysis of the response of RC beams affected by rebar corrosion. In this context, the experimental response of a set of corroded beams was analyzed, to gain further insights on the effects of corrosion, both in terms of residual strength and deformation capacity. The results from the experimental tests have been used as reference for the analytical and numerical analyses developed to investigate the effectiveness of different modelling strategies. The third aim of the research, explicated through objective ***O3***, involved the analysis of potentials and limitations of the application of Multi-Temporal Differential Synthetic Aperture Radar Interferometry (MT-DInSAR) in the field of civil structural health monitoring. The use of this technique can be in fact an effective aid to improve the estimation and monitoring of deformation demands in constructions subjected to ground settlements. Some fundamental aspects of the MT-DInSAR techniques have been firstly recalled, and specific issues which arise when these techniques are adopted to monitoring deformation at the scale of single constructions have been addressed. The key results obtained addressing the aforementioned research objectives are summarized in the following, highlighting the main findings and recalling the limitations of the adopted approaches. Some suggestions for further future research are then provided.

6.2 Main findings of the presented research work and concluding remarks

6.2.1 Analytical framework for deformation capacity and ductility assessment of reinforced concrete beam sections

An analytical framework for studying the flexural behaviour of RC beam sections was formulated considering several possible yielding and failure modes. This approach allowed to analyze the behaviour of beam section with different geometric layout and material characteristics, also addressing the cases in which the cross-sectional area of steel rebars is reduced by the effects of corrosion. A particular relevant aspect considered

in the adopted approach regards the implementation of failure modes which consider the occurrence of the spalling of the concrete cover. Moreover, the analysis of failure modes involving steel rebars rupture highlighted the key role of ultimate steel strain, to which in several situations quite low values need to be assigned. Those are the cases, for example, in which it is to be accounted for effects due to low-cycle fatigue, pre-cracking of steel due to buckling of reinforcement in members subjected to cycling loading, or degradation phenomena such as reinforcement corrosion. A specific tool has been developed, which allows the identification of yielding and failure modes considering the variability of some material and geometrical parameters of the sections. In addition, starting from the proposed comprehensive framework, a simplified closed-form analytical formulation for the evaluation of deformation capacity and ductility of RC beam sections has been derived, which can be an effective tool to be used in the design and assessment engineering practices.
It has been shown that in many situations considering the spalling of the concrete cover allows significantly high ductility values to be achieved. In parallel, by analyzing results from parametric evaluations, it has been possible to observe that the loss of section bending strength due to the spalling of the concrete cover is in many cases limited. Therefore, the proposed formulation allows deformation capacity evaluations to be carried out avoiding excessive and unnecessary conservatism. A possible improvement of the proposed methodology involve the implementation of steel constitutive laws which consider post-yielding hardening. In addition, the proposed failure mode domains formulation could be enhanced in order to be able to consider uncertainty in geometric and material parameters.

6.2.2 Modelling effects of rebar corrosion on deformation capacity using approaches based on sectional analysis

The study of the response of corroded beam members has been performed from different points of view, analyzing results from experimental tests and testing the predictive capabilities of different analytical and numerical modelling strategies. Special attention was devoted to the study of the structural consequences caused by corrosion of the longitudinal bottom reinforcement. Various models and formulations adoptable to represent deterioration of geometric and mechanical characteristics of corroded rebars were considered and employed in simulating the response of RC beams tested in a recently performed experimental campaign. The results of the analyses revealed that modelling strategies traditionally used in the engineering practice can actually provide safe-side estimations of the residual strength of corroded members but may not be as effective for the assessment of their residual deformation capacity. In particular, it has been observed that the choice of the pitting factor, combined with the definition of the corrosion level, plays an important role and its variation may significantly influence the simulated structural response. In addition, the performed analyses showed the effects on the structural response of different choices in defining the corrosion level. In particular, it has been highlighted the importance of adequately modelling the spatial variability along the beams of the mechanical properties of the sections affected by corrosion. It has also been shown how the traditional approaches tested in the present work do not allow

for a proper representation of the deformation localization phenomena observed in heavily corroded beams. In order to improve current assessment procedures for members affected by reinforcement corrosion, improved strategies for modelling corrosion effects on steel rebar properties may be adopted, actually accounting for the pit lengths and distribution, in addition to the usually considered pit depths.

6.2.3 Use of MT-DInSAR data to improve estimation of deformation demand due to ground settlements

In analyzing the relevant issues which characterize the use of MT-DInSAR data in the field of structural monitoring, several aspects have been considered. Some issues have been highlighted which are specifically due to the typology of data provided as final product of the MT-DInSAR processing, i.e., the displacement time series and average deformation velocity along the satellite line of sight for each PS of the scene. In particular, the presence of PSs over areas of interest and the accuracy of spatial location of PSs represent some of the critical aspects which in many cases can make it difficult to use this kind of data for the structural monitoring performed at the single constructions scale, especially to estimate and monitor differential displacements to be used for evaluation of deformation demands in structural members. In this context, some specific considerations have been drawn regarding the aspects which limit the use MT-DInSAR data. In particular, the resolution of the radar images used, the topography of the urban area studied, the orientation of the buildings and the reflectivity characteristics of the terrain surrounding them are some of the main causes that can limit the presence of PSs over and around a construction. When PSs are not present in a zone of interest, spatial resampling techniques can be an option in order to obtain such information. Among these techniques, spatial interpolation can be a powerful tool, though it must be used with caution. A related aspect concerns the fact that in order to reconstruct the Vertical and East-West components of the ground point displacements, at least in an approximate manner, PSs obtained from SAR images of both ascending and descending acquisition geometry are required. To solve these problems, at least on structures of relevant interest, it is desirable the installation of corner reflectors, which increases the possibility of obtaining PSs at strategic locations of interest.
Finally, a critical aspect to be considered in the use of differential displacements provided by MT-DInSAR techniques concerns the fact that the obtained displacement values correspond to the cumulative displacements developed only during the observation period. Therefore, if the ongoing deformation phenomenon began prior to the date on which SAR images were acquired for the area of interest, it is not possible to know the true total magnitude of the differential displacements to which the structure is subjected. This aspect may represent a relevant limitation in the use of MT-DInSAR data for the evaluation of structural response. However, in some cases, the observation history may be sufficiently long to include the entire duration of the deformation process, for example in some cases of subsidence phenomena due to underground tunnel excavations.

6.3 Recommendations for further future research

The results obtained and presented in the thesis may be refined and improved in further developments of the research. Moreover, achieved results allowed to formulate some insights which can be useful in outlining future research aspects to be addressed in the field of performance-based design and assessment of RC members. The following aspects are in particular highlighted, which can be pursued in future investigations:

- From the developed comprehensive analytical framework for ultimate curvature and ductility capacity, effective rules for detailing RC sections can be developed, to be used for guaranteeing a satisfactory ductility capacity;
- The proposed formulation for sectional analysis can be enhanced in order to be applicable also for the analysis of column sections, by implementing effects of confinement on the behaviour of core concrete. Moreover, the developed framework can be used as a basis for proposing analytical formulations for deformation capacity at the element level, actually considering different sectional failure modes;
- Future research works which can include improvements of models for a more detailed description of the mechanical characteristics of corroded rebars; in particular, studies aimed at providing models for the description of the pit depth and length distribution along corroded bars should be pursued;
- Investigations should be carried out for addressing proposals of assessment approaches for corroded structures which explicitly consider different procedure for different knowledge of the corrosion state, also exploring different possibilities for defining the corrosion level;
- The analysis of possible integrations of MT-DInSAR data with other types of remote sensing data as well as with data obtained from on-site monitoring should be addressed, in order to pursue steps to overcome some of the current limits of MT-DInSAR applications in structural assessment;
- Possibilities offered by SAR images provided by most recently launched satellite constellations need to be explored, exploiting possible improvements in spatial resolution and deformation measures accuracy;
- Further advancements in post-processing of MT-DInSAR data should be proposed to fully exploit their information, also considering applications on different structural typologies (i.e., buildings, infrastructures, retaining structures, etc.), in order to make those data an effective tool for the monitoring of civil structures and infrastructures.

A

Formulations for conditions representing transitions between different failure modes of doubly reinforced concrete beam sections

A.1 Introduction

In Chapter 2 the conditions which define the transition between different possible failure modes for a doubly reinforced concrete beam section have been introduced. A complete list of transition conditions has been defined and illustrated in Fig. 2.7, identifying eleven conditions in total. In the following, analytical expressions which define each transition condition are reported, by means of closed-form expressions which provide the ratio ρ'/ρ as a function of the ratio c/H and of other parameters. Obviously, for all the conditions only results associated to positive values of ratio ρ'/ρ are to be considered. The provided expressions for the transition conditions have been derived considering the materials constitutive laws for steel and concrete reported in Chapter 2. Therefore, their validity is strictly limited in the case such material constitutive laws are considered.

In the provided expressions, the spalling depth at failure s_u needs to be taken as null if cover spalling cannot be acceptable (e.g., in the case the associated bending strength loss would exceed a target limit). Otherwise, if spalling of the concrete cover at failure can be considered, the spalling depth s_u is taken equal to the value s_{lim}, for which proper values have been suggested in Chapter 2.

Where not otherwise explicitly stated, the mean stress factor α is taken equal to α_{III}, where the latter term is expressed by eq. (2.14), also herein reported:

$$\alpha_{III} = \left[1 - \frac{1}{3} \cdot \left(\frac{\varepsilon_{c0}}{\varepsilon_c}\right)\right] - Z \cdot \frac{\varepsilon_{c0} - \varepsilon_{cu}}{2} \cdot \left[1 - \left(\frac{\varepsilon_{c0}}{\varepsilon_c}\right)\right] \tag{A.1}$$

Note that steel yielding and ultimate strains ε_{sy} and ε_{su} expect positive (tension) values, while concrete strains ε_{c0} and ε_{cu} expect negative (compression) values.

A.2 Formulations for transition conditions

A.2.1 Transition condition U1

Significant values of c/H ratio necessary for the definition of the transition condition:

$$\begin{cases} \left(\frac{c}{H}\right)_{U1,y,c} = \frac{1}{\left(1+\frac{\varepsilon_{cu}-\varepsilon_{su}}{\varepsilon_{cu}+\varepsilon_{sy}}\right)+\frac{s_u}{c}\cdot\left(1-\frac{\varepsilon_{cu}-\varepsilon_{su}}{\varepsilon_{cu}+\varepsilon_{sy}}\right)} \\ \left(\frac{c}{H}\right)_{U1,0} = \frac{1}{\left(1+\frac{\varepsilon_{cu}-\varepsilon_{su}}{\varepsilon_{cu}}\right)+\frac{s_u}{c}\left(1-\frac{\varepsilon_{cu}-\varepsilon_{su}}{\varepsilon_{cu}}\right)} \\ \left(\frac{c}{H}\right)_{U1,y,t} = \frac{1}{\left(1+\frac{\varepsilon_{cu}-\varepsilon_{su}}{\varepsilon_{cu}-\varepsilon_{sy}}\right)+\frac{s_u}{c}\cdot\left(1-\frac{\varepsilon_{cu}-\varepsilon_{su}}{\varepsilon_{cu}-\varepsilon_{sy}}\right)} \end{cases} \tag{A.2}$$

Range of c/H ratio values for which the transition condition applies:

$$\left(\frac{c}{H}\right)_{U1,y,c} \le \frac{c}{H} \le 0.5 \tag{A.3}$$

In the case the following inequalities on ratio ρ'/ρ apply, the section reaches concrete failure:

- If $\frac{c}{H} \le \left(\frac{c}{H}\right)_{U1,y,c}$:

$$\frac{\rho'}{\rho} < 1 - \alpha_{III}\cdot\frac{1}{\omega}\cdot\frac{\varepsilon_{cu}}{\varepsilon_{cu}-\varepsilon_{su}}\cdot\left[1-\frac{c}{H}\cdot\left(1+\frac{s_u}{c}\right)\right] \tag{A.4}$$

Note: The curve described by eq. (A.4) is not actually employed, since it does not satisfy the condition set by eq. (A.3). Actually, if it would be used, an ambiguity in the determination of the section failure mode would arise when transition conditions expressed by equations (A.4) would be (A.42) compared.

- If $\left(\frac{c}{H}\right)_{U1,y,c} \le \frac{c}{H} \le \left(\frac{c}{H}\right)_{U1,0}$:

$$\begin{cases} k' = \frac{\varepsilon_{cu}}{\varepsilon_{sy}}\cdot\left[\frac{\frac{c}{H}\left(1-\frac{s_u}{c}\right)}{1-\frac{c}{H}\left(1+\frac{s_u}{c}\right)}\cdot\frac{\varepsilon_{cu}-\varepsilon_{su}}{\varepsilon_{cu}}-1\right] \quad (k'\ge 0) \\ \frac{\rho'}{\rho} < \frac{1}{k'} - \alpha_{III}\cdot\frac{1}{k'}\cdot\frac{1}{\omega}\cdot\frac{\varepsilon_{cu}}{\varepsilon_{cu}-\varepsilon_{su}}\cdot\left[1-\frac{c}{H}\cdot\left(1+\frac{s_u}{c}\right)\right] \end{cases} \tag{A.5}$$

- If $\left(\frac{c}{H}\right)_{U1,0} \le \frac{c}{H} \le \left(\frac{c}{H}\right)_{U1,y,t}$:

$$\begin{cases} k' = \frac{\varepsilon_{cu}}{\varepsilon_{sy}}\cdot\left[\frac{\frac{c}{H}\left(1-\frac{s_u}{c}\right)}{1-\frac{c}{H}\left(1+\frac{s_u}{c}\right)}\cdot\frac{\varepsilon_{cu}-\varepsilon_{su}}{\varepsilon_{cu}}-1\right] \quad (k'\le 0) \\ \frac{\rho'}{\rho} > \frac{1}{k'} - \alpha_{III}\cdot\frac{1}{k'}\cdot\frac{1}{\omega}\cdot\frac{\varepsilon_{cu}}{\varepsilon_{cu}-\varepsilon_{su}}\cdot\left[1-\frac{c}{H}\cdot\left(1+\frac{s_u}{c}\right)\right] \end{cases} \tag{A.6}$$

- If $\frac{c}{H} \geq \left(\frac{c}{H}\right)_{U1,y,t}$:

$$\frac{\rho'}{\rho} > -1 + \alpha_{III} \cdot \frac{1}{\omega} \cdot \frac{\varepsilon_{cu}}{\varepsilon_{cu}-\varepsilon_{su}} \cdot \left[1 - \frac{c}{H} \cdot \left(1 + \frac{s_u}{c}\right)\right] \tag{A.7}$$

A.2.2 Transition condition U2

Significant values of c/H ratio necessary for the definition of the transition condition:

$$\begin{cases} \left(\frac{c}{H}\right)_{U2,y,c} = \frac{1}{\left(1+\frac{\varepsilon_{cu}-\varepsilon_{sy}}{\varepsilon_{cu}+\varepsilon_{sy}}\right)+\frac{s_u}{c}\left(1-\frac{\varepsilon_{cu}-\varepsilon_{sy}}{\varepsilon_{cu}+\varepsilon_{sy}}\right)} \\ \left(\frac{c}{H}\right)_{U2,0} = \frac{1}{\left(1+\frac{\varepsilon_{cu}-\varepsilon_{sy}}{\varepsilon_{cu}}\right)+\frac{s_u}{c}\left(1-\frac{\varepsilon_{cu}-\varepsilon_{sy}}{\varepsilon_{cu}}\right)} \\ \left(\frac{c}{H}\right)_{U2,y,t} = \frac{1}{2} \end{cases} \tag{A.8}$$

Range of c/H ratio values for which the transition condition applies:

$$0 \leq \frac{c}{H} \leq 0.5 \tag{A.9}$$

In the case the following inequalities on ratio ρ'/ρ apply, the section reaches concrete failure with bottom steel yielded in tension.

- If $\frac{c}{H} \leq \left(\frac{c}{H}\right)_{U2,y,c}$:

$$\frac{\rho'}{\rho} \geq 1 - \alpha_{III} \cdot \frac{1}{\omega} \cdot \frac{\varepsilon_{cu}}{\varepsilon_{cu}+\varepsilon_{sy}} \cdot \left[1 - \frac{c}{H} \cdot \left(1 + \frac{s_u}{c}\right)\right] \tag{A.10}$$

- If $\left(\frac{c}{H}\right)_{U2,y,c} \leq \frac{c}{H} \leq \left(\frac{c}{H}\right)_{U2,0}$:

$$\begin{cases} k' = \frac{\varepsilon_{cu}}{\varepsilon_{sy}} \cdot \left[\frac{\frac{c}{H}\left(1-\frac{s_u}{c}\right)}{1-\frac{c}{H}\left(1+\frac{s_u}{c}\right)} \cdot \frac{\varepsilon_{cu}-\varepsilon_{sy}}{\varepsilon_{cu}} - 1\right] \quad (k' \geq 0) \\ \frac{\rho'}{\rho} \geq \frac{1}{k'} - \alpha_{III} \cdot \frac{1}{k'} \cdot \frac{1}{\omega} \cdot \frac{\varepsilon_{cu}}{\varepsilon_{cu}-\varepsilon_{sy}} \cdot \left[1 - \frac{c}{H} \cdot \left(1 + \frac{s_u}{c}\right)\right] \end{cases} \tag{A.11}$$

- If $\left(\frac{c}{H}\right)_{U2,0} \leq \frac{c}{H} \leq \left(\frac{c}{H}\right)_{U2,y,t}$:

$$\begin{cases} k' = \frac{\varepsilon_{cu}}{\varepsilon_{sy}} \cdot \left[\frac{\frac{c}{H}\left(1-\frac{s_u}{c}\right)}{1-\frac{c}{H}\left(1+\frac{s_u}{c}\right)} \cdot \frac{\varepsilon_{cu}-\varepsilon_{sy}}{\varepsilon_{cu}} - 1\right] \quad (k' \leq 0) \\ \frac{\rho'}{\rho} \leq \frac{1}{k'} - \alpha_{III} \cdot \frac{1}{k'} \cdot \frac{1}{\omega} \cdot \frac{\varepsilon_{cu}}{\varepsilon_{cu}-\varepsilon_{sy}} \cdot \left[1 - \frac{c}{H} \cdot \left(1 + \frac{s_u}{c}\right)\right] \end{cases} \tag{A.12}$$

A.2.3 Transition condition U3

Significant values of c/H ratio necessary for the definition of the transition condition:

$$\begin{cases} \left(\frac{c}{H}\right)_{U3,y,c} = \frac{1}{\left(1+\frac{\varepsilon_{c0}-\varepsilon_{su}}{\varepsilon_{c0}+\varepsilon_{sy}}\right)} \\ \left(\frac{c}{H}\right)_{U3,0} = \frac{1}{\left(1+\frac{\varepsilon_{c0}-\varepsilon_{su}}{\varepsilon_{c0}}\right)} \\ \left(\frac{c}{H}\right)_{U3,y,t} = \frac{1}{\left(1+\frac{\varepsilon_{c0}-\varepsilon_{su}}{\varepsilon_{c0}-\varepsilon_{sy}}\right)} \end{cases} \tag{A.13}$$

Range of c/H ratio values for which the transition condition applies:

$$0 \le \frac{c}{H} \le 0.5 \tag{A.14}$$

In the case the following inequalities on ratio ρ'/ρ apply, the section reaches steel failure with sound concrete, which already has achieved or overcome the peak strength:

- If $\frac{c}{H} \le \left(\frac{c}{H}\right)_{U3,y,c}$:

$$\frac{\rho'}{\rho} < 1 - \frac{2}{3}\cdot\frac{1}{\omega}\cdot\frac{\varepsilon_{c0}}{\varepsilon_{c0}-\varepsilon_{su}}\cdot\left(1-\frac{c}{H}\right) \tag{A.15}$$

- If $\left(\frac{c}{H}\right)_{U3,y,c} \le \frac{c}{H} \le \left(\frac{c}{H}\right)_{U3,0}$:

$$\begin{cases} k' = \frac{\varepsilon_{c2}}{\varepsilon_{sy}}\cdot\left(\frac{\frac{c}{H}}{1-\frac{c}{H}}\cdot\frac{\varepsilon_{c0}-\varepsilon_{su}}{\varepsilon_{c0}}-1\right) \quad (k' \ge 0) \\ \frac{\rho'}{\rho} < \frac{1}{k'} - \frac{2}{3}\cdot\frac{1}{k'}\cdot\frac{1}{\omega}\cdot\frac{\varepsilon_{c0}}{\varepsilon_{c0}-\varepsilon_{su}}\cdot\left(1-\frac{c}{H}\right) \end{cases} \tag{A.16}$$

- If $\left(\frac{c}{H}\right)_{U3,0} \le \frac{c}{H} \le \left(\frac{c}{H}\right)_{U3,y,t}$:

$$\begin{cases} k' = \frac{\varepsilon_{c2}}{\varepsilon_{sy}}\cdot\left(\frac{\frac{c}{H}}{1-\frac{c}{H}}\cdot\frac{\varepsilon_{c0}-\varepsilon_{su}}{\varepsilon_{c0}}-1\right) \quad (k' \le 0) \\ \frac{\rho'}{\rho} > \frac{1}{k'} - \frac{2}{3}\cdot\frac{1}{k'}\cdot\frac{1}{\omega}\cdot\frac{\varepsilon_{c0}}{\varepsilon_{c0}-\varepsilon_{su}}\cdot\left(1-\frac{c}{H}\right) \end{cases} \tag{A.17}$$

- If $\frac{c}{H} \ge \left(\frac{c}{H}\right)_{U3,y,t}$:

$$\frac{\rho'}{\rho} > 1 - \frac{2}{3}\cdot\frac{1}{\omega}\cdot\frac{\varepsilon_{c0}}{\varepsilon_{c0}-\varepsilon_{su}}\cdot\left(1-\frac{c}{H}\right) \tag{A.18}$$

It is worth noting that, for chosen values of parameters ω, ε_{c0} and ε_{su}, only one of the (A.16) and (A.17) can provide positive values of ρ'/ρ ratio. In the domains configuration *Type 1* illustrated in Chapter 2, the portion of the curve associated to transition condition U3 which is described by eq. (A.16) is characterized by the presence of (at least some)

positive ρ'/ρ values, while the portion described by eq. (A.17) provides only negative values of ρ'/ρ and so it is not present in the graphs.
Actually, it is highly relevant to establish which one of the two equations (A.16) and (A.17) provides positive ρ'/ρ values (and so it appears in failure mode domains graphs) since it greatly influences the failure modes which will be present in domains graphs. In order to determine it, it is useful to note that considering c/H values for which coefficient k' tends to zero, one of the two (A.16) and (A.17) will certainly provide a positive ρ'/ρ, while the other one will give a negative value of ρ'/ρ.
So, it is convenient to investigate the sign of the ρ'/ρ value provided, for instance, by eq. (A.16) when k' tends to zero. In particular, it will be positive if the following relation applies:

$$\lim_{k'\to 0}\left(\frac{\rho'}{\rho}\right) > 0 \tag{A.19}$$

where ρ'/ρ is calculated using eq. (A.16). It can be shown that Eq. (A.19) is satisfied if the following condition applies:

$$\varepsilon_{su} > -\varepsilon_{c0}\cdot\left(\frac{\alpha}{\omega}-2\right) \quad with \quad \varepsilon_{c0} < 0 \tag{A.20}$$

Otherwise, if condition expressed by eq. (A.20) is not meet, eq. (A.17) will be the one which provide (at least some) positive values of ρ'/ρ. It is worth to recall again that, in order to obtain results shown for domain configuration *Type 1* in Chapter 2, condition expressed by Eq. (A.20) needs to be satisfied.

A.2.4 Limit condition U4

Significant values of c/H ratio necessary for the definition of the transition condition:

$$\begin{cases}\left(\frac{c}{H}\right)_{U4,y,c} = \frac{1}{\left(1+\frac{\varepsilon_{cu}-\varepsilon_{su}}{\varepsilon_{cu}+\varepsilon_{sy}}\right)}\\ \left(\frac{c}{H}\right)_{U4,0} = \frac{1}{\left(1+\frac{\varepsilon_{cu}-\varepsilon_{su}}{\varepsilon_{cu}}\right)}\\ \left(\frac{c}{H}\right)_{U4,y,t} = \frac{1}{\left(1+\frac{\varepsilon_{cu}-\varepsilon_{su}}{\varepsilon_{cu}-\varepsilon_{sy}}\right)}\end{cases} \tag{A.21}$$

Range of c/H ratio values for which the transition condition applies:

$$0 \le \frac{c}{H} \le 0.5 \tag{A.22}$$

In the case the following inequalities on ratio ρ'/ρ apply, the section reaches steel failure with partial spalling of the concrete cover:

- If $\frac{c}{H} \leq \left(\frac{c}{H}\right)_{U4,y,c}$:

$$\frac{\rho'}{\rho} < 1 - \alpha_{III} \cdot \frac{1}{\omega} \cdot \frac{\varepsilon_{cu}}{\varepsilon_{cu}-\varepsilon_{su}} \cdot \left(1 - \frac{c}{H}\right) \tag{A.23}$$

- If $\left(\frac{c}{H}\right)_{U4,y,c} \leq \frac{c}{H} \leq \left(\frac{c}{H}\right)_{U4,0}$:

$$\begin{cases} k' = \frac{\varepsilon_{cu}}{\varepsilon_{sy}} \cdot \left(\frac{\frac{c}{H}}{1-\frac{c}{H}} \cdot \frac{\varepsilon_{cu}-\varepsilon_{su}}{\varepsilon_{cu}} - 1\right) \quad (k' \geq 0) \\ \frac{\rho'}{\rho} < \frac{1}{k'} - \alpha_{III} \cdot \frac{1}{k'} \cdot \frac{1}{\omega} \cdot \frac{\varepsilon_{cu}}{\varepsilon_{cu}-\varepsilon_{su}} \cdot \left(1 - \frac{c}{H}\right) \end{cases} \tag{A.24}$$

- If $\left(\frac{c}{H}\right)_{U4,0} \leq \frac{c}{H} \leq \left(\frac{c}{H}\right)_{U4,y,t}$:

$$\begin{cases} k' = \frac{\varepsilon_{cu}}{\varepsilon_{sy}} \cdot \left(\frac{\frac{c}{H}}{1-\frac{c}{H}} \cdot \frac{\varepsilon_{cu}-\varepsilon_{su}}{\varepsilon_{cu}} - 1\right) \quad (k' \leq 0) \\ \frac{\rho'}{\rho} > \frac{1}{k'} - \alpha_{III} \cdot \frac{1}{k'} \cdot \frac{1}{\omega} \cdot \frac{\varepsilon_{cu}}{\varepsilon_{cu}-\varepsilon_{su}} \cdot \left(1 - \frac{c}{H}\right) \end{cases} \tag{A.25}$$

- If $\frac{c}{H} \geq \left(\frac{c}{H}\right)_{U4,y,t}$:

$$\frac{\rho'}{\rho} > 1 - \alpha_{III} \cdot \frac{1}{\omega} \cdot \frac{\varepsilon_{cu}}{\varepsilon_{cu}-\varepsilon_{su}} \cdot \left(1 - \frac{c}{H}\right) \tag{A.26}$$

Following the same approach adopted for condition U3, regarding transition condition U4 it is important to consider how the curves represented by equations (A.24) and (A.25) vary with parameters ω, ε_{cu} and ε_{su}. In particular, it is important to determine which one of the two equations (A.24) and (A.25) provides positive ρ'/ρ values (and so it appears in failure mode domains graphs), because it influences the failure modes which will be present in domains graphs.
In doing so, it is convenient to analyze the sign of the ρ'/ρ value provided, for instance, by eq. (A.24) when k' tends to zero. In particular, such a value will be positive if the following relation applies:

$$\lim_{k' \to 0} \left(\frac{\rho'}{\rho}\right) > 0 \tag{A.27}$$

where ρ'/ρ is calculated using eq. (A.24). It can be shown that eq. (A.27) is satisfied if the following condition applies:

$$\varepsilon_{su} > -\varepsilon_{cu} \cdot \left(\frac{\alpha}{\omega} - 2\right) \quad with \quad \varepsilon_{cu} < 0 \tag{A.28}$$

Otherwise, if condition expressed by eq. (A.28) is not met, Eq. (A.25) will be the one which provide (at least some) positive values of ρ'/ρ. It is worth to recall again that, in order to obtain results shown for domain configuration *Type 1* in Chapter 2, condition expressed by Eq. (A.28) needs to be satisfied. It is also to be noted that the respect of Eq. (A.28) guarantees also the Eq. (A.20) to be satisfied.

A.2.5 Transition condition U5

Range of c/H ratio values for which the transition condition applies:

$$\left(\frac{c}{H}\right)_{U2,y,c} \leq \frac{c}{H} \leq 0.5 \tag{A.29}$$

In the case the following inequality on ratio ρ'/ρ apply, the section reaches concrete failure with bottom steel elastic in tension and top steel yielded in compression.

$$\begin{cases} k = -\frac{\varepsilon_{cu}}{\varepsilon_{sy}} \cdot \left[\frac{\varepsilon_{sy}}{\varepsilon_{cu}} + \frac{\left(1-2\cdot\frac{c}{H}\right)}{\left(\frac{\varepsilon_{cu}}{\varepsilon_{cu}+\varepsilon_{sy}}\right)\cdot\frac{c}{H}\left(1-\frac{s_u}{c}\right)}\right] & (k>0) \\ \frac{\rho'}{\rho} \leq k - \alpha_{III} \cdot \frac{1}{\omega} \cdot \frac{c}{H} \cdot \frac{\varepsilon_{cu}}{\varepsilon_{cu}+\varepsilon_{sy}} \cdot \left(1-\frac{s_u}{c}\right) \end{cases} \tag{A.30}$$

A.2.6 Transition condition U6

Range of c/H ratio values for which the transition condition applies:

$$\left(\frac{c}{H}\right)_{U4,y,t} \leq \frac{c}{H} \leq 0.5 \tag{A.31}$$

In the case the following inequality on ratio ρ'/ρ apply, the section reaches concrete failure with bottom steel yielded in tension and top steel yielded in tension.

$$\frac{\rho'}{\rho} \leq \alpha_{III} \cdot \frac{1}{\omega} \cdot \frac{\varepsilon_{cu}}{\varepsilon_{cu}-\varepsilon_{sy}} \cdot \frac{c}{H} \cdot \left(1-\frac{s_u}{c}\right) - 1 \tag{A.32}$$

A.2.7 Transition condition U7

Range of c/H ratio values for which the transition condition applies:

$$\left(\frac{c}{H}\right)_{U1,y,t} \leq \frac{c}{H} \leq \left(\frac{c}{H}\right)_{U2,y,t} \tag{A.33}$$

In the case the following inequality on ratio ρ'/ρ apply, the section reaches concrete failure with bottom steel yielded in tension and top steel yielded in compression.

$$\frac{\rho'}{\rho} \leq 1 - \alpha_{III} \cdot \frac{1}{\omega} \cdot \frac{\varepsilon_{cu}}{\varepsilon_{cu}+\varepsilon_{sy}} \cdot \frac{c}{H} \cdot \left(1-\frac{s_u}{c}\right) \tag{A.34}$$

A.2.8 Transition condition U8

Range of c/H ratio values for which the transition condition applies:

$$\frac{\varepsilon_{sy}}{\varepsilon_{sy}+\varepsilon_{su}} \leq \frac{c}{H} \leq \left(\frac{c}{H}\right)_{U3,y,t} \tag{A.35}$$

In the case the following inequality on ratio ρ'/ρ apply, the section reaches steel failure with concrete having no reached its peak strength and top steel yielded in tension.

$$\begin{cases} \varepsilon_c = \varepsilon_{sy} \cdot \dfrac{\left(\frac{\varepsilon_{sy}}{\varepsilon_{sy}-\varepsilon_{su}}\right)-\left(\frac{c}{H}\right)\cdot\left(\frac{\varepsilon_{sy}+\varepsilon_{su}}{\varepsilon_{sy}-\varepsilon_{su}}\right)}{\left(\frac{\varepsilon_{sy}}{\varepsilon_{sy}-\varepsilon_{su}}\right)-\left(\frac{c}{H}\right)\cdot\left(1+\frac{\varepsilon_{sy}+\varepsilon_{su}}{\varepsilon_{sy}-\varepsilon_{su}}\right)} \\ \alpha_I = \left[-\frac{1}{3}\cdot\left(\frac{\varepsilon_c}{\varepsilon_{c0}}\right)^2 + \left(\frac{\varepsilon_c}{\varepsilon_{c0}}\right)\right] \\ \frac{\rho'}{\rho} \leq \alpha_I \cdot \frac{1}{\omega} \cdot \left[\left(\frac{\varepsilon_{sy}}{\varepsilon_{sy}-\varepsilon_{su}}\right) - \left(\frac{c}{H}\right)\cdot\left(\frac{\varepsilon_{sy}+\varepsilon_{su}}{\varepsilon_{sy}-\varepsilon_{su}}\right)\right] - 1 \end{cases} \tag{A.36}$$

A.2.9 Transition condition U9

Range of c/H ratio values for which the transition condition applies:

$$\left(\frac{c}{H}\right)_{U3,y,t} \leq \frac{c}{H} \leq \left(\frac{c}{H}\right)_{U4,y,t} \tag{A.37}$$

In the case the following inequality on ratio ρ'/ρ apply, the section reaches steel failure with sound concrete which though has reached its peak strength and top steel yielded in tension.

$$\begin{cases} \varepsilon_c = \varepsilon_{sy} \cdot \dfrac{\left(\frac{\varepsilon_{sy}}{\varepsilon_{sy}-\varepsilon_{su}}\right)-\left(\frac{c}{H}\right)\cdot\left(\frac{\varepsilon_{sy}+\varepsilon_{su}}{\varepsilon_{sy}-\varepsilon_{su}}\right)}{\left(\frac{\varepsilon_{sy}}{\varepsilon_{sy}-\varepsilon_{su}}\right)-\left(\frac{c}{H}\right)\cdot\left(1+\frac{\varepsilon_{sy}+\varepsilon_{su}}{\varepsilon_{sy}-\varepsilon_{su}}\right)} \\ \alpha_{II} = \left[1-\frac{1}{3}\cdot\frac{\varepsilon_{c0}}{\varepsilon_c}\right] - \left[\eta\cdot\left(1-\frac{\varepsilon_{c0}}{\varepsilon_c}\right)\right] \\ \frac{\rho'}{\rho} \leq \alpha_{II} \cdot \frac{1}{\omega} \cdot \left[\left(\frac{\varepsilon_{sy}}{\varepsilon_{sy}-\varepsilon_{su}}\right) - \left(\frac{c}{H}\right)\cdot\left(\frac{\varepsilon_{sy}+\varepsilon_{su}}{\varepsilon_{sy}-\varepsilon_{su}}\right)\right] - 1 \end{cases} \tag{A.38}$$

A.2.10 Transition condition U10

Range of c/H ratio values for which the transition condition applies:

$$\left(\frac{c}{H}\right)_{U3,y,c} \leq \frac{c}{H} \leq \left(\frac{c}{H}\right)_{U4,y,c} \tag{A.39}$$

In the case the following inequality on ratio ρ'/ρ apply, the section reaches steel failure with sound concrete which though has reached its peak strength and top steel yielded in compression.

$$\begin{cases} \varepsilon_c = -\varepsilon_{sy} \cdot \dfrac{\left(\frac{\varepsilon_{sy}}{\varepsilon_{sy}+\varepsilon_{su}}\right) - \left(\frac{c}{H}\right)\cdot\left(\frac{\varepsilon_{sy}-\varepsilon_{su}}{\varepsilon_{sy}+\varepsilon_{su}}\right)}{\left(\frac{\varepsilon_{sy}}{\varepsilon_{sy}+\varepsilon_{su}}\right) - \left(\frac{c}{H}\right)\cdot\left(1+\frac{\varepsilon_{sy}-\varepsilon_{su}}{\varepsilon_{sy}+\varepsilon_{su}}\right)} \\ \alpha_{II} = \left[1 - \frac{1}{3}\cdot\frac{\varepsilon_{c0}}{\varepsilon_c}\right] - \left[\eta\cdot\left(1-\frac{\varepsilon_{c0}}{\varepsilon_c}\right)\right] \\ \dfrac{\rho'}{\rho} \leq 1 - \alpha_{II}\cdot\dfrac{1}{\omega}\cdot\left[\left(\dfrac{\varepsilon_{sy}}{\varepsilon_{sy}+\varepsilon_{su}}\right) - \left(\dfrac{c}{H}\right)\cdot\left(\dfrac{\varepsilon_{sy}-\varepsilon_{su}}{\varepsilon_{sy}+\varepsilon_{su}}\right)\right] \end{cases} \tag{A.40}$$

A.2.11 Transition condition U11

Range of c/H ratio values for which the transition condition applies:

$$\left(\frac{c}{H}\right)_{U4,y,c} \leq \frac{c}{H} \leq \left(\frac{c}{H}\right)_{U1,y,c} \tag{A.41}$$

In the case the following inequality on ratio ρ'/ρ apply, the section reaches steel failure with partially spalled concrete cover and top steel elastic in compression.

$$\frac{\rho'}{\rho} \geq 1 + \alpha_{III}\cdot\frac{1}{\omega}\cdot\left(\frac{\varepsilon_{cu}}{\varepsilon_{sy}+\varepsilon_{su}}\right)\cdot\left(1-2\cdot\frac{c}{H}\right) \tag{A.42}$$

B

Analytical expressions for parameters used in the evaluation of ultimate curvature and spalling-induced strength loss

B.1 Introduction

Within the analytical framework for the analysis of doubly reinforced concrete beam sections presented in Chapter 2, the ultimate curvature of a section can be expressed as a function of the non-dimensional parameters $\left(\frac{x_u - s_u}{H}\right)$ and $\left(1 - \frac{c}{H} - \frac{x_u}{H}\right)$. Moreover, the ratio s_u/c needs to be assumed or calculated, in order to evaluate the bending strength loss due to cover spalling.

For concrete-side failure modes, i.e., modes A to E, the spalling depth at failure s_u needs to be taken as null if cover spalling cannot be acceptable (e.g., in the case the associated bending strength loss would exceed a target limit). Otherwise, if spalling of the concrete cover at failure can be considered, the spalling depth s_u is taken equal to the value s_{lim}, for which proper values have been suggested in Chapter 2. For all concrete-side failure modes, the mean stress factor α is taken equal to α_{III}, where the latter term is expressed by eq. (2.14), also herein reported:

$$\alpha_{III} = \left[1 - \frac{1}{3} \cdot \left(\frac{\varepsilon_{c0}}{\varepsilon_c}\right)\right] - Z \cdot \frac{\varepsilon_{c0} - \varepsilon_{cu}}{2} \cdot \left[1 - \left(\frac{\varepsilon_{c0}}{\varepsilon_c}\right)\right] \tag{B.1}$$

Ultimate conditions F to J are characterized by a steel failure without spalling of the concrete cover. So, for those failure modes the depth of the spalled cover at failure s_u is null.

Failure mode K can actually develop only in the case the spalling of cover at failure can be considered acceptable. For this ultimate condition the spalling depth at failure s_u is in the range $0 < s_u < s_{lim}$ and it can be evaluated imposing section equilibrium.

In the following, analytical expressions for the calculation of the aforementioned parameters are provided for all the failure modes presented in Chapter 2 but modes F, G and L. The two former ones are in fact never occurring in practical cases, while the latter is not considered in the proposed framework, since hardening of steel is neglected based on the adopted constitutive law for steel. Note that steel strains expect positive (tension) values, while concrete strains expect negative (compression) values.

B.2 Formulations for different failure modes

B.2.1 Failure mode A

For failure mode A, the term $\frac{x_u - s_u}{H}$ can be computed as follows:

$$\frac{x_u - s_u}{H} = \frac{\frac{\varepsilon_{cu}}{\varepsilon_{sy}}\left(1+\frac{\rho'}{\rho}\right) + \sqrt{\left[\frac{\varepsilon_{cu}}{\varepsilon_{sy}}\left(1+\frac{\rho'}{\rho}\right)\right]^2 - 4\cdot\frac{\alpha_{III}}{\omega}\cdot\frac{\varepsilon_{cu}}{\varepsilon_{sy}}\left[\left(1+\frac{\rho'}{\rho}\right)\cdot\frac{c}{H}\left(1-\frac{s_u}{c}\right)+\left(1-2\cdot\frac{c}{H}\right)\right]}}{2\cdot\frac{\alpha_{III}}{\omega}} \tag{B.2}$$

B.2.2 Failure mode B

For failure mode B, the term $\frac{x_u - s_u}{H}$ can be computed as follows:

$$\frac{x_u - s_u}{H} = \frac{\frac{\varepsilon_{cu}}{\varepsilon_{sy}}\frac{\rho'}{\rho} + \sqrt{\left(\frac{\varepsilon_{cu}}{\varepsilon_{sy}}\frac{\rho'}{\rho}\right)^2 - 4\cdot\frac{\alpha_{III}}{\omega}\cdot\frac{\varepsilon_{cu}}{\varepsilon_{sy}}\left[\frac{c}{H}\left(1-\frac{s_{lim}}{c}\right)+\left(1-2\cdot\frac{c}{H}\right)\right]}}{2\cdot\frac{\alpha_{III}}{\omega}} \tag{B.3}$$

B.2.3 Failure mode C

For failure mode C, the term $\frac{x_u - s_u}{H}$ can be computed as follows:

$$\frac{x_u - s_u}{H} = \frac{1+\frac{\rho'}{\rho}}{\frac{\alpha_{III}}{\omega}} \tag{B.4}$$

B.2.4 Failure mode D

For failure mode D, the term $\frac{x_u - s_u}{H}$ can be computed as follows:

$$\frac{x_u - s_u}{H} = \frac{1+\frac{\varepsilon_{cu}}{\varepsilon_{sy}}\frac{\rho'}{\rho} + \sqrt{\left(1+\frac{\varepsilon_{cu}}{\varepsilon_{sy}}\frac{\rho'}{\rho}\right)^2 - 4\cdot\frac{\alpha_{III}}{\omega}\cdot\frac{\varepsilon_{cu}}{\varepsilon_{sy}}\frac{\rho'}{\rho}\cdot\frac{c}{H}\left(1-\frac{s_{lim}}{c}\right)}}{2\cdot\frac{\alpha_{III}}{\omega}} \tag{B.5}$$

B.2.5 Failure mode E

For failure mode E, the term $\frac{x_u - s_u}{H}$ can be computed as follows:

$$\frac{x_u - s_u}{H} = \frac{1-\frac{\rho'}{\rho}}{\frac{\alpha_{III}}{\omega}} \tag{B.6}$$

B.2.6 Failure mode H

The general expression for the term $1-\frac{c}{H}-\frac{x_u}{H}$ for failure mode H is the following:

$$1-\frac{c}{H}-\frac{x_u}{H}=\frac{\frac{1}{\omega}\cdot\left(1-\frac{c}{H}\right)\cdot[1-Z\cdot(\varepsilon_{su}-\varepsilon_{c0})]-1-\frac{\rho'}{\rho}}{2\cdot\frac{1}{\omega}\cdot\left[1-\frac{1}{3}\cdot\frac{\varepsilon_{c0}}{\varepsilon_{su}}+\frac{Z}{2}\cdot\frac{(\varepsilon_{su}-\varepsilon_{c0})^2}{\varepsilon_{su}}\right]}+ \\ +\frac{\sqrt{\left\{\frac{1}{\omega}\cdot\left(1-\frac{c}{H}\right)\cdot[1-Z\cdot(\varepsilon_{su}-\varepsilon_{c0})]-1-\frac{\rho'}{\rho}\right\}^2-4\cdot\frac{1}{\omega^2}\cdot\varepsilon_{su}\cdot\left(1-\frac{c}{H}\right)^2\cdot\frac{Z}{2}\left[1-\frac{1}{3}\frac{\varepsilon_{c0}}{\varepsilon_{su}}+\frac{Z}{2}\cdot\frac{(\varepsilon_{su}-\varepsilon_{c0})^2}{\varepsilon_{su}}\right]}}{2\cdot\frac{1}{\omega}\cdot\left[1-\frac{1}{3}\cdot\frac{\varepsilon_{c0}}{\varepsilon_{su}}+\frac{Z}{2}\cdot\frac{(\varepsilon_{su}-\varepsilon_{c0})^2}{\varepsilon_{su}}\right]} \tag{B.7}$$

In the case of $Z=0$, which applies if the *PR* law for is obtained concrete, and Eq. (B.7) can be simplified as follows:

$$1-\frac{c}{H}-\frac{x_u}{H}=\frac{\frac{1}{\omega}\left(1-\frac{c}{H}\right)-1-\frac{\rho'}{\rho}}{\frac{1}{\omega}\cdot\left(1-\frac{1}{3}\cdot\frac{\varepsilon_{c0}}{\varepsilon_{su}}\right)} \tag{B.8}$$

B.2.7 Failure mode I

The general expression for the term $1-\frac{c}{H}-\frac{x_u}{H}$ for failure mode I is the following:

$$1-\frac{c}{H}-\frac{x_u}{H}=\frac{\frac{1}{\omega}\left(1-\frac{c}{H}\right)\cdot[1-Z\cdot(\varepsilon_{c0}-\varepsilon_{su})]-\frac{\varepsilon_{su}}{\varepsilon_{sy}}\cdot\frac{\rho'}{\rho}-1}{2\cdot\frac{1}{\omega}\cdot\left[\left(1-\frac{1}{3}\cdot\frac{\varepsilon_{c0}}{\varepsilon_{su}}\right)+\frac{Z}{2}\cdot\frac{(\varepsilon_{su}-\varepsilon_{c0})^2}{\varepsilon_{su}}\right]}+ \\ +\frac{\sqrt{\left\{\frac{1}{\omega}\cdot\left(1-\frac{c}{H}\right)\cdot[1-Z\cdot(\varepsilon_{c0}-\varepsilon_{su})]-\frac{\varepsilon_{su}}{\varepsilon_{sy}}\cdot\frac{\rho'}{\rho}-1\right\}^2-4\cdot\frac{1}{\omega}\cdot\left[\left(1-\frac{1}{3}\cdot\frac{\varepsilon_{c0}}{\varepsilon_{su}}\right)+\frac{Z}{2}\cdot\frac{(\varepsilon_{su}-\varepsilon_{c0})^2}{\varepsilon_{su}}\right]\cdot\left[\frac{1}{\omega}\cdot\frac{Z}{2}\cdot\varepsilon_{su}\cdot\left(1-\frac{c}{H}\right)^2-\frac{\varepsilon_{su}}{\varepsilon_{sy}}\cdot\frac{\rho'}{\rho}\cdot\left(1-2\cdot\frac{c}{H}\right)\right]}}{2\cdot\frac{1}{\omega}\cdot\left[\left(1-\frac{1}{3}\cdot\frac{\varepsilon_{c0}}{\varepsilon_{su}}\right)+\frac{Z}{2}\cdot\frac{(\varepsilon_{su}-\varepsilon_{c0})^2}{\varepsilon_{su}}\right]} \tag{B.9}$$

In the case of $Z=0$, which applies if *PR* law is obtained for concrete, and Eq. (B.9) can be simplified as follows:

$$1-\frac{c}{H}-\frac{x_u}{H}=\frac{\frac{1}{\omega}\left(1-\frac{c}{H}\right)-\frac{\varepsilon_{su}}{\varepsilon_{sy}}\cdot\frac{\rho'}{\rho}-1+\sqrt{\left[\frac{1}{\omega}\left(1-\frac{c}{H}\right)-\frac{\varepsilon_{su}}{\varepsilon_{sy}}\cdot\frac{\rho'}{\rho}-1\right]^2+4\cdot\frac{1}{\omega}\left(1-\frac{1}{3}\cdot\frac{\varepsilon_{c0}}{\varepsilon_{su}}\right)\cdot\frac{\varepsilon_{su}}{\varepsilon_{sy}}\cdot\frac{\rho'}{\rho}\cdot\left(1-2\cdot\frac{c}{H}\right)}}{2\cdot\frac{1}{\omega}\cdot\left(1-\frac{1}{3}\cdot\frac{\varepsilon_{c0}}{\varepsilon_{su}}\right)} \tag{B.10}$$

B.2.8 Failure mode J

The general expression for the term $1-\frac{c}{H}-\frac{x_u}{H}$ for failure mode J is the following:

$$1-\frac{c}{H}-\frac{x_u}{H}=\frac{\frac{1}{\omega}\cdot\left(1-\frac{c}{H}\right)\cdot[1-Z\cdot(\varepsilon_{c0}-\varepsilon_{su})]-1+\frac{\rho'}{\rho}}{2\cdot\frac{1}{\omega}\cdot\left[1-\frac{1}{3}\frac{\varepsilon_{c0}}{\varepsilon_{su}}+\frac{Z}{2}\frac{(\varepsilon_{su}-\varepsilon_{c0})^2}{\varepsilon_{su}}\right]}+ \\ +\frac{\sqrt{\left\{\frac{1}{\omega}\cdot\left(1-\frac{c}{H}\right)\cdot[1-Z\cdot(\varepsilon_{c0}-\varepsilon_{su})]-1+\frac{\rho'}{\rho}\right\}^2-4\cdot\frac{1}{\omega^2}\cdot\left[1-\frac{1}{3}\frac{\varepsilon_{c0}}{\varepsilon_{su}}+\frac{Z}{2}\frac{(\varepsilon_{su}-\varepsilon_{c0})^2}{\varepsilon_{su}}\right]\cdot\frac{Z}{2}\varepsilon_{su}\cdot\left(1-\frac{c}{H}\right)^2}}{2\cdot\frac{1}{\omega}\cdot\left[1-\frac{1}{3}\frac{\varepsilon_{c0}}{\varepsilon_{su}}+\frac{Z}{2}\frac{(\varepsilon_{su}-\varepsilon_{c0})^2}{\varepsilon_{su}}\right]} \tag{B.11}$$

In the case of $Z=0$, which applies if the parabola – rectangle law is adopted, Eq. (B.11) can be simplified as follows:

$$1-\frac{c}{H}-\frac{x_u}{H}=\frac{\frac{1}{\omega}\cdot\left(1-\frac{c}{H}\right)-1+\frac{\rho'}{\rho}}{\frac{1}{\omega}\cdot\left(1-\frac{1}{3}\frac{\varepsilon_{c0}}{\varepsilon_{su}}\right)} \tag{B.12}$$

B.2.9 Failure mode K

For failure mode K, the term $1-\frac{c}{H}-\frac{x_u}{H}$ can be expressed as:

$$1-\frac{c}{H}-\frac{x_u}{H}=\frac{1+\frac{\varepsilon_{su}}{\varepsilon_{sy}}\frac{\rho'}{\rho}-\sqrt{\left(1+\frac{\varepsilon_{su}}{\varepsilon_{sy}}\frac{\rho'}{\rho}\right)^2+4\cdot\frac{\alpha_{III}}{\omega}\frac{\varepsilon_{cu}}{\varepsilon_{sy}}\frac{\rho'}{\rho}\cdot\left(1-2\cdot\frac{c}{H}\right)}}{-2\cdot\frac{\varepsilon_{cu}}{\varepsilon_{su}}\frac{\alpha_{III}}{\omega}} \tag{B.13}$$

The corresponding value of spalling depth at failure is:

$$\frac{s_u}{c}=\frac{1-\frac{c}{H}+\frac{\varepsilon_{cu}}{\varepsilon_{su}}}{\frac{c}{H}}\cdot\frac{1+\frac{\varepsilon_{su}}{\varepsilon_{sy}}\frac{\rho'}{\rho}-\sqrt{\left(1+\frac{\varepsilon_{su}}{\varepsilon_{sy}}\frac{\rho'}{\rho}\right)^2+4\cdot\frac{\alpha_{III}}{\omega}\frac{\varepsilon_{cu}}{\varepsilon_{sy}}\frac{\rho'}{\rho}\cdot\left(1-2\cdot\frac{c}{H}\right)}}{-2\cdot\frac{\varepsilon_{cu}}{\varepsilon_{su}}\frac{\alpha_{III}}{\omega}} \tag{B.14}$$

C

An analytical procedure for modelling member response of doubly reinforced concrete beams in four-point bending

C.1 Introduction

The four-point bending loading scheme is an elementary classic scheme used in experimental tests to study the structural response of reinforced concrete (RC) beams and can be used to study both the shear behaviour of beams in the shear spans as well as the bending behaviour of the beams taking advantage from the presence of the constant moment zone. While the analytical calculation of internal actions for this type of structure is obviously straightforward, evaluation of associated deflections considering inelastic member behaviour can require more specific tools, as those commonly used in performance-based assessment of RC structures [4]. However, drawing inspiration from the analytical framework proposed in Chapter 2 for the sectional analytical of doubly reinforced concrete beams, an analytical approach is herein proposed for the analysis of those beams at the member level, considering different failure modes including those which consider the spalling of the concrete cover.

A doubly reinforced concrete section can achieve several different flexural failure modes, as was shown in Chapter 2, depending on the geometric and material characteristics of the section. Accordingly the member response is influenced in terms of both strength and deformation capacity by the behaviour at the sectional level. However, an approach actually considering all possible failure modes and different cases would also result in a greater burden in its use, making such a solution itself not always suitable to be adopted in engineering practice. As a matter of fact, if additional complexity needs to be introduced, it may make sense to make use of more advanced and detailed numerical simulations.

In Chapter 2 it has been also shown however that for beam sections with rather standard characteristics (i.e., which are characterized by a failure mode configuration of *Type 1*) an effective estimation of the sectional behaviour can be pursued considering only a few possible failure modes, without neglecting any relevant phenomena which can affect the response of the section. For this reason, in the proposed procedure only few failure modes are taken into account by assuming that the critical sections of the member would achieve a failure mode configuration of *Type 1*. This also implicitly means that the proposed formulations may not be suitable for study conditions with failure mode configurations different from *Type 1*, for which other (not considered) sectional failure modes may occur. This may be the case of existing deteriorated beams, such as for example those whose effective sectional properties have been modified by the presence of corrosion in the reinforcement.

Although being inspired from the framework proposed in Chapter 2, some relevant differences are present in the approach proposed herein. As an example, steel hardening is considered explicitly, as well as the possible presence of a non-null axial load on the beam.

The loading scheme assumed in the proposed approach is specifically adopted to be representative of the loading condition experienced by beams tested in the experimental campaign described in Chapter 3, for which the constant moment zone and the shear spans have the same length. However, The proposed approach can be also profitably used in engineering practice applications. Moreover, from the solutions retrieved for the

considered four-point bending scheme it is obviously possible to derive also solutions for other schemes useful in practice, as for example a three-point bending scheme or a cantilever scheme, which are representative of a large number of practical situations.

C.2 FUNDAMENTAL HYPOTHESES AND NOTATION

In Fig. C.1 the calculation scheme for the analyzed beam specimens is reported. The analytical calculations have been performed using the hypothesis that the displacement remains small and so the deformed configuration is not so different from the undeformed one, i.e., geometry non-linearities are not considered.

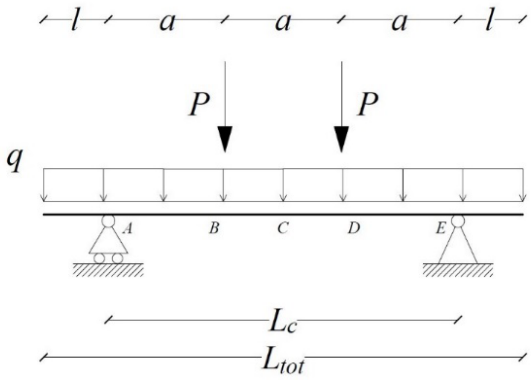

Fig. C.1 Calculation scheme for the generic beam specimen neglecting the friction effects

The following parameters are used in the description of the calculation scheme:

- L_{tot} Total length of the beam
- L_c Length of the central span of the beam
- a Length of one-third of the central span of the beam
- l Length of the cantilever appendices at both sides of central span
- q Distributed load due to self-weight of the beam
- P Force applied at one-third of the central span of the beam

In order to compare analytical results with experimental ones, it is useful to define also the total load F due to the vertical concentrated loads:

$$F = 2 \cdot P \tag{C.1}$$

For the purpose of analyzing the flexural behaviour of the beams it is useful to evaluate the acting bending moment at mid-span of the beam $M_{E,c}$, expressed as:

$$M_{E,c} = P \cdot a + q \cdot \left(\frac{3}{2} \cdot a + l\right) \cdot \left(\frac{3}{4} \cdot a - \frac{1}{2} \cdot l\right) \tag{C.2}$$

Inverting eq. (C.2) and using eq. (C.1) it is possible to express the total load F due to concentrated loads P as a function of the acting bending moment at mid-span M_C, as follows:

$$F = 2 \cdot \frac{M_{E,c} - q \cdot \left(\frac{3}{2} \cdot a + l\right) \cdot \left(\frac{3}{4} a - \frac{1}{2} l\right)}{a} \tag{C.3}$$

Regarding the shear behaviour of the beam, it is worth to also express the shear action V_A acting on the side portions of the beam span:

$$V_A = \frac{F}{2} + q \cdot \left(\frac{3}{2} \cdot a + l\right) \tag{C.4}$$

The load F can be in this case expressed as follows as a function of the shear V_A:

$$F = 2 \cdot \left[V_A - q \cdot \left(\frac{3}{2} \cdot a + l\right)\right] \tag{C.5}$$

Obviously, for equilibrium to be assured, expressions (C.3) and (C.5) provide exactly the same result.

C.3 Response at sectional level

C.3.1 Condition of yielding of tension reinforcement

Sectional analysis can be employed to determine the section's flexural behaviour. The usual hypotheses of plain sections remaining plain in deformed configuration is adopted. The following constitutive laws for materials are employed:

- Bilinear law with hardening for reinforcing steel
- Law for concrete defined by a parabolic branch up to the peak strength, followed by a linear decreasing branch up to ultimate concrete compressive strain. Concrete is considered unconfined.

With reference to the concrete constitutive law, some parameters are worth to be recalled:

$$\alpha = -\frac{1}{3} \cdot \left(\frac{\varepsilon_c}{\varepsilon_{c0}}\right)^2 + \left(\frac{\varepsilon_c}{\varepsilon_{c0}}\right) \qquad if \quad \varepsilon_c \geq \varepsilon_{c2}$$
$$\gamma = \frac{\frac{1}{3} - \frac{1}{12}\left(\frac{\varepsilon_c}{\varepsilon_{c0}}\right)}{1 - \frac{1}{3}\left(\frac{\varepsilon_c}{\varepsilon_{c0}}\right)} \tag{C.6}$$

$$\alpha = \left[1 - \frac{1}{3} \cdot \left(\frac{\varepsilon_{c0}}{\varepsilon_c}\right)\right] - Z \cdot \frac{\varepsilon_{c0} - \varepsilon_c}{2} \cdot \left[1 - \left(\frac{\varepsilon_{c0}}{\varepsilon_c}\right)\right]$$
$$\gamma = \frac{\left[\frac{1}{12}\left(\frac{1}{3}\eta\right)\right] \cdot \left(\frac{\varepsilon_{c0}}{\varepsilon_c}\right)^2 - \left[\frac{1}{3} - \left(\frac{2}{3}\eta\right)\right] \cdot \left(\frac{\varepsilon_{c0}}{\varepsilon_c}\right) + \left[\frac{1}{2} - \left(\frac{1}{3}\eta\right)\right]}{\left[1 - \frac{1}{3}\frac{\varepsilon_{c0}}{\varepsilon_c}\right] - \left[\eta \cdot \left(1 - \frac{\varepsilon_{c0}}{\varepsilon_c}\right)\right]} \qquad if \quad \varepsilon_{cu} < \varepsilon_c < \varepsilon_{c2} \tag{C.7}$$

$$\eta = \frac{1}{2} \cdot Z \cdot (|\varepsilon_c| - |\varepsilon_{c0}|) \geq 0$$

$$\alpha = \left[1 - \frac{1}{3} \cdot \left(\frac{\varepsilon_{c0}}{\varepsilon_{cu}}\right)\right] - \eta \cdot \left[1 - \left(\frac{\varepsilon_{c0}}{\varepsilon_{cu}}\right)\right]$$

$$\gamma = \frac{\left[\frac{1}{12} - \left(\frac{1}{3}\eta\right)\right] \cdot \left(\frac{\varepsilon_{c0}}{\varepsilon_{cu}}\right)^2 - \left[\frac{1}{3} - \left(\frac{2}{3}\eta\right)\right] \cdot \left(\frac{\varepsilon_{c0}}{\varepsilon_{cu}}\right) + \left[\frac{1}{2} - \left(\frac{1}{3}\eta\right)\right]}{\left[1 - \frac{1}{3}\frac{\varepsilon_{c0}}{\varepsilon_{cu}}\right] - \left[\eta \cdot \left(1 - \frac{\varepsilon_{c0}}{\varepsilon_{cu}}\right)\right]} \qquad if \quad \varepsilon_c \leq \varepsilon_{cu} \tag{C.8}$$

$$\eta = \frac{1}{2} \cdot Z \cdot (|\varepsilon_{cu}| - |\varepsilon_{c0}|) \geq 0$$

The term Z is the slope of the post-peak linear softening branch of the concrete law. By using $Z = 0$, the *PR* law for concrete is obtained. In general, Z can be expressed as:

$$Z = \frac{0.5}{\varepsilon_{50u} - \varepsilon_{c0}} \tag{C.9}$$

The parameter ε_{50u} is the strain at which compressive strength has halved. If the *KP* law for concrete is adopted, for unconfined concrete the parameter ε_{50u} can be calculated as:

$$\varepsilon_{50u} = -\frac{3 + 0.29 \cdot f_c[MPa]}{145 \cdot f_c[MPa] - 1000} \tag{C.10}$$

Otherwise, the slope Z of the softening branch can be directly defined as desired.

The section behaviour is analyzed at three stages, namely:

- The yielding condition, identified either by yielding of bottom reinforcing steel of by the attainment of peak concrete strength in the most compressed fiber of the section
- The condition at which spalling initiate, identified by the attainment of concrete ultimate compressive strain in the outer fiber of the section
- The ultimate condition of the section, herein identified by either the complete spalling of the concrete cover or the attainment of ultimate tensile strain in bottom steel

In order to account for the axial force induced by the friction, the non-dimensional axial force ν is introduced in the formulation, with a positive sign for tension:

$$\nu = \frac{N}{b \cdot H} \quad with \ N > 0 \ for \ tension \tag{C.11}$$

In the following, the bending strength and the associated curvature value are calculated for each of the considered section conditions.

C.3.2 CONDITION OF YIELDING OF TENSION REINFORCEMENT

It is first necessary to determine whether the yielding condition will develop as bottom steel yielding or compressed concrete plasticization. In order to do so, it is useful to employ the analytical formulation for yielding mode domains.

In order to do so, the following parameter are needed:

$$\left(\frac{c}{H}\right)_0 = \frac{1}{2-\frac{\varepsilon_{sy}}{\varepsilon_{c0}}} \quad with\ \varepsilon_{c0} < 0 \tag{C.12}$$

Since for the studied beams the condition $\frac{c}{H} \leq \left(\frac{c}{H}\right)_0$ applies, the section experience yielding condition by means of steel yielding if the following statement is satisfied:

$$\frac{\rho'}{\rho} > \frac{1}{k'} - \frac{\nu}{\rho \cdot f_y \cdot k'} - \frac{2}{3} \cdot \frac{1}{k'} \cdot \frac{1}{\omega} \cdot \left(\frac{\varepsilon_{c0}}{\varepsilon_{c0}-\varepsilon_{sy}}\right) \cdot \left(1 - \frac{c}{H}\right) \tag{C.13}$$

With coefficient k' expressed by:

$$k' = -\frac{\varepsilon_{c0}}{\varepsilon_{sy}} \cdot \left(1 + \frac{1}{1-\frac{1}{\frac{c}{H}}} \cdot \frac{\varepsilon_{c0}-\varepsilon_{sy}}{\varepsilon_{c0}}\right) \tag{C.14}$$

Since condition (C.13) is satisfied, the section reaches its yielding condition when the bottom reinforcement yields. The ratio ξ between neutral axis depth and effective depth at yielding is provided by the smallest positive root of the equation:

$$\left\{\left[\frac{1}{3} \cdot \left(\frac{\varepsilon_{sy}}{\varepsilon_{c0}}\right)^2 - \left(\frac{\varepsilon_{sy}}{\varepsilon_{c0}}\right)\right] \cdot \frac{1}{\omega} \cdot \left(1 - \frac{c}{H}\right)\right\} \cdot \boldsymbol{\xi^3} + \left\{1 - \frac{\nu}{\rho \cdot f_y} + \frac{\rho'}{\rho} + \left(\frac{\varepsilon_{sy}}{\varepsilon_{c0}}\right) \cdot \frac{1}{\omega} \cdot \left(1 - \frac{c}{H}\right)\right\} \cdot \boldsymbol{\xi^2} + \\ + \left\{-2 \cdot \left(1 - \frac{\nu}{\rho \cdot f_y}\right) - \frac{\rho'}{\rho} \cdot \left(\frac{1}{1-\frac{c}{H}}\right)\right\} \cdot \boldsymbol{\xi} + \left\{1 - \frac{\nu}{\rho \cdot f_y} + \frac{\rho'}{\rho} \cdot \left(\frac{\frac{c}{H}}{1-\frac{c}{H}}\right)\right\} = 0 \tag{C.15}$$

The non-dimensional neutral axis depth at yielding $\frac{x_y}{H}$ can be obtained from the ratio ξ as follows:

$$\frac{x_y}{H} = \left(1 - \frac{c}{H}\right) \cdot \xi \tag{C.16}$$

The bending strength M_y and the curvature ϕ_y associated to the yielding condition are then expressed by equations (C.17) and (C.18), respectively:

$$M_y = f_y \cdot \rho \cdot b \cdot H^2 \cdot \left\{\frac{\alpha}{\omega} \cdot \frac{x_y}{H} \cdot \left[\frac{c}{H} - \gamma \cdot \frac{x_y}{H}\right] + 1 - 2 \cdot \frac{c}{H} + \frac{\nu}{\rho \cdot f_y} \cdot \left(\frac{1}{2} - \frac{c}{H}\right)\right\} \tag{C.17}$$

$$\phi_y = \frac{1}{1-\xi} \cdot \frac{1}{1-\frac{c}{H}} \cdot \frac{\varepsilon_{sy}}{H} \tag{C.18}$$

In the section yielding condition the concrete doesn't have reached the peak strength yet. So, the coefficients α and γ need to be calculated according to equation (C.6).
The strain at the top section fiber ε_c can be expressed as:

$$\varepsilon_c = -\varepsilon_{sy} \cdot \frac{\xi}{1-\xi} \tag{C.19}$$

Once the coefficients α and γ are known, the yielding curvature and the yielding moment can be evaluated.

C.3.3 CONDITION OF BEGINNING OF CONCRETE COVER SPALLING

The condition of beginning of concrete cover spalling is associated with the achievement of the strain value $\varepsilon_{c0} = -2‰$ on the outmost compressed fiber of the section. The first parameters needed for the evaluation of the associated bending moment and curvature values are the non-dimensional neutral axis depth $\frac{x_{sp}}{H}$ and the stress rate in bottom steel at the onset of spalling k_{sp}, which can be calculated dependently of the mode through which actually the spalling initiation actually occur. In order to determine that, the analytical formulations of failure mode domains without spalling presented in Chapter 2 are employed, slightly modified to take into account for axial load and steel hardening. First of all, it is necessary to check if the failure mode domains assume the domains configuration *Type 1*. The check is satisfied if the following requirements are met:

$$\omega > \frac{1}{\left(\frac{f_t}{f_y}+\frac{\nu}{\rho \cdot f_y}\right)} \cdot \frac{\alpha}{\left(2-\frac{\varepsilon_{su}}{\varepsilon_{cu}}\right)} \quad with \ \varepsilon_{cu} < 0 \tag{C.20}$$

$$0.075 \leq \frac{c}{H} \leq 0.25 \tag{C.21}$$

$$\frac{\rho'}{\rho} \geq 0.5 \tag{C.22}$$

For the analyzed case, all the previous conditions are satisfied, so the failure mode domains without spalling assume the *Type 1* configuration described in Chapter 2. Reference value for the ratio between reinforcements $(\rho'/\rho)_{DE}$ can be computed as:

$$\left(\frac{\rho'}{\rho}\right)_{DE} = 1 - \frac{\alpha}{\omega} \cdot \frac{c}{H} \cdot \frac{\varepsilon_{cu}}{\varepsilon_{cu}+\varepsilon_{sy}} \cdot \left(1 - \frac{s_{lim}}{c}\right) - \frac{\nu}{\rho_s \cdot f_y} - r_E \cdot \left[\left(1 - \frac{\varepsilon_{cu}}{\varepsilon_{sy}}\right) + \frac{\frac{\varepsilon_{cu}}{\varepsilon_{sy}}\left[1-\frac{c}{H}\right]}{\frac{c}{H}\frac{\varepsilon_{cu}}{\varepsilon_{cu}+\varepsilon_{sy}}}\right] \tag{C.23}$$

If $\frac{\rho'}{\rho} > \left(\frac{\rho'}{\rho}\right)_{DE}$ failure mode "D" is achieved according to the classification provided in Chapter 2. In such a case, the non-dimensional neutral axis depth $\frac{x_{sp}}{H}$ and the coefficients k_{sp} and k'_{sp} can be calculated as:

$$\frac{x_{sp}}{H} = \frac{-B+\sqrt{B^2-4\cdot A\cdot C}}{2\cdot A} \tag{C.24}$$

$$k_{sp} = -\frac{\varepsilon_{cu}}{\varepsilon_{sy}}\cdot\left(\frac{1-\frac{c}{H}}{\frac{x_{sp}}{H}}-1\right) \tag{C.25}$$

$$k'_{sp} = -\frac{\varepsilon_{cu}}{\varepsilon_{sy}}\cdot\left(1-\frac{\frac{c}{H}}{\frac{x_{sp}}{H}}\right) \tag{C.26}$$

where:

$$A = \left[\frac{\alpha}{\omega}\right] \tag{C.27}$$

$$B = \left[-\frac{\varepsilon_{cu}}{\varepsilon_{sy}}\cdot\frac{\rho'_s}{\rho_s}-1+r_E\cdot\left(1+\frac{\varepsilon_{cu}}{\varepsilon_{sy}}\right)+\frac{\nu}{\rho_s\cdot f_y}\right] \tag{C.28}$$

$$C = \left\{-\frac{\varepsilon_{cu}}{\varepsilon_{sy}}\cdot r_E\cdot\left[\frac{c}{H}-1\right]+\frac{\varepsilon_{cu}}{\varepsilon_{sy}}\cdot\frac{\rho'_s}{\rho_s}\cdot\frac{c}{H}\right\} \tag{C.29}$$

If otherwise $\frac{\rho'}{\rho} < \left(\frac{\rho'}{\rho}\right)_{DE}$ failure mode "E" is achieved according to the classification provided in Chapter 2, so the non-dimensional neutral axis depth $\frac{x_{sp}}{H}$ and the coefficients k_{sp} and k'_{sp} can be calculated as:

$$\frac{x_{sp}}{H} = \frac{-B+\sqrt{B^2-4\cdot A\cdot C}}{2\cdot A} \tag{C.30}$$

$$k_{sp} = -\frac{\varepsilon_{cu}}{\varepsilon_{sy}}\cdot\left(\frac{1-\frac{c}{H}}{\frac{x_{sp}}{H}}-1\right) \tag{C.31}$$

$$k'_{sp} = -\frac{\varepsilon_{cu}}{\varepsilon_{sy}}\cdot\left(1-\frac{\frac{c}{H}}{\frac{x_{sp}}{H}}\right) \tag{C.32}$$

where:

$$A = \left[\frac{\alpha}{\omega}\right] \tag{C.33}$$

$$B = \left[-\frac{\varepsilon_{cu}}{\varepsilon_{sy}}\cdot\frac{\rho'_s}{\rho_s}\cdot r_E-1+r_E\cdot\left(1+\frac{\varepsilon_{cu}}{\varepsilon_{sy}}\right)+\frac{\nu}{\rho_s\cdot f_y}+\frac{\rho'_s}{\rho_s}\cdot(1-r_E)\right] \tag{C.34}$$

$$C = \left\{-\frac{\varepsilon_{cu}}{\varepsilon_{sy}}\cdot r_E\cdot\left[\frac{c}{H}-1-\frac{\rho'_s}{\rho_s}\cdot\frac{c}{H}\right]\right\} \tag{C.35}$$

The term r_E in the previous equations represent the hardening ratio, i.e., the ratio between the post-yielding tangent modulus E_s^* and the initial elastic modulus of steel E_s:

$$r_E = \frac{E_s^*}{E_s} \geq 0 \tag{C.36}$$

Once the non-dimensional neutral axis depth $\frac{x_{sp}}{H}$ and the coefficient k_{sp} are known, is it then possible to obtain the bending strength M_{sp} and the curvature ϕ_{sp} associated to the condition of spalling initiation. Expressions for M_{sp} and ϕ_{sp} are as follows:

$$M_{sp} = f_y \cdot \rho \cdot b \cdot H^2 \cdot \left\{ \frac{\alpha}{\omega} \cdot \frac{x_{sp}}{H} \cdot \left[\frac{c}{H} - \gamma \cdot \frac{x_{sp}}{H} \right] + 1 + \right. \\ \left. + r_E \cdot \left(k_{sp} - 1\right) \cdot \left(1 - 2 \cdot \frac{c}{H}\right) - \frac{\nu}{\rho \cdot f_y} \cdot \left(\frac{1}{2} - \frac{c}{H}\right) \right\} \tag{C.37}$$

$$\phi_{sp} = -\frac{\varepsilon_{cu}}{H} \cdot \frac{1}{\frac{x_{sp}}{H}} \tag{C.38}$$

For the condition in which spalling begins, the extreme concrete fiber has reached the ultimate concrete compressive strain. So, the coefficients α and γ need to be calculated according to equation (C.8).

C.3.4 Condition of failure achieved by the achievement of ultimate compressive strain in core concrete after the complete spalling of the cover

An approach analogous to that used in the previous section is adopted, though employing the analytical formulations of failure mode domains with spalling of the concrete cover. The reference value for the ratio between reinforcements $(\rho'/\rho)_{DE}$ can be computed in this case as:

$$\left(\frac{\rho'}{\rho}\right)_{DE} = 1 - \frac{\alpha}{\omega} \cdot \frac{c}{H} \cdot \frac{\varepsilon_{cu}}{\varepsilon_{cu} + \varepsilon_{sy}} \cdot \left(1 - \frac{s_{lim}}{c}\right) - \frac{\nu}{\rho_s \cdot f_y} + \\ - r_E \cdot \left[\left(1 - \frac{\varepsilon_{cu}}{\varepsilon_{sy}}\right) + \frac{\frac{\varepsilon_{cu}}{\varepsilon_{sy}} \cdot \left[1 - \frac{c}{H} \cdot \left(1 + \frac{s_{lim}}{c}\right)\right]}{\frac{c}{H} \cdot \frac{\varepsilon_{cu}}{\varepsilon_{cu} + \varepsilon_{sy}} \cdot \left(1 - \frac{s_{lim}}{c}\right)} \right] \tag{C.39}$$

If $\frac{\rho'}{\rho} > \left(\frac{\rho'}{\rho}\right)_{DE}$, mode "D" is achieved and the non-dimensional depth $\frac{x_u - s_u}{H}$ as well as the coefficients k_u and k'_u can be calculated as:

$$\left(\frac{x-s}{H}\right)_u = \frac{-B + \sqrt{B^2 - 4 \cdot A \cdot C}}{2 \cdot A} \tag{C.40}$$

$$k_u = -\frac{\varepsilon_{cu}}{\varepsilon_{sy}} \cdot \left[\frac{1 - \frac{c}{H}\left(1 + \frac{s_{lim}}{c}\right)}{\left(\frac{x-s}{H}\right)_u} - 1 \right] \tag{C.41}$$

$$k'_u = -\frac{\varepsilon_{cu}}{\varepsilon_{sy}} \cdot \left[1 - \frac{\frac{c}{H}\left(1 - \frac{s_{lim}}{c}\right)}{\left(\frac{x-s}{H}\right)_u} \right] \tag{C.42}$$

where:

$$A = \left[\frac{\alpha}{\omega}\right] \tag{C.43}$$

$$B = \left[-\frac{\varepsilon_{cu}}{\varepsilon_{sy}} \cdot \frac{\rho'_s}{\rho_s} - 1 + r_E \cdot \left(1 + \frac{\varepsilon_{cu}}{\varepsilon_{sy}}\right) + \frac{\nu}{\rho_s \cdot f_y}\right] \tag{C.44}$$

$$C = \left\{-\frac{\varepsilon_{cu}}{\varepsilon_{sy}} \cdot r_E \cdot \left[\frac{c}{H} \cdot \left(1 + \frac{s_{lim}}{c}\right) - 1\right] + \frac{\varepsilon_{cu}}{\varepsilon_{sy}} \cdot \frac{\rho'_s}{\rho_s} \cdot \frac{c}{H} \cdot \left(1 - \frac{s_{lim}}{c}\right)\right\} \tag{C.45}$$

If otherwise $\frac{\rho'}{\rho} < \left(\frac{\rho'}{\rho}\right)_{DE}$ failure mode "E" is achieved according to the classification provided in Chapter 2, so the non-dimensional neutral axis depth $\frac{x_u}{H}$ and the coefficients k_u and k'_u can be calculated as:

$$\left(\frac{x-s}{H}\right)_u = \frac{-B+\sqrt{B^2-4 \cdot A \cdot C}}{2 \cdot A} \tag{C.46}$$

$$k_u = -\frac{\varepsilon_{cu}}{\varepsilon_{sy}} \cdot \left[\frac{1-\frac{c}{H}\left(1+\frac{s_{lim}}{c}\right)}{\left(\frac{x-s}{H}\right)_u} - 1\right] \tag{C.47}$$

$$k'_u = -\frac{\varepsilon_{cu}}{\varepsilon_{sy}} \cdot \left[1 - \frac{\frac{c}{H}\left(1-\frac{s_{lim}}{c}\right)}{\left(\frac{x-s}{H}\right)_u}\right] \tag{C.48}$$

where:

$$A = \left[\frac{\alpha}{\omega}\right] \tag{C.49}$$

$$B = \left[-\frac{\varepsilon_{cu}}{\varepsilon_{sy}} \cdot \frac{\rho'_s}{\rho_s} \cdot r_E - 1 + r_E \cdot \left(1 + \frac{\varepsilon_{cu}}{\varepsilon_{sy}}\right) + \frac{\nu}{\rho_s \cdot f_y} + \frac{\rho'_s}{\rho_s} \cdot (1 - r_E)\right] \tag{C.50}$$

$$C = \left\{-\frac{\varepsilon_{cu}}{\varepsilon_{sy}} \cdot r_E \cdot \left[\frac{c}{H} \cdot \left(1 + \frac{s_{lim}}{c}\right) - 1 - \frac{\rho'_s}{\rho_s} \cdot \frac{c}{H} \cdot \left(1 - \frac{s_{lim}}{c}\right)\right]\right\} \tag{C.51}$$

In the aforementioned cases, the core concrete has reached the ultimate concrete compressive strain. So, the coefficients α and γ need to be calculated according to equation (C.8).
In order to take into account for the possible occurrence of failure modes "K" and "L", i.e., failures in which the steel rupture occurs during the spalling of the concrete cover, the maximum achievable curvature $\phi_{u,max}$ needs to be evaluated:

$$\phi_{u,max} = \frac{1}{H} \cdot \frac{\varepsilon_{su}-\varepsilon_{cu}}{1-\frac{c}{H}\left(1+\frac{s_{lim}}{c}\right)} \tag{C.52}$$

Then, to check whether one of the two failure modes "K" and "L" is prone to occur, the maximum ultimate curvature needs to be compared with the curvature values obtained for failure modes "D" and "E". If the maximum achievable curvature is higher than the

other two, then failure mode "D" or "E" is achieved. Conversely, failure mode "K" or "L" occurs.

To evaluate the bending strength M_u and the associated curvature ϕ_u two cases are considered. If the failure mode is of type "D" or "E", then M_u and ϕ_u can be computed as follows:

$$M_u = f_y \cdot \rho \cdot b \cdot H^2 \cdot \left\{ \frac{\alpha}{\omega} \cdot \left(\frac{x-s}{H}\right)_u \cdot \left[\frac{c}{H} \cdot \left(1 - \frac{s_u}{c}\right) - \gamma \cdot \left(\frac{x-s}{H}\right)_u \right] + 1 + \right. \\ \left. + r_E \cdot (k_u - 1) \cdot \left(1 - 2 \cdot \frac{c}{H}\right) - \frac{\nu}{\rho \cdot f_y} \cdot \left(\frac{1}{2} - \frac{c}{H}\right) \right\} \tag{C.53}$$

$$\phi_u = -\frac{\varepsilon_{cu}}{H} \cdot \frac{1}{\left(\frac{x-s}{H}\right)_u} \tag{C.54}$$

Conversely, if failure mode is either of type "K" or "L", the simplified approach suggested in section 2.6 of Chapter 2 is adopted, in which it is assumed that the ultimate curvature ϕ_u obtained for failure modes with steel rupture during the spalling of the concrete cover is approximately equal to the maximum achievable ultimate curvature $\phi_{u,max}$ expressed by eq. (C.52). Accordingly, the bending strength M_u and the associated curvature ϕ_u for this cases are calculated as follows:

$$M_u = f_y \cdot \rho \cdot b \cdot H^2 \cdot \left\{ \frac{\alpha}{\omega} \cdot \left(\frac{x-s}{H}\right)_u \cdot \left[\frac{c}{H} \cdot \left(1 - \frac{s_u}{c}\right) - \gamma \cdot \left(\frac{x-s}{H}\right)_u \right] + 1 + \right. \\ \left. + r_E \cdot (k_u - 1) \cdot \left(1 - 2 \cdot \frac{c}{H}\right) - \frac{\nu}{\rho \cdot f_y} \cdot \left(\frac{1}{2} - \frac{c}{H}\right) \right\} \tag{C.55}$$

$$\phi_u = \frac{1}{H} \cdot \frac{\varepsilon_{su} - \varepsilon_{cu}}{1 - \frac{c}{H}\left(1 + \frac{s_{lim}}{c}\right)} \tag{C.56}$$

where:

$$\left(\frac{x-s}{H}\right)_u = -\frac{\varepsilon_{cu}}{\varepsilon_{su}} \cdot \left(1 - \frac{c}{H} - \frac{x}{H}\right)_u \tag{C.57}$$

$$\left(\frac{s}{H}\right)_u = \frac{1}{\frac{c}{H}} - 1 + \frac{1}{\frac{c}{H}} \cdot \left(\frac{\varepsilon_{cu}}{\varepsilon_{su}} - 1\right) \cdot \left(1 - \frac{c}{H} - \frac{x}{H}\right)_u \tag{C.58}$$

$$\left(1 - \frac{c}{H} - \frac{x}{H}\right)_u = \frac{\varepsilon_{su}}{\varepsilon_{su} - \varepsilon_{cu}} \cdot \left[1 - \frac{c}{H} \cdot \left(1 + \frac{s_{lim}}{c}\right)\right] \tag{C.59}$$

Also in the cases the failure mode is of type "K" or "L", the coefficients α and γ need to be calculated according to equation (C.8).

C.4 Response at member level

C.4.1 Overview

In the following is presented a method to analytically evaluate the capacity curve for beam specimens in four-points bending loading condition, as the curve representing the relation between total force F due to the concentrated loads and vertical displacement δ_C measured at beams midspan.
The displacement δ_C is due to the combined action of the beam self-weight and of the concentrated loads. However, the contribution due to self-weight is very small compared to the one due to the concentrated loads and can therefore be neglected in the computation of deflections. The vertical displacement at mid-span developed by the beam is schematized as the sum of two different contributions, respectively associated to flexural deformations and shear deformations. Deformations due to slip between rebars and concrete (also referred as fix-end rotation contributions) are not taken into account in the present case, since the rebars were well anchored in the beam zones with nearly no bending action.
In Fig. C.2, bending moment and shear distributions along the beam are presented. In addition, curvature distributions up to yielding and after yielding of the tension reinforcement are provided. For the latter case, the usual plastic hinge approach has been adopted for the curvature distribution [8], [4], in which the plastic deformation is supposed to be concentrated in a fictitious length L_{pl}, named plastic hinge length.

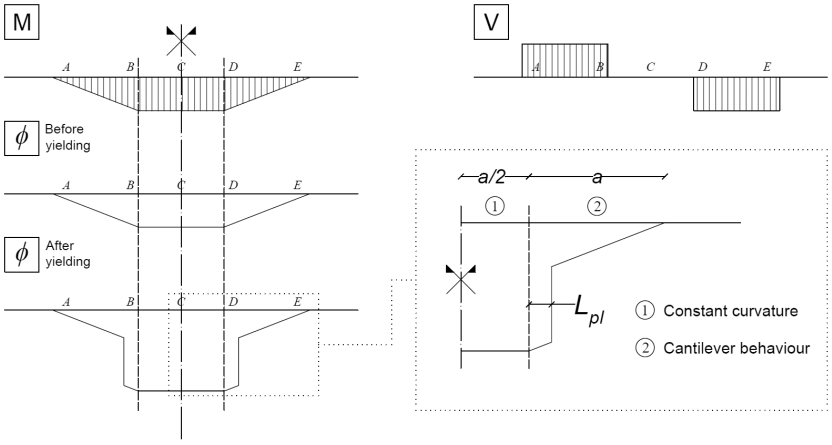

Fig. C.2 Bending moment, shear and curvature distributions along the beam

Mid-span displacement is be calculated by means of both integration of curvature distribution (for the portion having constant bending moment) and chord rotations (for the side-portions having a cantilever type behaviour). Formulations for chord rotation capacity have been adopted according to Eurocode 8 – Part 3 [24] and can also be found in Fardis [4], together with a critical discussion on their applicability and limitations.

The following notation is herein adopted for curvatures, rotations and chord rotations:

- δ^i Displacement of section i
- δ^{ij} Relative displacement between sections i and j of the beam
- θ^{ij} Chord rotation between sections i and j of the beam
- φ^i Rotation of a section i
- ϕ^i Curvature of a section i

C.4.2 DISPLACEMENTS CALCULATION AT SECTION FLEXURAL YIELDING

C.4.2.1 *Calculation of deflections*

The calculation of the displacement δ_y^C can be performed considering the half-beam scheme represented at the right-bottom part of Fig. C.2. Starting from the mid-span and moving to the support, displacement contributions can be calculated and added together. The displacement δ_y^{CD} is supposed only due to pure flexural deformations and can so be obtained by means of double integration of the curvature distribution in the portion of constant bending moment:

$$\delta_y^{CD} = \int_0^{a/2} \left[\int \phi(x)dx\right] dx = \frac{1}{2} \cdot \phi_y^C \cdot \left(\frac{a}{2}\right)^2 \tag{C.60}$$

On the other hand, the displacement δ^{DE} can be evaluated as:

$$\delta_y^{DE} = \phi_y^D \cdot a + \theta_y^{DE} \cdot a = \frac{1}{2} \cdot \phi_y^C \cdot a^2 + \theta_y^{DE} \cdot a \tag{C.61}$$

The first term on the right-hand-side of eq. (C.61) represents the contribution due to the rotation of point D, while the second term is associated to the chord rotation between points D and E. The latter can be evaluated using equation "A.10b" reported in Eurocode 8 – Part 3 [24] at section "A.3.2.4", neglecting the term associated to the fix-end rotation. So, the following expression is used for the chord rotation θ_y^{DE}:

$$\theta_y^{DE} = \phi_y^D \cdot \frac{a+a_s \cdot z}{3} + 0.0014 \cdot \left(1 + 1.5 \cdot \frac{H}{a}\right) \tag{C.62}$$

Since $\delta^E = 0$ being vertically supported, the displacement δ^C can be expressed as $\delta_y^C = \delta_y^{CE}$, so:

$$\delta_y^C = \delta_y^{CD} + \delta_y^{DE} \tag{C.63}$$

By substituting equations (C.60), (C.61) and (C.62) into equation (C.63), the following expression for δ_y^C can be obtained:

$$\delta^C = \frac{1}{2} \cdot \phi_y^C \cdot \left(\frac{a}{2}\right)^2 + \frac{1}{2} \cdot \phi_y^C \cdot a^2 + \left[\phi_y^D \cdot \frac{a+a_s \cdot z}{3} + 0.0014 \cdot \left(1 + 1.5 \cdot \frac{H}{a}\right)\right] \cdot a \tag{C.64}$$

It could be useful to rearrange expression (C.64) to separately highlighting the contributions due to flexure and shear:

$$\delta_y^C = \left\{\left[\frac{5}{8}\cdot\phi_y^C\cdot a^2\right]+\left[\frac{1}{3}\cdot\phi_y^D\cdot a^2\right]\right\}+ \\ +\left\{\left[\frac{1}{3}\cdot\phi_y^D\cdot(a_s\cdot z)\cdot a\right]+\left[0.0014\cdot\left(1+1.5\cdot\frac{H}{a}\right)\cdot a\right]\right\} \tag{C.65}$$

In the left bracket of eq. (C.65), the flexure contributions are inserted. On the other hand, shear contribution and corrective terms are contained in the right bracket. In particular, the following terms can be identified:

- $\left[\frac{5}{8}\cdot\phi^C\cdot a^2\right]$ — *Flexural* contribution associated to the constant moment portion
- $\left[\frac{1}{3}\cdot\phi^D\cdot a^2\right]$ — *Flexural* contribution associated to the cantilever portion
- $\left[\frac{1}{3}\cdot\phi^D\cdot(a_s\cdot z)\cdot a\right]$ — *Shear cracking* contribution associated to the cantilever portion
- $\left[0.0014\cdot\left(1+1.5\cdot\frac{H}{a}\right)\cdot a\right]$ — *Corrective* contribution, explained in Fardis [4]

A fairly good approximation of the inner level arm z can be obtained using the classical expression:

$$z\cong 0.9\cdot d \tag{C.66}$$

C.4.2.2 *Identifying the occurrence of shear cracking*

The term a_s in eqs. (C.64) and (C.65) is a zero-one variable which accounts for the presence of deformations due to shear cracking. In particular, if shear cracking occurs before yielding of the tension longitudinal reinforcement, then the term a_s is taken as 1; otherwise, it is taken as 0. The occurrence of the shear cracking before flexural yielding can be identified comparing the yielding load with the shear cracking load. In literature works, different choices can be found regarding the definition of the shear cracking load [10], [4]. In the present study, shear cracking is considered to take place when the beam is subjected to a shear action higher than the shear strength without shear reinforcement $V_{R,c}$. Such shear strength can be evaluated for example according to the formulation provided by equation "6.2a" reported in section "6.2.2" of Eurocode 2 – Part 1-1 [129].

That equation is herein presented in a rearranged form, as reported at section "3.2.3.2" of Fardis [4]:

$$V_{R,c} = \left\{ max\left[180 \cdot (100 \cdot \rho)^{\frac{1}{3}} \; ; \; 35 \cdot \sqrt{1 + \sqrt{\frac{0.2}{d}}} \cdot f_c^{\frac{1}{6}} \right] \cdot \left(1 + \sqrt{\frac{0.2}{d}} \right) \cdot f_c^{\frac{1}{3}} - 0.15 \cdot \nu \right\} \cdot b \cdot d \tag{C.67}$$

In equation (C.67) the shear cracking strength $V_{R,c}$ is obtained in $[kN]$ if section width b and effective height d are provided in $[m]$ and concrete compressive strength f_c is provided in $[MPa]$ and taken positive for tension. In equation (C.67) the non-dimensional axial load ν is positive for tension. However, if a tensile axial load is acting on the member, the shear cracking strength $V_{R,c}$ must be taken as zero.
In order to determine the value of coefficient a_s is then useful to evaluate the value of total force F due to concentrated loads associated to the yielding condition and the occurrence of the shear cracking.

The load associated to the yielding condition F_y can be expressed as:

$$F_y = 2 \cdot \frac{M_y - q \cdot \left(\frac{3}{2} a + l\right) \cdot \left(\frac{3}{4} a - \frac{1}{2} l\right)}{a} \tag{C.68}$$

where the bending moment at yielding M_y is expressed by equation (C.17). On the other hand, the total load associated to shear cracking F_{sc} can be calculated from equation (C.69):

$$F_{sc} = 2 \cdot \left[V_{R,c} - q \cdot \left(\frac{3}{2} \cdot a + l \right) \right] \tag{C.69}$$

So, the evaluation of the coefficient a_s can be performed as follows:

$$\begin{cases} if \quad F_{sc} \leq F_y \quad \rightarrow \quad a_s = 1 \\ if \quad F_{sc} > F_y \quad \rightarrow \quad a_s = 0 \end{cases} \tag{C.70}$$

C.4.3 Displacements calculation after section flexural yielding

C.4.3.1 *Calculation of deflections*

The displacement δ^{CD} is calculated in the same manner as previously shown for the case of beam which has not yet reached yielding:

$$\delta^{CD} = \frac{1}{2} \cdot \phi^C \cdot \left(\frac{a}{2} \right)^2 \tag{C.71}$$

Again, also the displacement δ_{DE} can be evaluated as the same of the previous case:

$$\delta^{DE} = \varphi^D \cdot a + \theta^{DE} \cdot a = \frac{1}{2} \cdot \phi^C \cdot a^2 + \theta^{DE} \cdot a \tag{C.72}$$

The chord rotation θ^{DE} can be evaluated for this case using equation "A.4" reported in Eurocode 8 – Part 3 [24] at section "A.3.2.2", neglecting the term associated to the fix-end rotation. So, the following expression is used for the chord rotation θ^{DE}:

$$\theta^{DE} = \theta_y^{DE} + \left(\phi^D - \phi_y^D\right) \cdot L_{pl} \cdot \left(1 - \frac{L_{pl}}{2 \cdot a}\right) \tag{C.73}$$

where:

$$\theta_y^{DE} = \phi_y^D \cdot \frac{a + a_s \cdot z}{3} + 0.0014 \cdot \left(1 + 1.5 \cdot \frac{H}{a}\right) \tag{C.74}$$

The term a_s in equation (C.74) is calculated accordingly to the procedure explained in the previous section. As in the previous case, to obtain the displacement δ^C is sufficient to sum the two contributions δ^{CD} and δ^{DE}, as stated by equation (C.63). It is the possible to rearrange the expression of δ^C as follows:

$$\begin{aligned}\delta^C = {} & \frac{1}{2} \cdot \phi^C \cdot \left(\frac{a}{2}\right)^2 + \frac{1}{2} \cdot \phi^C \cdot a^2 + \\ & + \left[\phi_y^D \cdot \frac{a + a_s \cdot z}{3} + 0.0014 \cdot \left(1 + 1.5 \cdot \frac{H}{a}\right) + \left(\phi^D - \phi_y^D\right) \cdot L_{pl} \cdot \left(1 - \frac{1}{2} \cdot \frac{L_{pl}}{a}\right)\right] \cdot a\end{aligned} \tag{C.75}$$

It is useful again to separate the terms associated to flexure and shear deformations, as follows:

$$\begin{aligned}\delta^C = {} & \left\{\left[\frac{5}{8} \cdot \phi^C \cdot a^2\right] + \left[\frac{1}{3} \cdot \phi_y^D \cdot a^2 + \left(\phi^D - \phi_y^D\right) \cdot L_{pl} \cdot a \cdot \left(1 - \frac{1}{2} \cdot \frac{L_{pl}}{a}\right)\right]\right\} + \\ & + \left\{\left[\frac{1}{3} \cdot \phi_y^D \cdot (a_s \cdot z) \cdot a\right] + \left[0.0014 \cdot \left(1 + 1.5 \cdot \frac{H}{a}\right) \cdot a\right]\right\}\end{aligned} \tag{C.76}$$

As in the previous case, in the left bracket, the flexure contributions are inserted. On the other hand, shear contribution and corrective terms are contained in the right bracket. In particular, the following terms can be separately identified:

- $\left[\frac{5}{8} \cdot \phi^C \cdot a^2\right]$
  Flexural contribution associated to the constant moment portion
- $\left[\frac{1}{3} \cdot \phi_y^D \cdot a^2 + \left(\phi^D - \phi_y^D\right) \cdot L_{pl} \cdot a \cdot \left(1 - \frac{L_{pl}}{2 \cdot a}\right)\right]$
  Flexural contribution associated to the cantilever portion
- $\left[\frac{1}{3} \cdot \phi_y^D \cdot (a_s \cdot z) \cdot a\right]$
  Shear cracking contribution associated to the cantilever portion
- $\left[0.0014 \cdot \left(1 + 1.5 \cdot \frac{H}{a}\right) \cdot a\right]$
  Corrective contribution, explained in Fardis [4]

C.4.3.2 *Definition of plastic hinge length*

The adopted approach for calculating member deflections made use of the chord rotation expressed by eq. (C.73) to compute of the flexural contributions due to the cantilever beam portions located at both sides of the constant moment zone (Fig. C.2). The associated flexural contribution in terms of deflection δ_{flex}^{DE}, as reported just above, can be expressed as:

$$\delta_{flex,conv}^{DE} = \frac{1}{3} \cdot \phi_y^D \cdot a^2 + \left(\phi^D - \phi_y^D\right) \cdot L_{pl} \cdot a \cdot \left(1 - \frac{L_{pl}}{2 \cdot a}\right) \tag{C.77}$$

The aforementioned formulation is commonly adopted in engineering practice [24], [4], and can be obtained by integrating the conventional curvature distribution illustrated in Fig. C.3b. This distribution is derived assuming that, close to the ultimate condition, the plastic part of the curvature is constant and equal to $\phi^D - \phi_y^D$ over a length L_{pl}, next to the end section of the cantilever on the side of the constant moment zone. The plastic hinge length L_{pl} is a conventional quantity, i.e., it does not represent an actual length measurable in a physical RC member. This is due to the fact that the curvature distribution occurring in reality is different from that of Fig. C.3b, and actually much more similar to the distribution represented in Fig. C.3a [4]. This latter one is characterized by a triangular curvature distribution over the plasticization length l_{pl}, which in turn is defined as:

$$l_{pl} = \left(1 - \frac{M_y^D}{M^D}\right) \cdot a \qquad with \quad M^D > M_y^D \tag{C.78}$$

It can be seen from eq. (C.78) that the distribution represented in Fig. C.3a can only be adopted if the bending strength of the end section (e.g., section B or D in Fig. C.1) is monotonically increasing after yielding. This means that a major drawback in the adoption of this distribution is that it is not suitable in cases for which the moment-curvature law of the end section shows a post-peak softening branch before reaching failure. On the other hand, by instead adopting the approach of Fig. C.3b based on the conventional plastic hinge length, the calculation of deflections can be performed no matter the characteristics of the moment-curvature law for the end section.

In order to determine a proper value for the plastic hinge length L_{pl}, the only real criterion which should be considered is the ability to provide a good match with experimental values of ultimate deformation capacity in terms of deflections or chord rotations. Among the various possibilities, the best choices for expressions of the plastic hinge length seem to be linear combinations of the shear span a and the section height H [4]. The plastic hinge length L_{pl} should be assumed taking into account for a series of factors, including the values of curvatures ϕ^D and ϕ_y^D and eventual influences of the rotation capacity due to size effects. In particular, the plastic hinge length should be assumed accordingly to the adopted constitutive law for concrete and reinforcing steel, paying a special attention to the parameter governing the deformation capacity at sectional level, i.e., the ultimate compressive strain of concrete and the ultimate tensile strain of the reinforcement.

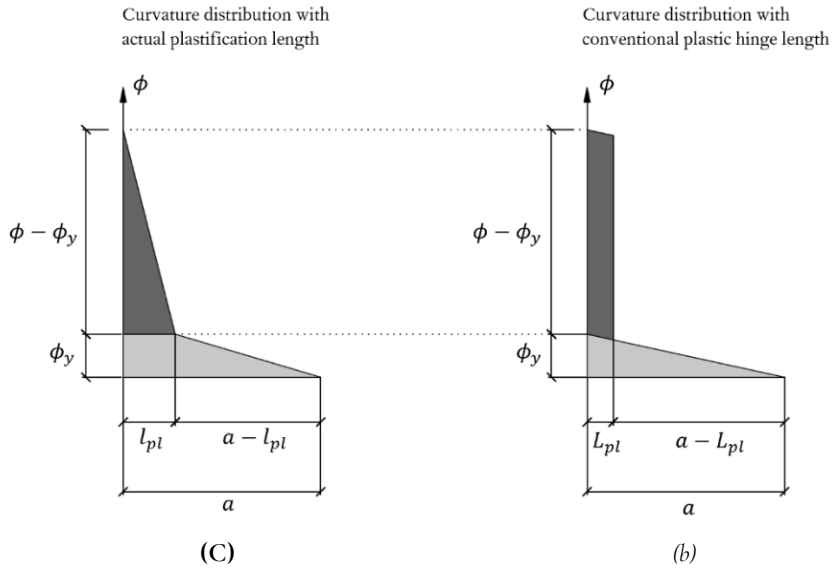

Fig. C.3 Curvature distributions close to the ultimate condition for the end section of a cantilever beam (a) Distribution considering actual plasticization length; (b) Distribution considering conventional plastic hinge length

Within the approach presented in this Appendix, both concrete and steel failure modes have been considered. For the intermediate condition representative of the beginning of cover spalling, described in section C.3.3, the limit condition for the section is on the concrete side, occurring when the outmost fiber of the concrete cover reaches the spalling strain ε_{sp}. Typically, a value $\varepsilon_{sp} - 4‰$ can be adopted for identifying the onset of cover spalling phenomenon [89]. For the ultimate condition occurring on the concrete side, i.e., by means of failure modes "D" or "E" (as described in section C.3.4), the failure is reached when the core concrete reaches its ultimate compressive strain ε_{cu}. In case the section failure would be reached on the steel side, by means of the occurrence of failure mode "K" or "L", the steel ultimate tensile strain ε_{su} would be reached in the bottom reinforcement of the section. However, despite having defined the types of the adopted constitutive laws for reinforcing steel and concrete (which is considered unconfined), the presented approach has been illustrated without providing values to be used for the ultimate strains ε_{cu} and ε_{su}. So, in order to select of a proper value for the plastic hinge length, case by case considerations may be needed. Different possible choices of the plastic hinge length performed in accordance with constitutive models adopted for concrete and steel have examined by Fardis [4]. In the following, possible choices for plastic hinge length models to be adopted within the presented approach for calculating the member deflections at different stages are proposed.

For the stage of beginning of cover spalling, the limit condition for the section is achieved on the concrete side and with an assumed concrete strain $\varepsilon_{sp} - 4‰$. To evaluate the plastic hinge length equation "A.9" presented at section "A3.2.2" of Eurocode

8 – Part 3 [24] can be used, neglecting the term associated to fix-end rotations. So, for this stage the plastic hinge length can be calculated as follows:

$$L_{pl} = \frac{a}{30} + 0.2 \cdot H \tag{C.79}$$

For the stage of section failure, whether it would occur on the concrete or on the steel side, a more conservative estimation of the plastic hinge length is suggested, proposing the use of the following formulation from Paulay and Priestley [9], again neglecting the term associated to fix-end rotations:

$$L_{pl} = 0.08 \cdot a \tag{C.80}$$

Since in the presented approach different limit strains and different curvature formulations have been proposed for analyzing different stages of the sectional response , it may be difficult to properly choosing between the traditionally proposed plastic hinge length models, which have been derived to be used in combination with specific constitutive laws and values of limit strains. Using different plastic hinge length formulations for modelling the deformations at different stages of the response for the cantilever's end section it may be effective. However, an alternative possibility is also adoptable if the plastic hinge length is directly analytically calculated from an actual, i.e., not conventional, curvature distribution (as for example the one represented in Fig. C.3a).
As an example, it may be possible to use a plastic hinge length L_{pl} with the curvature distribution as in Fig. C.3b, chosen so that it would lead to a flexural contribution to the deflection $\delta_{flex,conv}^{DE}$ equal to the one that would be obtained considering the approximated actual curvature distribution of Fig. C.3a, indicated as $\delta_{flex,actual}^{DE}$ and expressed as:

$$\delta_{flex,actual}^{DE} = \frac{1}{3} \cdot \phi_y^D \cdot a^2 + \frac{1}{2} \cdot \left(\phi^D - \phi_y^D\right) \cdot l_{pl} \cdot a - \frac{1}{6} \cdot \left(\phi^D - \phi_y^D\right) \cdot l_{pl}^2 + \\ + \frac{1}{6} \cdot \phi_y^D \cdot l_{pl} \cdot a - \frac{1}{6} \cdot \phi_y^D \cdot l_{pl}^2 \tag{C.81}$$

By equating eq. (C.77) with eq. (C.81) and solving for L_{pl}, it is possible to determine the desired value of the plastic hinge length:

$$L_{pl} = \left\{1 - \sqrt{1 - \left[\left(\frac{l_{pl}}{a}\right) - \frac{1}{3} \cdot \left(\frac{l_{pl}}{a}\right)^2\right] - \frac{2}{3 \cdot (\mu_\phi - 1)} \cdot \left[\left(\frac{l_{pl}}{a}\right) - \frac{1}{2} \cdot \left(\frac{l_{pl}}{a}\right)^2\right]}\right\} \cdot a \tag{C.82}$$

Despite considering the dependence on the curvature ductility capacity μ_ϕ, the eq. (C.82) provides values for the plastic hinge length which area approximately equal to $L_{pl} \approx 0.5 \cdot l_{pl}$, as also reported by Fardis [4]. It is worth to remark that, obviously, the formulation

for plastic hinge length expressed by eq. (C.82) can only be adopted if the cantilever's end section is characterized by a moment-curvature law with a monotonically increasing post-yielding branch, in order to satisfy the condition stated in eq. (C.78). Throughout the dissertation, whenever the calculation approach proposed In this appendix is adopted, the plastic hinge length is calculated using eq. (C.82) when possible. However, as it can be observed analyzing the different terms in eq. (C.76), with the considered loading scheme the largest part of the deflection at midspan is mainly due to the central portion of the beam, and such contribution Is overwhelming with respect to the others. So, in the studied case the effect of varying the plastic hinge length formulation really does affect the ultimate deflection in a nearly negligible way.

C.5 Discussion

In this appendix an analytical approach for evaluating the structural response of a beam loaded with a four-points bending scheme has been provided, with special reference to the scheme adopted for the experimentally tested beams described in Chapter 3. The proposed approach draws inspiration from the analytical framework illustrated in Chapter 2 for the analysis of the sectional behaviour in doubly reinforced concrete beams. The main scope of the proposed formulation is to provide a tool to enabling a deeper understanding of the structural response of beam members, especially in terms of deformation capacity. In fact, by analyzing the developed formulation it is possible to highlight which are the parameters actually involved in the evaluation of strengths and deflections, as well as their role and relevance in the structural response. Moreover, the proposed approach having been developed by sequentially modelling the mechanical behaviour at the material, sectional and member levels, it allows to get a deep understanding of the influence of different modeling choices on the global structural response.

Other significant aspects which have been addressed by developing the proposed approach deals with the need to modelling those phenomena which in RC members do not arise at the sectional level, but only when the member response is considered. In particular, shear deformations have been taken into account following the approach proposed by Biskinis [101] and Fardis [4]. The method involves computing the effects of shear deformation on the member deflections by means of a modification of the curvature distribution along the shear span, associated to higher strains developing in tensile longitudinal reinforcement due to the presence of shear actions (i.e., adopting the so called "bending moment translation" rule). Contribution to deflections due to fixed-end rotations have not been considered, assuming that the sections at cantilevers' end do not experience slippage of the rebars (considering the symmetric loading scheme and assuming perfect bond). The estimation of chord rotations for cantilever parts have been pursued using mechanical (i.e., not empirical) approaches. In order to do so, some considerations about the curvature distributions to be adopted to obtain member deflections by integration have been provided. The use of curvature distributions which approximately represent the actual real distributions may represent an effective approach, provided that additional contributions to deformations such as those due to

shear or fixed-end rotations are separately computed in terms of rotations and later added. However, this kind of approach presents two main drawbacks, i.e., i) it does not allow to take into account for size effects; ii) it cannot be adopted if the moment-curvature law of the cantilever's end section is characterized by a softening branch, since in such a case the analytical integration of curvatures along the beam axis is not possible anymore. To overcome the aforementioned issues, a common approach used in practice is that of performing curvature integration considering a conventional curvature distribution, which adopts a plasticization zone having a conventional length called the plastic hinge length. This indeed allows to perform the integration without worrying about the aforementioned problem of curvature localization due to softening. Moreover, since the plastic hinge length is not a physical but a conventional length, additional contributions can be added to it to directly take into account for various effects (e.g., shear deformations, fixed-end rotations, size effects). On the other hand, the drawback of such an approach lays obviously in the fact that since the plastic hinge length has not a direct physical meaning, its definition can be not straightforward. However, as point out previously, since in the studied case the contribution to member deflection due to the plastic rotations at cantilevers' end are quite negligible with respect to the contributions generated by the bending of the constant moment zone, the influence of choosing different formulations for the plastic hinge lengths are very limited.

In the end, it is worth to highlight some limitations of the proposed approach, which can be although be addressed and solved in future developments of the research. In the current proposed formulations, only few possible different failure modes for the sections have been considered. This is not an issue in itself, since it has been shown in Chapter 2 that for beam sections characterized by a failure mode configuration *Type 1* (representative of the majority of section layouts adopted in engineering practice) the response can actually be modelled satisfactorily considering only few possible failure modes. However, this fact can instead become an issue if the approach is used for the analysis of beams with a non-conventional sectional reinforcement layout. It may be the case, for example, of beams affected by reinforcement corrosion. In such situations, in fact, failure mode domains for the beam sections may assume other configurations than *Type 1* (see Chapter 2 and the work by Stella et al. [100]) and so presents failure modes not considered in the proposed approach, which can lead to an incorrect estimation of curvature deformation capacity. Another limitation of the proposed approach lays in the fact that section characteristics have been assumed to be uniform all over the member axis. This fact makes the presented methodology not suitable to be applied for study beams with sectional characteristics varying along the axis, such as happen in the case of deteriorated members with non-uniform damage along the beam length (e.g., in the case of reinforcement corrosion). Knowing the fundamental hypothesis and the limitations of the proposed approach can enable its use in a more conscious way and can also allow the future development of possible enhancements.

References

[1] Landolfo R, Formisano A, Di Lorenzo G, Di Filippo A. Classification of european building stock in technological and typological classes. J Build Eng 2022;45. doi:10.1016/j.jobe.2021.103482.

[2] Valentina P, Georgios T, Sousa ML. Building Stock Inventory to assess seismic vulnerability across Europe. Publication office of the European Union; 2018. doi:10.2760/530683.

[3] United Nations Office for Disaster Risk Reduction. Sendai Framework for Disaster Risk Reduction 2015 - 2030. Sendai, Japan: 2015.

[4] Fardis MN. Seismic design, assessment and retrofitting of concrete buildings: based on EN-Eurocode 8. vol. 8. Springer Science & Business Media; 2009.

[5] Beeby AW. Ductility in reinforced concrete: Why is it needed and how is it achieved? Struct Eng 1997;75:311–8.

[6] Panagiotakos TB, Fardis MN. Deformations of reinforced concrete members at yielding and ultimate. ACI Struct J 2001;98:135–48.

[7] Panagiotakos TB, Fardis MN. Estimation of inelastic deformation demands in multistorey RC frame buildings. Earthq Eng Struct Dyn 1999;28:501–28.

[8] Park R, Paulay T. Reinforced Concrete Structures. Wiley; 1975. doi:10.1002/9780470172834.

[9] Paulay T, Priestley MJN. Seismic Design of Reinforced Concrete and Masonry Buildings. Hoboken, NJ, USA: John Wiley & Sons, Inc.; 1992. doi:10.1002/9780470172841.

[10] Priestley MJN, Calvi GM, Kowalsky MJ. Displacement based seismic design of structures. IUSS Press; 2007.

[11] Veletsos A. S., Newmark N. M. Effect of Inelastic Behavior on the Response of Simple Systems to Earthquake Motions. Proc. 2nd World Conf. Earthq. Eng., Tokio, Japan: 1960, p. 895–912.

[12] Blume JA, Newmark NM, Corning LH. Design of Multistory Reinforced Concrete Buildings for Earthquake Motions. Chicago: Portland Cement Association; 1961.

[13] Fardis MN. Capacity design: Early history. Earthq Eng Struct Dyn 2018;47:2887–96. doi:10.1002/eqe.3110.

[14] Hollings JP. Reinforced concrete seismic design. Bull New Zeal Soc Earthq Eng 1969;2:217–50.

[15] Moehle JP. Displacement-based design of RC structures subjected to earthquakes. Earthq Spectra 1992;8:403–28.

[16] Iverson JK, Principal LoBuono P, Hawkins NM. Performance of Precast/ Prestressed Concrete Building Structures During Northridge Earthquake. PCI J 1994;39:38–55.

[17] Gould NC, Kallros MK, Dowty SM. Northridge concrete parking ptructures and the Northridge Earthquake: Performance and resulting building code changes.

STRUCTUREMag 2019:48–54.
[18] Muto K, Takahashi R, Aida I, Ando N, Hisada T, Nakagawa K, et al. Non-linear response analyzers and applications to earthquake resistant design. Proceddings 2nd World Conf. Earthq. Eng., Japan: 1960, p. 649–68.
[19] Calvi GM, Kingsley GR. Displacement-based seismic design of multi-degree-of-freedom bridge structures. Earthq Eng Struct Dyn 1995;24:1247–66. doi:10.1002/eqe.4290240906.
[20] Kowalsky MJ, Priestley MJN, Macrae GA. Displacement-based design of RC bridge columns in seismic regions. Earthq Eng Struct Dyn 1995;24:1623–43.
[21] Panagiotakos TB, Fardis MN. Deformation-controlled earthquake-resistant design of rc buildings. J Earthq Eng 1999;3:495–518. doi:10.1080/13632469909350357.
[22] Panagiotakos TB, Fardis MN. A displacement-based seismic design procedure for RC buildings and comparison with EC8. Earthq Eng Struct Dyn 2001;30:1439–62. doi:10.1002/eqe.71.
[23] USGS. Northridge, CA Earthquake Damage. Collect USGS Still Images Tak after January 17, 1994 Northridge Earthq Highlighting Damage to Build Infrastruct 1994. https://www.usgs.gov/media/images/northridge-ca-earthquake-damage-27.
[24] CEN. Eurocode 8: Design of structures for earthquake resistance - Part 3: Assessment and retrofitting of buildings. 2005.
[25] Biskinis D, Fardis MN. Flexure-controlled ultimate deformations of members with continuous or lap-spliced bars. Struct Concr 2010;11:93–108. doi:10.1680/stco.2010.11.2.93.
[26] Grammatikou S, Biskinis D, Fardis MN. Effect of load cycling, FRP jackets, and lap-splicing of longitudinal bars on the effective stiffness and ultimate deformation of flexure-controlled RC members. J Struct Eng 2018;144:4018056.
[27] The International Federation for Structural Concrete. Model Code for concrete structures 2010. 2013.
[28] Fardis MN. From force-to displacement-based seismic design of concrete structures and beyond. Eur. Conf. Earthq. Eng. Thessaloniki, Greece, 2018, p. 101–22.
[29] Grammatikou S, Fardis MN, Biskinis D. Energy dissipation models for RC members and structures. Earthq Eng Struct Dyn 2019;48:287–305. doi:10.1002/eqe.3136.
[30] Grammatikou S, Fardis MN, Biskinis D. Energy dissipation in reinforced concrete members before or after yielding. Earthq Eng Struct Dyn 2022;51:974–97. doi:10.1002/eqe.3600.
[31] Tso WK, Zhu TJ, Heidebrecht AC. Seismic energy demands on reinforced concrete moment-resisting frames. Earthq Eng Struct Dyn 1993;22:533–45.
[32] Manfredi G. Evaluation of seismic energy demand. Earthq Eng Struct Dyn 2001;30:485–99.
[33] Teran-Gilmore A, Jirsa JO. Energy demands for seismic design against low-cycle fatigue. Earthq Eng Struct Dyn 2007;36:383–404. doi:10.1002/eqe.663.

[34] Desbrousses RLE, Lin L. Enhancing Building Resistance to Differential Settlement with Canadian Seismic Design Provisions. Pract Period Struct Des Constr 2021;26:04021011. doi:10.1061/(asce)sc.1943-5576.0000575.

[35] Lin L, Hanna A, Sinha A, Tirca L. High-rise building subjected to excessive settlement of its foundation: A case study. Int J Struct Integr 2017;8:210–21. doi:10.1108/IJSI-05-2016-0019.

[36] Laefer DF, Ceribasi S, Long JH, Cording EJ. Predicting RC Frame Response to Excavation-Induced Settlement. J Geotech Geoenvironmental Eng 2009;135:1605–19. doi:10.1061/ASCEGT.1943-5606.0000128.

[37] Hayes JR, Woodson SC, Pekelnicky RG, Poland CD, Corley WG, Sozen M. Can Strengthening for Earthquake Improve Blast and Progressive Collapse Resistance? J Struct Eng 2005;131:1157–77. doi:10.1061/ASCE0733-94452005131:81157.

[38] Lew HS, Bao Y, Pujol S, Sozen MA. Experimental study of reinforced concrete assemblies under column removal scenario. ACI Struct J 2014;111:881–92. doi:10.14359/51686739.

[39] Brunesi E, Parisi F. Progressive collapse fragility models of European reinforced concrete framed buildings based on pushdown analysis. Eng Struct 2017;152:579–96. doi:10.1016/j.engstruct.2017.09.043.

[40] Praxedes C, Yuan X-X. Robustness Assessment of Reinforced Concrete Frames under Progressive Collapse Hazards: Novel Risk-Based Framework. J Struct Eng 2021;147:04021119. doi:10.1061/(asce)st.1943-541x.0003075.

[41] Muttoni A, Ruiz MF. Levels-of-approximation approach in codes of practice. Struct. Eng. Int. J. Int. Assoc. Bridg. Struct. Eng., vol. 22, 2012, p. 190–4. doi:10.2749/101686612X13291382990688.

[42] CEB. Bulletin 218: Ductility - Reinforcement. Lausanne, Switzerland: 1993.

[43] CEB. Bulletin 242: Ductility of Reinforced Concrete Structures. Lausanne, Switzerland: 1998.

[44] Bigaj AJ. Structural dependence of rotation capacity of plastic hinges in RC beams and slabs. Delft University of Technology, 1999.

[45] Fardis M, Carvalho E, Elnashai A, Faccioli E, Pinto PE, Plumier A. Designers' Guide to EN 1998-1 and 1998-5. Eurocode 8: Design Provisions for Earthquake Resistant Structures. ICE, Thomas Telford Ltd; 2005. doi:10.1680/dgte8.33481.

[46] Rodriguez J, Ortega LM, Casal J. Load carrying capacity of concrete structures with corroded reinforcement. Constr Build Mater 1997;II:239–48.

[47] Hanjari KZ, Utgenannt P, Lundgren K. Experimental study of the material and bond properties of frost-damaged concrete. Cem Concr Res 2011;41:244–54. doi:10.1016/j.cemconres.2010.11.007.

[48] Esposito R, Anaç C, Hendriks MAN, Çopuroğlu O. Influence of the Alkali-Silica Reaction on the Mechanical Degradation of Concrete. J Mater Civ Eng 2016;28:04016007. doi:10.1061/(asce)mt.1943-5533.0001486.

[49] Kashani MM, Maddocks J, Dizaj EA. Residual Capacity of Corroded Reinforced Concrete Bridge Components: State-of-the-Art Review. J Bridg Eng 2019;24:03119001. doi:10.1061/(asce)be.1943-5592.0001429.

[50] Ou YC, Tsai LL, Chen HH. Cyclic performance of large-scale corroded reinforced concrete beams. Earthq Eng Struct Dyn 2012;41:593–604. doi:10.1002/eqe.1145.

[51] Coronelli D, Gambarova P. Structural Assessment of Corroded Reinforced Concrete Beams: Modeling Guidelines. J Struct Eng 2004;130:1214–24. doi:10.1061/ASCE0733-94452004130:81214.

[52] Zandi Hanjari K, Kettil P, Lundgren K. Analysis of Mechanical Behavior of Corroded Reinforced Concrete Structures. ACI Struct J 2011;108:532–41.

[53] Zhu W, François R, Coronelli D, Cleland D. Effect of corrosion of reinforcement on the mechanical behaviour of highly corroded RC beams. Eng Struct 2013;56:544–54. doi:10.1016/j.engstruct.2013.04.017.

[54] Du Y. Effect of reinforcement corrosion on structural concrete ductility. University of Birmingham, 2001.

[55] Fardis MN. Seismic Assessment and Retrofitting of Concrete Structures with Corroded Reinforcement. Proc. CACRCS days 2021, Parma, Italy: 2021, p. 159–62.

[56] Finozzi I, Saetta A, Budelmann H. Structural response of reinforcing bars affected by pitting corrosion: experimental evaluation. Constr Build Mater 2018;192:478–88. doi:10.1016/j.conbuildmat.2018.10.088.

[57] Zeng C, Zhu JH, Xiong C, Li Y, Li D, Walraven J. Analytical model for the prediction of the tensile behaviour of corroded steel bars. Constr Build Mater 2020;258. doi:10.1016/j.conbuildmat.2020.120290.

[58] Matthews S, Bigaj-van Vliet A, Walraven J, Mancini G, Dieteren G. fib Model Code 2020: Towards a general code for both new and existing concrete structures. Struct Concr 2018;19:969–79. doi:10.1002/suco.201700198.

[59] Walraven J. Assessment of concrete structures with corroded reinforcement: development of recommendations. Proc. CACRCS 2021, Parma, Italy: 2021, p. 85–90.

[60] Coronelli D. Resistance of corroded RC beams: Extending fib Model Code 2010 models. Struct Concr 2020;21:1747–62. doi:10.1002/suco.201900311.

[61] Bonano M, Manunta M, Pepe A, Paglia L, Lanari R. From previous C-band to new X-band SAR systems: Assessment of the DInSAR mapping improvement for deformation time-series retrieval in urban areas. IEEE Trans Geosci Remote Sens 2013;51:1973–84. doi:10.1109/TGRS.2012.2232933.

[62] Macchiarulo V, Milillo P, Blenkinsopp C, Reale C, Giardina G. Multi-Temporal InSAR for transport infrastructure monitoring: Recent trends and challenges. Proc Inst Civ Eng Bridg Eng 2021. doi:10.1680/jbren.21.00039.

[63] Selvakumaran S, Sadeghi Z, Collings M, Rossi C, Wright T, Hooper A. Comparison of in-situ and InSAR monitoring for the assessment of bridge thermal expansion. Proc Inst Civ Eng - Smart Infrastruct Constr 2022:1–18. doi:10.1680/jsmic.21.00008.

[64] Giannico C, Ferretti A, Alberti S, Jurina L, RIcci M, Sciotti A. Application of satellite radar interferometry for structural damage assessment and monitoring. Proc. 3rd Int. Symp. Life-Cycle Civ. Eng., Vienna, Austria: CRC Press; 2012.

[65] Chen X, Achilli V, Fabris M, Menin A, Monego M, Tessari G, et al. Combining sentinel-1 interferometry and ground-based geomatics techniques for monitoring buildings affected by mass movements. Remote Sens 2021;13:452. doi:10.3390/rs13030452.

[66] Giardina G, Milillo P, DeJong MJ, Perissin D, Milillo G. Evaluation of InSAR monitoring data for post-tunnelling settlement damage assessment. Struct Control Heal Monit 2019;26. doi:10.1002/stc.2285.

[67] Macchiarulo V, Milillo P, DeJong MJ, González Martí J, Sánchez J, Giardina G. Integrated InSAR monitoring and structural assessment of tunnelling-induced building deformations. Struct Control Heal Monit 2021;28. doi:10.1002/stc.2781.

[68] MathWorks. Matlab R2021a 2021. https://nl.mathworks.com/products/matlab.html (accessed June 2022).

[69] Di Carlo F, Isabella P, Rinaldi Z, Spagnuolo S. Influence of corrosion on the flexural behavior of corroded reinforced concrete beams. Proc. CACRCS 2021, Parma, Italy: 2021, p. 131–4.

[70] Di Carlo F, Meda A, Rinaldi Z. Experimental behaviour of corroded R.C. beams: Critical aspects for engineering practise. Eng Struct 2022.

[71] McKenna F. OpenSees: A framework for earthquake engineering simulation. Comput Sci Eng 2011;13:58–66. doi:10.1109/MCSE.2011.66.

[72] Petracca M, Candeloro F, Camata G. STKO User Manual 2017.

[73] CEN. Eurocode 2: Design of concrete structures - Part 1-1: General rules and rules for buildings. Brussels: European Committee for Standardization; 2014.

[74] ReLUIS Consortium and Italian Department of Civil Protection. DPC-ReLUIS 2019-2021 2019. https://www.reluis.it/it/progetti-dpc-reluis/dpc-reluis-2019-2021.html (accessed June 7, 2022).

[75] Rosen PA, Hensley S, Joughin IR, Li FK, Madsen SN, Rodríguez E, et al. Synthetic aperture radar interferometry. Proc IEEE 2000;88:333–80. doi:10.1109/5.838084.

[76] ASI - Italian Space Agency. COSMO-SkyMed Web Site 2010. http://www.cosmo-skymed.it/en/index.htm (accessed June 7, 2022).

[77] Covello F, Battazza F, Coletta A, Lopinto E, Fiorentino C, Pietranera L, et al. COSMO-SkyMed an existing opportunity for observing the Earth. J Geodyn 2010;49:171–80. doi:10.1016/j.jog.2010.01.001.

[78] Berardino P, Fornaro G, Lanari R, Sansosti E. A new algorithm for surface deformation monitoring based on small baseline differential SAR interferograms. IEEE Trans Geosci Remote Sens 2002;40:2375–83. doi:10.1109/TGRS.2002.803792.

[79] ESRI. ArcGIS Pro 2022. https://www.esri.com/en-us/arcgis/products/arcgis-pro/overview (accessed June 7, 2022).

[80] QGIS. QGIS - A Free and Open Source Geographic Information System 2022. https://www.qgis.org/en/site/ (accessed June 7, 2022).

[81] Aldrighetti G, Berto L, Gasparini A, Saetta A, Stella A, Talledo DA. Le nuove norme tecniche NTC2018 : domanda e capacità in termini di duttilità in curvatura di elementi in c.a. In: Braga F, Dall'Asta A, Gara F, editors. Atti del

XIII Convegno ANIDIS L'ingegneria sismica Ital., Ascoli Piceno, Italy: Pisa University Press; 2019, p. 585–600.

[82] Aldrighetti G, Berto L, Gasparini A, Saetta A, Stella A, Talledo DA. Ductility assessment in R.C. beams: explicit evaluation and detail rules. Proc. Ital. Concr. Days 2021, Naples, Italy: 2021.

[83] Magenes G. Le ricerche ReLUIS a supporto della normativa. La Ric. Ital. Ing. sismica e le attività di RELUIS a 40 anni dal terremoto Camp., 2020.

[84] Ministero delle Infrastrutture e dei Trasporti. DM 17/01/2018 Aggiornamento delle «Norme tecniche per le costruzioni». Gazz Uff Della Repubb Ital 2018.

[85] ReLUIS Consortium and Italian Department of Civil Protection. Linee guida per l'utilizzo dei dati interferometrici satellitari ai fini dell'interpretazione del comportamento strutturale delle costruzioni. 2021.

[86] Pedeferri P, Bertolini L. La durabilità del calcestruzzo armato. Milano: McGraw.Hill; 2000.

[87] Bleijenberg AN. Renewal of civil infrastructure. Dutch national forecast for replacement and renovation. Delft, the Netherlands: 2021.

[88] Park R, Ruitong D. Ductility of Doubly Reinforced Concrete Beam Sections. ACI Struct J 1988;85:217–25.

[89] Kent DC, Park R. Flexural members with confined concrete. J Struct Div 1971.

[90] New Zealand Standards. NZS 3101.1&2: 2006 Concrete structures standard. New Zealand: 2006.

[91] Mander JB, Priestley MJN, Park R. Observed stress-strain behavior of confined concrete. J Struct Eng 1988;114:1827–49.

[92] Mander JB, Priestley MJN, Park R. Theoretical stress-strain model for confined concrete. J Struct Eng 1988;114:1804–26.

[93] Hao X, Visintin P, Oehlers DJ. Closed-Form Solutions for Quantifying the Ductility of Concrete Beams with Passively Restrained Concrete. J Struct Eng 2020;146:4020154.

[94] CEN. EN ISO 15630-1 - Steel for the reinforcement and prestressing of concrete-Test methods. 2019.

[95] Hillerborg A. Rotational capacity of reinforced concrete beams. Nord Concr Res 1988:121–34.

[96] Hillerborg A. Fracture mechanics concepts applied to moment capacity and rotational capacity of reinforced concrete beams. Eng Fract Mech 1990;35:233–40.

[97] Hillerborg A. Size dependency of the stress-strain curve in compression. In: Lennart E, Shah SP, editors. Anal. Concr. Struct. by Fract. Mech., CRC Press; 1991.

[98] Bigaj A, Walraven J. Size effects in plastic hinges of reinforced concrete members. HERON 2002;47:53–75.

[99] Park R. Ductility evaluation from laboratory and analytical testing. Proc. 9th world Conf. Earthq. Eng. Tokyo-Kyoto, Japan, vol. 8, 1988, p. 605–16.

[100] Stella A, Aldrighetti G, Berto L, Talledo DA, Saetta A. Influence of geometry and material parameters on the ultimate condition of doubly reinforced

concrete beams. Proc. 2021 Sess. 13th fib Int. PhD Symp., Marne-La-Vallée, Paris, France: fib; 2021, p. 98–105.
[101] Biskinis D. Resistance and deformation capacity of concrete members with or without retrofitting. University of Patras, Patras, Greece, 2007.
[102] Almusallam AA, AI-Gahtani AS, Aziz AR, Dakhil FH, Rasheeduzzafar. Effect of reinforcement corrosion on flexural behavior of concrete slabs. J Mater Civ Eng 1996;8:123–7.
[103] Mangat PS, Elgarf MS. Flexural Strength of Concrete Beams with Corroding Reinforcement. ACI Struct J 1999;96:149–58.
[104] Cairns J, Zhao Z. Behaviour of concrete beams with exposed reinforcement. Proc Inst Civ Eng Struct Build 1993;99:141–54.
[105] El Maaddawy T, Soudki K, Topper T. Long-Term Performance of Corrosion-DamagedReinforced Concrete Beams. ACI Struct J 2005;102:649–56.
[106] Ballim Y, Reid JC. Reinforcement corrosion and the deflection of RC beams - An experimental critique of current test methods. Cem Concr Compos 2003;25:625–32. doi:10.1016/S0958-9465(02)00076-8.
[107] Zarate Garnica GI, Lantsoght EOL, Yang Y. Monitoring structural responses during load testing of reinforced concrete bridges: a review. Struct Infrastruct Eng 2022:1–23. doi:10.1080/15732479.2022.2063906.
[108] Du Y, Clark LA, Chan AHC. Impact of reinforcement corrosion on ductile behavior of reinforced concrete beams. ACI Struct J 2007;104:285–93. doi:10.14359/18618.
[109] Berrocal CG, Löfgren I, Lundgren K. The effect of fibers on steel bar corrosion and flexural behaviour of corroded RC beams. Eng Struct 2018;163:409–25. doi:10.1016/j.engstruct.2018.02.068.
[110] Fernandez I, Herrador MF, Marí AR, Bairán JM. Structural effects of steel reinforcement corrosion on statically indeterminate reinforced concrete members. Mater Struct Constr 2016;49:4959–73. doi:10.1617/s11527-016-0836-2.
[111] Sutton MA, Cheng M, Peters WH, Chao YJ, McNeill SR. Application of an optimized digital correlation method to planar deformation analysis. Image Vis Comput 1986;4:143–50.
[112] Pan B, Qian K, Xie H, Asundi A. Two-dimensional digital image correlation for in-plane displacement and strain measurement: A review. Meas Sci Technol 2009;20. doi:10.1088/0957-0233/20/6/062001.
[113] International Digital Image Correlation Society. A Good Practices Guide for Digital Image Correlation. 2018. doi:10.32720/idics/gpg.ed1.
[114] Schreier H, Orteu JJ, Sutton MA. Image correlation for shape, motion and deformation measurements: Basic concepts, theory and applications. Springer US; 2009. doi:10.1007/978-0-387-78747-3.
[115] LePage WS, Daly SH, Shaw JA. Cross Polarization for Improved Digital Image Correlation. Exp Mech 2016;56:969–85. doi:10.1007/s11340-016-0129-2.
[116] Hild F, Roux S. Comparison of Local and Global Approaches to Digital Image Correlation. Exp Mech 2012;52:1503–19. doi:10.1007/s11340-012-9603-7.
[117] Pan B. Full-field strain measurement using a two-dimensional Savitzky-Golay

digital differentiator in digital image correlation. Opt Eng 2007;46:033601. doi:10.1117/1.2714926.

[118] Bornert M, Brémand F, Doumalin P, Dupré JC, Fazzini M, Grédiac M, et al. Assessment of digital image correlation measurement errors: Methodology and results. Exp Mech 2009;49:353–70. doi:10.1007/s11340-008-9204-7.

[119] Lava P, Cooreman S, Coppieters S, De Strycker M, Debruyne D. Assessment of measuring errors in DIC using deformation fields generated by plastic FEA. Opt Lasers Eng 2009;47:747–53. doi:10.1016/j.optlaseng.2009.03.007.

[120] Wang Y, Lava P, Reu P, Debruyne D. Theoretical Analysis on the Measurement Errors of Local 2D DIC: Part I Temporal and Spatial Uncertainty Quantification of Displacement Measurements. Strain 2016;52:110–28. doi:10.1111/str.12173.

[121] Wang Y, Lava P, Reu P, Debruyne D. Theoretical Analysis on the Measurement Errors of Local 2D DIC: Part II Assessment of Strain Errors of the Local Smoothing Method-Approaching an Answer to the Overlap Question. Strain 2016;52:129–47. doi:10.1111/str.12174.

[122] De Wilder K, Lava P, Debruyne D, Wang Y, De Roeck G, Vandewalle L. Experimental investigation on the shear capacity of prestressed concrete beams using digital image correlation. Eng Struct 2015;82:82–92. doi:10.1016/j.engstruct.2014.10.034.

[123] Fayyad TM, Lees JM. Experimental investigation of crack propagation and crack branching in lightly reinforced concrete beams using digital image correlation. Eng Fract Mech 2017;182:487–505. doi:10.1016/j.engfracmech.2017.04.051.

[124] Huang Z, Tu Y, Meng S, Sabau C, Popescu C, Sas G. Experimental study on shear deformation of reinforced concrete beams using digital image correlation. Eng Struct 2019;181:670–98. doi:10.1016/j.engstruct.2018.12.056.

[125] Gebhard L, Mata-Falcón J, Anton A, Dillenburger B, Kaufmann W. Structural behaviour of 3D printed concrete beams with various reinforcement strategies. Eng Struct 2021;240. doi:10.1016/j.engstruct.2021.112380.

[126] Park MK, Lantsoght EOL, Zarate Garnica GI, Yang Y, Sliedrecht H. Analysis of shear capacity of prestressed concrete bridge girders. ACI Struct J 2021;118:75–89. doi:10.14359/51733000.

[127] Nasser H, Van Steen C, Vandewalle L, Verstrynge E. An experimental assessment of corrosion damage and bending capacity reduction of singly reinforced concrete beams subjected to accelerated corrosion. Constr Build Mater 2021;286. doi:10.1016/j.conbuildmat.2021.122773.

[128] Berrocal CG, Fernandez I, Rempling R. The interplay between corrosion and cracks in reinforced concrete beams with non-uniform reinforcement corrosion. Mater Struct 2022;55:120. doi:10.1617/s11527-022-01956-2.

[129] CEN. Eurocode 2: Design of concrete structures - Part 1-1: General rules and rules for buildings. 2004.

[130] CEN. EN206-1 Concrete, Part 1: Specification, performance, production and conformity. British Standards Institution; 2000.

[131] ISO. ISO 1920-3 Testing of Concrete. Part 3: Making and curing test specimens. 2019.

[132] ISO. ISO 1920-4 Testing of concrete. Part 4: Strength of hardened concrete. 2020.
[133] L'Hermite R. Idées actuelles sur la technologie du bèton. Doc Tech Du Batim Des Trav Publics 1955.
[134] Neville AM. Some aspects of the strength of concrete. Civ Eng 1959;54.
[135] Neville AM. Properties of Concrete. 2nd ed. London: Pitman Publishing; 1972.
[136] El Maaddawy TA, Soudki KA. Effectiveness of Impressed Current Technique to Simulate Corrosion of Steel Reinforcement in Concrete. J Mater Civ Eng 2003;15:41–7. doi:10.1061/ASCE0899-1561200315:141.
[137] Malumbela G., Moyo P, Alexander M. A step towards standardisingaccelerated corrosion testson laboratory reinforcedconcrete specimens. J South African Inst Civ Eng 2012;54:78–85.
[138] Hong S, Zheng F, Shi G, Li J, Luo X, Xing F, et al. Determination of impressed current efficiency during accelerated corrosion of reinforcement. Cem Concr Compos 2020;108. doi:10.1016/j.cemconcomp.2020.103536.
[139] Imperatore S, Rinaldi Z. Mechanical behavior of corroded rebars and influence on the structural response of R/C elements. Concr. Repair, Rehabil. Retrofit. II, London: Taylor & Francis Group; 2009, p. 489–95.
[140] Rinaldi Z, Imperatore S, Valente C. Experimental evaluation of the flexural behavior of corroded P/C beams. Constr Build Mater 2010;24:2267–78. doi:10.1016/j.conbuildmat.2010.04.029.
[141] Meda A, Mostosi S, Rinaldi Z, Riva P. Experimental evaluation of the corrosion influence on the cyclic behaviour of RC columns. Eng Struct 2014;76:112–23. doi:10.1016/j.engstruct.2014.06.043.
[142] Coccia S, Imperatore S, Rinaldi Z. Influence of corrosion on the bond strength of steel rebars in concrete. Mater Struct Constr 2016;49:537–51. doi:10.1617/s11527-014-0518-x.
[143] Blaber J, Adair B, Antoniou A. Ncorr: Open-Source 2D Digital Image Correlation Matlab Software. Exp Mech 2015;55:1105–22. doi:10.1007/s11340-015-0009-1.
[144] Hao Kan W, Albino C, Dias-da-Costa D, Dolman K, Lucey T, Tang X, et al. Fracture toughness testing using photogrammetry and digital image correlation. MethodsX 2018;5:1166–77. doi:10.1016/j.mex.2018.09.012.
[145] Kani GNJ. The Riddle of Shear Failure and Its Solution. J Am Concr Inst 1964;61:441–67.
[146] Cairns J. Strength in shear of concrete beams with exposed reinforcement. Proc Instn Civ Engrs Structs Bldgs 1995;110:176–85.
[147] Jeppsson J, Thelandersson S. Behavior of Reinforced Concrete Beams with Loss of Bond at Longitudinal Reinforcement. J Struct Eng 2003;129:1376–83. doi:10.1061/ASCE0733-94452003129:101376.
[148] Dias-Da-Costa D, Valença J, Do Carmo RNF. Curvature assessment of reinforced concrete beams using photogrammetric techniques. Mater Struct Constr 2014;47:1745–60. doi:10.1617/s11527-013-0148-8.
[149] Di Carlo F, Meda A, Rinaldi Z. Numerical evaluation of the corrosion influence

on the cyclic behaviour of RC columns. Eng Struct 2017;153:264–78. doi:10.1016/j.engstruct.2017.10.020.

[150] Vv. Aa. Advances In Performance-Based Earthquake Engineering. Springer; 2010.

[151] Fardis MN. Performance-and displacement-based seismic design and assessment of concrete structures in fib Model Code 2010. Struct Concr 2013;14:215–29.

[152] Hobbs DW. Concrete deterioration: Causes, diagnosis, and minimising risk. Int Mater Rev 2001;46:117–44. doi:10.1179/095066001101528420.

[153] Angst UM, Geiker MR, Michel A, Gehlen C, Wong H, Isgor OB, et al. The steel–concrete interface. Mater Struct Constr 2017;50. doi:10.1617/s11527-017-1010-1.

[154] Popovics S. A numerical approach to the complete stress-strain curve of concrete. Cem Concr Res 1973;3:583–99.

[155] Menegotto M, Pinto PE. Method of analysis for cyclically loaded R.C. plane frames including changes in geometry and non-elastic behaviour of elements under combined normal force and bending. IABSE Symp. "Resistance Ultim. Deform. Struct. acted by weel-defined repeated loads," Lisboa, Portugal: 1973, p. 15–22. doi:10.5169/seals-13741.

[156] Filippou FE, Popov EP, Bertero V V. Effects of bond deterioration on hysteretic behavior of reinforced concrete joints. Berkeley, CA: 1983.

[157] Cabrera JG. Deterioration of Concrete Due to Reinforcement Steel Corrosion. vol. 18. 1996.

[158] Rodriguez J, Andrade CC. CONTECVET: A validated Users Manual for assessing the residual service life of concrete structures. Madrid: SW; 2001.

[159] Rodriguez J, Ortega LM, Casal J, Diez JM. Assessing structural conditions of concrete structures with corroded reinforcement. Concr. Repair, Rehabil. Prot., Dundee, Scotland: E & FN Spon; 1996, p. 65–78.

[160] Caprili S, Salvatore W, Valentini R. Corroded TempCore® vs dual-phase steel reinforcing bars. Constr Build Mater 2021;277. doi:10.1016/j.conbuildmat.2021.122301.

[161] Haefliger S, Kaufmann W. Influence of cross section loss on the stress-strain characteristics of corroded quenched and self-tempered reinforcing bars. Constr Build Mater 2021;282. doi:10.1016/j.conbuildmat.2021.122598.

[162] Haefliger S, Fomasi S, Kaufmann W. Influence of quasi-static strain rate on the stress-strain characteristics of modern reinforcing bars. Constr Build Mater 2021;287. doi:10.1016/j.conbuildmat.2021.122967.

[163] Zhao Z, Fu L. The probability distribution of pitting for accelerated corrosion reinforcement. Case Stud Constr Mater 2018;9. doi:10.1016/j.cscm.2018.e00193.

[164] Šavija B, Luković M, Hosseini SAS, Pacheco J, Schlangen E. Corrosion induced cover cracking studied by X-ray computed tomography, nanoindentation, and energy dispersive X-ray spectrometry (EDS). Mater Struct Constr 2015;48:2043–62. doi:10.1617/s11527-014-0292-9.

[165] Namita. Effects of Corrosion in Reinforcement | Signs & Preventive Measures 2018. CiviliDigital.com (accessed June 21, 2022).

[166] Plizzari G, Schumm C. Sul Collasso dell'Aderenza per Sfilamento della Barra e

Spacco del Calcestruzzo. Stud. e Ric., vol. 12, Milano, Italy: Politecnico di Milano; 1990, p. 81–116.

[167] Andrade C. Approach to the residual strength of steel bars due to corrosion. Proc. CACRCS 2021, Parma, Italy: 2021, p. 13–8.

[168] Gonzalez JA, Andrade C, Alonso C, Feliu S. Comparison of rates of general corrosion and maximum pitting penetration on concrete embedded steel reinforcement. Cem Concr Res 1995;25:258–64.

[169] Val D V, Melchers RE. Reliability of deteriorating RC slab bridges. J Struct Eng 1997;123:1638–44.

[170] Biondini F, Vergani M. Damage modeling and nonlinear analysis of concrete bridges under corrosion. In: Biondini F, Frangopol D, editors. Bridg. Maintenance, Safety, Manag. Resil. Sustain., London: Taylor & Francis Group; 2012, p. 949–57.

[171] Uomoto I:, Misra S. Behavior of Concrete Beams and Columns in Marine Environment When Corrosion of Reinforcing Bars Takes Place. ACI Symp., 1988, p. 109–15.

[172] Somerville G, Andrade C, Fagerlund G, Lagerblad B, Rodriguez J, Tuutti K. The residual service life of reinforced concrete structures. 1995.

[173] Biondini F, Vergani M. Deteriorating beam finite element for nonlinear analysis of concrete structures under corrosion. Struct Infrastruct Eng 2015;11:519–32. doi:10.1080/15732479.2014.951863.

[174] Kashani MM, Crewe AJ, Alexander NA. Use of a 3D optical measurement technique for stochastic corrosion pattern analysis of reinforcing bars subjected to accelerated corrosion. Corros Sci 2013;73:208–21. doi:10.1016/j.corsci.2013.03.037.

[175] Kioumarsi MM, Hendriks MAN, Kohler J, Geiker MR. The effect of interference of corrosion pits on the failure probability of a reinforced concrete beam. Eng Struct 2016;114:113–21. doi:10.1016/j.engstruct.2016.01.058.

[176] Manfredi G, Pecce M. A refined R.C. beam element including bond-slip relationship for the analysis of continuous beams. Comput Struct 1998;69:52–63.

[177] McKinley D. Field observations of structures damaged by settlements. J Soil Mech Found Div 1964:249–68.

[178] Boscardin MD, Cording EJ. Building Response To Excavation-Induced Settlement. J Geotech Eng 1989;115:1–21. doi:10.1061/(ASCE)0733-9410(1989)115:1(1).

[179] Meyerhof GG. The settlement analysis of building frames. Struct Eng 1947:369–409.

[180] Bishara AG, Jang S-Z. Settlement-induced forces in concrete bridges. J Struct Div 1980:1423–36.

[181] Skempton AW, Macdonald DH. The allowable settlements of buildings. Proc Inst Civ Eng 1956;5:727–68. doi:10.1680/ipeds.1956.12202.

[182] Polshin DE, Tokar RA. Maximum Allowable Non-uniform Settlement of Structures. Proc. 4th Int. Conf. Soil Mech. Found. Eng., London: 1957.

[183] Poulos HG, Carter JP, Small JC. Foundations and retaining structures -

Research and practice. Proc. XV Int. Conf. Soil Mech. Found. Eng., Istambul: 2001, p. 2527–606.

[184] Burland JB, Wroth CP. Settlement of buildings and associated damage. Proc Br Geotech Soc Conf Settl Struct 1974:611–54.

[185] Boone SJ. Ground-movement-related building damage. J Geotech Eng 1996;122:886–96.

[186] Finno RJ, Voss Jr FT, Rossow E, Blackburn JT. Evaluating Damage Potential in Buildings Affected by Excavations. J Geotech Geoenvironmental Eng 2005;131:1199–210. doi:10.1061/ASCE1090-0241200513 1:101199.

[187] Negulescu C, Foerster E. Parametric studies and quantitative assessment of the vulnerability of a RC frame building exposed to differential settlements. Nat Hazards Earth Syst Sci 2010;10:1781–92. doi:10.5194/nhess-10-1781-2010.

[188] Fotopoulou S, Karafagka S, Pitilakis K. Vulnerability assessment of low-code reinforced concrete frame buildings subjected to liquefaction-induced differential displacements. Soil Dyn Earthq Eng 2018;110:173–84. doi:10.1016/j.soildyn.2018.04.010.

[189] Miano A, Mele A, Prota A. Fragility curves for different classes of existing RC buildings under ground differential settlements. Eng Struct 2022;257. doi:10.1016/j.engstruct.2022.114077.

[190] Cigna F, Lasaponara R, Masini N, Milillo P, Tapete D. Persistent scatterer interferometry processing of COSMO-skymed stripmap HIMAGE time series to depict deformation of the historic centre of Rome, Italy. Remote Sens 2014;6:12593–618. doi:10.3390/rs61212593.

[191] Osmanoğlu B, Sunar F, Wdowinski S, Cabral-Cano E. Time series analysis of InSAR data: Methods and trends. ISPRS J Photogramm Remote Sens 2016;115:90–102. doi:10.1016/j.isprsjprs.2015.10.003.

[192] Cascini L, Ferlisi S, Fornaro G, Lanari R, Peduto D, Zeni G. Subsidence monitoring in Sarno urban area via multi-temporal DInSAR technique. Int J Remote Sens 2006;27:1709–16. doi:10.1080/01431160500296024.

[193] Stramondo S, Bozzano F, Marra F, Wegmuller U, Cinti FR, Moro M, et al. Subsidence induced by urbanisation in the city of Rome detected by advanced InSAR technique and geotechnical investigations. Remote Sens Environ 2008;112:3160–72. doi:10.1016/j.rse.2008.03.008.

[194] Scifoni S, Bonano M, Marsella M, Sonnessa A, Tagliafierro V, Manunta M, et al. On the joint exploitation of long-term DInSAR time series and geological information for the investigation of ground settlements in the town of Roma (Italy). Remote Sens Environ 2016;182:113–27. doi:10.1016/j.rse.2016.04.017.

[195] Cerchiello V, Tessari G, Velterop E, Riccardi P, Defilippi M, Pasquali P. Building Damage Risk by Modeling Interferometric Time Series. IEEE Geosci Remote Sens Lett 2017;14:509–13. doi:10.1109/LGRS.2017.2651938.

[196] Peduto D, Nicodemo G, Maccabiani J, Ferlisi S. Multi-scale analysis of settlement-induced building damage using damage surveys and DInSAR data: A case study in The Netherlands. Eng Geol 2017;218:117–33. doi:10.1016/j.enggeo.2016.12.018.

[197] Drougkas A, Verstrynge E, Van Balen K, Shimoni M, Croonenborghs T, Hayen R, et al. Country-scale InSAR monitoring for settlement and uplift damage calculation in architectural heritage structures. Struct Heal Monit 2020. doi:10.1177/1475921720942120.

[198] Bru G, Herrera G, Tomás R, Duro J, de la Vega R, Mulas J. Control of deformation of buildings affected by subsidence using persistent scatterer interferometry. Struct Infrastruct Eng 2013;9:188–200. doi:10.1080/15732479.2010.519710.

[199] Yang K, Yan L, Huang G, Chen C, Wu Z. Monitoring building deformation with InSAR: Experiments and validation. Sensors (Switzerland) 2016;16. doi:10.3390/s16122182.

[200] Weissgerber F, Colin-Koeniguer E, Nicolas JM, Trouvé N. 3D monitoring of buildings using TerraSAR-X InSAR, DInSAR and PolSAR capacities. Remote Sens 2017;9. doi:10.3390/rs9101010.

[201] Miano A, Mele A, Calcaterra D, Martire D Di, Infante D, Prota A, et al. The use of satellite data to support the structural health monitoring in areas affected by slow-moving landslides: a potential application to reinforced concrete buildings. Struct Heal Monit 2021. doi:10.1177/1475921720983232.

[202] Di Carlo F, Miano A, Giannetti I, Mele A, Bonano M, Lanari R, et al. On the integration of multi-temporal synthetic aperture radar interferometry products and historical surveys data for buildings structural monitoring. J Civ Struct Heal Monit 2021;11:1429–47. doi:10.1007/s13349-021-00518-4.

[203] Di Martire D, Iglesias R, Monells D, Centolanza G, Sica S, Ramondini M, et al. Comparison between Differential SAR interferometry and ground measurements data in the displacement monitoring of the earth-dam of Conza della Campania (Italy). Remote Sens Environ 2014;148:58–69. doi:10.1016/j.rse.2014.03.014.

[204] Milillo P, Perissin D, Salzer JT, Lundgren P, Lacava G, Milillo G, et al. Monitoring dam structural health from space: Insights from novel InSAR techniques and multi-parametric modeling applied to the Pertusillo dam Basilicata, Italy. Int J Appl Earth Obs Geoinf 2016;52:221–9. doi:10.1016/j.jag.2016.06.013.

[205] Emadali L, Motagh M, Haghshenas Haghighi M. Characterizing post-construction settlement of the Masjed-Soleyman embankment dam, Southwest Iran, using TerraSAR-X SpotLight radar imagery. Eng Struct 2017;143:261–73. doi:10.1016/j.engstruct.2017.04.009.

[206] Sousa JJ, Bastos L. Multi-temporal SAR interferometry reveals acceleration of bridge sinking before collapse. Nat Hazards Earth Syst Sci 2013;13:659–67. doi:10.5194/nhess-13-659-2013.

[207] Lazecky M, Perissin D, Bakon M, Sousa JM, Hlavacova I. Potential of satellite InSAR techniques for monitoring of bridge deformations IT 4Innovations VSB-TU Ostrava Ostrava, Czech Republic milanUazecky@vsblcz. 2015.

[208] Hoppe E, Bruckno B, Campbell E, Acton S, Vaccari A, Stuecheli M, et al. Transportation Infrastructure Monitoring Using Satellite Remote Sensing.

Mater. Infrastructures, vol. 1(5), 2016, p. 185–98.

[209] Cusson D, Trischuk K, Hébert D, Hewus G, Gara M, Ghuman P. Satellite-Based InSAR Monitoring of Highway Bridges: Validation Case Study on the North Channel Bridge in Ontario, Canada. Transp Res Rec 2018;2672:76–86. doi:10.1177/0361198118795013.

[210] Selvakumaran S, Plank S, Geiß C, Rossi C, Middleton C. Remote monitoring to predict bridge scour failure using Interferometric Synthetic Aperture Radar (InSAR) stacking techniques. Int J Appl Earth Obs Geoinf 2018;73:463–70. doi:10.1016/j.jag.2018.07.004.

[211] Milillo P, Giardina G, Perissin D, Milillo G, Coletta A, Terranova C. Pre-collapse space geodetic observations of critical infrastructure: The Morandi Bridge, Genoa, Italy. Remote Sens 2019;11. doi:10.3390/rs11121403.

[212] Milillo P, Giardina G, Perissin D, Milillo G, Coletta A, Terranova C. Supplementary Materials: Pre-Collapse SpaceGeodetic Observations of Critical Infrastructure: TheMorandi Bridge, Genoa, Italy. Remote Sensing 2019, 6,Article No. remotesensing-506958. Remote Sens 2019;8:S1–6. doi:10.3390/S1.

[213] Lanari R, Reale D, Bonano M, Verde S, Muhammad Y, Fornaro G, et al. Comment on "Pre-Collapse Space Geodetic Observations of Critical Infrastructure: The Morandi Bridge, Genoa, Italy" by Milillo et al. (2019). Remote Sens 2020;12:4011. doi:10.3390/rs12244011.

[214] Milillo P, Giardina G, Perissin D, Milillo G, Coletta A, Terranova C. Reply to Lanari, R., et al. comment on "pre-collapse space geodetic observations of critical infrastructure: The morandi bridge, Genoa, Italy" by Milillo et al. (2019). Remote Sens 2020;12:1–5. doi:10.3390/rs12244016.

[215] Cusson D, Rossi C, Ozkan IF. Early warning system for the detection of unexpected bridge displacements from radar satellite data. J Civ Struct Heal Monit 2021;11:189–204. doi:10.1007/s13349-020-00446-9.

[216] Macchiarulo V, Milillo P, Blenkinsopp C, Giardina G. Monitoring deformations of infrastructure networks: A fully automated GIS integration and analysis of InSAR time-series. Struct Heal Monit 2022. doi:10.1177/14759217211045912.

[217] Farneti E, Cavalagli N, Costantini M, Trillo F, Minati F, Venanzi I, et al. A method for structural monitoring of multispan bridges using satellite InSAR data with uncertainty quantification and its pre-collapse application to the Albiano-Magra Bridge in Italy. Struct Heal Monit 2022. doi:10.1177/14759217221083609.

[218] Mair RJ, Taylor RN, Burland JB. Prediction of ground movements and assessment of risk of building damage due to bored tunnelling. Proc. Int. Symp. Geotech. Asp. Undergr. Constr. Soft Gr., London: A.A. Balkema; 1996, p. 713–8.

[219] Halim D, Wong KS. Prediction of Frame Structure Damage Resulting from Deep Excavation. J Geotech Geoenvironmental Eng 2012;138:1530–6. doi:10.1061/(asce)gt.1943-5606.0000682.

[220] FEMA. FEMA 356 - Prestandard and commentary for the seismic rehabilitation of buildings. 2000.

[221] Di Domenico M, Ricci P, Verderame GM. Empirical calibration of hysteretic

parameters for modelling the seismic response of reinforced concrete columns with plain bars. Eng Struct 2021;237. doi:10.1016/j.engstruct.2021.112120.

[222] Peck RB. Deep excavations and tunneling in soft ground. Proc. 7th Int. Conf. Soil Mech. Found. Eng., 1969, p. 225–90.

[223] Attewell PB, Yeates J, Selby AR. Soil movements induced by tunnelling and their effects on pipelines and structures. 1986.

[224] Colesanti C, Wasowski J. Investigating landslides with space-borne Synthetic Aperture Radar (SAR) interferometry. Eng Geol 2006;88:173–99. doi:10.1016/j.enggeo.2006.09.013.

[225] Franceschetti G, Lanari R. Synthetic Aperture Radar Processing. CRC Press LLC: Boca Raton, FL; 1999.

[226] TRE Altamira. InSAR at a glance 2022. https://site.tre-altamira.com/insar/ (accessed June 30, 2022).

[227] Bürgmann R, Rosen PA, Fielding EJ. Synthetic aperture radar interferometry to measure Earth's surface topography and its deformation. vol. 28. 2000.

[228] Sansosti E, Berardino P, Bonano M, Calò F, Castaldo R, Casu F, et al. How second generation SAR systems are impacting the analysis of ground deformation. Int J Appl Earth Obs Geoinf 2014;28:1–11. doi:10.1016/j.jag.2013.10.007.

[229] Talledo DA, Miano A, Bonano M, Di Carlo F, Lanari R, Manunta M, et al. Satellite radar interferometry: Potential and limitations for structural assessment and monitoring. J Build Eng 2022;46. doi:10.1016/j.jobe.2021.103756.

[230] Ferretti A, Prati C, Rocca F. Permanent scatterers in SAR interferometry. IEEE Trans Geosci Remote Sens 2001;39:8–20. doi:10.1109/36.898661.

[231] Ferretti A, Fumagalli A, Novali F, Prati C, Rocca F, Rucci A. A new algorithm for processing interferometric data-stacks: SqueeSAR. IEEE Trans. Geosci. Remote Sens., vol. 49, 2011, p. 3460–70. doi:10.1109/TGRS.2011.2124465.

[232] Hooper A, Zebker H, Segall P, Kampes B. A new method for measuring deformation on volcanoes and other natural terrains using InSAR persistent scatterers. Geophys Res Lett 2004;31:1–5. doi:10.1029/2004GL021737.

[233] Foumelis M. Vector-based approach for combining ascending and descending persistent scatterers interferometric point measurements. Geocarto Int 2018;33:38–52. doi:10.1080/10106049.2016.1222636.

[234] Berto L, Doria A, Saetta A, Stella A, Talledo DA. Assessment of the applicability of DInSAR techniques for structural monitoring of cultural heritage and archeological sites. Civ. Struct. Heal. Monit. Proc. CSHM-8 Work., Naples: Springer; 2021.

Acknowledgements

This dissertation would not have been completed without the contribution of many people, who cheered for me and supported and helped me tirelessly all along the way. I would like to thank them all deeply.

First of all, I would like to express my deepest gratitude to my supervisor, Prof. Anna Saetta, who offered me the opportunity to undertake this challenging and joyful journey. Her experienced guidance and constant availability to discuss ideas, proposals and even troubling situations, have been really a fundamental aid in the completion of this work. She also granted me the priceless freedom of pursuing my research following my own instinct and attitudes. It is an opportunity that not everyone can find enjoyable, but also which is not so often everybody granted. In addition, she really made possible for me to address various research topics and to develop them by working with different groups also from other research institutions. In such a context, her vast knowledge on many civil engineering and structural mechanics aspects was really helpful in navigating this dense and multifaceted journey.

I would like to thank my co-supervisor, Dr. Luisa Berto, for the tireless support and for being a constant source of inspiration and knowledge on concrete structures mechanics. She often provided me with many materials which would have been very hard to find without her broad as well as deep experience in this field. She also is a good mentor, and discussions with her helped me not only in the research work, but also in dealing with the overall experience of the PhD. She has been always available even in hard times, those times when anyone needs to see the light to overcome the troubles.

I would like to thank my co-supervisor, Dr. Diego Alejandro Talledo, who introduced me to the field of nonlinear numerical analyses of concrete and masonry structures, in which he has an extensive and broad experience. It was from him that I learned the uncompromised attitude and the critic analytical view which are the keys to do scientific research. We also had the opportunity to share together some social moments at conferences and meetings, during which I got to see the cheerful person and mentor he is, beyond the dedicated scientist. He has been always available for discussing my research and to provide useful suggestions and comments, which very often proved to be highly relevant to improve the work.

I would like to thank Prof. Max Hendriks for having hosted me in the Concrete Structures group at TU Delft for my visiting research period abroad. This has been one of the most valuable experiences in my life so far, not only because of the opportunities I had to share and discuss research aspects and ideas, but especially for the wonderful people I met and for the experience of living in another country and of learning many new things. His kindness and constant availability made me feel welcome from day one. In addition, discussions with him have been always fruitful and useful to improve my work and my research attitude.

I would like to thank Prof. Alberto Meda and Dr. Yuguang Yang for the reviews and useful comments they provided for the improvement of the thesis. I am very grateful to Prof. Meda, who also granted me the valuable opportunity to develop a part of my research work with experiments on corroded beams performed at Tor Vergata University in Rome, allowing me to "touch with my hands" many aspects related to deterioration of reinforced concrete elements due to reinforcement corrosion. Dr. Yuguang Yang allowed me to work with him on a very interesting topic during my research stay at TU Delft, combining the problems on shear behaviour of concrete elements with those due to rebars corrosion, always sharing with me his genuine passion and dedication for research. Discussions with him have been always enlightening and his availability to explain to me concepts which were new to me has been really a precious help.

I would like to thank Prof. Roberto Scotta and Prof. Antonia Larese, who from the beginning believed in me and supported me on many occasions, with suggestions and encouragements. I would like to thank Dr. Lorenzo De Stefani, who hosted me in his office in the very first months of my PhD. Together, we shared quite a lot of nice moments, and his friendship is a precious gift to me. I would like to thank Eng. Alessandro Gasparini, whose sharp mind and vast knowledge on structural behaviour of concrete structures have been really helpful in improving some aspects of the research work. I also would like to mention my gratitude to Prof. György Balázs, for the kind encouragements and the suggestions he provided me at the *fib* PhD Symposium and in Venice.

I would like to thank all the nice, kind and very supportive colleagues and friends with whom I shared this journey. In particular, Gianluca Bottin, Sara Brandolese, Luca Franco, Giovanni Frison, Enrico Lazzarini, Luca Marchi, Valentina Pertile and Davide Trutalli. One particular thanks goes to Irene Rocca, with whom I shared the office in the second half of my PhD, and who always supported (and put up with) me on good and bad days. Her help and support were really valuable to me, especially during the period when I wrote this thesis. Another great thanks goes to Gianluca Aldrighetti, who on the beginning of my PhD asked me to start collaborating with him to tackle some problems on ductility of reinforced concrete members. Little did I know that I was entering the rabbit hole that would have later provided me with the main topic of my research.

I would like to thank all the wonderful people I met in the Concrete Structures group at TU Delft, in particular Beyazit Aydin, Albert Bosman, Hao Cheng, Yitao Huang, Mohammed Ibrahim, Jiandong Lu, Shozab Mustafa, Sandra Nunes, Jakub Pawlowicz, Mauro Poliotti, Zhenxu Qian, Daniela Tavera-Diaz, Gabriela Zarate Garnica, Fengqiao Zhang and Yubau Zhou. They made me feel at home from the first day we met, and the time we spent together seemed far longer than the six months I spent in Delft. We shared many nice moments and also had several very useful discussions dealing with research aspects of concrete structures. Their friendship is without doubt the most precious gift I received from my experience abroad.

I would like to thank all the teachers I have had during my years of study. Studying and learning is a privilege that we often take for granted. Even more underestimated, is sometimes the contribution a teacher can make to students. Not in terms of knowledge transfer, but through increasing curiosity, self-esteem and awareness of their own capabilities and desires. In particular, I would like to thank Prof. Pier Francesco Costantini and Prof. Umberto Ghione, who fostered my curiosity towards civil engineering. Moreover, I would like to thank Prof. Rosa Volpi, my math teacher in high school, who taught with great passion and believed in me. I am sometimes surprised, and at the same time grateful, that mechanical behaviour of a reinforced concrete section can be in some cases described by a simple quadratic function.

I would like to thank my whole family, who has been always with me during this journey.

In particular, I would like to thank my brothers Enrico and Riccardo, who are at the same time wonderful friends and with whom we have shared countless nice and fun moments, as well as many important ones.

I would also like to thank all my friends, that always cheer me up and have often encouraged me during the PhD.

My greatest gratitude goes to Serena, who has constantly and tirelessly stood by my side and cheered for me all along the way, with love. We have grown and changed a lot, together. She can understand me on the fly, and I am deeply grateful for the wonderful life we share together. Thank you for being with me. Life is beautiful, with you.

Finally, I wish to deeply thank my parents, Loredana and Vanni, whose unconditional love I have received since I was born, and who always supported me. This work is thanks to them.

Civil structures and infrastructure can be exposed to various hazards that can induce other internal actions in addition to those due to service loads. In various situations, structures need to be able to deform almost not reducing their strength and without fail, to some extent. In other words, they must have sufficient *deformation capacity*.

Such an ability is for example very useful to accommodate redistribution of internal actions in statically indeterminate structures, as well as to avoid failure due to imposed deformations such as those due to differential ground settlements below the foundations. In addition, in many cases inelastic deformation capacity really is a fundamental property for structures, e.g. when they should be able to survive strong earthquakes without collapsing.

In this work, deformation capacity of reinforced concrete beams is addressed, first providing an analytical framework to analyze deformation capacity and ductility at sectional level. Then, the simulation performances of different practice-oriented analytical and numerical modelling approaches are tested, with the aim of check their capability in providing estimations of the failure mode and deformation capacity of both sound and corroded reinforced concrete beams, understanding some of the current limits of this type of approaches. Finally, in order to foster possible improvements in the estimation of deformation demands in buildings subjected to ground settlements, the applications of a promising satellite remote sensing technique (MT-DInSAR) to monitor ground deformations in urban areas has been analyzed, highlighting major potentials and current limitations.

Overall, the tools and insights proposed in the present work aim to be useful in fostering the improvement of engineering practices employed for performance-based design and assessment of reinforced concrete structures.

IUAV
Università Iuav
di Venezia